

University of Nottingham

UK | CHINA | MALAYSIA

Design of lattice structures with optimised and intrinsic thermomechanical isolation

By

Poom Juasiripukdee

Thesis submitted to the University of Nottingham for the degree of Doctor of Philosophy

March 2023

Abstract

The geometrical complexity enabled by additive manufacturing (AM) provides new functionalities that have not previously been possible because of tool access limits in machining processes. Structure with low or tailorable coefficients of thermal expansion (CTE) are a growing research topic, with applications identified in aerospace, optical measurement systems, and precision instruments. In this thesis, I propose a new and practicable design method for tessellating cellular (or lattice) structures which provide low planar CTE, with an emphasis on meeting the performance requirements of a precision instrument support frame. The research presents the low planar CTE bi-material structural design concept, based on a repeating AM unit cell and high-CTE inserts. The design is an assembly of two parts: a lattice outer part and a cylindrical inner part, made of homogenous materials with different positive CTEs. To study thermal expansion, finite element modelling is used on thirteen lattice designs. The numerical models show that one lattice design (the final variation) using Nylon 12 and ultra-high molecular weight polyethylene (UHMWPE) yielded an effective in-plane CTE of 1×10^{-9} K^{-1} (cf. 109×10^{-6} K^{-1} for solid Nylon 12). Moreover, the numerical models also show that planar tailored thermal expansion can be achieved by controlling the internal AM lattice geometry and by suitable selection of fabrication materials. To investigate the CTE of the structures, a thermal expansion experiment is developed and conducted using an interferometric dilatometer with a plane mirror technique and a hot plate. Steel gauge blocks with linear CTEs of 11.5×10^{-6} K^{-1} are used as reference materials to verify the experiment, measured in the range of 30 °C to 34 °C. The total uncertainty of the measurement is evaluated following the Guide to the expression of uncertainty in measurement (GUM), and estimated from measurements of three different lengths of specimens (40 mm, 50 mm and 60 mm) to be 2.4 to 3.3×10^{-6} K^{-1} on the steel gauge material. The percentage errors of the measured CTEs of the steel gauge materials compared to the data sheet are approximately ± 2%. The thermal expansion experiment is used to measure the CTEs of the Nylon 12 lattice outer part, the UHMWPE cylindrical inner part, and two selected lattice structures. The percentage errors of the measured CTEs of the Nylon 12 lattice outer part and the UHMWPE cylindrical inner part materials compared to the data sheet are approximately 2% and 12%, respectively. However, for the two selected lattice structures, the CTEs obtained from the experimental results show significant differences from the simulated results. These results highlight that thermal expansion experiments can be improved to achieve more accurate CTE results from measuring all specimens. Factors leading to CTE uncertainties are also determined, by using one lattice structure to demonstrate the key parameters in terms of configurations and material properties. Finally, I demonstrate the use of the final iteration of the low planar CTE bi-material structural design concept in this PhD including the

restrictions for implementation, elastic modulus determination, and deformation mechanism determination. The final iteration is implemented into a lattice structure for a metrology frame of an optical vertical dilatometer. In this study, I discuss the outcomes of the thesis as a whole, showing that the combination of design optimisation and additive manufacturing can be used to achieve low CTE structures and, therefore, low thermal expansion machine frames of a few tens of centimetres in height. These results are essential for engineering structures for low or tailorable CTE within the macro-scale of materials. In future work, thermal and mechanical performances can be improved by exploring new unit cell designs and new materials for additive manufacturing.

Declaration

I, Poom Juasiripukdee, hereby declare that this thesis titled “Design of lattice structures with optimised and intrinsic thermomechanical isolation” is my work from the time of my PhD at the University of Nottingham under the supervision of Professor Richard Leach, Professor Ian Ashcroft and Dr Ian Maskery and that it has never been previously submitted for the award of any degree, diploma or any similar type of recognition, except as specified in the text.

This work has been funded by the Ministry of Science and Technology of Thailand.

Acknowledgements

First and foremost, I would like to thank Professor Richard Leach for giving me the precious opportunity to do my PhD at the University of Nottingham. I would like to express my gratitude to my supervisors Professor Richard Leach, Professor Ian Ashcroft, and especially Dr Ian Maskery for their support, patience, motivation and precious knowledge. I am really appreciative of the help my supervisors gave to me when I was conducting the research and writing the thesis. Many thanks to my internal assessor Dr Samanta Piano for her valuable comments and feedback. My appreciation also extends to all staff and technicians at the Advanced Manufacturing Technology Research Group, Centre for Additive Manufacturing and Faculty of Engineering at the University of Nottingham for all of their support during my PhD research. I would also like to thank my colleagues Waiel Elmadih, Ifeanyichukwu Echeta, Rong Su, Amrozia Shaheen, Adam Thomson, Wahyudin Syam, Teguh Santoso, Karim Shah, Lars Körner, Sofia Catalucci, Carlos Gomez, Afaf Remani, Helia Hooshmand and Mohammed Isa, for helping me in so many ways.

I would also like to thank all my friends in Nottingham and Thailand, who have been very supportive during my PhD research. Last but not least, I am deeply grateful to my lovely family (my father Mongkol, my mother Puangthong, and my two lovely sisters Pim and Pan) for their love, support and encouragement. I have received much from them over the years, and I would not be where I am today without them.

Publications

Journal paper

Juasiripukdee P, Maskery I, Ashcroft I and Leach R 2021 Low thermal expansion machine frame designs using lattice structures *Applied Sciences* **11** 9135

Poster

Juasiripukdee P, Maskery I, Ashcroft I and Leach R 2020 Low thermal expansion machine frame designs using lattice structures. In: Special Interest Group: Thermal Issues, (Aachen, Germany: euspen)

Table of Contents

Abstract 2

Declaration 4

Acknowledgements 5

Publications 6

Journal paper 6

Poster 6

List of Figures 12

List of Tables 21

1 Introduction 23

1.1 Background to the project 23

1.2 Research questions 28

1.3 Thesis structure 28

2. A review of low thermal expansion machine frame designs using lattice structures 30

2.1. Introduction to low thermal expansion machine frame design using lattice structures 30

2.2. Design of precision machine frames 30

2.2.1. Loops 31

2.2.2. Stiffness 33

2.2.3. Structural Configurations 33

2.2.4. Kinematics in the design of a precision machine 34

2.2.5. Material selection 36

2.3. Lattice structure 40

2.4. Designed lattice structure for thermal expansion 44

2.5. Manufacturing of lattice structures for thermal performance 56

2.6. Testing the lattice structures 61

2.7. Conclusion 65

3. Methodology and method 66

3.1. Methodology and method for the design of lattice structures for low coefficient of thermal expansion 68

3.2. Methodology and method for finite element simulation of lattice structures 72

3.3. Methodology and method for the manufacture of the lattice structures 76

3.4. Methodology and method for the thermal expansion experimentation of the lattice structures 79

3.5. Conclusion 83

4. Design of lattice structures for low coefficient of thermal expansion 84

4.1. Introduction to the design of lattice structures for low coefficient of thermal expansion 84

4.2. Method for the design of lattice structures for low coefficient of thermal expansion 85

4.3. Evolution of designs 88

4.3.1. Iteration 1 series 90

4.3.2. Iteration 2 series 94

4.3.3. Iteration 3 series 100

4.3.4. Iteration 4 series 103

4.4. Results of the lattice structure for low coefficient of thermal expansion 112

4.4.1. Low planar CTE lattice results 112

4.4.2. Low planar CTE lattice results obtained by varying design parameters 114

4.4.3. Pattern selection for low-CTE lattice design 118

4.5. Discussion of lattice structures for low coefficient of thermal expansion 120

4.6. Conclusion 123

5. Finite element simulation of lattice structures 124

5.1. Introduction to finite element simulation of lattice structures 124

5.2. Method for the finite element simulation of the lattice structures 125

5.3. Parameters affecting finite element results 132

5.3.1. Method: procedure type 132

5.3.2. Method: boundary conditions 133

5.3.3. Finite element mesh: creating partitions for contact 134

5.3.4. Finite element mesh: creating partitions for mesh density reduction 135

5.3.5. Finite element mesh: mesh type 137

5.4. Discussion of finite element simulation of lattice structures 140

5.5. Conclusion 141

6. Lattice structure thermal expansion experiments 142

6.1. Method for thermal expansion experimentation for lattice structures 142

6.2. Experimental hardware design 150

6.2.1. Heating system 151

6.2.2. Laser interferometer system 152

6.2.3. Thermal expansion experimental frame 154

6.3. Experimental correction and uncertainty 155

6.3.1. Mathematical model of the measurement 159

6.3.2. Standard uncertainties of the displacement measurement system 162
6.4. Experimental validation and results 170
6.4.1. Experimental validation 170
6.4.2. Experimental results 172
6.5. Determination of the main influencing factors on CTE results of Iteration 3.1 176
6.6. Discussion of lattice structure thermal expansion experiments 178
6.7. Conclusion 183
7. Implementation of the lattice structures into a metrology frame 185
7.1. Implementation of Iteration 4.1 into a metrology frame 185
7.1.1. Elastic modulus determination 187
7.1.2. Determination of the deformation mechanism 188
7.1.3. Implementation of Iteration 4.1 for an optical vertical dilatometer 192
7.2. Discussion of Implementation of the lattice structures into a metrology frame 194
7.3. Conclusion 195
8. General discussion, conclusions and future work 197
8.1. General discussion of the thesis 197
8.1.1. Contribution 1 197
8.1.2. Contribution 2 198
8.2. Conclusions 200
8.3. Future work 200
8.3.1. Design of lattice structures for low coefficient of thermal expansion 200
8.3.2. Finite element simulation of lattice structures 201

8.3.3. Thermal expansion experiments for lattice structures 201

8.3.4. Implementation of the lattice structures into a metrology frame 202

Bibliography 203

Appendix 213

Engineering drawing of Iteration 2.4 213

Engineering drawing of Iteration 3.1 214

Engineering drawing of Iteration 4.1 215

List of Figures

Figure 1.1 Illustration of an example of heat transfer mechanisms, from the Zippy Facts website [8]. 24

Figure 1.2 Schematic representation of a CMM. 25

Figure 1.3 Schematic representation of a horizontal optical dilatometer 26

Figure 1.4 Example of lattice structures from 3D Printing [26]. 27

Figure 2.1 Illustration of frame configurations (a) open section frame and (b) closed section frame, taken from Precision Machine Design [27]. 34

Figure 2.2 Common types of kinematic couplings: type I Kelvin clamp (left), type II Kelvin clamp (right), taken from Basics of Precision Engineering [32] 35

Figure 2.3 Geometrical parameters for a ball-groove kinematic coupling (the illustration was taken from Basics of Precision Engineering [32]). 36

Figure 2.4 Elastic modulus E plotted against density ρ, taken from Materials Selection in Mechanical Design 5th Edition [40]. 37

Figure 2.5 The linear thermal expansion coefficient α plotted against thermal conductivity λ, taken from Materials Selection in Mechanical Design 5th Edition [40] 38

Figure 2.6 Thermal conductivity λ plotted against thermal diffusivity *a*, taken from Materials Selection in Mechanical Design 5th Edition [40]. 38

Figure 2.7 Examples of cellular solids. (a) a cancellous bone [56], (b) a foam [57], and (c) a honeycomb [58]. 40

Figure 2.8 Examples of lattice structures. (a) a bone segment [52], (b) a car seat [53], (c) a shoe midsole [54] and (d) a helmet [55]. 41

Figure 2.9 Examples of shapes of composed structures. (a) strut-based [18] (b) surface-based structures [17] 42

Figure 2.10 Examples of geometrical dimensions. (a) 2D [65] and (b) 3D lattice structures [66]. 42

Figure 2.11 Examples of tailored thermal expansion dimensions (a) 2D [67] and (b) 3D [68]. 42

Figure 2.12 Examples of lattice structures using TO (a unit cell boundary is presented in the dashed square box), where red regions represent high-CTE phases, blue regions represent low-CTE phases, and white regions represent voids [77]. 45

Figure 2.13 Lakes lattice. (a) a hexagonal lattice cell with curved bi-material ribs and (b) a tetrakaidecahedral foam cell [82]. 46

Figure 2.14 An example of a 2D microstructural architecture achieving tunable thermal expansion [88]. 46

Figure 2.15 Illustration of hexagonal lattice material designed for zero thermal expansion and maximum specific stiffness in bending by Parsons [24]. 47

Figure 2.16 UCSB lattices: stretch-dominated planar lattices (grey is a high-CTE phase and black is a low-CTE phase) [90]. 48

Figure 2.17 Lattice proposed by Jefferson et al.: a planar hexagonal grid thermally stable structure (grey is high expansion phase, yellow is low expansion phase, and white is void) [93]. 48

Figure 2.18 Workflow of additive manufacturing processes [96]. 56

Figure 2.19 Stereolithography setup [100]. 57

Figure 2.20 PolyJet technology setup [102]. 58

Figure 2.21 Selective Laser Sintering setup [100]. 59

Figure 2.22 Examples of 3D metamaterials produced by cutting metallic sheets, then assembled and bonded using either brazing or laser welding [66]. 59

Figure 2.23 An example of bimetal antichiral metamaterials with ligaments and nodes [86]. 60

Figure 2.24 Illustration of the construction of a Michelson-type with retroreflectors. 63

Figure 2.25 Illustration of the conceptual configuration of a plane mirror interferometer. 64

Figure 3.1 Overall methodology of the project. 67

Figure 3.2 Processes of the design of lattice structures for low coefficient of thermal expansion. 70

Figure 3.3 Concept of a typical single unit cell (left) and a 4 × 4 lattice structure (right).....71

Figure 3.4 Processes of the finite element simulation of lattice structures.....74

Figure 3.5 Example of how the cylindrical inner part (red) was inserted into the centre of the lattice outer part (blue).....77

Figure 3.6 First batch of the specimens' lattice outer parts (Iteration 2.4) in different sizes: (1) (18.96 × 18.96 × 18.96) mm, (2) (23.69 × 23.69 × 23.69) mm, (3) (28.43 × 28.43 × 28.43) mm, (4) (37.91 × 37.91 × 37.91) mm and (5) (47.39 × 47.39 × 47.39) mm.....78

Figure 3.7 Processes of thermal expansion experimentation for lattice structures.....80

Figure 4.1 Concept of a single unit cell (left) and a 4 × 4 lattice structure (right) of tailorable thermal expansion structure in this PhD.....85

Figure 4.2 Illustration of the creation of a model using lattice outer part of Iteration 3 as an example. (a) A 2D sketch of a layer, (b) a 2D model of a layer of the lattice outer part with examples of parametric constraints, (c) a 3D model of the four different orientational stacked layers and (d) a 3D model of the lattice outer part.....87

Figure 4.3 Illustrations of the evolution of designs.....89

Figure 4.4 Configurational concept of the tailorable thermal expansion lattice structure: (a) the 1D lattice before the temperature rise, (b) the 1D lattice after the temperature rise, (c) the developing 2D lattice before the temperature rise, (d) the developing 2D lattice after the temperature rise, (e) the trimmed 2D lattice before the temperature rise, and (f) the trimmed 2D lattice after the temperature rise.....91

Figure 4.5 Illustrations of Iteration 1 (a) before temperature change (blue is the lattice outer part with low CTE and red is the cylindrical inner part with high CTE) and (b) a contour plot of strain in the Z-axis after temperature rise with the deformation factor of 5 (the black lines denote the undeformed configurations).....92

Figure 4.6 Illustration of Iteration 1.1.....93

Figure 4.7 Illustration of Iteration 1.2: (a) the 90 ° rotated layer, (b) isometric view, and (c) a contour plot of von Mises Stress following temperature rise with a deformation factor of 3.....94

Figure 4.8 Illustration of Iteration 2 (a) top view of a layer with annotations, (b) top view of a layer coloured by parts (c) top view of a pair of two opposite layers, (d) isometric view of a pair of two opposite layers controlled thermal expansion in the Z-axis, (e) isometric view of a pair of two opposite layers controlled thermal expansion in the X-axis and (f) isometric view of a unit cell. 96

Figure 4.9 Contour plots of von Mises Stress after the temperature rise for Iteration 2.4 with a deformation factor of 1. 97

Figure 4.10 Contour plots of strain after the temperature rise for Iteration 2.4 with a deformation factor of 1: (a) the unit cell strain in the X-axis and (b) the unit cell strain in the Z-axis. 97

Figure 4.11 Illustration of Iteration 2 series (a) top view of Iteration 2.1, (b) top view of Iteration 2.2, (c) top view of Iteration 2.3, (d) top view of Iteration 2.4 and (e) isometric view of Iteration 2.4. 98

Figure 4.12 Iteration 2 with the five configurations considered. 99

Figure 4.13 Iteration 3 (a) top view of a layer with annotations and (b) isometric view of a unit cell with annotations. 101

Figure 4.14 Contour plots of von Mises Stress after the temperature rise for Iteration 3.1 with a deformation factor of 1. 102

Figure 4.15 Contour plots of strain after the temperature rise for Iteration 3.1 with a deformation factor of 1: (a) the unit cell strain in the X-axis and (b) the unit cell strain in the Z-axis. 102

Figure 4.16 Iteration 3 with the five configurations considered. 103

Figure 4.17 Designing spaces: (a) previous Iterations and (b) Iteration 4 series. 104

Figure 4.18 Iteration 4: (a) top view of a layer with annotations and (b) isometric view of a unit cell with annotations. 106

Figure 4.19 Contour plots of von Mises Stress after the temperature rise for Iteration 4 with a deformation factor of 2: (a) the unit cell with a plane for cross-section and (b) the unit cell with the cross-sectional area. 107

Figure 4.20 Contour plots of strain after the temperature rise for Iteration 4 with a deformation factor of 1: (a) the unit cell strain in the X-axis and (b) the unit cell strain in the Z-axis. 107

Figure 4.21 Iteration 4.1: (a) top view of a layer with annotations and (b) isometric view of a unit cell with annotations. 109

Figure 4.22 Contour plots of von Mises Stress after temperature rise for Iteration 4.1 with a deformation factor of 2 (a) the unit cell with a plane for cross-section and (b) the unit cell with the cross-sectional area. 110

Figure 4.23 Contour plots of strain after temperature rise for Iteration 4.1 with a deformation factor of 1: (a) the unit cell strain in the X-axis and (b) the unit cell strain in the Z-axis. 110

Figure 4.24 A 4 × 1 × 4 lattice of Iteration 4.1. 110

Figure 4.25 Annotation and patterns of the lattices of Iteration 4.1: (a) top view and front view of the unit cell and (b) patterns of 2 × 1 × 2 lattices. 111

Figure 4.26 Illustration of 1 × 1 × 1, 2 × 1 × 2, 3 × 1 × 3 and 4 × 1 × 4 lattices of Iteration 4.1. 112

Figure 4.27 Simulation results of Iterations 1, 1.1, 1.2, 2.1 and 2.2 using trend lines, where $\Delta L *$is the relative change in the change in length, $\Delta LLattice$ is the change in length of the designed lattice, $\Delta Lsolid\ mat1$ is the change in length of the solid volume of the lattice outer part material, $\alpha 1$ is the CTE of the lattice outer part material, and $\alpha 2$ is the CTE of the cylindrical inner part material. 113

Figure 4.28 Effective CTE results for Iterations 2.2 - 2.4 and the Iteration 3 series. 114

Figure 4.29 Illustration of Iteration 4.1's top view and side view of (a) the $(DL) = 0.30$ model, (b) the $(DL) = 0.50$ model, and (c) the $(DL) = 0.73$ model. 115

Figure 4.30 Low planar CTE lattice results of Iteration 4.1 obtained by varying the ratios DL and $\alpha 2\alpha 1$ and its surface fit, where L is the original length of the lattice, D is the original diameter of the cylindrical inner part, and $\alpha 2\alpha 1$ is the ratio of CTEs of the cylindrical inner part material and the lattice outer part material. 116

Figure 4.31 Low planar CTE lattice results of Iteration 4.1 by varying $\alpha 1$ and $\alpha 2$, and its surface fit, where $\alpha 1 *$ is the relative change in the CTE of Nylon 12, $\Delta\alpha 1$ is the change in the CTE of Nylon 12, $\alpha 1$ is the original value of the CTE of Nylon 12, $\alpha 2 *$ is the relative change in the CTE of UHMWPE, $\Delta\alpha 2$ is the change in the CTE of UHMWPE, and $\alpha 2$ is the original value of the CTE of UHMWPE. 117

Figure 4.32 Low planar CTE lattice results of Iteration 4.1 by varying $E1$ and $E2$, and its surface fit, where $E1 *$ is the relative change in the elastic modulus of Nylon 12, $\Delta E1$ is the change in the elastic

modulus of Nylon 12, $E1$ is the original value of the elastic modulus of Nylon 12 (1.8 × 10^9 Pa [126]), $E2*$ is the relative change in the elastic modulus of UHMWPE, $\Delta E2$ is the change in the elastic modulus of UHMWPE, and $E2$ is the original value of the elastic modulus of UHMWPE (7 × 10^8 Pa [127]). 118

Figure 4.33 The effect of layer alignment on the deformation of the 2 × 1 × 2 lattice outer part of Iteration 4.1: (a) example of the 1st pattern, (b) example of the cross-section of the 1st pattern, (c) example of the cross-section of the 1st pattern at Layer 2, and (d) any of the connecting layers of the other patterns. 120

Figure 4.34 The total volume of Iteration 4.1's (10 × 10 × 10) mm unit cell by varying the DL ratio between 0.3 and 0.73. 122

Figure 5.1 Representative example of the converged mesh of the (20 × 20 × 20) mm low-CTE concept lattice unit cell and its boundary conditions applied on a lattice unit cell design [124]. 125

Figure 5.2 Example of a 3D model of the 1D tailorable thermal expansion lattice (Iteration 1.1) with the predefined surfaces (highlighted in red): (a) the lattice outer part and (b) the cylindrical inner part. 126

Figure 5.3 An example of a 2D tailorable thermal expansion lattice (Iteration 2.4) with the predefined sections (highlighted in red): (a) the lattice outer part with the predefined surfaces, (b) the cylindrical inner part with the predefined surfaces and (c) the lattice outer part with the predefined set (Set-1). 127

Figure 5.4 Example of the position of parts in a lattice structure: (a) a 1 × 1 × 1 lattice of Iteration 3.1 and (b) a 2 × 1 × 2 lattice of Iteration 3.1. 128

Figure 5.5 Illustration of defining a surface-to-surface contact for the lattice structure. The 2nd pair interaction (outer.Surf-2) was defined as a master surface and inner.Surf-1 was defined as a slave surface. 129

Figure 5.6 Summary of all the boundary conditions applied in the lattice structure. 130

Figure 5.7 Examples of results from the FEA simulation of the lattice: (a) a contour plot of von Mises stress and (b) a contour plot of the magnitude of displacement change. 132

Figure 5.8 Illustrations of (20 × 20 × 20) mm Iteration 4.1 with partitions for contact (a) the cylindrical inner part and (b) the lattice outer part. 135

Figure 5.9 Contour plot of contact pressure between two surfaces of Iteration 4.1 when the temperature was raised. 135

Figure 5.10 Illustrations of converged meshes of (20 × 20 × 20) mm Iteration 4.1: (a) without partitions and (b) with partitions in high stress regions and (c) with partitions and highlighted in high stress regions 136

Figure 5.11 Contour plot of von Mises stress of Iteration 4.1 with the dashed boxes indicating high stress regions when the temperature was raised. 137

Figure 5.12 Illustrations of mesh element types: (a) the first-order hexahedral element C3D8, b) the first-order tetrahedral element C3D4 and (c) the second-order tetrahedral elements C3D10. 137

Figure 5.13 Finite element mesh density convergence for the low-CTE lattice cell: (a) comparison between C3D4 and C3D10, and (b) C3D10 and their deviations [124]. 139

Figure 5.14 Illustration of contact properties between a master surface and a slave surface. 140

Figure 6.1 Final assembly of the thermal expansion experimental set-up using aluminium extrusions with a cross-section of (30 x 30) mm. 145

Figure 6.2 The thermal expansion experimental set-up: (a) the first development and (b) the final development. 146

Figure 6.3 Illustration of the positions of the thermocouples and the mirror for (a) steel gauge blocks, (b) the nylon 12 lattice outer part, (c) the UHMWPE cylindrical inner part and (d) Iterations 2.4 and 3.1. 147

Figure 6.4 Plane mirror interferometer path set-up: (a) reference path and (b) measurement path, where R is the retroreflector, QWP is the quarter wave plate, PBS is the polarisation beam splitter, and M is the optical mirror. 148

Figure 6.5 Interface of PicoLog 6 during the experiment. 149

Figure 6.6 Interface of CARTO Capture during the experiment 149

Figure 6.7 Experimental set-up of the heating system. 152

Figure 6.8 Schematic representation of the laser interferometer system. 153

Figure 6.9 The bottom kinematic seat board.....154

Figure 6.10 Illustration of the thermal expansion measuring machine: (a) front view and (b) side view, which can be adjusted by the laser interferometer system in multi-movement: X is the translation in the X-axis, θX is the rotation around the X-axis, Z is the translation in the Z-axis, θZ is the rotation around the Z-axis and the dashed dotted lines represent lines of symmetry in the Y-axis. 155

Figure 6.11 Schematic representation of the measurement and its errors. 156

Figure 6.12 Schematic representation of the experimental set-up of the thermal expansion measuring machine.....157

Figure 6.13 Misalignment parameters for a plane-mirror target from “Chapter 4 – Displacement Measuring Interferometry” of Handbook of Optical Dimensional Metrology [110]. 162

Figure 6.14 The air temperature in the acrylic box, the aluminium plate, the outer surface of the acrylic box, and the metrology frame (a) before installing the layers of the aluminium bubble insulation foil and (b) after installing the layers of the aluminium bubble insulation foil. 170

Figure 6.15 Temperature of the air in the acrylic box, the aluminium plate, and the average temperature of the 50 mm steel gauge box (a) before the installations, (b) after installing the layers of the aluminium bubble insulation foil, and (c) after installing the layers of the aluminium bubble insulation foil and the axial fan. 171

Figure 6.16 CTE results of the three different sizes of the steel gauge blocks. 172

Figure 6.17 Illustration of the lattice structures placed in the experimental set-up: (a) a 1 × 2 × 1 lattice with a plane mirror (b) a 1 × 1 × 1 lattice and (c) a 3D view of the 1 × 1 × 1 lattice (three axes indicate the object coordinates).....173

Figure 6.18 Illustration of Iteration 3.1 showing (a) a unit cell with the location of the cross-sectional area, and (b) the cross-section of the unit cell with annotations. 176

Figure 6.19 Differences in the in-plane CTE of Iteration 3.1 when potential key parameters were varied from −0.2 to 0.2. 177

Figure 6.20 Low planar CTE lattice results of Iterations 2.4 and 3.1 by varying the average temperature change of the entire experiment. 181

Figure 6.21 Low planar CTE lattice results of Iterations 2.4 and 3.1 by varying the rotations of the plane mirror of the entire experiment. 182

Figure 7.1 A 4 × 1 × 4 lattice of Iteration 4.1 with the possible locations for loading application on the structure..... 185

Figure 7.2 Illustration of a unit cell of Iteration 4.1: (a) contour plot of the strain along the Y-axis when the temperature was increased (with a deformation factor of 2) and (b) the reduced region to eliminate excess material in the parts along the Y-axis. 186

Figure 7.3 A representation of Iteration 4.1, used for FE structural analysis. 187

Figure 7.4 The in-plane CTE for a unit cell of Iteration 4.1 compressed by applied loads equivalent to a range of 0 % to 5.0 % strain along the Y-axis. 189

Figure 7.5 Contour plots of von Mises Stress after temperature increase (with a deformation factor of 1) for the unit cell of Iteration 4.1 compressed by applied loads equivalent to a value of strain along the Y-axis (a) 0.1 % strain, (b) 0.4 % strain, (c) 1.5 % strain, (d) 2.0 % strain and (e) 5.0 % strain. 192

Figure 7.6 Illustration of precision measurement equipment with the 8 × 4 × 6 lattice; an optical vertical dilatometer (taken and modified from Juasiripukdee et al.'s work [124]). (a) A 3D view and (b) a top view. 193

List of Tables

Table 2.1 Summary of current tailored thermal expansion lattice structures. 50

Table 3.1 LPBF manufacturing parameters used to manufacture the lattice structure [18]. 77

Table 3.2 The diameter of the cylindrical inner geometries of the specimens' lattice outer parts in different sizes. 79

Table 4.1 The configurational parameters of Iteration 2 series 99

Table 4.2 Configurational parameters of Iteration 3 series 103

Table 4.3 In-plane CTEs of Iterations 2.4, 3.1, 4 and 4.1. 114

Table 4.4 In-plane CTEs of the designs of the 2 × 1 × 2 lattice. 119

Table 4.5 In-plane CTEs of the designs. 120

Table 5.1 Properties of Nylon 12 and UHMWPE. 128

Table 5.2 Summary of minimum memory requirements to analyse iterations. 131

Table 5.3 Five sets of boundary conditions applied to the lattice structure. 133

Table 5.4 In-plane CTE of the boundary conditions and their percentage difference compared to BC1. 134

Table 5.5 The required RAM, ROM and total CPU time for Iteration 4.1 with and without partitions. 141

Table 6.1 Specifications of Cole-Parmer StableTemp Ceramic Top Hot Plate [135]. 143

Table 6.2 Specifications of Pico Technology USB TC-08 Temperature Data Logger [136] 143

Table 6.3 Specifications of RS PRO Type K Thermocouple [137]. 143

Table 6.4 Specifications of the Renishaw XL-80 laser system [138, 139]. 144

Table 6.5 Duration of the thermal expansion experimentation of the specimens. 150

Table 6.6 The influencing quantities considered in the experiment. 158

Table 6.7. Sensitivity of the measured length L with respect to environmental (atmospheric) conditions on a laser interferometer system [15]. 164

Table 6.8 Summation of uncertainties due to the measurement of the refractive index of air. 165

Table 6.9 Summation of uncertainties due to the thermal effects on the metrology frame. 165

Table 6.10 Summation of uncertainties due to the thermal effects on the hot plate. 166

Table 6.11 Summation of uncertainties due to the thermal effects on the experimental set-up 167

Table 6.12 Summation of uncertainties caused by the dead path length. 167

Table 6.13 Summation of sources of uncertainty and their associated degrees of freedom. 169

Table 6.14 Summation of the expanded uncertainty of all specimens. 175

Table 6.15 Summation of the coefficients of thermal expansion of all specimens. 175

Table 6.16 The potential key parameter changed and their effects on the in-plane CTE of Iteration 3.1. 178

Table 6.17 Summation of the ratios of uncertainty sources with respect to the largest source. 180

1 Introduction

1.1 Background to the project

Numerous applications require precise dimensional measurements, however, the obtention of such measurements with high accuracy requires an understanding of potential interferences in the measurement system, especially those resulting from the equipment itself or from the surrounding environment. The primary interfering sources include vibration and thermal effects. This PhD research focuses on one of the main problems in precision measurement: thermal expansion.

The thermal expansion of solids is a fundamental property representing dimensional changes induced by temperature changes in a solid [1]. A temperature rise generally enlarges the object size, while a temperature drop reduces the object size. There are material-specific relationships connecting material relative expansions and changes in temperature, called coefficients of thermal expansion (CTE). Changes in length can be expressed as in equation 1.1:

$$\Delta L = \alpha_L L_o \Delta T \qquad 1.1$$

where ΔL is the change in length of the material, L_o is the original length of the material, α_L is the linear coefficient of thermal expansion of the material, and ΔT is the change in temperature between the initial and final temperatures.

One of the important factors in accurate dimensional metrology is accurate temperature measurement [2]. The reference temperature for industrial length measurement is defined to be 20 °C by the International Organization for Standardization (ISO) [3]. This reference temperature is used for standards and has been adopted as the temperature at which the dimensions of components are given in engineering drawings. Significant length changes can occur if measurements are made at temperatures other than 20 °C. For example, a 100 mm steel component (with CTE of 11.5×10^{-6} K^{-1} taken from the Good Practice Guide No. 149 by the National Physical Laboratory (NPL) [4]) would have expanded by 1.15×10^{-6} m at 21 °C. In low precision engineering, this may be of no consequence. However, this thermal expansion must be considered in higher precision engineering fields, such as the calibration of secondary length standards or higher precision engineering measurements with optical instruments (camera, fringe projection, etc.), where uncertainties in the region of optical wavelengths can be significant. The thermal expansion should not be greater than the resolution of the precision measurement equipment [5], so that it does not dominate the measurement uncertainty

of the instrument. Additionally, the resolutions of point optical probe, laser line probe, and machine vision sensors are approximately in ranges of (1−3) × 10^{-6} m, (10−50) × 10^{-6} m and (5−100) × 10^{-6} m, respectively [5].

The performance of precision mechanical systems is often dictated by thermal sensitivity and stability [6]. The mechanical properties of the various materials and mechanical joints found in a mechanical design can generate stress distributions as the system reacts to temperature changes. As the temperature fluctuates over time, the mechanism can potentially expand or contract, leading to distortion. The general heat transfer mechanisms related to precision machine design are conduction, convection and radiation [7], as illustrated in Figure 1.1. Conduction is the thermal transfer of heat through a solid or stationary fluid and fundamentally occurs as a result of the atomic motion inside the material increasing with an increase in its energy state. Convection is the transfer of temperature by a fluid moving over and around a solid. Radiation is thermal transfer resulting from interactions between electromagnetic waves within a given medium.

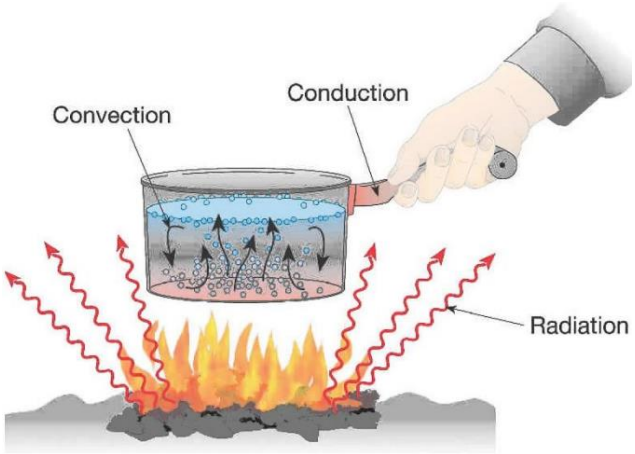


Figure 1.1 Illustration of an example of heat transfer mechanisms, from the Zippy Facts website [8].

The three thermal transfer mechanisms are present in all machine and instrument designs, especially in precision systems where sensitivity to small variations in the environment can cause significant impacts on the system's overall functionalities [6]. For example, conductive heat transfer is prevalent where heat sources (such as optical instruments, motors, pumps, and hot plates) are attached to frames and structures, resulting in a temperature gradient within the structure which can create unwanted expansion and motion of the machine over time. Convective heat transfer can be often found in electrical circuits, such as electrical cabinets or computer cases, where heat is generated at a constant rate to the ambient air, and this heat needs to be removed to maintain the system operating at its optimal performance. Finally, radiative heat transfer can be found in some heat sources, such as lights and people working within the area, resulting in a temperature gradient within the environment.

Generally, As a natural insulator, trapped air makes it difficult for convection currents to form. Convection and conduction heat transfer are thus lessened by confined air [9]. As for radiative heat transfer can be reduced by insulating the heat for the heat sources [10].

One typical example of measurement machine system problems is manifest in a coordinate measuring machine (CMM), as shown in Figure 1.2. A CMM is a common device that utilises discrete points on an object's surface to measure geometry. In the constant ambient temperature (20 °C), temperature in the CMM structure can be changes up to ± 1.1 °C [11], resulting in errors in the position measurement. Additionally, the CMM frame is subjected to heated loads from both internal and external sources. Externally, the air circulation and heat generated by humans in close proximity to the system are potential heat sources. Internally, expansions from air-bearing, heated motors and electronic devices and friction from moving surfaces can generate head loads. These sources are capable of causing a gradient in the frame's temperature, which leads to thermal expansion in the frame. The thermal expansion can result in angular rotations and frame shape distortions that affect relative positions between an end effector (e.g. a touch probe and an optical sensor) and a measurable object [12], which can cause errors in the position measurement.

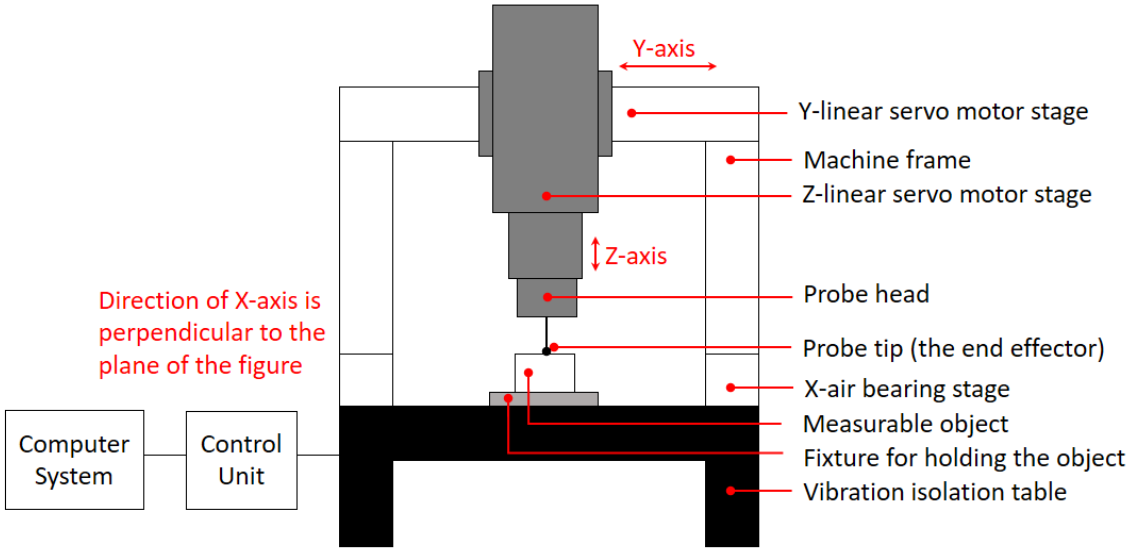


Figure 1.2 Schematic representation of a CMM.

Another simple example of measurement machine system problems is present in an optical dilatometer, as shown in Figure 1.3. An optical dilatometer is a non-contact device for measuring the thermal expansions of a specimen. The specimen is illuminated by a laser, creating optical interference fringes. The interference fringes' proportionate movement is used to determine the thermal expansion of the specimen, which is measured by a camera system. Heated loads from external sources are the air circulation and heat generated by humans in close proximity to the system. Heated

loads from internal sources are the heating unit and electronic devices such as the laser source and the camera system. These sources create a temperature gradient to the base frame, which can lead to frame shape distortions, resulting in errors in the position measurement.

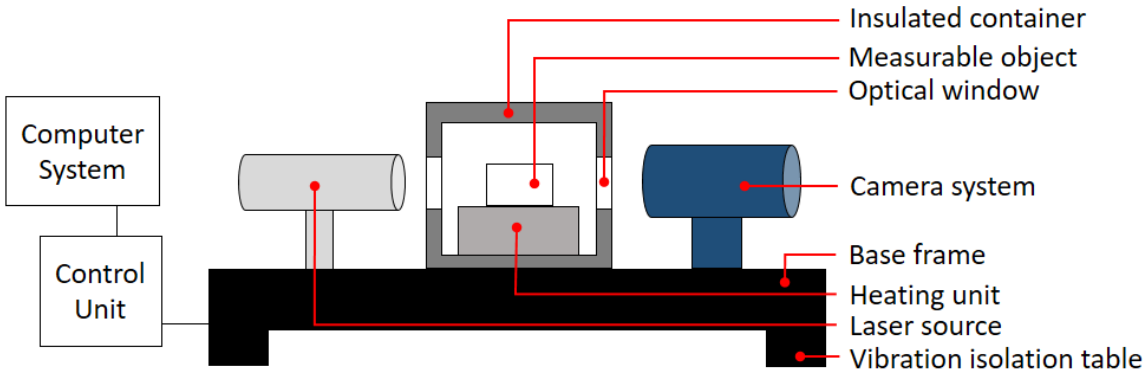


Figure 1.3 Schematic representation of a horizontal optical dilatometer.

One standard to reduce thermal interference is to control the ambient temperature around the measurement system. According to the UKAS accreditation for laboratories [13], the standard temperature is defined at 20 °C. For general gauge work, the temperature of working volume should be maintained within 20 ± 2 °C, and the temperature variation at any position should not exceed 2 °C per day and 1 °C per hour. In this case, the temperature in the laboratory can be controlled by using a set of sensors, air conditioners and heaters. The sensors are used to measure the ambient temperature in the room and send data to the central controller. The controller controls the air conditioners and heaters, referring to the set temperature.

Unfortunately, even in controlled laboratory environments, temperature fluctuations can still cause alignment drift in high-precision measuring machines, as their support frames undergo thermal expansion and contraction [14]. Haitjema [15] demonstrated that temperature fluctuations can lead to significant measurement uncertainties and represent a significant precision engineering problem in dimensional metrology applications such as length measurement with different materials and temperatures, displacement measurement using a laser interferometer, screw thread measurement, polygon measurement and many others.

Therefore, precision engineers are attempting to reduce thermal expansion in measurement systems by designing machines following accredited design guidelines for the reduction of thermal disturbances in instruments and machines, such as Basics of Precision Engineering, Chapter 11 [14], which provides design guidelines for optimal behaviour of force loops. This includes, for example, matching the CTEs of the different materials used in machine components and structures, implementing geometrical and thermal symmetry (heat transfer, thermal capacity and CTEs) to the

structure, establishing the thermal centre point to create zero thermal expansion in a single point, and optimising between thermal stability and structural dynamics of the structure. These guidelines for the design of measurement machines will be detailed in Chapter 2.

Material selection is one of the factors that precision engineers consider for designing measurement machines. It is desirable to use materials with low (ideally zero) CTE, such as composite materials. However, low-CTE materials are challenging to design and fabricate. For example, Invar is a low-CTE material which is difficult to machine. Particularly when annealed, it is malleable and highly ductile. The removal of burrs left over from cutting Invar presents a major difficulty. Each part machined requires its own deburring method. Alternatively for material selection, the geometrical complexity enabled by additive manufacturing (AM) provides new opportunities for low-CTE structures for precision measurement machines but, to the authors' knowledge, there is no established design route to achieve this. Lattice structures that can be considered a material and produced by AM are seen as a potential for designing precision measurement machine frames.

Lattice structures (as seen in Figure 1.4) are seen as a potential replacement for solid materials, giving advantages including decreased part production time and weight reduction [16, 17]. Additional characteristics of these structures that have drawn interest are the absorption of energy in different types of loading [16-18], incrementing thermal dissipation in designed parts [19] and reducing noise and vibration [20-22]. Besides, designing structures with low or tailorable CTE is a growing research topic, with applications identified in aerospace, optical measurement systems, and precision instruments [23-25]. This is an available opportunity to obtain machine frames with low-CTE lattice structures.



Figure 1.4 Example of lattice structures from 3D Printing [26].

Motivated by the aforementioned (given examples in [14, 15]), this research aims at designing a machine frame of a few tens of centimetres in height to support precision measurement equipment (e.g., cameras and optical projection systems). Such a frame would ultimately be created using lattice structures, used in a temperature-controlled metrology laboratory, with a temperature range between 19 °C and 23 °C. The thermal expansion of the frame over this temperature range should not be greater than the resolution of the precision measurement equipment [5], so that it does not dominate the instrument's measurement uncertainty.

1.2 Research questions

This research focuses on design of lattice structures with optimised and intrinsic thermomechanical isolation. The following research questions arise:

1. How can lattice structures be designed, analysed and manufactured for controlling thermal expansion to achieve zero thermal expansion?
2. How can the thermal expansion of lattice structures with the size of (50 × 50 × 50) mm be measured?
3. How can tunable thermal expansions lattice strutures be implemented?

1.3 Thesis structure

To answer the research questions in Subchapter 1.2, the thesis is structured as follows:

- Chapter 2 presents an overview of the topic of "Design Of Lattice Structures With Optimised And Intrinsic Thermomechanical Isolation" as an introduction to this PhD project. The chapter details the design of machine frames, general lattice structures, lattice structures for a tailorable coefficient of thermal expansion, the manufacture of lattice structures for tailorable CTE and relevant testing on lattice structures, including finite element testing and experimentation.
- Chapter 3 identifies the knowledge gap related to this project, provides an overview of the general methodology, presents flowcharts for all project stages and encountered challenges and describes the experimental methods conducted to manufacture the lattices.
- Chapter 4 describes the general concepts used in all designs, the experimental methods conducted to design the lattices, an evolution of the designs with an emphasis on the designs, and the CTE results of the lattice structures for a low CTE. Additionally, one of the designs discussed demonstrates the determination of the main influential factors on CTE results.

- Chapter 5 presents the experimental methods conducted to perform finite element, the effect of finite element parameters on thermal expansion simulation results and explains how the parameters were selected, including procedure type, boundary conditions, partitions for contacts partitions for reducing mesh density, and mesh type.
- Chapter 6 describes the experimental methods conducted to perform thermal expansion experimentation, the final thermal expansion experimentation, including the selected experimental hardware, the experimental correction used and its uncertainty, the experimental validation, and thermal expansion results from the experiment.
- Chapter 7 describes the implementation of the lattice structures into a metrology frame. The construction of the final metrology frame design is presented.
- Chapter 8 constitutes the main discussion of this PhD project, the overall conclusions attained and suggestions for future work.

2. A review of low thermal expansion machine frame designs using lattice structures

This chapter described all reviews related to this PhD. First, connections between the different topics of this chapter are described. Second, the considered principles in precision machine frame design are detailed. Third, general information about the designed lattice structure is presented, followed by previously designed lattice structures for controlling lattice structure's coefficients of thermal expansion (CTE). Then, the technologies employed to fabricate the lattices are described, and available testing methods to evaluate their performance are delivered. Finally, conclusion is drawn.

2.1. Introduction to low thermal expansion machine frame design using lattice structures

Many techniques can reduce thermal expansion in machine frames. Since thermal expansion is proportional to the difference in temperature, controlling the ambient temperature in the surrounding environment of the machine is a suitable solution. This can be implemented by applying thermal insulators or using a set of sensors with an air conditioner or a heater in the controlled room. Another solution is to design the machine frame, with thermal symmetry and applying thermal centre principles. This research proposes an alternative solution using a low-CTE structure to design precision machine frames. Additive manufacturing (AM) techniques enable engineers to design parts that are highly complex and impossible to manufacture using conventional methods. Lattice structures are seen as a potential replacement for solid volumes manufactured using AM techniques. In this research, tailorable thermal expansion lattice structures are proposed as a replacement for precision machine frame materials. Designed lattice structures are studied to obtain a low CTE. Before the implementation of such structures in AM, tailorable thermal expansion lattice structures must be designed and fabricated, followed by a computational evaluation and physical testing for their thermal expansion which are the focus of this thesis.

2.2. Design of precision machine frames

The structure of a machine provides mechanical support for all of its components. Slocum [27] suggested that the main design considerations for a machine frame are stiffness, structural configuration and structural connectivity. Each of these is related to the design strategy. Attaining measurement repeatability is the primary aim in the design development of a precision machine frame. Repeatability can be achieved by performing measurements using the same procedure, device

or instrument, testing conditions and location, with the measurements being well grouped. The primary purpose of designing a machine frame is to ensure accuracy and precision while performing an operation or measurement. Accuracy is the ability to determine the true measurement quantity of a reference, while precision is the ability to obtain the same measured quantity value over multiple measurements [28]. In this subchapter, the considered factors for the precision machine frame design are described.

2.2.1. Loops

Loops are close paths across the assembly chain from one machine element to another. The purposes of loops are mainly to keep elements stiff, keep forces small and moments smaller, maintain stable temperatures, avoid temperature gradients in the machine frame, and ensure that resonant frequencies are high while loops are kept small [29]. In this thesis, loops can be implemented in designing the thermal expansion experimental frame in Chapter 6. In order to design the precision machine frame, four typical types of loops are considered with an account for relevant design factors:

- Force loops

Force loop is the assembly chain from one machine element to another directs the forces producing motion throughout the machine as a closed path. The closed path starts from the tip of the end effector through multiple machine elements to the effective point on the workpiece, where the effective point is the point machined by a tool or measured with a probe, as illustrated in Figure 1.2, Chapter 1. The forces entering the force loop can be process forces, forces resulting from machine dynamics, or forces created by thermal stresses. These forces will deform machine elements around the force loop, which cause errors of the measurement to the position of the end effector and the workpiece [14].

In order to control the aforementioned forces, Kroll [30] introduced the functional independence design principle. The functional independence design principle can be achieved by developing functions that perform only one task. This design principle can be divided into two sub-functions: minimising deformation due to process forces and minimising deformation due to thermal loads. Deformation due to cutting forces can be minimised by ensuring solid cross-sections in machine frames. Positioning errors are usually minimal in stiff frames with solid cross-sections. Deformation due to inertia forces can be minimised by selecting hollow cross-sections in machine frames. Frames with hollow cross-sections can typically reduce mass and dynamic errors. The precision engineer's task

is to fabricate a precision machine frame with an optimal trade-off. Deformation due to thermal loads can be minimised by applying solid cross-sections with low-CTE materials in the machine frame [14].

- Structural loops

A structural loop is a path across the assembly chain from one machine element to another which provides physical support and maintains relative position between specific elements. A machine may contain one or more structural loops. The function of a structural loop is to keep the following errors minimal: kinematic errors, thermomechanical errors, errors due to loads, dynamic errors, and errors in motion control and control software [31].

- Metrology loops

A metrology loop is a path across the assembly chain from one machine element to another that provides a machine's positioning reference. A metrology loop should remain rigid and as small as possible to avoid environmental effects and eliminate measurement errors. In optical instruments, much of the metrology loop consists of the air path through which the beam travels, due to the instruments' reliability on the wavelengths of their sources for length traceability. Fluctuations in the air temperature, barometric pressure, humidity and chemical composition of air paths cause changes in the refractive index and subsequent changes in the wavelength of the light [31].

- Thermal loops

A thermal loop is a path across the assembly chain from one machine element to another that determines the relative position between specific objects under changing temperatures. Thermal loads can originate from internal heat disturbances such as motors, friction, gas expansion in air-bearings, manufacturing processes, sensors and electronics, or from external disturbances such as ambient temperature changes or operator heat [14]. Following the linear coefficient of thermal expansion equation [14], the thermal expansion of components in a thermal loop changes the relative position between two objects in one direction. The equation used to calculate thermal expansion is:

$$\Delta L = \sum_{i} L_i \alpha_i \Delta T_i - \sum_{j} L_j \alpha_j \Delta T_j \qquad 2.1$$

such that components i cause the two components to drift apart in the considered direction under the temperature change ΔT, components j cause the two components to approach in the considered direction under the temperature change ΔT, L_i is the original length of components i, L_j is the original

length of components j, α_i is the linear coefficients of thermal expansion of components i and α_j is the linear coefficients of thermal expansion of components j.

Leach et al. [32] proposed design guidelines in Basics of Precision Engineering that can eliminate thermal interferences in a precision machine frame:

- Matching CTEs in a metrology loop by choosing the right α_i, α_j, $L_i$and L_j into Equation 2.1, resulting in $\Delta L = 0$.
- Designing a symmetric machine structure in terms of geometry, heat transfer, thermal capacity and CTEs
- Creating an intersection at the thermal centre: zero thermal expansion at one point between components
- Optimising the machine structure using thermal stability versus dynamics

2.2.2. Stiffness

Stiffness is the resistance to a force causing a structural member to deform and is a direct measure of the ability of a machine to maintain precision while performing an operation or a measurement. For many precision applications, high-stiffness structures are required within the force loop components, and strength is typically not considered [33].

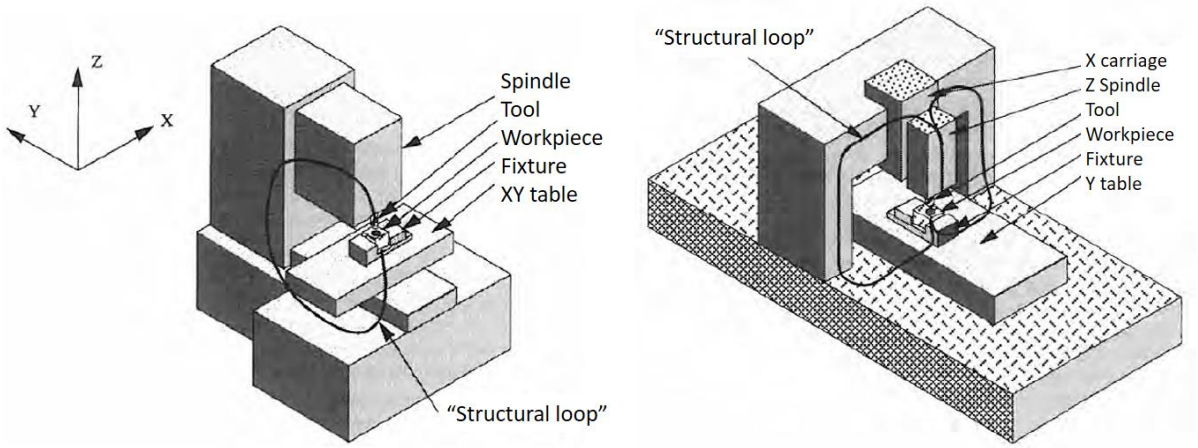
2.2.3. Structural Configurations

Configuration design is an important stage in machine frame design. The frames are commonly built by convectional manufacturing, such as milling, boring, slotting, deburring, grinding, drilling, and so on [33]. Liang et al [34] suggested that an optimal configuration can improve the stiffness of the machine frame and minimise the deformation caused by thermal effects and gravity. There are two typical configurations used in designing a metrology frame:

- Open section (C or G) frames

Open section frames are commonly used in small machines, and are compact, easy to assemble, and facilitate working area access for fixturing and part handling, as seen in Figure 2.1a. Examples of this type are BW-D500 by Nikon (non-contact measurement) and Form Talysurf Intra by Taylor Hobson (contact measurement). Machines can be designed to operate in either the horizontal or vertical direction. However, open section frames are more sensitive to thermal and mechanical deformation than closed sections, and the lack of geometrical symmetry leads to uncontrollable thermal gradients

and moments. Therefore, great care is required when designing a precision machine with an open frame [27].



(a) (b)

Figure 2.1 Illustration of frame configurations (a) open section frame and (b) closed section frame, taken from Precision Machine Design [27].

- Closed section (bridge or portal) frames

Closed section frames are commonly used in large machines, as seen in Figure 2.1b. The symmetrical structure frame can improve the rigidity of the machine tool and reduce thermal deformation. This type can be found in commercial markets, e.g., InfiniteFocus G5 by Alicona, Nexview™ NX2 by Zygo (non-contact measurement) and CRYSTA-Apex S by Mitutoyo (contact measurement). It is impossible to isolate all heat sources from the machine structure, but it is possible to create equal thermal expansion in all paths of the metrology loop [14]. Thermal symmetry can be efficiently designed in this type of frame. For example, centring heat sources around the machine frame provide a stiffer structural loop between the tip of the end effector and the workpiece.

2.2.4. Kinematics in the design of a precision machine

In structural connectivity, all components are connected to create a machine. The principles of kinematic design are introduced to assemble all components appropriately. Karim et al. [35] stated that kinematic design is used to determine (1) the functional relationships between the pieces of a mechanism, machine, or other mechanical system; (2) how these parts are interrelated; and (3) how these parts move relative to one another in the design of a machine, mechanism, or any moving mechanical system. These three elements are the foundational and fundamental concerns in the design process. Mason [36] suggested that before considering other factors like materials, manufacturing processes and costs, decisions about kinematic design in a machine must be made.

Failure of the kinematics of a mechanism, machine, or other mechanical system can lead to poor choices in other design factors in the design process, such as bearing types and manufacturing tolerances, resulting in high design costs, substandard performance, or unsatisfactory reliability.

In general, kinematic design is an essential factor in achieving accurate movements. Whitehouse [37] asserted that the other main use of kinematics is relocation, and it is necessary to reposition a specimen or instrument in its original position after being removed.

Two of the most commonly used kinematic clamp designs are the type I Kelvin clamp and the type II Kelvin clamp [38], as seen in Figure 2.2. Type I Kelvin clamp was designed with three balls on the upper part of the coupling. The balls rest inside a trihedral hole, in a V-groove, and on a flat surface of the lower part of the coupling. The geometry of the type I clamp provides a well-defined translational location depending on the trihedral hole's position. However, it is asymmetric. As for the type II Kelvin clamp, the three balls on the upper part of the coupling rest in three V-grooves on the opposing part. For this type, V-grooves in the lower part of the coupling are arranged at 120° so that the three balls meet their centroids. This design also has independent thermal expansion effects. Type II Kelvin clamp geometry is less complicated to manufacture than type I geometry is. Type I Kelvin clamp and type II Kelvin clamp designs are commonly used for mounting specimens or instruments. Williamson et al. [39] studied the deformations which occur when two surfaces touch. He claims that Type I Kelvin clamp and type II Kelvin clamp designs can be removed from an instrument and accurately relocated. An extra force to secure connections is ensured by gravity, magnets, or springs upon applications.

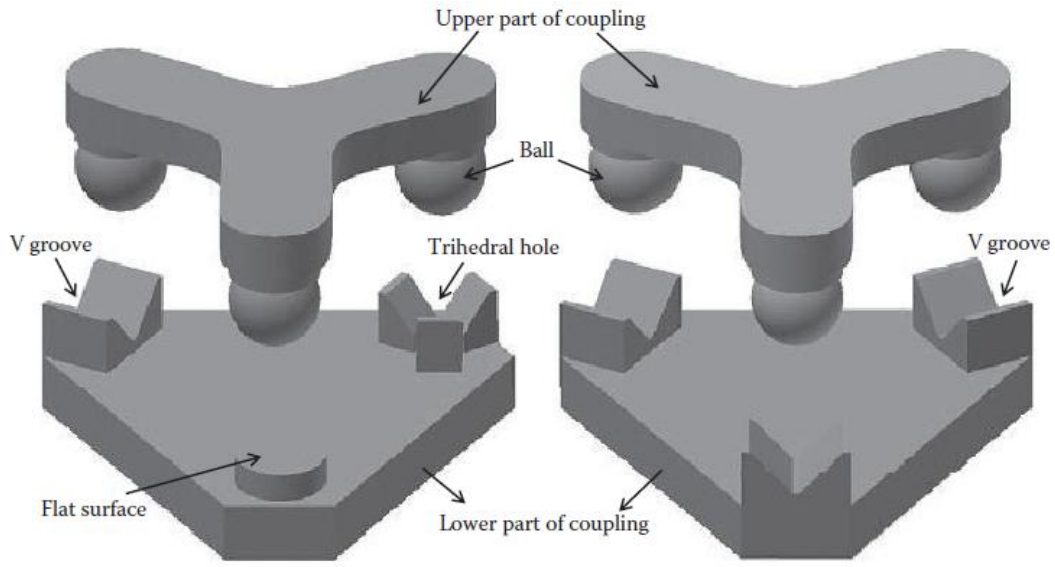


Figure 2.2 Common types of kinematic couplings: type I Kelvin clamp (left), type II Kelvin clamp (right), taken from Basics of Precision Engineering [32].

In addition to geometrical stability, the stability and overall stiffness of a kinematic coupling are maximised when the three coupling ball and groove centerlines (angle bisectors) and the normals to the planes containing pairs of contact force vectors, intersect at the coupling centroid of the coupling triangle [35], as shown in Figure 2.3.

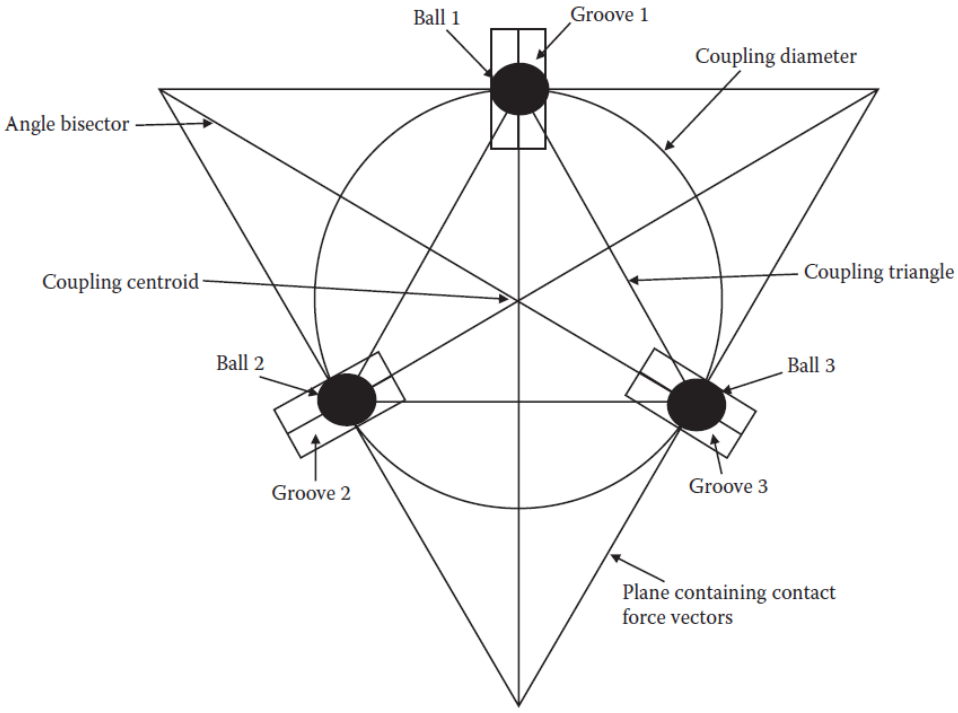


Figure 2.3 Geometrical parameters for a ball-groove kinematic coupling (the illustration was taken from Basics of Precision Engineering [32]).

Moreover, static stability can be ensured by applying a sufficient preload to hold the coupling together. A preload must be high, repeatable, and not alter the remainder of the structure to achieve appropriate coupling stiffness. The coupling layout can affect the stiffness of the kinematic coupling. When all contact force vectors cross the coupling plane at 45° angles, stiffness is equal in all directions. The inside angles of the coupling triangle can be changed to adjust coupling stiffness. In this thesis, kinematic design can be found in designing the laser interferometer system in Subchapter 7.1.2 and Subchapter 8.1.3.

2.2.5. Material selection

The material selection criteria for precision machine frames are not necessarily the same as for other uses. The primary considerations are characteristics such as stiffness and thermal properties [37]. As far as mechanical and thermal properties are concerned, material selection is dependent on the application of the machine frame. In most selections, the material properties considered are: specific

stiffness (or specific modulus) E/ρ, thermal conductivity over the linear coefficient of thermal expansion λ/α, and thermal conductivity over thermal diffusivity λ/a, where E *is* the elastic modulus, ρ is the density, λ is thermal conductivity, α is the linear coefficient of thermal expansion and a is thermal diffusivity. These properties can be plotted on a logarithmic scale, where high values are favoured. Three graphs are referred to for material selection, as shown in Figure 2.4, Figure 2.5 and Figure 2.6.

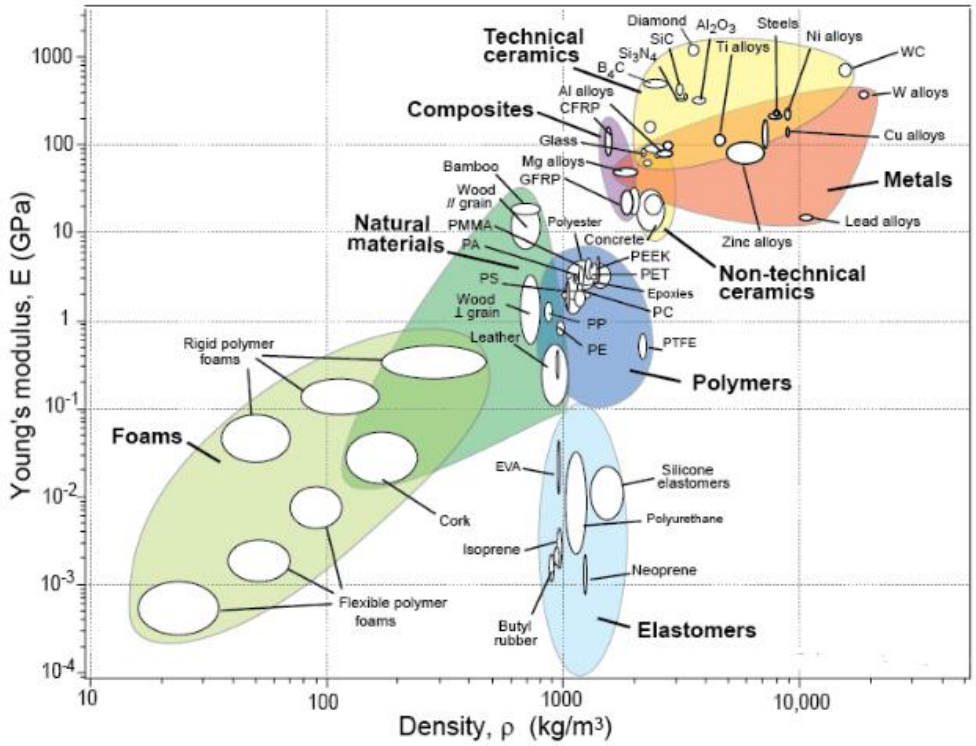


Figure 2.4 Elastic modulus E plotted against density ρ, taken from Materials Selection in Mechanical Design 5th Edition [40].

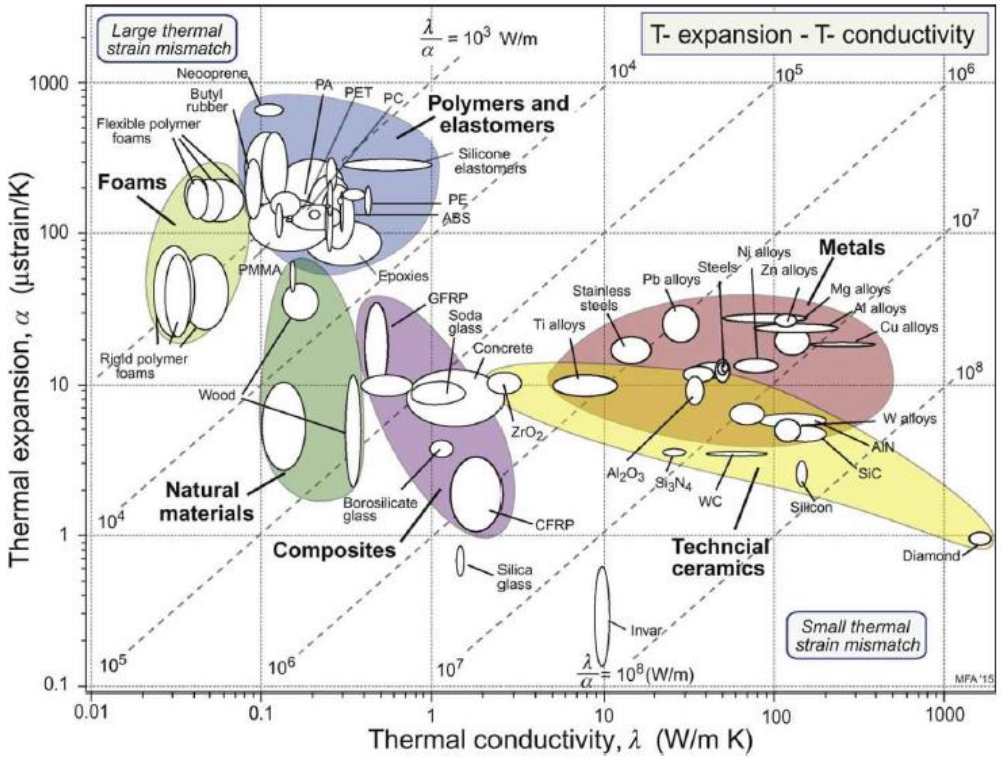


Figure 2.5 The linear thermal expansion coefficient α plotted against thermal conductivity λ, taken from Materials Selection in Mechanical Design 5th Edition [40].

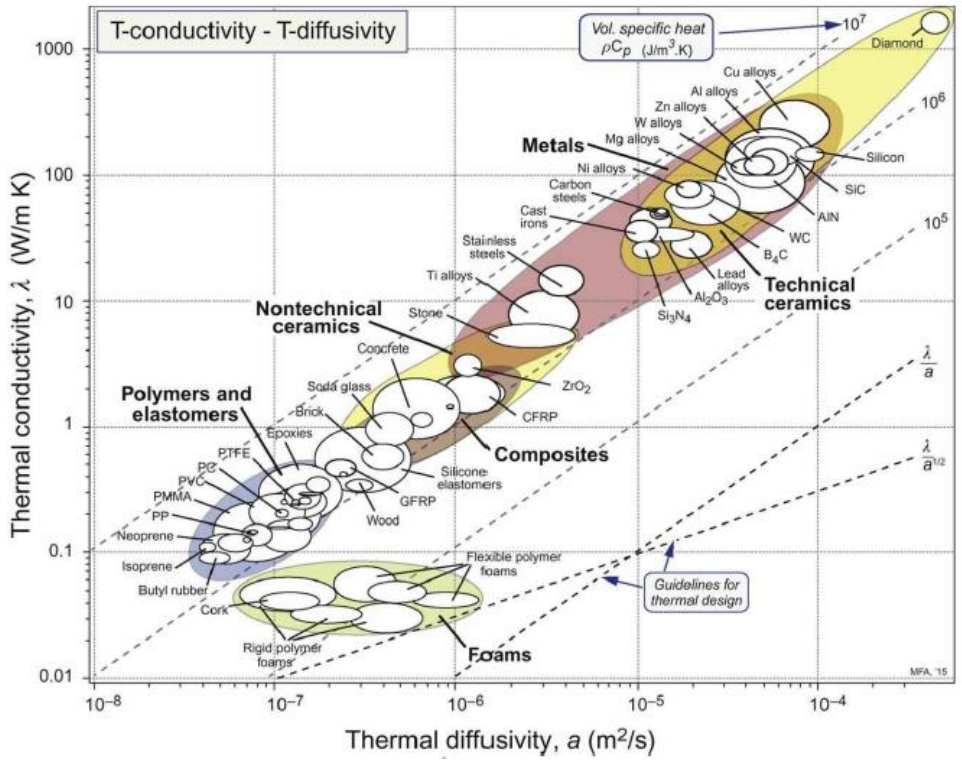


Figure 2.6 Thermal conductivity λ plotted against thermal diffusivity a, taken from Materials Selection in Mechanical Design 5th Edition [40].

The ratio E/ρ is a critical criterion to consider. This ratio represents self-weight deflection, which can be minimised by choosing a material with high stiffness and low mass. A high E/ρ ratio can also increase stability and reduce dynamic errors in the system. Figure 2.4 is a plot used to select materials for designs with limited stiffness, at minimum weights. Ceramics are very stiff, metals a little less, but both have elastic moduli greater than 10 GPa. Conversely, polymers are more flexible with elastic moduli between 0.8 and 8 GPa.

Almost all materials expand upon heating. Thermal expansion in structural precision machine frames can cause errors in the operation or measurement. In precision machine frame design, selecting structural materials with low CTEs can minimise thermal expansion issues in the system. The other considered parameter is thermal conductivity λ: the ability of a material to govern heat flow at steady state. Figure 2.5 is a plot used to select materials for designs with minimise thermal error. Figure 2.5 also shows that polymers have a very high CTE value, approximately 10 times greater than that of metals and a 100 times greater than that of ceramics. Choosing a high λ/α ratio can reduce distortion in the precision machine frame when the temperature changes.

The other ratio considered is thermal conductivity over thermal diffusivity λ/a. Thermal conductivity *a* is the ability of a material to govern heat flow at a transient. In the design, choosing a high value of the ratio λ/a means that the material may not transmit much heat, but it can quickly reach a steady state that helps protect the precision machine frame from sudden temperature changes. Figure 2.6 shows thermal conductivity plotted against thermal diffusivity.

By the aforementioned, these three material properties are important factors to consider for designing precision measuring machine frames. The appropriate material selections can increase stability and reduce dynamic errors in the system, reduce distortion in the precision machine frame when the temperature changes, and protect the precision machine frame from sudden temperature changes, resulting in minimising errors in position measurement.

Another field that are significantly grown is additive manufacturing (AM) technologies, such as binder jetting, material extrusion and powder bed fusion (PBF). Instead of using conventional manufacturing technologies to manufacture complex shapes, it is now possible to stack layers of different materials on top of one another, creating a crystal-like structure that does not grow naturally to obtain unique characteristics. Numerous advanced materials are now in the process of being developed using AM technologies. A metamaterial is any material engineered to exhibit a property not found in naturally occurring materials. A lattice structure is one such example, as it is composed of interconnected networks of solid struts or plates that form parts into cells and are made from repeating cell units.

Lattice structures offer unusual properties which cannot be obtained from natural materials, such as a negative Poisson's ratio [41-46], negative stiffness [45], significantly high specific stiffness [16, 18, 41, 47, 48], and other unique properties. Lattice structures are the focus of this PhD research and will be explored in detail in Subchapter 2.3.

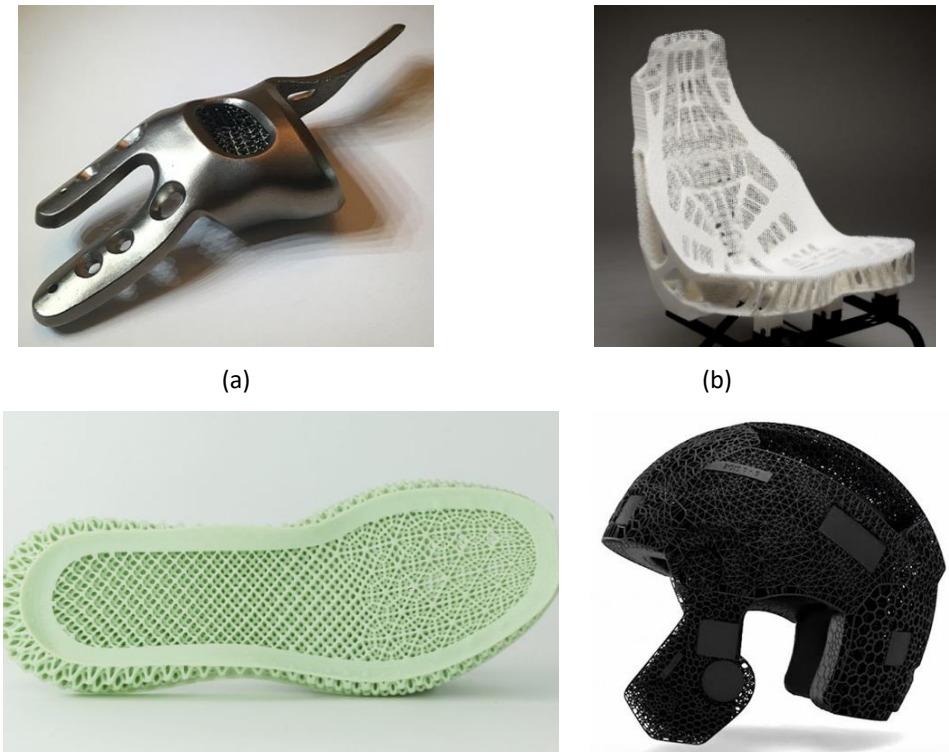
2.3. Lattice structure

A cellular solid is a material with interconnected networks of solid struts or plates that form a structure. Typical examples of cellular solid structures are cancellous bones, foams, and honeycombs, as shown in Figure 2.7. An interesting metamaterial where structural designs in three-dimensional (3D) printing and AM technologies are used is lattice structures, making them a non-stochastic type of cellular solid structures [48, 49]. Lattice structures can reduce the mass of workpieces by reducing the amount of material [50]. Figure 2.8 shows real-life examples such as bone segments [51, 52], car seats [53], shoe midsoles [54] and helmets [55].



(a) (b) (c)

Figure 2.7 Examples of cellular solids. (a) a cancellous bone [56], (b) a foam [57], and (c) a honeycomb [58].



(a) (b)

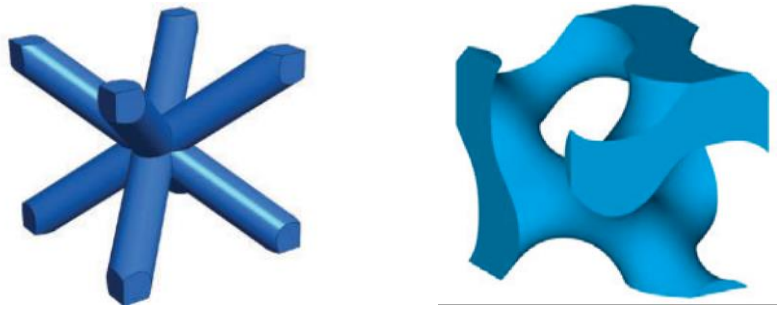
(c) (d)

Figure 2.8 Examples of lattice structures. (a) a bone segment [52], (b) a car seat [53], (c) a shoe midsole [54] and (d) a helmet [55].

The benefits of lattice structures beyond solid volumes [50] are manifest in several fields. Such benefits include a reduction in weight, leading to a decreased material use and lower manufacturing times [16-18], in addition to the absorption of energy under different types of loading [16-18], incrementing thermal dissipation in designed parts [19] and reducing noise and vibration [20-22, 59, 60]. Using AM processes, lattices can be made from a wide range of materials, from biocompatible polymers [61] to metal alloys [17, 62].

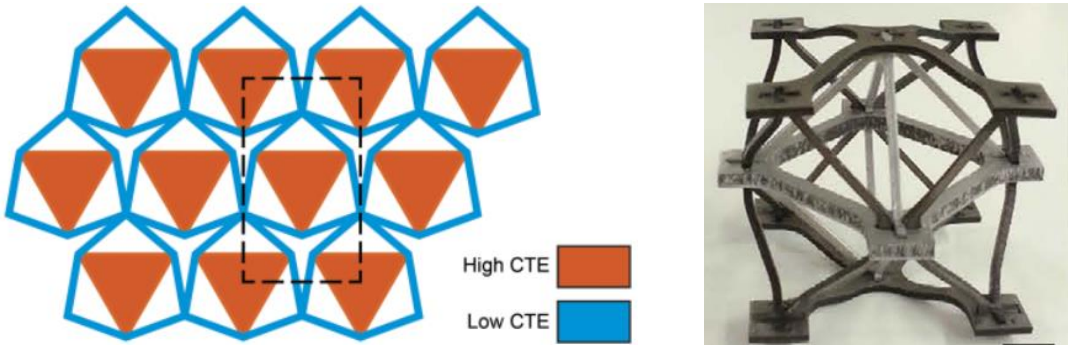
Lattices are made from repeating cell units. A unit cell is the smallest repeating element in a lattice structure [49]. The major characteristic of a lattice structure is symmetry, either translational symmetry, rotation symmetry, or both. Three typical factors that influence the displacement and von Mises stress of a lattice structure are material properties, patterns of geometry, and density of the structure [63]. Contour plots of von Mises stress of a lattice structure determine whether the structure will yield or fracture. A lattice structure can be considered both a structure and a material [64]. As a regular structure, it can be analysed using finite element (FE) testing, and as a material, its properties can be analysed and compared with equivalent fully-dense (solid volume) materials. There are numerous considerations to account for when fabricating lattice structures. These include the shapes

of composed structures (strut-based and surface-based structures, as shown in Figure 2.9), geometrical dimensions (2D and 3D lattice structures, as shown in Figure 2.10), the number of tailored thermal expansion dimensions (as shown in Figure 2.11), applications, and others.



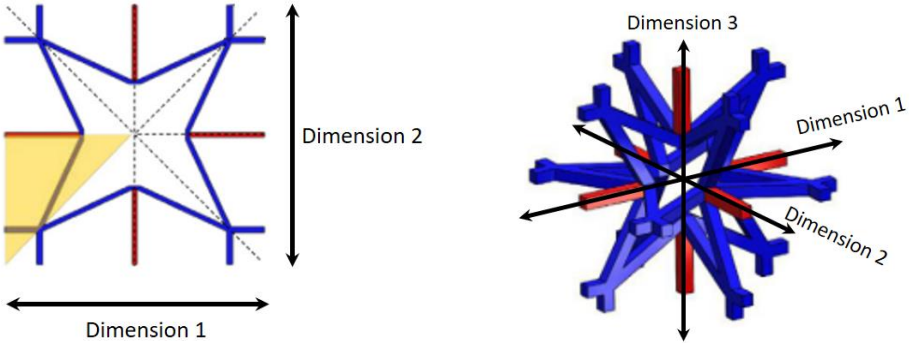
(a) (b)

Figure 2.9 Examples of shapes of composed structures. (a) strut-based [18] (b) surface-based structures [17].



(a) (b)

Figure 2.10 Examples of geometrical dimensions. (a) 2D [65] and (b) 3D lattice structures [66].



(a) (b)

Figure 2.11 Examples of tailored thermal expansion dimensions (a) 2D [67] and (b) 3D [68].

Gibson and Ashby investigated and reviewed cellular structures and provided a relationship relating the characteristics of cellular structures to their elastic modulus and density. The applied formulas were based on the Gibson-Ashby model of deformation [50], obtained from the experimental results

of honeycomb and foam structures. The relative elastic modulus of the lattice and relative density of the lattice equations are presented in Equations 2.2 and 2.3:

$$E^* = \frac{E_{latt.}}{E_{sol.}} \quad 2.2$$

$$\rho^* = \frac{\rho_{latt.}}{\rho_{sol.}} \quad 2.3$$

where $E_{latt.}$ is the elastic modulus of the lattice, $E_{sol.}$ is the elastic modulus of the lattice material, E^* is the relative elastic modulus of the lattice, $\rho_{latt.}$ is the density of the lattice, $\rho_{sol.}$ is the density of the lattice material and ρ^* is the relative density of the lattice.

Equations 2.2 and 2.3 define the relationship between the mechanical properties of lattice structures and their fully-dense material. The mechanical properties (e.g., the elastic modulus and Poisson's ratio) of each lattice structure perform differently, even when made from the same material. Each lattice structure has its own material properties, microstructure and geometry, internal and external, which are not the same throughout the entire lattice. Therefore, some lattices are not considered isotropic, but are anisotropic materials with regards to their mechanical properties [69, 70].

As for CTE, Gibson et al. [50] stated that almost all lattice structures conserve the same CTEs of their solid forms (homogenous material), as described in Chapter 1 in the equation of the coefficient of thermal expansion. In lattice structures, void spaces are placed within the internal geometry without changing global dimensions. In other words, void spaces are spaces which do not contain any material in the structural design domain [71]. Lattice structures expand equally in every direction; therefore, their thermal expansion is considered isotropic. Since there is less material in lattice structures than in other similar geometries due to the presence of voids, their elastic modulus is lower. The thermal stresses generated by the temperature gradient of lattice structures is also smaller due to the low values of the elastic modulus compared to other solids. The relationship between stress and a temperature changes can be expressed as in Equation 2.4, which leads to lattice structures obtaining good thermal-shock resistance [50]. Since the areas of contact between surfaces are small, the heat that transfers to lattice structures is insignificant, causing low thermal conductivity in lattices and enabling them to be good candidates for thermal insulation [72-76]. The normal stress due to temperature changes can be written as:

$$\sigma = -E\alpha_L \Delta T \quad 2.4$$

where σ is the normal stress of the lattice structure, E is the elastic modulus of the lattice structure, α_L is the linear coefficient of thermal expansion of the lattice material, and ΔT is the change in temperature between the initial and final temperatures.

2.4. Designed lattice structure for thermal expansion

As described in Subchapter 2.3, the CTE of any material has the same value as that of its solid form. In nature, materials with a positive CTE expand when heated, while those with a negative CTE contract upon heating. There are uncommon negative thermal expansion (NTE) materials, such as glasses in the titania-silica family, silicon, and germanium, including Kevlar, carbon fibres, and plastically deformed Invar [77]. Although zero thermal expansion cannot be proven in nature, Invar and other similar alloys show extremely low (close to zero) CTE values. These have been used for some thermal expansion control applications.

The design of structures with low or tailorable CTEs is a growing research field, with applications in aerospace, optical measurement systems, and precision instruments [23, 24, 78]. Many researchers employed the topology optimisation (TO) procedure, a mathematical method to optimise the layout of a design in a given condition, such as void spaces, loads, and boundary constraints, to create suitable lattice structures with maximised thermomechanical performance. The primary shapes of the internal geometries are designed within a unit square. This method takes advantage of the thermal deformation mechanisms of a composite material's internal geometry for controlling CTEs. In 1996, Sigmund et al. [77] proposed three-phase composites (Invar, nickel and voids) using TO to design structures with positive, zero, and negative CTEs, as seen in Figure 2.12. The composites consisted of two different material phases and void phases. In the early simulating stage of this research, materials with the same elastic modulus and varied only for CTEs were assumed in the analysis. Akihiro et al. [79] and Takezawa et al. [80] applied the same approach to the internal geometry of porous composites, resulting in planar negative CTE structures. Takezawa et al. [80] concluded that topology optimisation is the most effective structural design method for minimising thermally induced stress and maximising structural stiffness. Their structures had CTEs in the range of 300% to 1000% of those of the constituent materials, thus demonstrating that advanced computer design techniques can be used to create tailorable CTE structures.

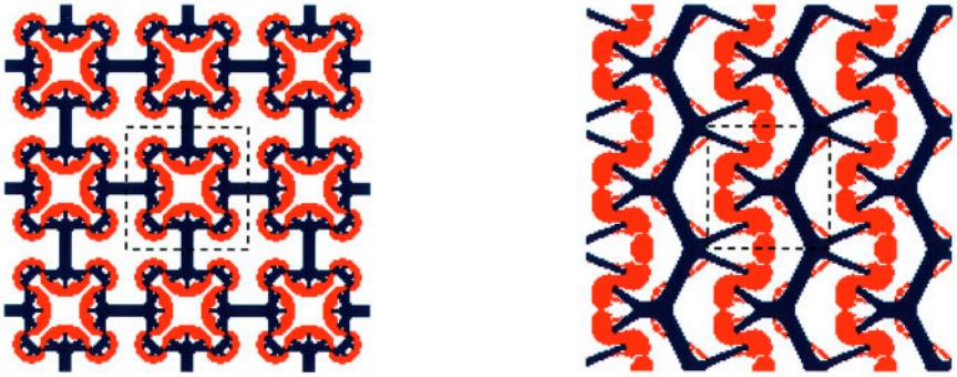
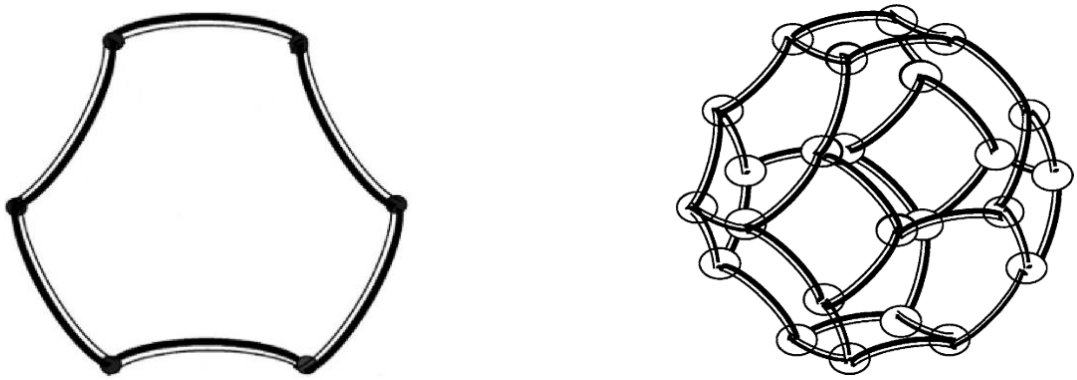


Figure 2.12 Examples of lattice structures using TO (a unit cell boundary is presented in the dashed square box), where red regions represent high-CTE phases, blue regions represent low-CTE phases, and white regions represent voids [77].

Following another novel design route, Lake [81] based their tailorable CTE structure on a repeating hexagonal lattice with bi-material ribs, as shown in Figure 2.13a. The ribs were made of two bonded layers with different CTEs, resulting in unequal thermal expansion. One material expanded higher than the other, bending under increasing temperature. From this concept, Lakes [82] also proposed a tetrakaidecahedral foam cell, a 3D lattice containing curved bi-material rib elements (as seen in Figure 2.13b), resulting in large positive, zero, and large negative CTE structures. A lattice structure consisting of equilateral triangular cells made of curved bi-material rib elements called 'Lehman-Lakes lattice' was also proposed, resulting in zero thermal expansion with a considerable stiffness [83, 84]. Likewise, Zhang et al. [85] proposed a modified Lehman-Lakes lattice through combining the lattice with a single-material layer to obtain higher stiffness (34% higher) and lower weight (17% less) compared to the optimal Lehman-Lakes lattice. Wu et al. [86] similarly proposed 2D and 3D lattices with bi-material elements. Their 2D lattices had aluminium and copper as constituent materials (with CTE = 23×10^{-6} K^{-1} and 18.5×10^{-6} K^{-1}, respectively), resulting in an effective CTE of -68.1×10^{-6} K^{-1} between the operating temperatures of 303.15 K and 773.15 K. The 3D lattices showed negative thermal expansions and inaccurate results, due to dimensional deviations in geometries manufactured using an AM machine. Yu et al. [87] similarly proposed lattices combining the bending mechanism of the bi-material beam and the unique deformation mechanism of chiral lattice structures. Five sets of chiral lattice composite structures with tailorable CTEs were proposed. The research found that the CTEs of the lattice structures based on the bi-material ribs concept are dependent on the geometry and number of constituent unit cells: changing the number of unit cells can tailor the CTEs of the lattice structures.



(a) (b)

Figure 2.13 Lakes lattice. (a) a hexagonal lattice cell with curved bi-material ribs and (b) a tetrakaidecahedral foam cell [82].

In another novel design approach, Hopkins et al. [88] proposed Polytope Sector-Based Synthesis (PSS) that helped arrange symmetric sectors within a periodic unit cell for 2D and 3D microstructural architectures. PSS was applied to a triangular sector of strut-based lattices using synthesised sectors, achieving the desired CTE, as shown in Figure 2.14. Hopkins et al. stated that lattice structures for controlled thermal expansion should have low thermal expansion but high thermal conductivity, since low-CTE lattice structures facilitate contraction. Besides, lattice structures with high thermal conductivity can rapidly conduct heat generated from several sources throughout the entire lattice. Hence, the dimensions of the lattice would uniformly change, which could minimise the thermal drift error.

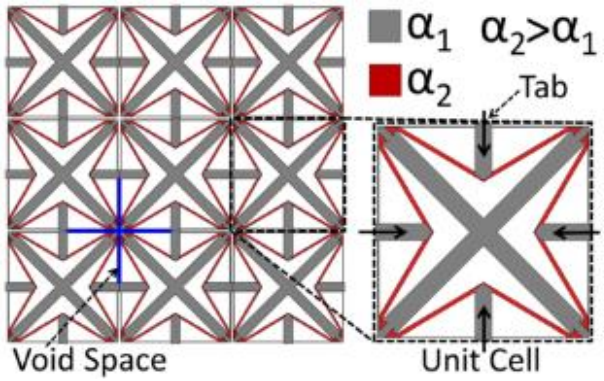


Figure 2.14 An example of a 2D microstructural architecture achieving tunable thermal expansion [88].

The metamaterials mentioned in the previous subchapter are used in controlled thermal expansion lattice structures. In general, metamaterial geometries consist of several struts made of two or more materials with dissimilar CTEs, as shown in Figure 2.11. CTEs of metamaterials are mainly influenced by the relationship of internal geometry parameters such as the angle between two struts, the length of struts, the thickness of struts, the diameter of struts, and the lattice structure's relative density. 2D [66, 67] and 3D structures [68] were designed and analysed by varying parameters such as length,

angle, and material properties, resulting in positive results, near-zero results, and negative PR and CTE. However, 2D [66, 67] and 3D structures [68] were only simulated using FEA. Other researcher [24] proposed the use of cellular metal composites via combining planar honeycomb and hexagonal layers in the internal geometry, as shown in Figure 2.15. Although planar honeycomb layers gave positive PRs while the hexagonal layers gave negative PRs, the thermal expansion of these lattice structures could be controlled by the thickness of each layer, resulting in zero thermal expansion. Jin [89] stated that the lattice members deformed mechanically and thermally when the temperature changed. The members should not fail thermomechanically under thermomechanical loads, such as exceeding the limits of the allowable stress or the melting temperature during the design process.



Figure 2.15 Illustration of hexagonal lattice material designed for zero thermal expansion and maximum specific stiffness in bending by Parsons [24].

Steeves et al. [90] introduced stretch-dominated planar lattices, as shown in Figure 2.16. The structures are known as UCSB lattices and can provide a unique combination of low CTE with high stiffness. The lattices were composed of laser cut metallic sheets, namely titanium (with CTE = 10.3 × 10^{-6} K^{-1}) and an aluminium alloy (with CTE = 25.6 × 10^{-6} K^{-1}). Using suitable parameters, the lattice structures could provide near-zero thermal expansion (less than 2 × 10^{-6} K^{-1}) within a temperature range of 50 °C to 250 °C. The concept was recently explored in thin films of approximately 1 µm thickness by Yamamoto et al. [91], resulting in an experimental CTE of −0.6 × 10^{-6} K^{-1}, significantly lower than the designed CTE (1.1 × 10^{-6} K^{-1}) between room temperature and 185 °C. A different approach was proposed by Berger et al. (2011) who used joints in stretch-dominated planar lattices. The bonded joints were substituted by pin joints with slender members, achieving lower densities with a high stiffness. Furthermore, the mechanical properties of stretch-dominated planar lattices were analysed [92], resulting in a high PR, including zero PR. As such, lattice structures were proven to be suitable structures for use in functionally graded structures where mechanical properties differ locally in CTE, stiffness, strength, and PR. This concept additionally offers opportunities to implement auxetic lattice designs for controlled thermal expansion, such as chiral lattice structures [87].

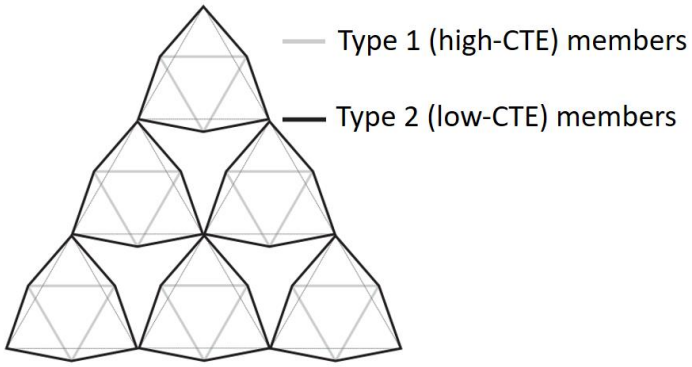


Figure 2.16 UCSB lattices: stretch-dominated planar lattices (grey is a high-CTE phase and black is a low-CTE phase) [90].

Another type of controllable thermal expansion lattices is tailorable thermal expansion structures presented by Jefferson et al. [93], as shown in Figure 2.17. Jefferson et al. proposed a lattice with two dissimilar materials and an assembly step in which the voids of a continuous honeycomb structure were filled with 'inserts' of a higher-CTE material. This formed a hybrid structure with a predicted CTE close to zero. However, this concept has not been conducted in physical experiments. Examples that required such assembly processes were octet lattice bi-materials using the pretension snap-fit technique for connecting aluminium panels and titanium inserts [66], as shown in Figure 2.10b. Additional examples include multi-stable mechanical metamaterials using the interlocking assembly method with multi-materials [94].

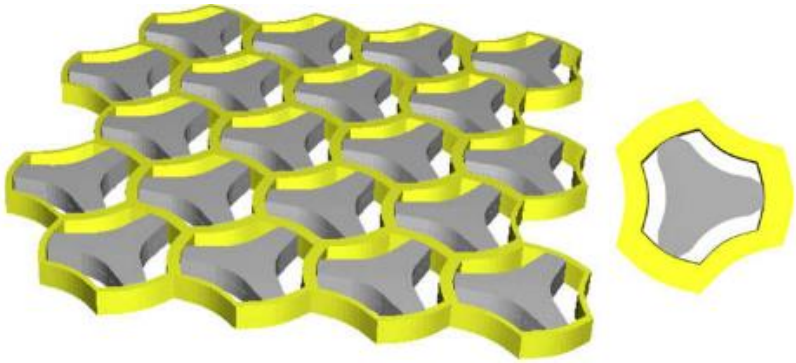


Figure 2.17 Lattice proposed by Jefferson et al.: a planar hexagonal grid thermally stable structure (grey is high expansion phase, yellow is low expansion phase, and white is void) [93].

In summary, several concepts of lattice structures were proposed to tailor thermal expansion, such as TO lattice, Lakes lattice, AFRL lattice, Lehman-Lakes lattice and UCSB lattice. Bi-material solutions for low and tailorable CTE structures were thoroughly examined, and summarised in Table 2.1. Based on Table 2.1, previous bi-material lattice designs have been fabricated in a wide range of techniques such as cutting, drilling, laser cutting, laser welding, electro-discharge machining, photolithography, material jetting, including fused deposition modelling [95] with a variety of metals and polymers such

as Invar, nickel, steel, aluminium, copper, stainless steel, titanium, VeroWhitePlus and TangoBlackPlus, and have shown effective CTEs in the range of $-4 \times 10^{-4}\ K^{-1}$ to $1 \times 10^{-3}\ K^{-1}$. Additionally, it can be noticed that selected materials were restricted by the limited material selection associated with their machine, e.g., VeroWhitePlus and TangoBlackPlus (taken from polymers), aluminium and copper (taken from metals), Ti–6Al–4V and Al6061 (taken from metals) or matching metal with Invar; however, that is a challenge to manufacture Invar, as discussed in Subchapter 1.1.

Table 2.1 Summary of current tailored thermal expansion lattice structures.

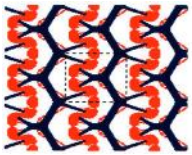
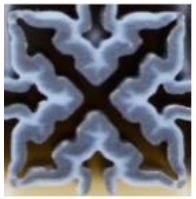
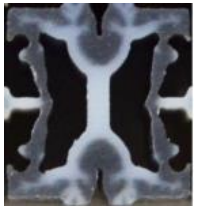
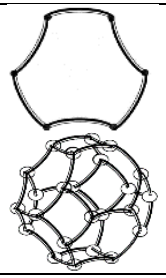
Paper Title (Published year)	Design lattice	Structure Type	Selected Materials	Manufacturing Technique	Measurement Technique	Effective CTE/ $\times 10^{-6}$ K^{-1}
Composites with extremal thermal expansion coefficients (1996)		Composites with extremal CTEs using topology optimisation	Invar (with CTE = 0.8×10^{-6} K^{-1}) and nickel (with CTE = 13.4×10^{-6} K^{-1})	-	Analysis: FEA	−4.97 to 35.0
Porous composite with negative thermal expansion obtained by photopolymer additive manufacturing (2015)		A porous material with planar negative CTE	VeroWhitePlus and TangoBlackPlus	Material jetting; Objet Connex 500 (Stratasys Ltd., USA)	Analysis: FEA Experiment: laser scanning dilatometer	−434 to 396
Design methodology for porous composites with tunable thermal expansion produced by multi-material topology optimization and additive manufacturing (2017)		Porous composites with tunable CTE	VeroWhitePlus and TangoBlackPlus	Material jetting; Objet Connex 500 (Stratasys Ltd., USA)	Analysis: FEA Experiment: laser scanner; SL-1600A (Shinagawa Refractories Co.,Ltd)	−300 to 1000
Cellular solids with tunable positive or negative thermal expansion of unbounded magnitude (2007)		A repeating hexagonal lattice with bi-material ribs (called 'Lakes lattice')	Two materials with a CTE difference of 10^{-5} K^{-1}	-	Analysis: Calculation from the equations in the research	Large positive, zero, and large negative

Table 2.1 Summary of current tailored thermal expansion lattice structures (continued).

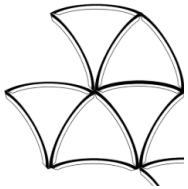
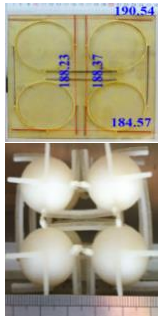
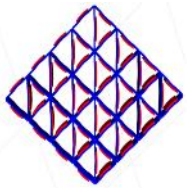
Title (Published year)	Design lattice	Structure Type	Selected Materials	Manufacturing technique	Measurement Technique	Effective CTE / × 10^{-6} K^{-1}
Stiff lattices with zero thermal expansion (2012)		Triangular lattice metamaterials composed of bi-layer curved rib elements developed from Lakes lattice. (called 'Lehman-Lakes lattice')	Invar (with CTE = 1 × 10^{-6} K^{-1} and modulus = 140GPa) and steel (with CTE = 12 × 10^{-6} K^{-1} and modulus = 200GPa)	-	Analysis: calculation from the research's equations	Zero
Isotropic negative thermal expansion metamaterials (2016)		2D and 3D lattices with bi-material elements	• 2D design: Aluminium (with CTE = 23 × 10^{-6} K^{-1}) and copper (with CTE = 18.5 × 10^{-6} K^{-1}) • 3D: VeroWhitePlus (with CTE = 38 12 × 10^{-6} K^{-1}) and TangoPlus (with CTE = 62.12 × 10^{-6} K^{-1})	• 2D design: cutting machine, drilling process • 3D design: material jetting (Objet350 connex2, Stratasys Ltd.)	Analysis: FEA Experiment: material test-a dilatometer Lattice test- DIC with CCD camera	• 2D design: −68.1 • 3D design: −80 to −10
A new design of dual-constituent triangular lattice metamaterial with unbounded thermal expansion (2018)		Dual-constituent triangular lattice metamaterial developed from Lehman–Lakes lattice (called 'DTLM lattice')	Steel (with CTE = 12 × 10^{-6} K^{-1}) and Invar (with CTE = 1 × 10^{-6} K^{-1})	-	Analysis: calculation from the equations in the research and FEA	−2580

Table 2.1 Summary of current tailored thermal expansion lattice structures (continued).

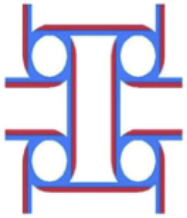
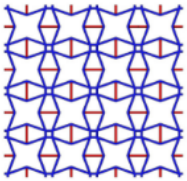
Title (Published year)	Design lattice	Structure Type	Selected Materials	Manufacturing technique	Measurement Technique	Effective CTE / × 10^{-6} K^{-1}
Drastic tailorable thermal expansion chiral planar and cylindrical shell structures explored with finite element simulation (2019)		Planar chiral lattices and cylindrical shells	Stainless steel 431 or Al7075, and Invar	-	Analysis: FEA	−65.77 to 91.64
Tailorable thermal expansion hybrid structures (2009)		A continuous honeycomb structure with inserts (called 'AFRL lattice')	Two different CTE materials	-	Analysis: FEA	Near-zero
Structurally efficient three-dimensional metamaterials with controllable thermal expansion (2016)		The octet lattice bi-materials)	Ti–6Al–4V (with CTE = 11.5 × 10^{-6} K^{-1}) and Al6061 (with CTE = 23 × 10^{-6} K^{-1})	Conventional technique; a laser cutting	Analysis: FEA Experiment: DIC with CCD camera	0.17
Metamaterials with negative Poisson's ratio and non-positive thermal expansion (2017)		2D metamaterials using bi-material re-entrant planar lattice structures	Stainless steel 431 (with CTE = 10.3 × 10^{-6} K^{-1}) or Al7075 (with CTE = 23 × 10^{-6} K^{-1}), and Invar (with CTE = 1,1 × 10^{-6} K^{-1})	-	Analysis: FEA	−3 to 2.5

Table 2.1 Summary of current tailored thermal expansion lattice structures (continued).

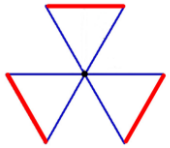
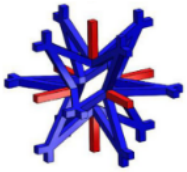
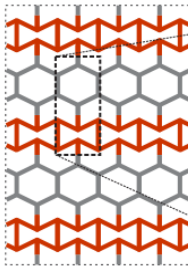
Title (Published year)	**Design lattice**	**Structure Type**	**Selected Materials**	**Manufacturing technique**	**Measurement Technique**	**Effective CTE / × 10^{-6} K^{-1}**
Design and analysis of lattice cylindrical shells with tailorable axial and radial thermal expansion (2018)		Lattice cylindrical shells with tailorable axial and radial CTE	Stainless steel 431 or Al7075, and Invar	-	Analysis: FEA	−64.6 to 88.0
Three-dimensional metamaterials with a negative Poisson's ratio and a non-positive coefficient of thermal expansion (2018)		3D metamaterials using bi-material re-entrant planar lattice structures	Stainless steel 431 (with CTE = 10.3 × 10^{-6} K^{-1}) or Al7075 (with CTE = 23 × 10^{-6} K^{-1}), and Invar (with CTE = 1.1 × 10^{-6} K^{-1})	-	Analysis: FEA	−8.69 to −5.22
Lightweight cellular metal composites with zero and tunable thermal expansion enabled by ultrasonic additive manufacturing, modeling, manufacturing, and testing (2019)		Lightweight cellular metal composites	• Titanium (with CTE = 8.6 × 10^{-6} K^{-1}) and Aluminium alloy (with CTE = 23.6 × 10^{-6} K^{-1})	Ultrasonic AM and EDM	Analysis: FEA Experiment: DIC with CMOS camera	−14 to 17.1

Table 2.1 Summary of current tailored thermal expansion lattice structures (continued).

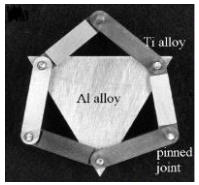
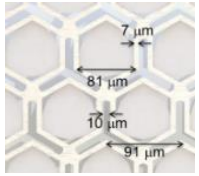
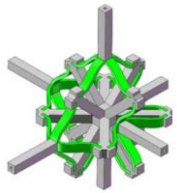
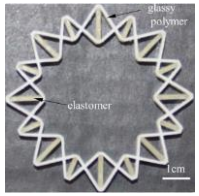
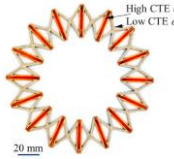
Title (Published year)	Design lattice	Structure Type	Selected Materials	Manufacturing technique	Measurement Technique	Effective CTE / × 10^{-6} K^{-1}
Concepts for structurally robust materials that combine low thermal expansion with high stiffness (2007)		Stretch-dominated planar lattices with low CTE with high stiffness (called 'UCSB lattice')	Al7075 (with CTE = 25.6 × 10^{-6} K^{-1}) and Ti–6Al–4V (with CTE = 10.3 × 10^{-6} K^{-1})	Laser cutting and laser welding	Analysis: FEA Experiment: a scanning laser extensometer.	Zero with high stiffness
The design of bonded bimaterial lattices that combine low thermal expansion with high stiffness (2011)		UCSB lattice with space-filling design	Ti–6Al–4V (with CTE = 9.4 × 10^{-6} K^{-1}) and Aluminium alloy (with CTE = 24.3 × 10^{-6} K^{-1})	Electro discharge machining (EDM)	Analysis: FEA Experiment: Digital Image Correlation (DIC) with CCD camera	−0.9
Thin films with ultra-low thermal expansion (2014)		Stretch-dominated planar lattices in the micro-scale (thin film) developed from the UCSB lattice	Ti–6Al–4V (with CTE = 9.4 × 10^{-6} K^{-1}) and Aluminium alloy (with CTE = 24.3 × 10^{-6} K^{-1})	Photolithography, electron-beam evaporation, and metal lift-off processes.	Analysis: FEA Experiment: DIC with CCD camera	−0.6
1D to 3D multi-stable architected materials with zero Poisson's ratio and controllable thermal expansion (2020)		1D to 3D multi-stable architected materials with zero Poisson's ratio and controllable CTE	Polyamide 12 and glass beads reinforced polyamide 12	Multi Jet Fusion (MJF) technology by HP Jet Fusion 3D 4200 printing machine	Analysis: Calculation from the research's equations	Large positive, zero, and large negative

Table 2.1 Summary of current tailored thermal expansion lattice structures (continued).

Title (Published year)	Design lattice	Structure Type	Selected Materials	Manufacturing technique	Measurement Technique	Effective CTE / × 10^{-6} K^{-1}
Hoberman-sphere-inspired lattice metamaterials with tunable negative thermal expansion (2018)		Hoberman-sphere-inspired lattice metamaterials	Teflon with acrylic, aluminium with titanium, and aluminium with Invar	-	Analysis: FEA	−1040 to 10
Experimental demonstration of lightweight lattice metamaterials with controllable low thermal expansion (2021)		Hoberman-sphere-inspired lattice metamaterials	Epoxy acrylate and epoxy acrylate doped with 20% Zirconium tungstate	Photolithography	Analysis: FEA Experiment: DIC with CCD camera	10

2.5. Manufacturing of lattice structures for thermal performance

Manufacturing is a family of processes that transform conceptual designs into physical parts that can be implemented in numerous applications. Advanced concepts can be produced using available techniques and machinery. Many factors need to be considered for the manufacturing of physical workpieces, such as the degree of complexity that can be handled by the manufacturing machine, the machine's available materials, the manufacturing costs and others. Lattice structures can be produced either using conventional or additive manufacturing (AM) processes. Non-AM methods (such as turning, drilling, milling, slotting, and grinding) can produce honeycombs, thin sandwich panels, and foams, however, AM is generally prefered for the manufacturing of lattice structures.

AM technologies have been used in industrial sectors such as aerospace manufacturing, the automobile industry, the health care industry, the food industry, the electronics industry, and even the entertainment industry. They are alternative manufacturing techniques that offer opportunities for engineers to think outside the box. AM starts from a CAD model that is horizontally sliced into several layers. These layers are produced in sequence and bonded to fabricate a consolidated component, as seen in Figure 2.19. AM technologies allow for the achievement of higher degrees of geometrical complexity, even internally.

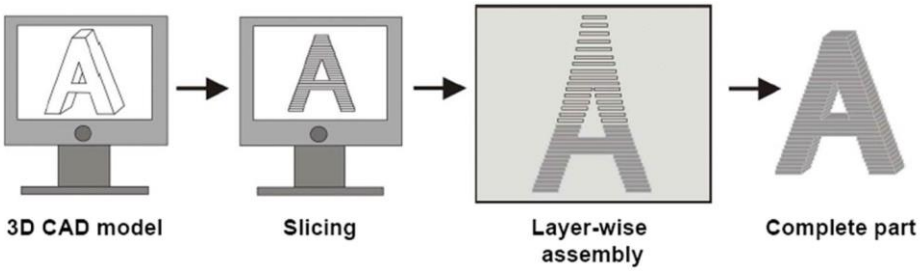


Figure 2.18 Workflow of additive manufacturing processes [96].

According to ASTM F2792 Standards [97], AM techniques are classified into seven categories: VAT Photopolymerisation, Material Jetting, Binder Jetting, Material Extrusion, Powder Bed Fusion, and Sheet Lamination. Three categories have been used to manufacture lattice structures for to improve thermal performance: VAT Photopolymerisation, Material Jetting, and Powder Bed Fusion [25] and Fused Deposition Modeling (FDM) [95]. However, only VAT Photopolymerisation, Material Jetting, and Powder Bed Fusion will be explained in this review.

Stereolithography (SLA) is a method that uses a process called VAT photopolymerisation [98]. Ultraviolet (UV) light is projected onto a photocurable resin (either acrylic or epoxy) which cures surfaces into solids, as shown in Figure 2.19. The process starts with a UV laser projected onto the top

surface (layer) of a reservoir of liquid photopolymer via an adjustable mirror. The laser travels across the entire targeted surface to create a cross-sectional pattern. Then, a platform submerged into the reservoir moves down between 0.05 and 0.15 mm (depending on the initial setup) from its initial position. A repetition of this cycle enables the the manufacture of the part layer by layer. The advantage of this method over the other 3D printing techniques is that it results in in high resolution printing (25 microns in Formlabs Form3 [99]). Another great advantage is that there are no clogging problems, since the SLA mechanism does not use a nozzle. However, high degrees of complexity require support structures that are made of the same material as the part and entail additional post-processing steps to be removed.

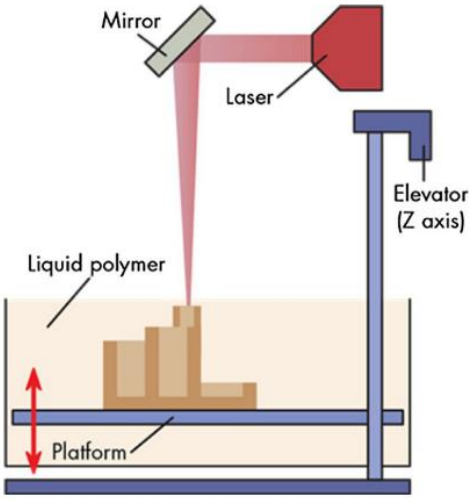


Figure 2.19 Stereolithography setup [100].

PolyJet or material jetting is another technique that uses drop-on-demand technology and is widely employed due to its ability to produce highly accurate parts with a smooth surface, as shown in Figure 2.20. Liquid material is sprayed onto a build platform through multiple print nozzles. The droplets from the nozzles are instantly cured by UV light and become solid, creating a thin layer. This process cycle is repeated many times until the part is finished. Parts with a high degree of complexity require support structures, which need to be removed using post-processing steps. The advantage of PolyJet is that it enables high resolution printing (14 microns in J735 Stratasys [101]) using full-colour multi-materials. However, parts manufactured using this technique are usually weak compared to other techniques such as Powder Bed Fusion (PBF) techniques.

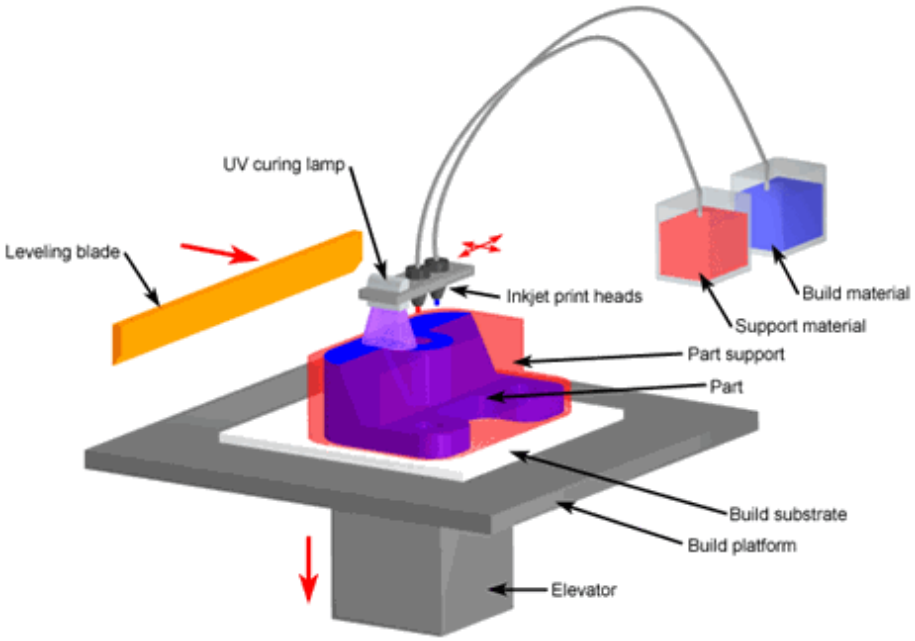


Figure 2.20 PolyJet technology setup [102].

Selective Laser Sintering (SLS) and Selective Laser Melting (SLM) are part of the family of Powder Bed Fusion (PBF) techniques, as illustrated in Figure 2.21. The principles of both techniques are similar except for the used materials; SLS uses resin for partial sintering, whereas SLM uses metal for full melting by using a high-power heating source that melts powder, which eventually transforms into a solidified layer. The SLS setup is composed of two chambers: a printing chamber and a powder reserve chamber heated to a temperature below the material melting point. The heating source is an XY-axis laser beam applied to the top powder layer on the printing chamber to sinter a predetermined pattern. After the sintering of each layer, the printing chamber moves down along the Z-axis to a predefined depth, and the powder reserve chamber moves up to expose material on the printing chamber using levelling drum rolls. This process cycle is repeated until the part is completed. After that, the unsintered powder (powder cake) is removed from the part. An advantage of this technique is that it does not require the use of support structures, enabling complex parts to be fabricated. Parts built using SLS shower a degree of smoothness lower than that found in parts built using SLA. However, only thermoplastic polymers can be printed using this technique. A recent study by Tasch et al. [103] suggested that SLS enables the manufacturing of features of sizes equal to or greater than 1 mm with a minimal compromise of mechanical properties, such as losses in stiffness, ultimate tensile strength, and elongation at necking, compared to smaller features of sizes less than 1 mm. When compared with large samples with minimal faults, small features either could not be built or were manufactured with a significant compromise of mechanical capabilities. [103].

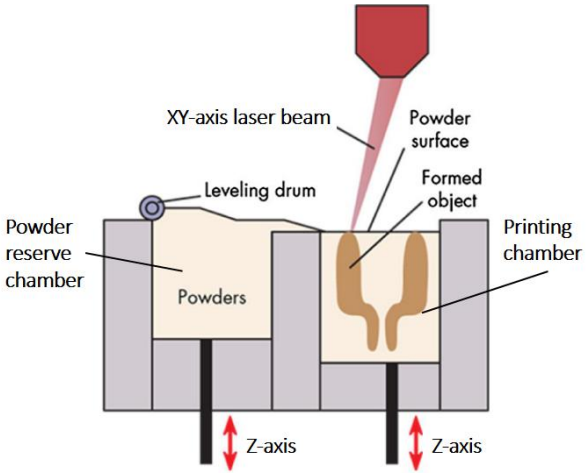


Figure 2.21 Selective Laser Sintering setup [100].

Although AM processes are advanced technologies that can produce lattice structures, lattices are still being manufactured using conventional manufacturing techniques. Hang et al. [66] manufactured a lattice structure with a few millimetres cell size using cutting for metallic sheets, then assembled it and finally bonded members using laser welding, as illustrated in Figure 2.22. Another example called UCSB lattices was presented by Berger et al. [65]. UCSB lattices were manufactured using electrical discharge machining (EDM), where 3-mm-thick sheets of Ti–6Al–4V lattice were cut and 7075-T6 aluminium alloy hexagonal units were milled. Following that, hexagonal units were press-fitted into the lattice centre. Another example was presented by Wu et al. [86] who produced 2D lattice structures using bi-material elements and a bimetal plate with aluminium and copper, as shown in Figure 2.23. A cutting machine was employed to cut aluminium and copper plates into strips of 1 mm thickness. Rings with grooved ears (circular nodes) and bimetal strips were drilled, and screws were used to firmly tighten them. Some drawbacks of these techniques are that they cannot achieve the high degree of complexity expected in lattice structures and require multiple processes to manufacture them.



Figure 2.22 Examples of 3D metamaterials produced by cutting metallic sheets, then assembled and bonded using either brazing or laser welding [66].

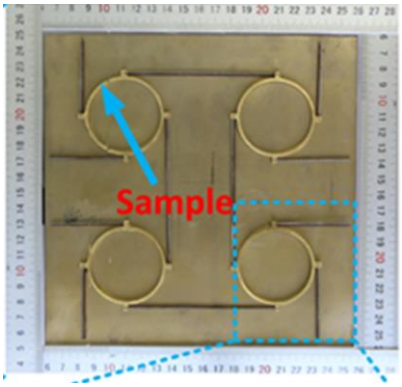




Figure 2.23 An example of bimetal antichiral metamaterials with ligaments and nodes [86].

AM machines are the primary machines employed for the production of highly complex lattice structures. Without AM technologies, certain lattice structures are impossible to be manufactured. For example, Invar-nickel lattices from TO [77] are built using SLA or surface micromachining techniques. Similarly, the TO lattices presented by Akihiro et al. [79] and Takezawa et al. [80] were produced using multi-material jetting with a mixture of photopolymeric materials (VeroWhitePlus and TangoBlackPlus). Material jetting was additionally used by Abueidda et al. [104] to fabricate surface-based lattices and investigate thermal expansion interrelationships between several materials, namely 934 epoxy, ZrW_2O_8 Zirconium tungstate, PMR15 polyimide, 2024 aluminium, borosilicate glass and Invar. However, dimensional deviations were noted in the lattices produced using material jetting, due to the limited precision of multi-material additive manufacturing processes [86].

A single manufacturing technique may not be sufficient to produce high-quality lattice structures, and a combination of AM techniques with conventional manufacturing processes is possible. Yamamoto et al. [91] manufactured stretch-dominated planar lattices in the micro-scale (thin film) using conventional and AM techniques. Aluminium and titanium were micro-fabricated to produce 1 µm-thick structured films using a conventional micro-fabrication technique. The aluminium hexagonal plates and the titanium frame were then deposited on a substrate using a combination of photolithography, electron-beam evaporation, and metal lift-off processes, then bonded by lap joints. Parsons introduced hexagonal lattice materials, and triangular lattice structures were manufactured using AM and computer numerical control (CNC) EDM (Parsons, 2019). Eight alternating layers of titanium and aluminium were consolidated using ultrasonic AM to create a composite plate. The plate was then cut into hexagonal cells or triangular cells using automated EDM.

High mechanical performances can be reached using either SLS or SLM machines to fabricate single-material lattice structures [17, 18, 21, 41, 42, 45, 49, 59, 60, 75, 76, 100, 105, 106]. Numerous materials

are available for these techniques, such as nylon 12 for SLS, aluminium (Al-Si10-Mg) and titanium (Ti-6Al-4V) for SLM.

From the aforementioned publications, it is clear that the designer of a low-CTE bi-material lattice needs to consider both the complexity and manufacturability of the lattice and the challenge of assembly. Our proposed approach is to simplify design requirements as much as possible to obtain a low-CTE lattice, by utilising high-CTE inserts of a simple cylindrical geometry and made from a commonly available polymer.

2.6. Testing the lattice structures

Two types of testing were considered to examine the lattice structures: finite element (FE) analysis and experimentation. FE testing provides numerical results, while experimentation renders physical workpieces. Difference between numerical and experimental results can be noted due to several factors such as the uncertainty of temperature in the experiment, undetermined surface friction in FE analysis, the uncertainty of the material's CTE obtained in FE analysis, including the general underestimation of displacement in FE analysis due to the reduce freedom of the FE and the approximations to strain inside elements – usually a linear or quadratic model, etc. To convert novel lattice structures with tunable thermomechanical properties into real applications, both thermal and mechanical analysis need to be carried out as lattice structures support different loads depending on the range of temperatures. Among many properties, it is noted that the primary property of interest is the coefficient of thermal expansion typically presented in most studies.

FE analysis is widely used to simulate lattice structure properties. Simulation can focus on the analysis of a single unit cell with appropriate input parameters. All parameters in the initial and final steps of simulation, such as the type of analysis, material properties, boundary conditions, and temperature, are assigned explicitly in a CAE software, and then the input files are run via the software. Finally, results are given at the end of processing. Apart from material properties and boundary conditions that need to be assigned, the mesh is another parameter that must be considered. Several types of mesh elements can be selected for analysis in thermomechanical simulations.

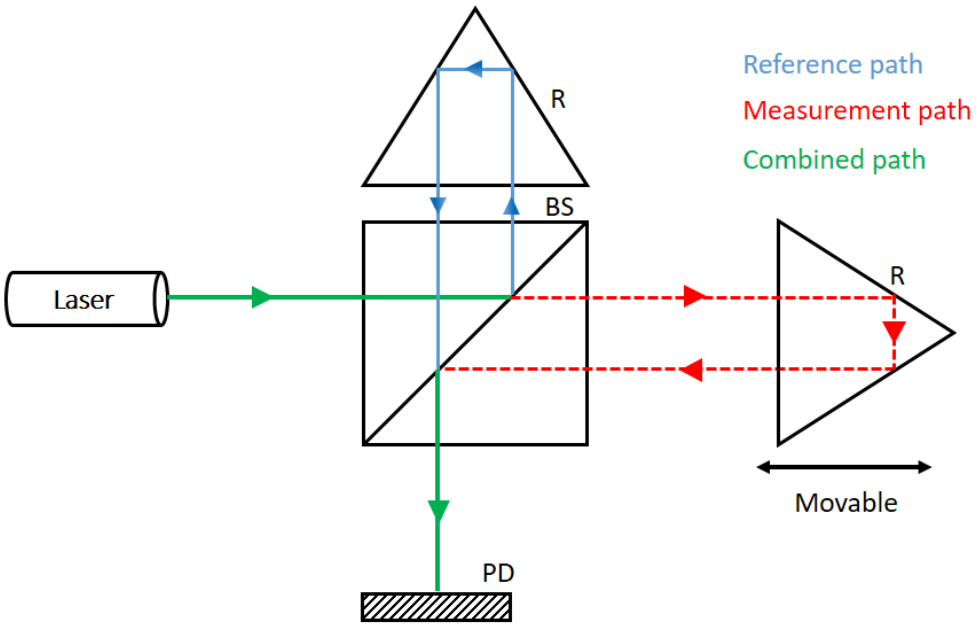
In previous research, some researchers used a low number of first degree elements, such as 1,000 eight-node brick elements, with reduced integration (C3D8R) [90] and 4,096 C3D8R elements [107]. As technologies developed, large numbers of first degree and higher degree elements are available. Many studies proposed that one unit cell be meshed differently using various element numbers and types. Examples of the use of first-degree elements include the study of Y. C. Zhang et al. [85] who

used 139,264 C3D8R elements, as well as Berger et al. [65] who applied approximately 50,000 to 70,000 C3D8R elements and Ai et al. [67, 68] who used 940 BEAM 189 elements. As for a higher degree of elements, Abueidda et al. [104] used 200,000 3D ten-node tetrahedral elements (C3D10), while others applied C3D10 elements [66, 91, 93]. Different combinations of numbers and types of elements were used for simulation, and the justification of numbers and elements depended on the researchers' experiences. In addition, the use of FEA was essential to obtain accurate results by verifying the results using mesh convergence tests.

As far as the tailorable thermal expansion lattice structures experiment is concerned, two processes are involved: heating and measuring. In some of the previous studies, lattice structures were simply slowly heated by heat sources such as a furnace [90], a laboratory hot plate [24, 65], an electrically heated oven [2], a vacuum drying oven [86, 108], or a heating chamber [66]. The testing temperature range depended on the melting temperature of the lattice structure materials, the heating source's limiting temperature, and the operating temperature of lattice structures in a specific application. Plenty of heating systems were used to uniformly heat specimens to their targeted temperatures. One such study [65] used a hot plate and slowly increased the temperature at 60 °C per hour, from room temperature to 220 °C. K-type thermocouples were placed in four specific locations all around a specimen, including its upper surface, with a glass plate on top to monitor the temperature change. Steeves et al. [90] used a furnace and placed thermocouples on the lattice structures. Another study [86] used two set-ups to perform different lattice structures. First, 2D (planar) tailored thermal expansion lattice structures were tested such that they were placed on a heating platform and covered with a quartz jar to prevent convection heat transfer to the surrounding environment. Second, 3D tailored thermal expansion lattice structures were placed in a vacuum drying oven with a rate of 4.5 K per minute. In this research, an infrared camera was used to monitor the surface temperature of the lattices in real-time.

In thermal expansion testing, the dimensional changes of lattice structures must be monitored. Non-contact measurement systems are widely used to measure dimensional changes, according to previous research. One of the advantages of using non-contact measurement systems is to avoid thermal conduction from specimens to the measurement system. Steeves, dos Santos e Lucato [90] used a scanning laser extensometer to measure the displacement change between adjacent lattice nodes. Two other studies [79, 80] used laser scanning dilatometry to measure strains. Many others researchers [24, 65, 66, 86] used a CCD camera with a zoom lens and a 2D digital image correlation (DIC) system to measure the displacement change of specimens.

A different instrument used to measure displacement changes of specimens is the laser interferometer. Interferometry is a measurement method that exploits the interfering nature of superimposed waves. The Michelson-type interferometer is a basic optical interferometer utilised to measure the displacement of a specimen and to produce interference between two light beams. The construction of a Michelson-type interferometer with retroreflectors instead of flat mirrors is shown in Figure 2.24. Retroreflectors are made up of three plane mirrors positioned in the shape of a cube's corner. Following the configuration of retroreflectors, the return beam is always parallel to the incident beam.



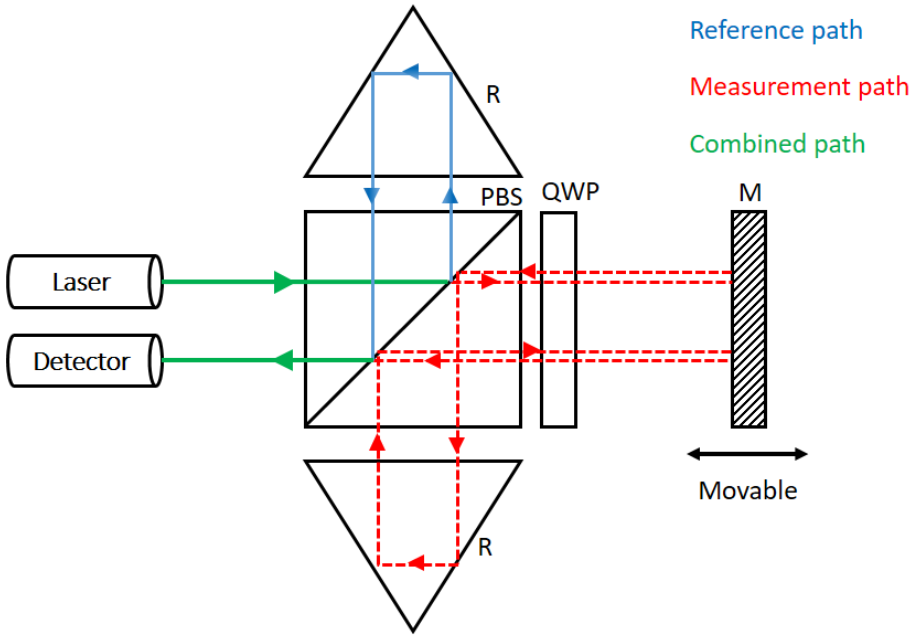
R = Retroreflector, BS = Beam splitter and PD = Photodetector

Figure 2.24 Illustration of the construction of a Michelson-type with retroreflectors.

The Michelson interferometer works by splitting a spatially coherent beam into two equal amplitude beams, creating a reference path and a measurement path, as shown in Figure 2.24. One beam, known as the 'reference beam', hits a fixed retroreflector, while the other, known as the 'measurement' beam, hits a movable retroreflector that can be moved longitudinally to the incident light wave. Both beams are reflected in a beam splitter and combined into a single beam known as the interference signal. Then, a combined beam travels towards a fixed photodetector. The intensity of the interference signal converges on a photodetector which renders an interference pattern that can be converted to a difference in the length of the paths travelled by the two beams [109].

Figure 2.24 shows the linear interferometer configuration with retroreflectors that are suitable for single-axis motion applications. A typical plane mirror, rather than a retroreflector, is the preferred object for dual-axis motion and is required for an X-Y stage, as shown in Figure 2.25. The quarter-wave

plate (QWP) converts linear polarisation from a laser source to circular polarisation. After the beam has been reflected by the moveable mirror and gone back through the QWP, the beam is then converted to orthogonal linear polarisation. The movable mirror or object mirror can be freely moved orthogonally to the line of sight without interfering with the beam paths. An additional benefit of this double pass configuration is a more refined measurement resolution [110].



R = Retroreflector, QWP = Quarter wave plate, PBS = Polarisation beam splitter and M = Mirror

Figure 2.25 Illustration of the conceptual configuration of a plane mirror interferometer.

Interferometry systems have been widely used in the literature. Okaji et al. [111] proposed an adaptive system measuring linear CTEs. The system was composed of a double-path optical heterodyne laser interferometer and a parallel spring strip supporting system. Optical misalignment self-compensation and excellent sensitivity in fringe detection were ensured. The total uncertainty of the measurement was estimated from measurements of twelve types of specimens to be 3 to 7 × 10^{-8} K^{-1} on materials that had linear CTEs of −1 to 23 × 10^{-8} K^{-1}. Wostenholm et al. [112] proposed an absolute interferometric technique where a microcomputer was used to analyse interference fringe patterns to determine length changes to an accuracy of 3 nm. Fused silica and copper were selected for the measurement the CTEs over the temperature range of 80 K to 800 K. Measurement accuracy above room temperature is limited by the stability of the interferometer temperature and the measurement is typically ± 0.1 × 10^{-6} K^{-1} or ± 4%. Another example of interferometer use was presented by the NPL, where Hughes [2] proposed an absolute interferometric dilatometer to measure the linear CTE of steel gauge blocks up to 125 mm long. Ten gauges were examined at temperatures between about 20 °C and 37 °C, resulting in ± 1 × 10^{-7} K^{-1} of the target uncertainty for the CTE of 100 mm steel gauge blocks. Okaji et al. [113] introduced an optical heterodyne

interferometric dilatometer for linear CTE measurements. In this study, ceramic and steel gauge blocks were measured in the range of –10 °C to 60 °C, resulting in uncertainty and reproducibility of the order of 1×10^{-9} K^{-1}. Corsetti [114] developed an interferometer to measure both the CTE and temperature-dependent refractive index coefficient dn/dt simultaneously of optical materials. Preliminary measurements of the CTE of the steel gauge block of a sample show agreement with literature values made by manufacturers and other research institutions. The linear CTE was found to be 10.65×10^{-6} K^{-1}, with the maximum value of the error bars being 0.1×10^{-6} K^{-1}. From these publications, it is clear that interferometry systems show excellent performance for the measurement of thermal expansion coefficients of solid materials, although there is no evidence that interferometers were used to measure the CTEs of lattice structures.

2.7. Conclusion

In this chapter, the considered principles in precision machine frame design were described. General information about the designed lattice structure was given, followed by the summary of previously designed lattice structures for controlling lattice structure's CTE. Then, the available technologies employed to fabricate the lattices were described, and available testing methods to evaluate their performance were delivered.

3. Methodology and method

This chapter explains the methodology and method followed to answer the research questions in Chapter 1 and provides an overview of the process flow. In the context of low thermal expansion machine frames using lattice structures, the gaps in knowledge related to design techniques, modelling methods, and thermal expansion experimentation are as follows:

- The literature contains little information on low thermal expansion lattice structures using the combination of additive manufacturing and conventional manufacturing process for fabrication.
- The literature contains little information on finite element simulations to investigate thermal expansion lattice structures.
- The literature documents little research on thermal expansion experiments for measuring lattice structures.
- The literature contains no information on low thermal expansion lattice structures for precision machine frames.

To address these knowledge gaps, this PhD research is divided into five stages: design of the lattices, finite element (FE) simulation of the lattices, manufacture of the lattices, thermal expansion experimentation of the lattices, and implementation of the lattices in the test case of a metrology frame.

Figure 3.1 illustrates the overall methodology employed in this PhD project. After identifying the problem (as described in Chapter 1), this project started by defining all the conditions related to the whole process. Then, the project was split into two paths that were worked on in parallel and later joined in the 'Test the design and collect the data' step. The sequence in the first path began with the design of the lattices stage, the finite element simulation of the lattices stage, and then the manufacture of the lattices stage. The second path started with designing, building and testing a thermal expansion measurement machine for the thermal expansion experimentation of the lattices. Then, manufactured lattices from the 'Manufacture of the lattices' stage were experimented with the 'Test the design and collect the data' step in the thermal expansion experimentation of the lattices of the second path. Finally, the resulting lattices were implemented into a low thermal expansion machine frame.

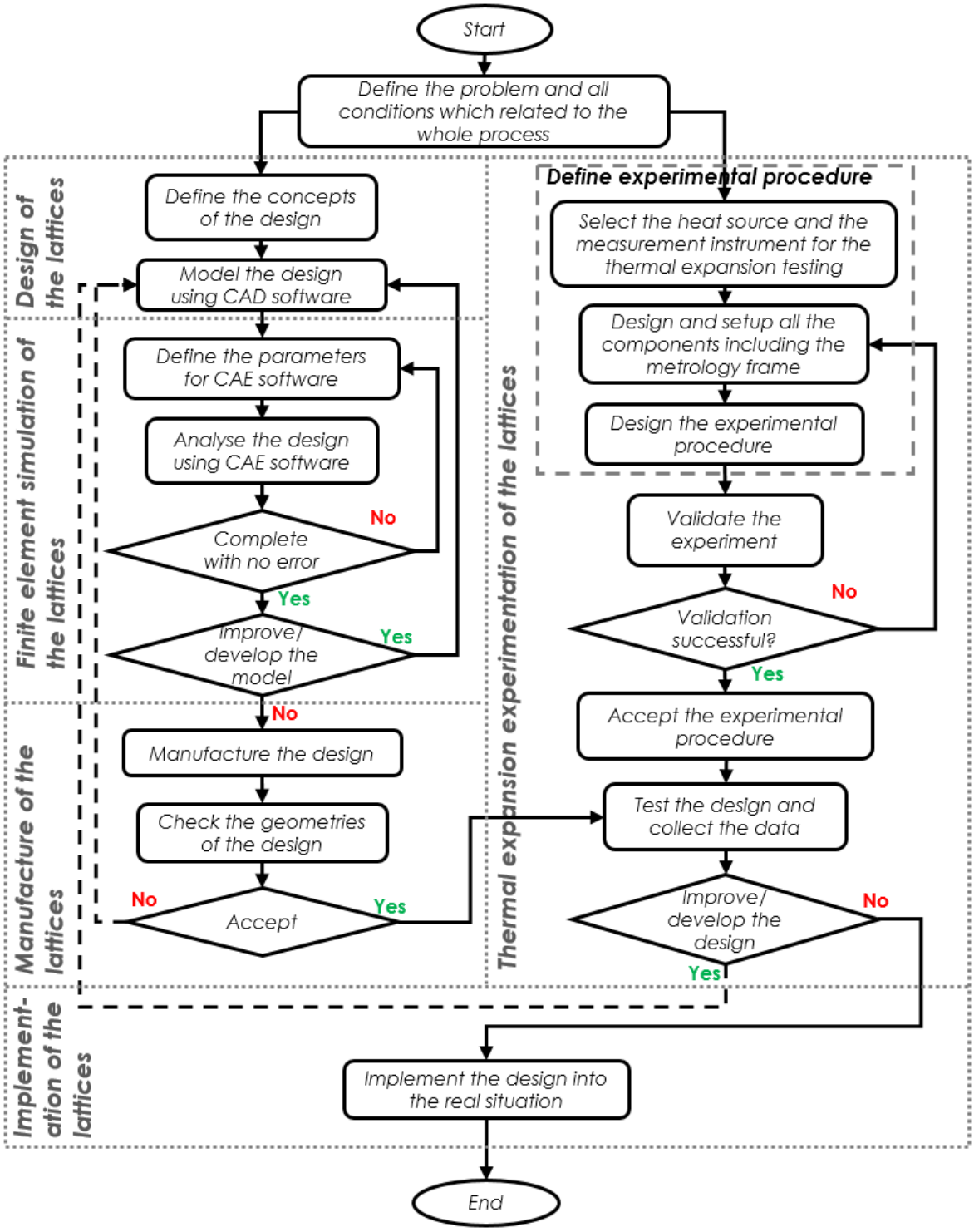


Figure 3.1 Overall methodology of the project.

The steps shown in Figure 3.1 were carried out repeatedly to achieve low thermal expansion lattices. After obtaining computational results from CAE software, the results were justified provided their analyses were completed with optimised computational resources. If this was not the case, the models were re-defined in the 'Define the parameters for CAE software' step. If their analyses were completed with optimised computational resources, they were justified again as to whether the models should

be improved or developed in the 'Design of the lattices' stage or forwarded to the next stage: the 'Manufacture of the lattices' stage. In the 'Manufacture of the lattices' stage, the manufactured lattices were justified in the 'Check the geometries of the design' step. If the lattice geometries were within a range of acceptable dimensions, which will be described in Chapter 4, then they would be thermally experimented on in the verified experiment of the 'Thermal expansion experiment of the lattices' stage. If the coefficient of thermal expansion (CTE) results of the manufactured lattices were within a range of expected CTE, they were accepted and used for implementation in the low thermal expansion metrology frame, whilst any unacceptable lattices were discarded or remodelled in the 'Design of the lattices' stage.

In the following subchapters, the details of each stage will be described. First, a methodology for the design of lattice structures for low coefficient of thermal expansion is presented. Second, a methodology for FE simulation of lattice structures is described. Third, a methodology for the manufacture of the lattice structures is presented and followed by a methodology for the thermal expansion experimentation of the lattice structures.

3.1. Methodology and method for the design of lattice structures for low coefficient of thermal expansion

The 'Design of the lattices' stage is significant in this project as it refers to the specific occasions when the designs need to be changed, either in terms of improvement or development. One piece of technology that enables working with the modelling is CAD software; graphic user interface (GUI) software allows for creating models from a computer. Several CAD software are available in commercial markets; for example, NX by Siemens PLM Software, Autodesk Inventor by Autodesk, and SolidWorks by Dassault Systèmes, amongst others. Mathematical modelling techniques used in the software are similar in nature, meaning that any software can be used.

The main challenge in designing the lattices relates to how to design lattice structures with low thermal expansion that are both manufacturable and meet the expected CTE. In the initial stage, 3D models of 1D tailorable thermal expansion lattices were developed to prove the design concept that the lattice structures' thermal expansions were controlled either in X- or Z-axes, which will be discussed in Iteration 1, Subchapter 4.3.1. Then, 3D models of 2D (planar) tailorable thermal expansion lattices with targeted performance were developed and manufactured for physical thermal expansion experiments, which will first appear in Iteration 1.2, Subchapter 4.3.1. The expected outcomes from the 'Design of the lattices' stage were 3D models including all geometries of lattice structures which can then be used in the 'Finite element simulation of the lattices' stage and the 'Manufacture of the lattices' stage.

Before the models were created, design requirements were defined. Relevant knowledge about designs from previous research was reviewed and compared, as described in Chapter 2. Many factors were considered during the 'Design of the lattices' stage. These considered factors were listed within the seven steps of our 'Design of the lattices' stage (as shown in Figure 3.2), which are as follows:

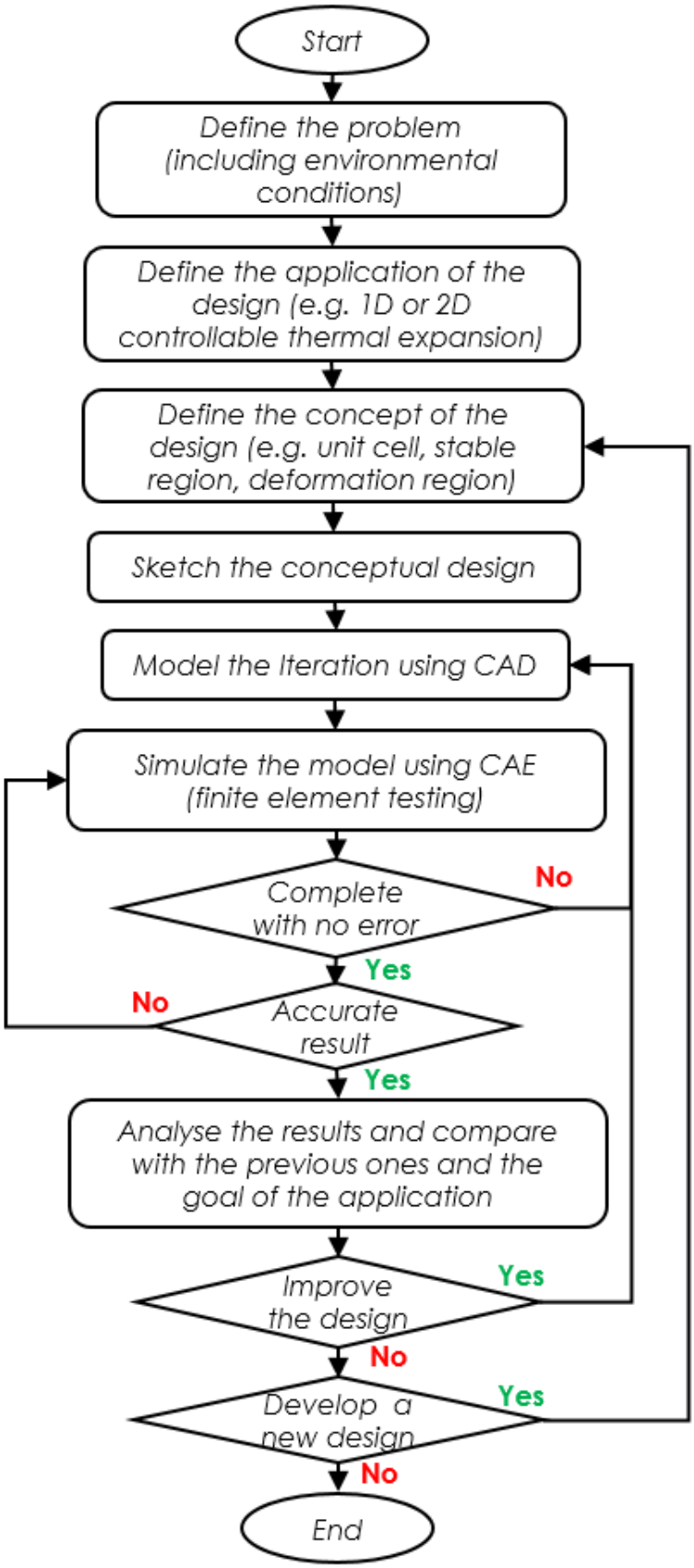


Figure 3.2 Processes of the design of lattice structures for low coefficient of thermal expansion.

Step 1: Problem definition – The causes and effects of the thermal expansion problem in precision machine frames, due to internal and external sources, were studied. The problem statement was defined as described in Chapter 1.

Step 2: Application definition – The application specifications to be applied to the machine frame were defined. These specifications included the target CTE, temperature range, isolation direction (for example, in 1D, 2D or 3D), static loads and loading directions.

Step 3: Concept definition – The design tools and specifications that would enable the realisation of the machine frame for the particular application, as mentioned in Step 2, were defined. These tools and specifications included defining the lattice types, auxetic material, constituent material, manufacturing route and material composition (single- or multi-material). These concepts were used when exploring different possible designs and when upgrading from one design to another. In this PhD, lattice structure concepts (as described in Subchapter 2.3) were applied. The essential requirement for creating a unit cell is repeatable and connectable to other cells by merging its constituent material/s to become a larger structure, as illustrated in Figure 3.3. Additionally, details of the designing lattice structure for this PhD will be described in Chapter 4.

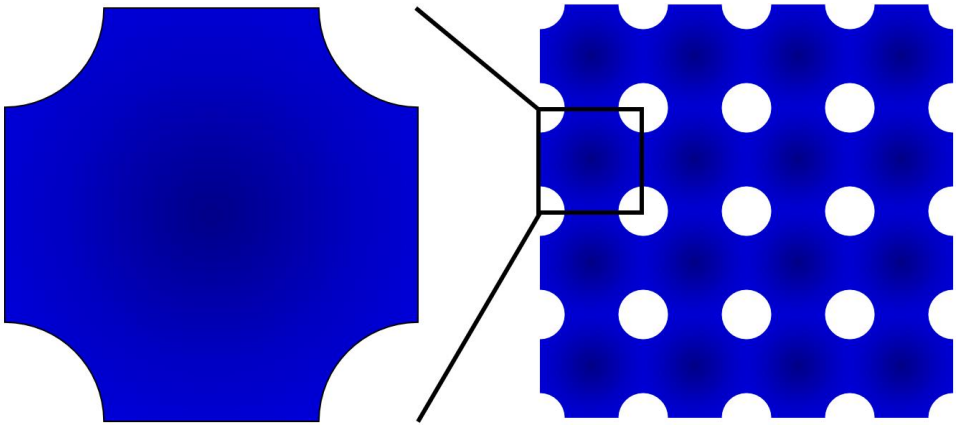


Figure 3.3 Concept of a typical single unit cell (left) and a 4 × 4 lattice structure (right).

Step 4: Designing a sketch – In this step, and based on the concepts defined in Step 3, the different designs and unit cell configurations were sketched. These were done with a combination of CAD software and conventional on-paper designs, and on-paper selected designs were then sketched in CAD.

Step 5: Modelling the iteration – The designs sketched in Step 4 were modelled or remodelled in CAD with actual dimensions and features, such as feature size and shape and overall structure dimensions. The CAD model began with 2D primitive shapes such as lines, circles, arcs, splines, ellipses, rectangles, and polygons with modified techniques such as scaling, trimming, fillet, and merging. Then, the 2D

sketches were created for 3D modelling using geometry modelling techniques, for example, extrusion, sweeping and revolving with boolean operations; union, intersection, and difference. There were also 3D primitive creation functions used to create models; however, a high complexity degree of the model was required for the 2D sketches.

Step 6: Simulation and numerical analysis – The low thermal expansion lattice designs were simulated using a numerical analysis via a CAE software package. This PhD research used FE analysis to simulate the performance. The details of FE analysis are described in Subsection 3.3. The analysis examined whether or not the designs met the performance sought in Step 2. Using simulation and numerical analysis provided a relatively inexpensive tool for auditing performance compared to experimental examination.

Step 7: Performance analyses and comparison – The simulated performance (i.e., CTE, maximum stress, and average displacement of interested nodes) obtained in Step 6 was analysed. The analyses included comparing the performance to previous iterations and the goal/target set in Step 2. This step revealed whether there was room for improvement of the tested design or not; when there was a structural limitation, then a new iteration was sought rather than improving the current iteration. When an iteration was improved, the target was to obtain lower CTE, enlarge or reduce geometrical sections/walls (to reduce stress or increase flexibility), and facilitate the manufacturing process. This also meant that some geometrical features were added or removed to achieve the goals set in Step 2.

Additionally, the experimental method for the design of lattice structures for low coefficient of thermal expansion followed in this PhD research will be presented in Subchapter 4.2.

3.2. Methodology and method for finite element simulation of lattice structures

To justify the lattice structures' improvement/development in the 'Design of the lattices' stage, CAE software was selected as it helped to decide whether the lattices should be experimented with, therefore, reducing the number of physical experiments. FE analysis is one of the techniques in CAE software used for simulation using numerical methods. The technique is widely used in a range of engineering fields to simulate the behaviour of an object or assembled objects under given conditions, thereby reducing the need for physical prototypes. Several FE analysis software are available in commercial markets; for example, NX by Siemens PLM Software, Abaqus FEA by Dassault Systèmes, and ANSYS by SpaceClaim Corporation. Most of the software mentioned has similar mathematical modelling techniques, meaning that any of them can be utilised.

The one challenge that FE analysis brought up was whether or not FEA predicted the performance of the lattice structures accurately and how input parameters could be optimised to achieve accurate results with fewer hardware resources used for computation, especially in larger structures (e.g., a 2 × 1 × 1 lattice (two unit cells) and, a 2 × 2 × 1 lattice (four unit cells)). The computational cost scales with the size of FE meshes and the number of lattice cells in the model.

In this research, the primary outcome of the 'Finite element simulation' stage was the average displacement on specific areas, which were analysed to achieve the target CTE of the lattices. The contour plot of von Mises stress was one of the outcomes used to locate areas of potential failure due to high local stress regions on the lattice and one that helped improve and develop the CAD models of lattice structures. Additionally, FE analysis validation/setup checks were performed for all designs (Iteration series 1, 2, 3 and 4), which will be presented in Chapter 5.

Figure 3.2 shows that FE simulation was a step in the 'Design of lattices' stage. However, more details (e.g., material properties, boundary conditions, FE definitions) must be defined and examined. Following the process of FE analysis from FE Procedures [115], the considered factors were grouped within the six steps of this 'Finite element simulation' stage (as shown in Figure 3.4), which are as follows:

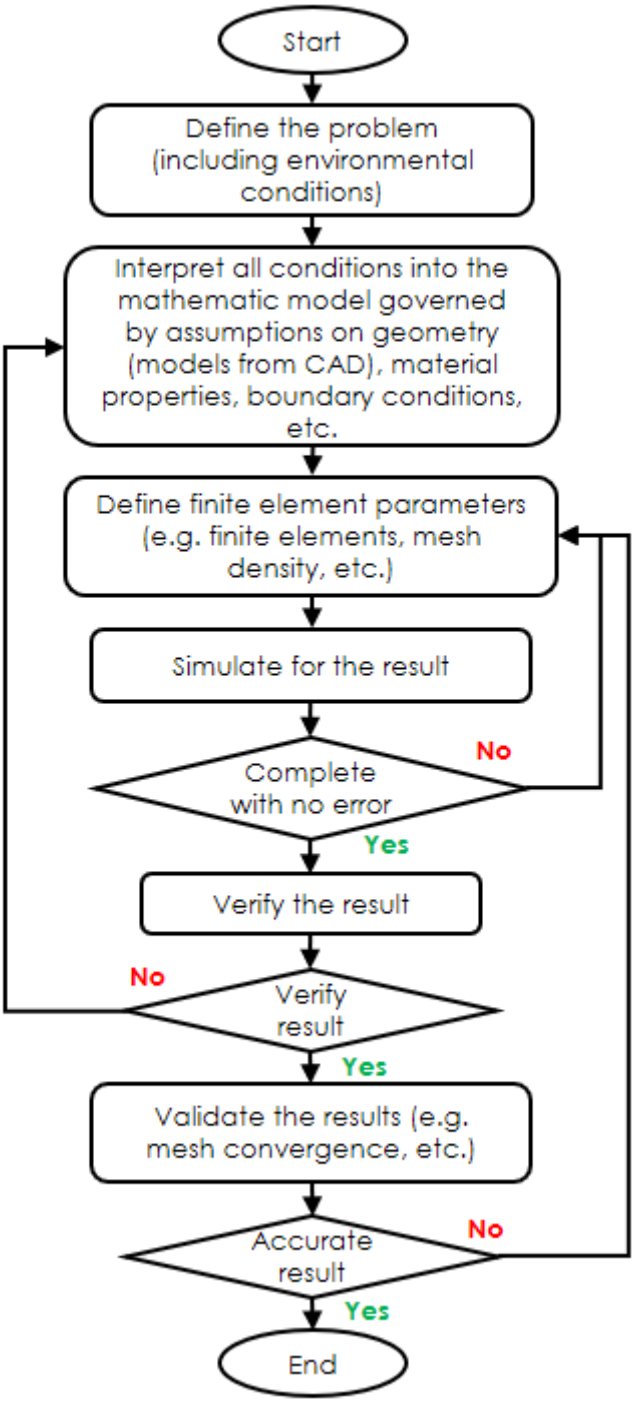


Figure 3.4 Processes of the finite element simulation of lattice structures.

Step 1: Problem definition – This information was taken from Step 1 of the 'Design of the lattices' stage. However, it was necessary to include all assumptions in the simulations as any additional information in predicting physical phenomena than the information contained in the mathematical model can not be expected.

Step 2: Mathematical model definition – The concept of the physical problem was converted into a form that can be solved: a mathematical model. The software could generate the mathematical model by identifying all design elements such as geometry (designed lattices from CAD software), material definition, and the definition of loads and boundary conditions in both the initial and final steps of the CAE software.

Step 3: FE parameter definition – The CAE software used FE analysis to solve the mathematical model described in Step 2. In this step, the geometry was divided into smaller and simpler shapes called finite elements by identifying the type of mesh elements and the number of elements in the software. This step was also used for refining the geometry when the numerical solution did not reach sufficient accuracy.

Step 4: Simulation – This step was run by a computer processor. Step 4 was the first step in considering whether the simulation was completed with no error. However, in some cases, the first attempts can yield complete or incomplete simulations with errors due to inappropriate input parameters (e.g., type of mesh, boundary conditions, etc.). Then, input parameters would be changed to obtain successful results. Moreover, the amount of processing time depends on the complexity of the mathematical model. For example, the mesh element shape function could be linear (first-order) or quadratic (second-order). A higher-order mathematical model or a very fine mesh model could render higher accuracy results, but it would also lead to more costly resources.

Step 5: Verification – In this step, the mathematical model and the results were examined as to whether they match assumptions with respect to the model and correctly reflect the physical problem and initial design.

Step 6: Validation – Mesh refinement is the process used to obtain sufficiently accurate results while incurring the lowest cost possible and the least processing time and hardware resources. Mesh refinement in this research was performed in three steps. The first step involved starting with a mesh that was as coarse as possible (a small number of elements), followed by an analysis of the model. Solving a coarse mesh would require fewer computational resources, but it might yield inaccurate results. The second step was to refine the mesh (higher number of elements), re-analyse the model, and then compare the re-analysed results with the results from the previous mesh. The third step was repeated in the second step until the results were considered as converging. This research used the CTE in specific areas as outcome results for validation.

Additionally, the experimental method for the FE simulation conducted to analyse the lattice structures followed in this PhD research , so other researchers can duplicate it if needed, and clearly understand all the steps involved, will be presented in Subchapter 5.2.

3.3. Methodology and method for the manufacture of the lattice structures

In this PhD research, the fabrication methods of the lattice structures were divided into manufacturing and hand-assembly. There were two groups of components: lattice outer parts and cylindrical inner parts, as illustrated in Figure 3.5. The lattice outer parts were made using an additive manufacturing (AM) process, namely polymer laser powder bed fusion (LPBF), as described in Chapter 2. The cylindrical inner parts were selected from a range of conventional industrial materials, and then machined by a computer numerical control (CNC) machine, and were, therefore, not restricted by the limited material selection associated with LPBF. Polyamide 12 (Nylon 12) was chosen as a relatively low-CTE material for the lattice outer parts. This material is particularly well processed by LPBF to enable the manufacturing of complex parts with a good combination of geometrical accuracy and mechanical performance [116]. Ultra-high-molecular-weight polyethylene (UHMWPE) was chosen as a relatively high-CTE material for the cylindrical inner part as it provides a high-value CTE, good impact resistance, very low coefficient of friction, and self-lubricating performance [117], which is advantageous for the assembly and performance of the proposed two-material structure. Then, the two parts were hand assembled by inserting the cylindrical inner parts into the centre of the lattice outer part. Figure 3.5 shows how the 1 × 1 × 1 lattice (a unit cell) was assembled by inserting the cylindrical inner part (red) into the centre of the lattice outer part (blue). The manufactured lattices were then examined to ensure their quality and correspondence to the CAD geometries. Once the manufactured lattices were verified, they were then tested for their performance in the thermal expansion experiment. In this PhD, no focus was put on the improvement of the quality of the lattice structures manufactured by the AM machine. However, predictions of the in-plane CTE corresponding to the lattice geometry uncertainties were studied, as described in Chapter 6.

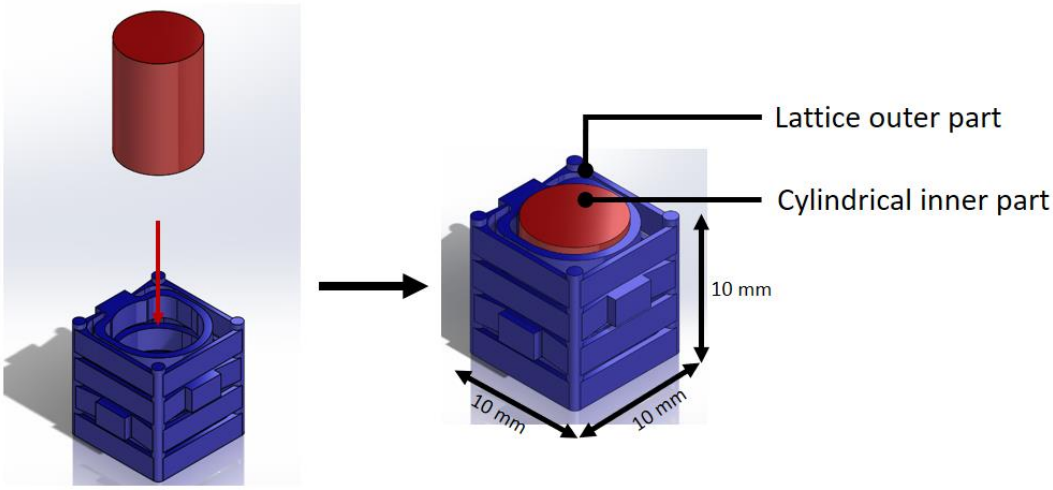


Figure 3.5 Example of how the cylindrical inner part (red) was inserted into the centre of the lattice outer part (blue).

As for the experimental method for the manufacture of the lattice structures, after receiving the STL files from the "Design of the lattices" stage, the STL files were input to an LPBF machine (FORMIGA P100, EOS) and manufactured in Nylon 12 at the Centre for Additive Manufacturing (CfAM), University of Nottingham. The relevant LPBF parameters are provided, such as laser power, scan speed, scan spacing and layer thickness [18]. The manufacturing parameters are shown in Table 3.1.

Table 3.1 LPBF manufacturing parameters used to manufacture the lattice structure [18].

Description	**Value**
Build chamber temperature set point	173 °C
Laser Power	21 W
Scan Speed	2500 mm/s
Scan Spacing	0.25 mm
Layer Thickness	0.1 mm

After manufacturing completion, the specimens were post-processed, and their performance was tested in a thermal expansion experiment of the lattice structure. The post-processing process is listed as follows:

- Careful removal of all un-sintered powder, especially the powder that remained stuck on the surfaces of the deformation mechanism geometry of the lattice outer parts of the specimens
- Scaling of the external dimensions (length × width × height) of the lattice outer parts of specimens, using a vernier calliper
- Scaling of the diameters of the cylindrical inner geometries of the lattice outer parts of the specimens, using a vernier calliper

- Scaling of the lengths and diameters of the cylindrical inner parts of the specimens using a vernier calliper

The first batch of the specimens' lattice outer parts (as shown in Figure 3.6) was manufactured in different sizes to verify the quality of the manufactured lattice structures and their correspondence to the nominal CAD design. After manufacturing, the specimens were weighed on a weighing scale to determine their mass and measured to evaluate dimensional deviations using a Vernier calliper, and an X-ray computed tomography (XCT) scanner (MCT225, Nikon X-ray). Table 3.2 shows the error percentages of the mass and diameters of the cylindrical inner geometries of the lattice outer parts of the specimens, compared to their nominal CAD designs. The results showed that the LPBF process yielded highly precise specimens with low error percentages with regards to mass, compared to measurements from the weighing scale and the CAD model (between −3.22 % and 1.45 %). Similarly, there were acceptably structures with low percentage of errors in the diameters of the cylindrical inner geometries of the lattice outer parts of the specimens, when compared to measurements from the vernier calliper and the CAD model (between −0.5 % and 2.17 %), and measurements from the XCT and the CAD model (between −0.22 % and 1.10 %).

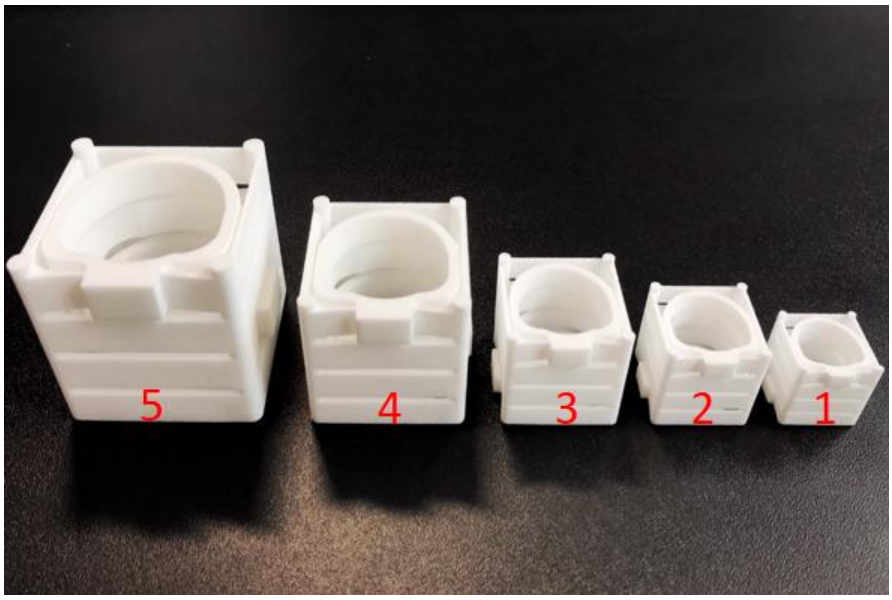


Figure 3.6 First batch of the specimens' lattice outer parts (Iteration 2.4) in different sizes: (1) (18.96 × 18.96 × 18.96) mm, (2) (23.69 × 23.69 × 23.69) mm, (3) (28.43 × 28.43 × 28.43) mm, (4) (37.91 × 37.91 × 37.91) mm and (5) (47.39 × 47.39 × 47.39) mm.

Table 3.2 The diameter of the cylindrical inner geometries of the specimens' lattice outer parts in different sizes.

#	Mass From CAD/ g	Diameter From CAD/ mm	Mass From A Weighing Scale/ g	Diameter From A Vernier Calliper/ mm	Diameter From The XCT/ mm	% Error Of The Mass When Comparing Between A Weighing Scale And CAD	% Error Of The Diameter When Comparing Between A Vernier Calliper And CAD	% Error Of The Diameter When Comparing Between The XCT and CAD
1	1.68	12.70	1.7±0.1	12.96±0.06	12.72	0.93±0.00	2.05±0.01	0.16
2	3.29	15.88	3.2±0.2	16.22±0.20	16.05	-2.73±0.09	2.17±0.03	1.10
3	5.68	19.05	5.6±0.1	19.34±0.15	19.14	-1.49±0.03	1.52±0.01	0.47
4	13.85	25.40	13.4±0.1	25.66±0.16	25.45	-3.22±0.02	1.02±0.01	0.20
5	26.32	31.75	26.7±0.3	31.59±0.21	31.68	1.45±0.01	−0.50±0.00	−0.22

Note: masses from the CAD were calculated from the density of Nylon 12 (0.93 g cm^{-3} from the datasheet [118]) and the volume was calculated from CAD models.

After the verification of the first batch, the other batches were fabricated. The two parts were then hand-assembled by inserting the cylindrical inner part into the centre of the lattice outer part. Following that, the "Thermal expansion experimentation of lattice structures" stage was initiated.

3.4. Methodology and method for the thermal expansion experimentation of the lattice structures

The simulation described in Subchapter 3.2, based on FE analysis, yielded values for stress and displacement of lattice structures, and the illustration of each iteration under the defined conditions. However, the structure needed to be examined physically to ensure and compare the results achieved in the computational and experimental stages.

The challenge mainly regards the unavailability of commercial thermal expansion testing machines that could measure the designed lattices with the size of (50 × 50 × 50) mm. Accordingly, such a machine had to be built and designed by the researcher to design the experimental procedure for this experimental set-up.

To design the machine, there were no rigorous rules to follow. A textbook providing a guideline for a general procedure of machine design [119] was adapted to design the thermal expansion testing machine in this PhD research. The most influential factors for building the thermal expansion measurement machine for lattice structures comprised eleven steps (as shown in Figure 3.7):

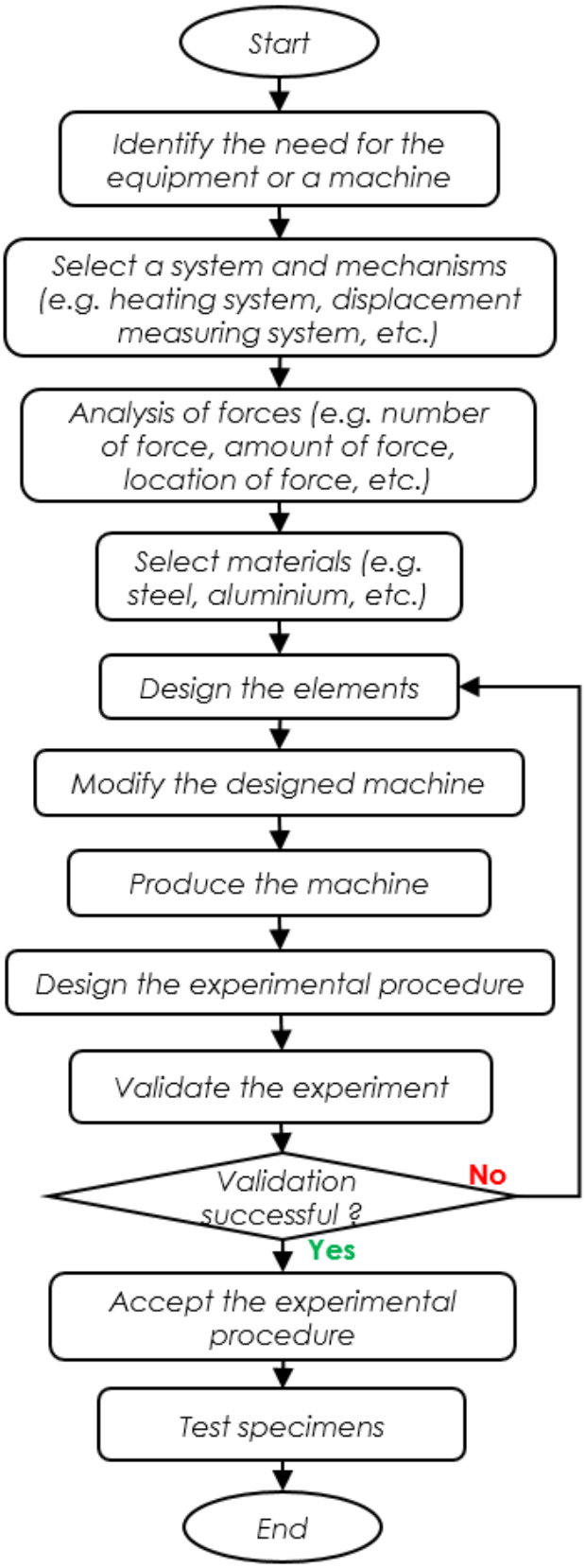


Figure 3.7 Processes of thermal expansion experimentation for lattice structures.

Step 1: Identification of the need for the equipment or machine – The information contained in the problem statement was used to create a thermal expansion measuring machine for manufactured lattice structures.

Step 2: Selection of a possible system and its mechanisms – To measure the thermal expansion of lattice structures, two main systems were needed: a heating system and a displacement measuring system (DMS). The heating system was used to heat the lattices from the bottom, while DMS measured the displacement change from the top of the lattices. In this research, two systems were appropriately selected for commercial markets and integrated into one system. The main part of the design was to combine and place all components in the appropriate position.

Step 3: Analysis of forces – Finding forces occurring on each structural member of the structure could help select the appropriate materials and sizes. There were no moving mechanisms in this design, so the only forces were the weight of the measuring equipment and the structure itself. However, ensuring that the design frame could hold the DMS weight was necessary.

Step 4: Selection of Materials – The appropriate material for each structural member of the machine can offer many benefits (for example, lower cost, higher availability of materials, and improved mechanical properties of materials). The heating system and DMS were selected from existing equipment. The maximum estimated weight of the DMS, including a measurement optics kit and a kinematic set-up, was approximately 4 kg. Aluminium was selected and constructed for the frame as it is an inexpensive material and nearly as strong as some metals, with about a third of the weight of steel (2.71 g/cm^3). It is also widely used in manufacturing precision engineering equipment [120-122]. The minimum 0.2% yield strength of aluminium is 190 MPa, meaning that it can hold a weight of up to 19 kg/mm^2, according to the datasheet from the manufacturer [121]. Therefore, there was no concern regarding the deformation of the frame structure.

Step 5: Design of elements – The information in Steps 2 to 4 was considered for the selection of the size of each structural member of the machine frame. Each member in this design should not be deflected or deformed, in conformity with the permissible limit. The deflection or deformation can cause an asymmetry in the frame structure, resulting in misalignment in the installation of the DMS. Therefore, ensuring that the design frame could hold the DMS weight properly was necessary. In this step, kinematic design is relevant as the frame is designed for highly accurate and precise equipment.

Step 6: Modification – Once Step 5 was completed, it was necessary to look for a range of available industrial materials and accordingly modify the dimensions of the designed parts in technical drawings, to fit with the sizes of industrial components (e.g., bolts and nuts). This step could reduce

the overall cost and production time. Detailed drawings were then produced, describing the assembly of all components and communicating the dimensions of the customised parts to engineers for manufacture.

Step 7: Production – Some parts were ordered from suppliers, such as members and their joints, bolts, washers and nuts. Other parts that could not be found in regular shop stocks and thus were manufactured in a workshop, such as kinematic seat boards for the laser interferometer. All components were assembled into a single structure.

Step 8: Experimental procedure design – Thermal expansion experimentation was carried out to test the dimensional changes of lattice specimens in response to temperature changes. To achieve accurate and precise results, temperature and displacement data were recorded during the whole period of the experiment. The temperature of the heating system was changed in at least three increments (e.g., incremental steps: 30 °C, 31 °C, 32 °C and 33 °C) to obtain an accurate trendline that reflected the relationship between displacement changes and temperature changes in the measured workpiece. The time duration of each increment must last long enough to reach the steady-state temperature, meaning that the measured temperature of the workpiece would not change even after a more extended period. Besides, there might be different temperatures in the measured workpiece at different locations, but the temperature at any given point would remain constant.

Step 9: Experimental validation – Validation of the machine was done by measuring the thermal expansion of reference materials with known CTE values. It was possible to improve and develop the system at this step physically, however, it must be noted that other factors could affect the results through systematic and random errors. Nonetheless, measurement results were corrected using a mathematical model described in Chapter 7. In this research, the error acceptance in measurements was 10 %.

Step 10: Accepting the experimental procedure – The machine has been accepted, and any uncertainty around the system was clarified. The machine could then be employed to test unknown CTE materials.

Step 11: Testing specimens – This was the final step for the 'Thermal expansion experimentation of the lattices' stage. Specimens were carefully tested following the experimental procedure, as described in Step 8.

Additionally, the experimental method followed to assess the thermal expansion of the lattice structures, will be described in Subchapter 6.1.

3.5. Conclusion

This chapter describes the methodology followed to address the research questions in Chapter 1 and provides an overview of the process flow. The gaps in knowledge related to design techniques, modelling methods and thermal expansion experimentation were identified. To address these knowledge gaps, this PhD research was divided into five stages: design, FE simulation, manufacture, thermal expansion experimentation and implementation of the lattice structures. In each stage, steps, challenges, and expected outcomes were described. The results achieved in each stage will be presented in Chapters 4 to 7.

4. Design of lattice structures for low coefficient of thermal expansion

This chapter describes details of the design of lattice structures for low coefficients of thermal expansion, implemented in thirteen iterations. First, an introduction addresses the general concepts used in all iterations. Second, method for design of lattice structures for low coefficient of thermal expansion is described. Third, the evolution of the designs is described. Fourth, results of the designs of the lattice structures for low coefficient of thermal expansion are presented. Then, the lattice structure results are discussed, and finally, a conclusion is drawn. The context of the general concepts used in the designs, notably iteration (4.1), have already been presented and published in Low Thermal Expansion Machine Frame Designs Using Lattice Structures [123, 124].

4.1. Introduction to the design of lattice structures for low coefficient of thermal expansion

The goal of the design of lattice structures for low coefficient of thermal expansion was to create a lattice that yields a CTE as close as possible to zero for a metrology frame with minimal, or zero, sensitivity to thermal expansion. A single-material lattice will generally possess a similar CTE to a solid structure composed of the same material [50]. On this basis, we focused on multi-material design solutions to obtain tailorable thermal expansion. The principal challenge was the design of the internal lattice geometry to minimise the structure's CTE using two different positive CTE materials with void spaces. When two materials with different CTEs are used, the structure could contract due to temperature increase, resulting from the unequal thermal expansion of the materials. We seized this opportunity from two materials with different CTEs to design tailorable thermal expansion lattice structures for a metrology frame.

In this PhD, the control of the lattice CTE was enabled through choosing a structure composed of two different positive CTE materials and void spaces. The low-CTE lattice was designed as a single unit cell then tessellated into a lattice structure, as shown in Figure 3.3. Following Jefferson et al. [93], the unit cell was composed of a lattice outer part (marked 'Low-CTE' in Figure 3.3) and a cylindrical inner part (marked 'High-CTE'). The lattice outer part was designed to be a complex part that incorporated the CTE-minimising mechanism. The cylindrical inner part was designed to be a source of compensating thermal expansion for CTE-minimisation. The two parts were manufactured separately then hand-assembled by inserting the cylindrical inner part into the centre of the lattice outer part. The lattice outer and cylindrical inner parts were fabricated using a polymer laser powder bed fusion (LPBF) and computer numerical control (CNC), respectively, as described in Subchapter 3.3. A cylindrical shape

was chosen for the cylindrical inner part given its rotational symmetry. A cylindrical shape could equally expand from the centre with the same temperature change, resulting in equal planar deformation. It was additionally convenient to manufacture/resize using a conventional manufacturing process.

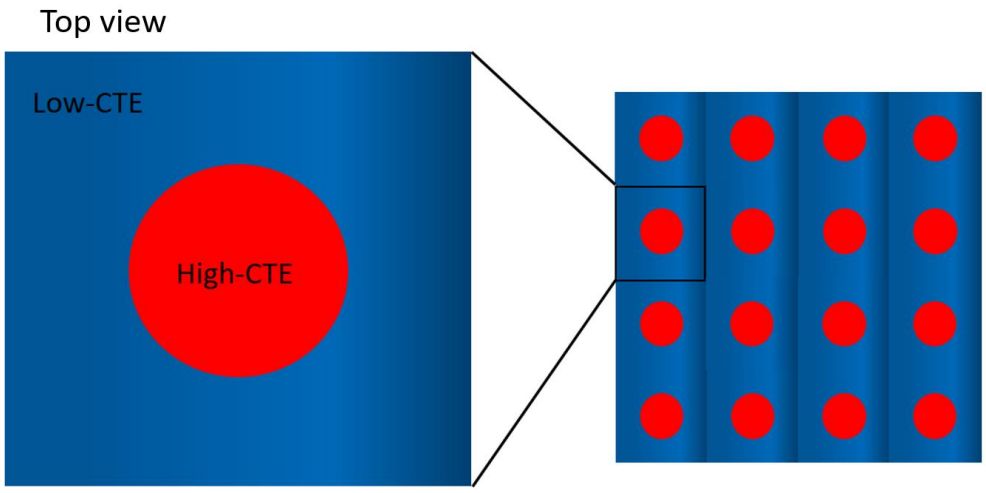


Figure 4.1 Concept of a single unit cell (left) and a 4 × 4 lattice structure (right) of tailorable thermal expansion structure in this PhD.

In this chapter, all lattice structures were created using a CAD software package. The lattices were tested as part of a thermal expansion simulation using CAE software, following the outlined methodology for the design of lattice structures with a low coefficient of thermal expansion and the finite element (FE) simulation of lattice structures, as described in Subchapters 3.1 and 3.2, respectively. Many iterations were created during the improvement and development stages. Additionally, the limitation that the tunable thermal expansion technique presented in this PhD is only relevant to temperature increase. Any reductions in temperature will achieve the same CTE as the lattice outer part material (the cylindrical inner part has no effect)

4.2. Method for the design of lattice structures for low coefficient of thermal expansion

The design of lattice structures for low coefficient of thermal expansion (CTE) was conducted following seven steps highlighted in Chapter 3, which are as follows:

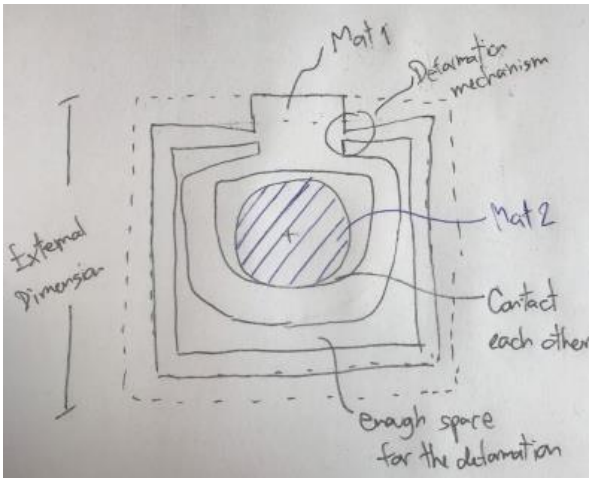
Step 1: Problem definition – Temperature fluctuations, even in controlled laboratory environments, can cause alignment drift in high-precision measuring machines, as their support frames undergo

thermal expansion and contraction [14]. This can lead to significant measurement uncertainty and, therefore, represent a significant issue in precision engineering [15].

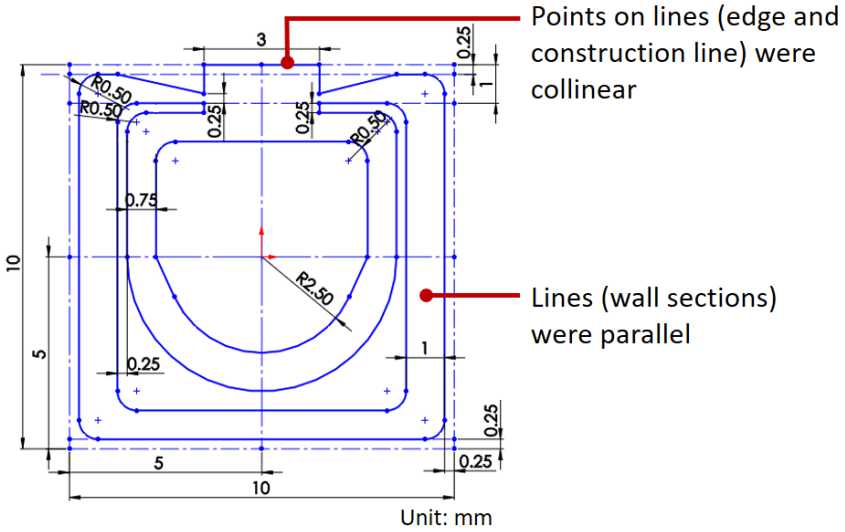
Step 2: Application definition – This research aimed to design a machine frame to support precision measurement equipment (for example, cameras and optical projection systems). The thermal expansion of the frame was evaluated with respect to temperature fluctuations in the range of 19 °C to 23 °C, which represents the temperature variation in a typical temperature-controlled metrology laboratory. The thermal expansion of the frame over this temperature range should not be greater than the resolution of the precision measurement equipment [5], so it does not dominate measurement uncertainty for the instrument.

Step 3: Concept definition – Based on the production facilities we had at our disposal, the LPBF technique was selected to fabricate all lattice structures for this research. The principal step for the fabrication of the lattice structures of the machine frame is to manufacture their smallest component called a 'unit cell'. A unit cell represents the simplest and smallest part based on which the overall structure can be constructed, as described in Chapter 2. A unit cell is also a simple geometry that enables controlling the CTE of the machine frame via its mechanism, which will be described in more detail in Chapter 5. The CTEs of lattice structures were controlled by deformation mechanisms created in the unit cell using two homogenous materials with two different positive CTEs. The design was an assembly of two parts: a lattice outer part and a cylindrical inner part, as shown in Figure 3.4. All iterations were created into three-dimensional (3D) models with tailorable thermal expansion ability, either 1D or 2D.

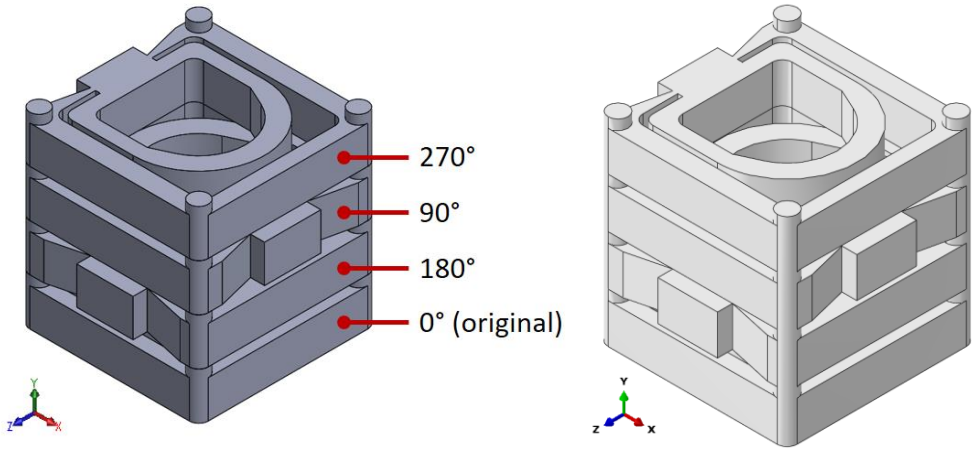
Step 4: Designing a sketch – From Step 3, the lattice outer parts were designed in several ways while the cylindrical inner parts were kept simple, using primitive shapes (cylinders) corresponding to the size of the designed cylindrical inner part in each iteration of the lattice outer parts. Numerous ideas for a controlled CTE unit cell were sketched on paper (as shown in Figure 4.2a), keeping in mind that all 2D and 3D designed shapes should fit in a square (10 × 10) mm and a cube (10 × 10 × 10) mm, respectively. It was convenient to rescale when the actual dimensions of the iterations were defined. All iterations were started by designing a 2D sketch (as seen in Figure 4.2a). This sketch was then transformed into a 3D model (as shown in Figure 4.2d) in Step 5. Some lattice outer parts were simply made of a number of 'layers'. The complete design strategy for the lattice structures and the rationale of selecting a 'layered ' lattice structure will be given in Suchapter 4.3.



(a)



(b)



(c) (d)

Figure 4.2 Illustration of the creation of a model using lattice outer part of Iteration 3 as an example. (a) A 2D sketch of a layer, (b) a 2D model of a layer of the lattice outer part with examples of parametric constraints, (c) a 3D model of the four different orientational stacked layers and (d) a 3D model of the lattice outer part.

Step 5: Model the iteration – SolidWorks version 2018 was used to remodel all the iterations sketched in Step 4. In this step, the models were carefully designed such that dimensions of all geometries in the iterations were larger than the manufacturing layer thickness of the LPBF machine, which was 0.1 mm [18], as seen in Figure 4.2d. All cylindrical inner parts of the iterations were modelled as cylinders with specific diameters and heights. As for the lattice outer parts of the iterations, a 2D sketch was first drawn before extruding a 3D model. Parametric constraints were applied in these models, forcing the geometric models to behave in the desired way. For example, the lines constructed for the wall sections were paralleled, and points of the line (representing the top edge) and the construction line were collinear (as seen in Figure 4.2b). Moreover, other parametric constraints were applied, mainly horizontal, vertical, intersection, coincident, perpendicular, equal, etc.

The processes described above enabled the modelling of the designs of the 3D models of 1D tailorable thermal expansion lattices. As for the 3D models of 2D tailorable thermal expansion lattices, the 3D model of a layer was duplicated to obtain more layers and stacked on top of the previously generated layer with different orientations around the Y-axis. For example, Iteration 3 was composed of four layers stacked on top of the previous layer with different orientations around the Y-axis: 0° (original), 180°, 90° and 270°, as shown in c. In the final process of modelling the lattice outer parts, all layers and their components were merged into a single part, as shown in Figure 4.2d. After the completion of the modelling process, the iterations were exported for further steps.

Step 6: Simulation and numerical analysis – Details of all conditions and parameters will be presented in Chapter 6. Additionally, FE analysis validation/setup checks were performed for all designs (Iteration series 1, 2, 3 and 4), will be presented in Chapter 5.

Step 7: Performance analysis and comparison – Computational results were compared to find the ones that can provide a low in-plane CTE. Details of the results and their comparison will be described.

4.3. Evolution of designs

To ensure that the designs were evolving, each configuration was created by either developing or improving the previous one, as shown in Figure 4.3, resulting in 13 iterations divided into four series. Each series of iterations represented a development in the designs. Within each series, the number after the decimal point represented an improvement in the designs. Decisions about whether a design required improvement or development were mainly based on CTE values. A lattice structure with a CTE value close to zero was preferred. The designs of lattice structures for low CTEs are described as follows:

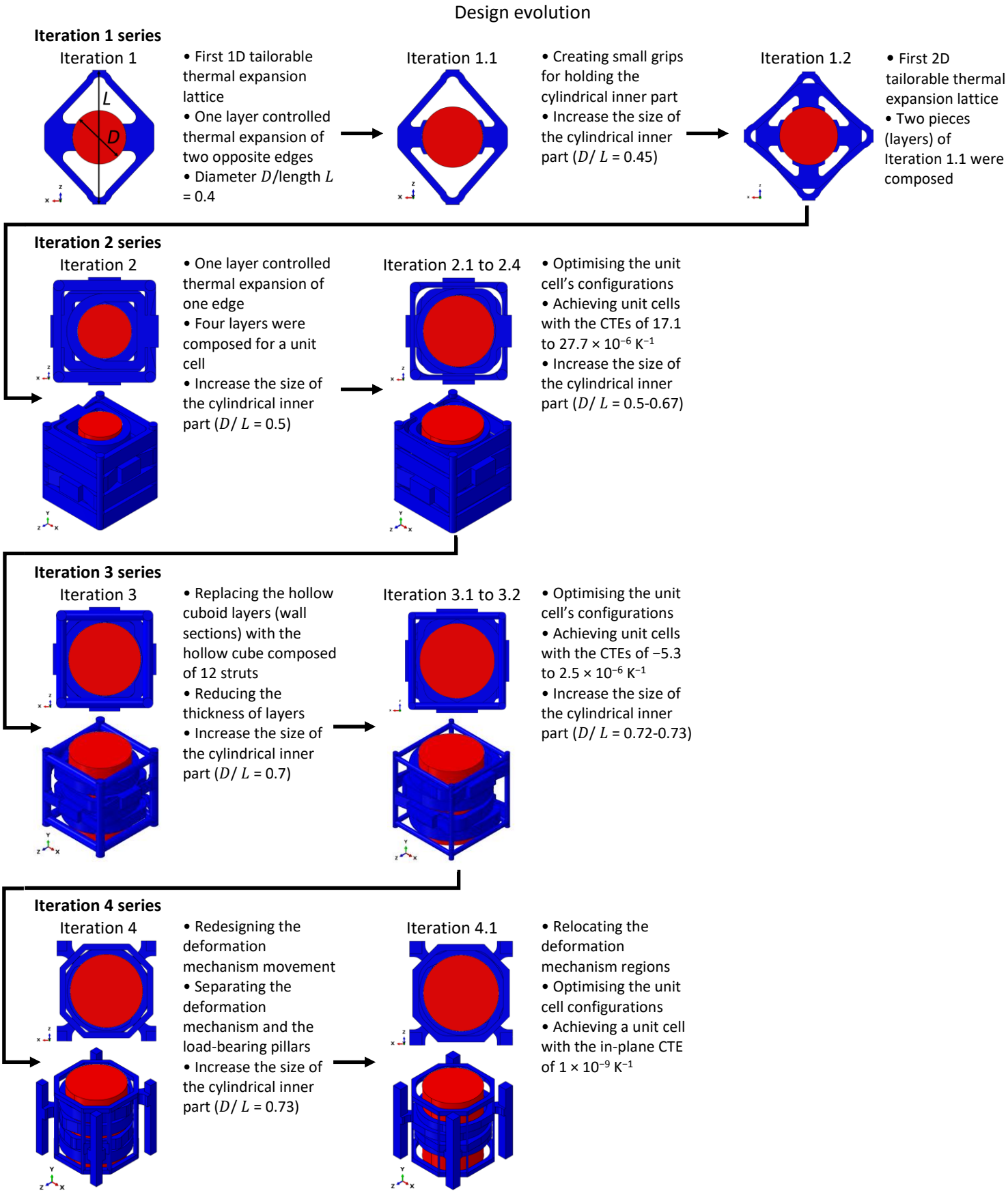


Figure 4.3 Illustrations of the evolution of designs.

4.3.1. Iteration 1 series

1. Iteration 1

The simplest design conducted in this study is shown in Figure 4.4a. The design started with one dimensional (1D) tailorable thermal expansion (as described in Subchapter 3.1). The design concept was initiated at the unit cell level of a lattice structure. First, the boundary of the design materials and void spaces was designed as a simple square (the dash-dotted square). To control dimensions along an axis of the lattice structure, a fitted-diamond (a square turned 45 °) frame was designed. The frame included attached structures which met a circle at the centre of the lattice structure. The design boundary (as shown in Figure 5.3a) was designed to indicate the original dimensions of the lattice structure and guide in designing structural configurations. The fitted diamond represents the lattice outer part, while the circle represents the cylindrical inner part. Four vertices laid on the boundary of the design were used to indicate the dimensions of the lattice structure: two vertices for the horizontal dimension and two for the vertical dimension. Following a temperature increase, the lattice outer and cylindrical inner parts would expand with respect to their material CTEs, as shown in Figure 5.3b. A material with a high CTE was assigned to the cylindrical inner part, and another material with a low CTE was assigned to the lattice outer part. Due to the mismatch of the CTEs of the two parts, the cylindrical inner part would expand more than the lattice outer part and would push the attached structures horizontally (in the X^+ and X^- directions) while the vertices indicating the vertical dimension of the lattice would move closer (in the Z^+ and Z^- directions) towards the centre. This thermal expansion compensation mechanism concept was previously used in research with different configurations, such as UCSB lattices [90] and AFRL lattices [93], as described in Chapter 2.

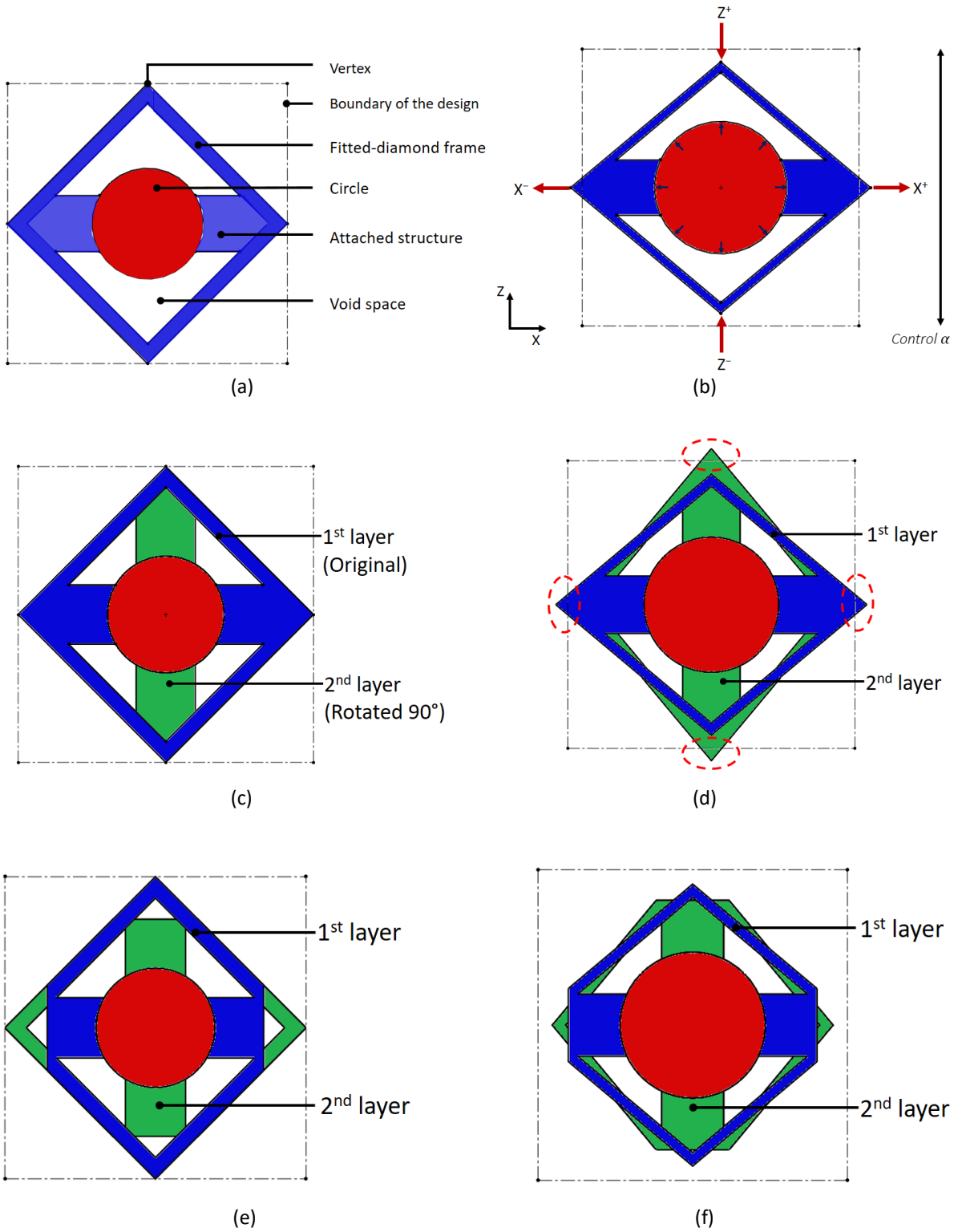
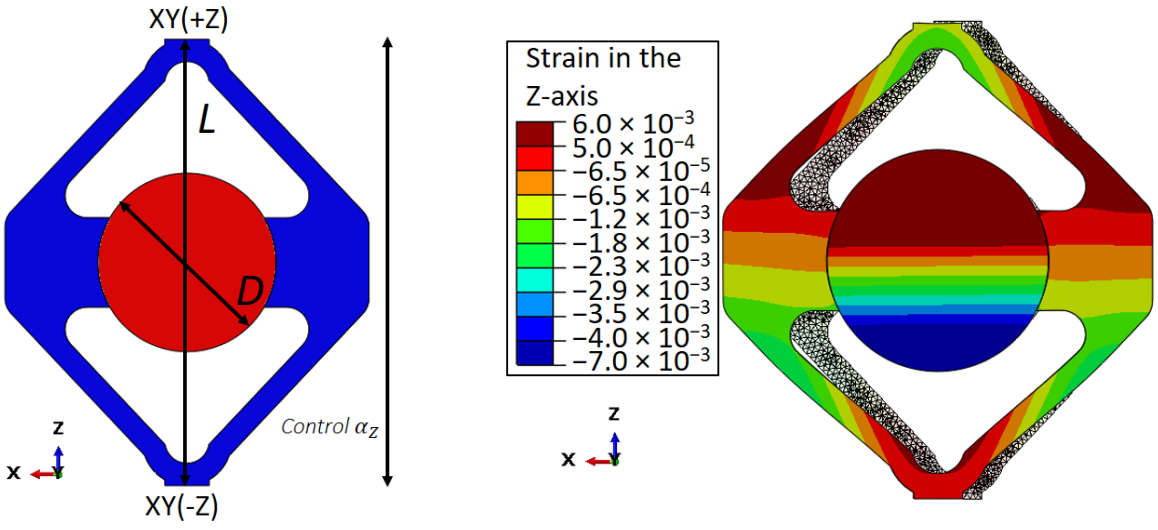


Figure 4.4 Configurational concept of the tailorable thermal expansion lattice structure: (a) the 1D lattice before the temperature rise, (b) the 1D lattice after the temperature rise, (c) the developing 2D lattice before the temperature rise, (d) the developing 2D lattice after the temperature rise, (e) the trimmed 2D lattice before the temperature rise, and (f) the trimmed 2D lattice after the temperature rise.

The 1D tailorable thermal expansion lattice was used to develop the 2D tailorable thermal expansion lattice by adding a similar 1D tailorable thermal expansion lattice in a different 90 ° orientation, as shown in Figure 4.4c. All configurations were kept within the boundary of the design. However, it can be noticed that the non-controlled vertices (highlighted in the circles in Figure 4.4d) expanded over the boundary of the design after the temperature rise, resulting in a large positive thermal expansion which did not meet the aim of the design. Four vertices of the lattice structure were trimmed to eliminate exceeding configurations (highlighted in the circles in Figure 4.4d): the two vertices in the horizontal direction of the 1st layer and the two vertices in the vertical direction of the 2nd layer (as shown in Figure 4.4e). With the trimmed 1st and 2nd layers combined, the lattice structure could yield 2D tailorable thermal expansion. Figure 4.4f shows the expanded configurations of the 2D tailorable thermal expansion following the rise in temperature. Additionally, the rationale behind selecting a 'layered' lattice structure instead of a more freeform 3D lattice was it could separately control for each axis or each edge. Adding a layer on the different axis can gain the number of controlled dimensions of the tailorable thermal expansion lattice structure.

Iteration 1 was designed by modifying the configurations of the configurational concept of the 1D tailorable thermal expansion lattice structure, as shown in Figure 4.5a. The ratio of the original diameter of the cylindrical inner part D over the original length of the lattice L was 0.4. All corners were additionally rounded to reduce stress.



(a) (b)

Figure 4.5 Illustrations of Iteration 1 (a) before temperature change (blue is the lattice outer part with low CTE and red is the cylindrical inner part with high CTE) and (b) a contour plot of strain in the Z-axis after temperature rise with the deformation factor of 5 (the black lines denote the undeformed configurations).

If the CTE of the cylindrical inner part material was high enough compared to the CTE of the lattice outer part material, the lattice structure could have contracted along the Z-axis during the temperature rise. Figure 4.5b shows a contour plot of strain in the Z-axis of Iteration 1 using the thermal expansion simulation described in Subchapter 4.2. By constraining the displacement of the XY(-Z) surface in the Z- direction to zero (as shown in Figure 4.5a), the XY(+Z) surface experienced a negative strain in the range of -1.2×10^{-3} to -6.5×10^{-4}, as illustrated in Figure 4.5b. It is demonstrated that the lattice structure was able to provide a low controlled thermal expansion along the Z-axis. Iteration 1 achieved near zero thermal expansion during the thermal expansion simulation where the CTE of the cylindrical inner part material was approximately 3.8 higher than the CTE of the lattice outer part material.

1. Iterations 1.1 and 1.2

As the design was able to control the 1D thermal expansion lattice, it was improved to reduce the thermal expansion of the lattice. In Iteration 1.1 (as shown in Figure 4.6), the thickness of the attached structures was reduced, leaving small grips to hold the cylindrical inner part, and increasing the length of link c (as illustrated in Figure 4.6). The D/L of Iteration 1.1 was increased from 0.4 (Iteration 1) to 0.45, allowing the larger cylindrical inner part to expand more than it did in the previous iteration.

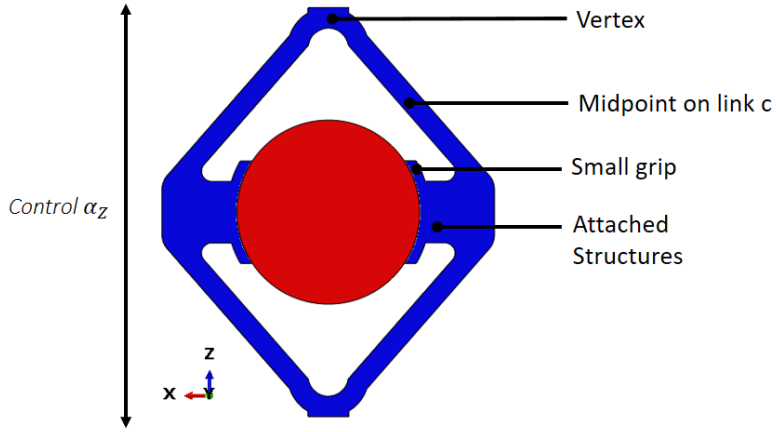


Figure 4.6 Illustration of Iteration 1.1.

Following the configurational concept of the 2D tailorable thermal expansion lattice structure (as shown in Figure 4.5e), Iteration 1.2 was designed for a novel 2D (planar) controllable thermal expansion lattice (as shown in Figure 4.7b) by combining one layer of Iteration 1.1 (as shown in Figure 4.6) in its original position with a second layer of Iteration 1.1 in a 90 ° rotated position (see Figure 4.7a). The two layers were connected using four small rods at the midpoint of each fitted-diamond edge, as shown in Figure 4.7b. Iteration 1.2 was able to control 2D thermal expansion, such that the original orientation of Iteration 1.1 (the bottom layer of the lattice shown in Figure 4.7b) controlled

thermal expansion along the Z-axis while the 90 ° rotated orientation (the top layer shown in Figure 4.7b) controlled thermal expansion along the X-axis.

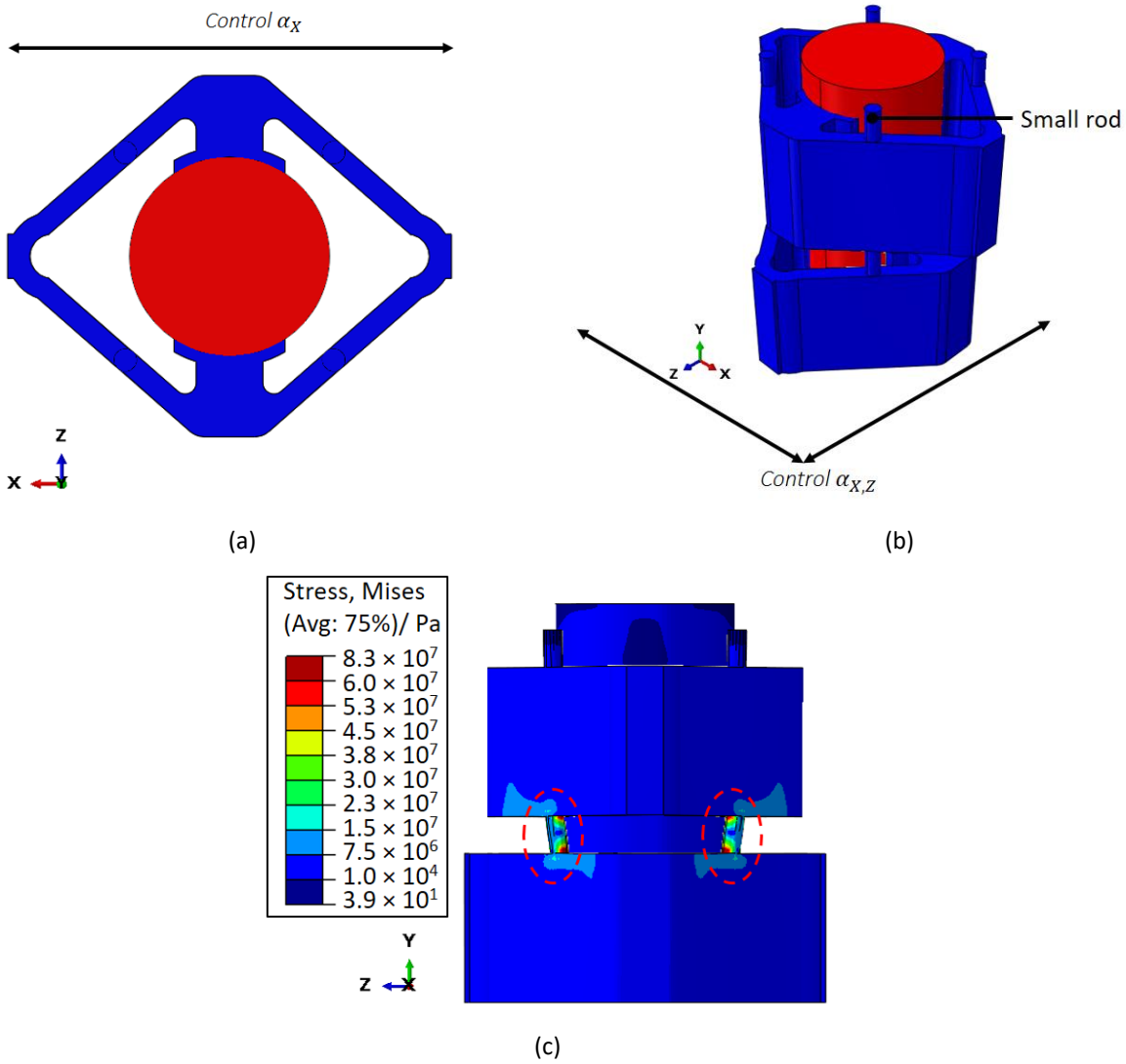


Figure 4.7 Illustration of Iteration 1.2: (a) the 90 ° rotated layer, (b) isometric view, and (c) a contour plot of von Mises Stress following temperature rise with a deformation factor of 3.

A drawback of this design was the high stress and moment placed on the four small rods when the lattice structure moved and bent during the temperature rise (highlighted in the circles in Figure 4.7c), which led to the unexpected deformation of layers and damaged the four small rods.

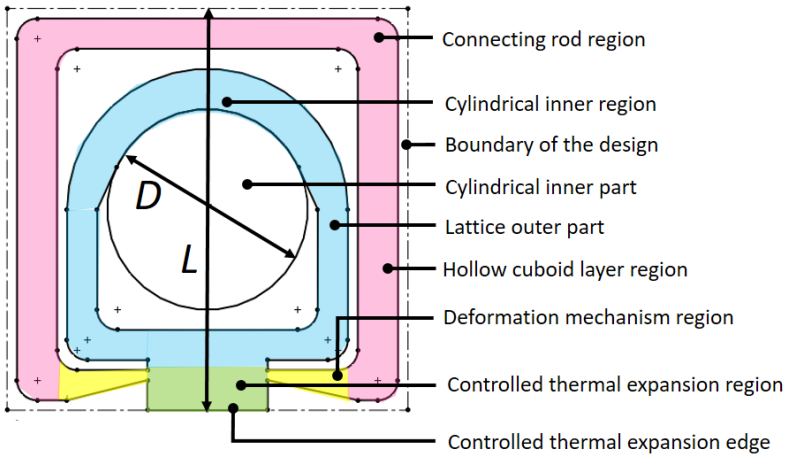
4.3.2. Iteration 2 series

1. Iteration 2

Iteration 2 was proposed using a hollow cuboid frame attached to the cylindrical inner part with internal geometry. Figure 4.8a shows the illustration of a layer of Iteration 2. The lattice outer part

was composed of a cylindrical inner region, controlled thermal expansion region, deformation mechanism region and hollow cuboid layer region, while the cylindrical inner part was located in the centre of the lattice outer part.

One layer could control only the thermal expansion of a specified edge. For example, Figure 4.8a and Figure 4.8b show the layer that could control the thermal expansion in the bottom edge located on the design's boundary. Two connected layers were required to make this deformation mechanism work in an axis; one layer with the original position (Figure 4.8b), and the other layer with the rotation of 180° around the Y-axis from the original position (Figure 4.8c). The hollow cuboid frames of two layers (Figure 4.8b and Figure 4.8c) were connected by the four connecting rods (Figure 4.8d), which enabled the deformation mechanism movement to control the controlled thermal expansion edges along an axis. This idea was developed by adding two opposite layers in the other axis (Figure 4.8e). Figure 4.8f shows a unit cell of Iteration 2, which could control the thermal expansion in the X- and Z-axes.



(a)

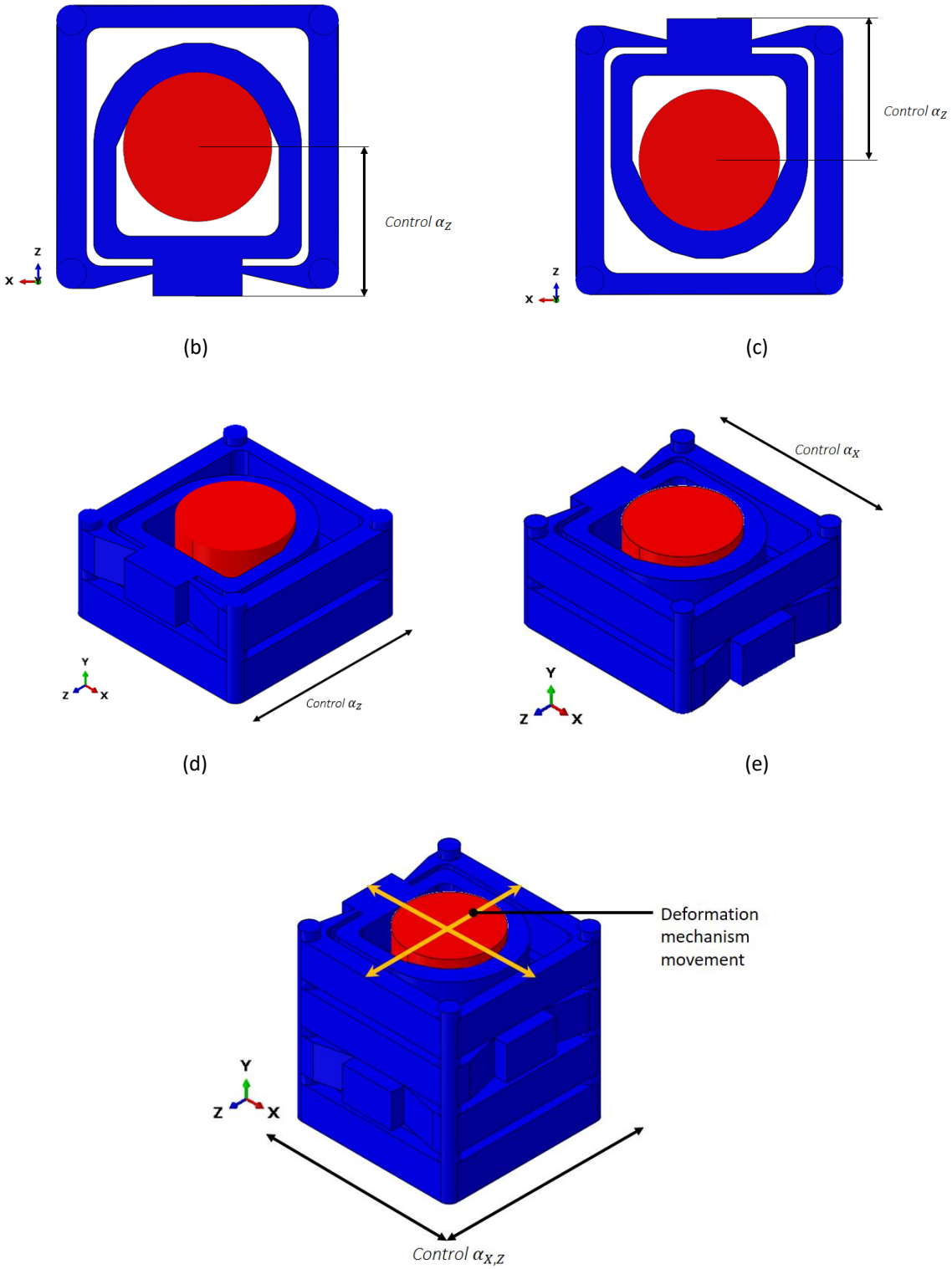


Figure 4.8 Illustration of Iteration 2 (a) top view of a layer with annotations, (b) top view of a layer coloured by parts, (c) top view of a pair of two opposite layers, (d) isometric view of a pair of two opposite layers controlled thermal expansion in the Z-axis, (e) isometric view of a pair of two opposite layers controlled thermal expansion in the X-axis and (f) isometric view of a unit cell.

The deformation mechanism region was intended to bend, while the hollow cuboid frame with four connecting rods was designed to be rigid when the cylindrical inner part expanded as result of the increased temperature. Figure 4.9 demonstrates the contour plot of von Mises Stress of one of Iteration 2 series (Iteration 2.4), following temperature increase. In the lattice outer part, high bending stresses occurred in the deformation mechanism regions (highlighted in the circles in Figure 4.9) and provoked a large distortion in the structure. The resultant bending produced a complementary deformation that minimised the structure's planar CTE. Figure 4.10 shows the contour plots of the strain in the X- and Z-axes of Iteration 2.4, generated as part of the thermal expansion simulation using the same boundary conditions, which will be described in Subchapter 5.1. Stain in the YZ(+X) plane and the XY(+Z) plane ranged between -3.7×10^{-3} and 7.5×10^{-3}, as illustrated in Figure 4.10a and Figure 4.10b, respectively.

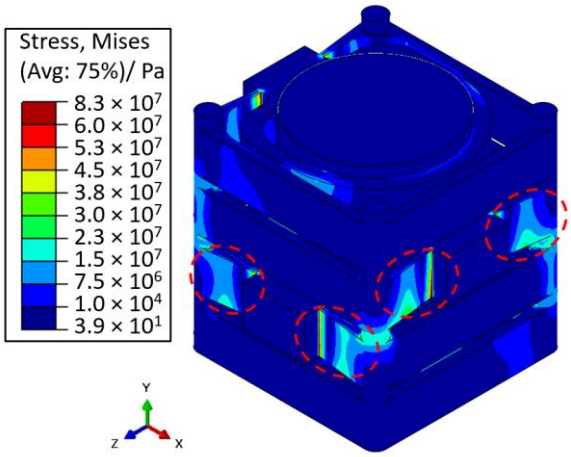
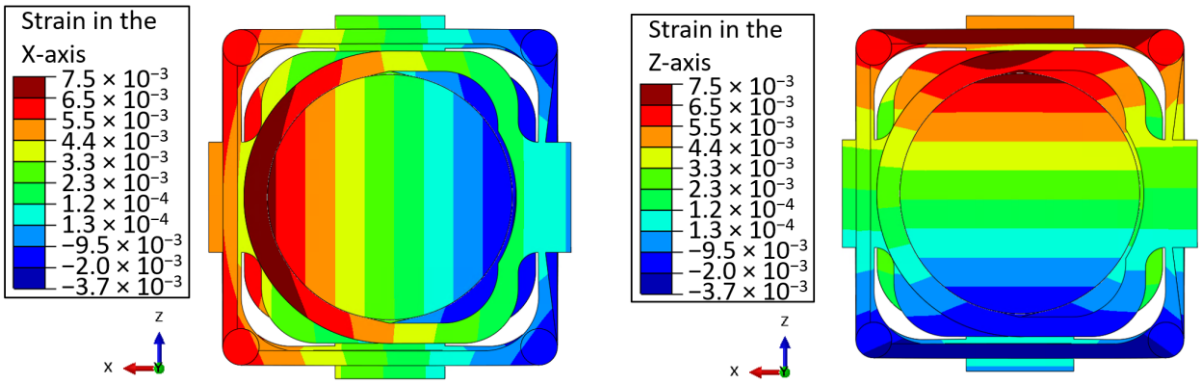


Figure 4.9 Contour plots of von Mises Stress after the temperature rise for Iteration 2.4 with a deformation factor of 1.



(a) (b)

Figure 4.10 Contour plots of strain after the temperature rise for Iteration 2.4 with a deformation factor of 1: (a) the unit cell strain in the X-axis and (b) the unit cell strain in the Z-axis.

2. Iterations 2.1, 2.2, 2.3 and 2.4

After the achievement of Iteration 2 (the simulated result achieved a zero thermal expansion in the X- and Z- axes when the CTE of the cylindrical inner part material was approximately 2.8 higher than the CTE of the lattice outer part material, which will be discussed in Subchapter 4.4), Iterations 2.1, 2.2, 2.3 and 2.4 were improved from the previous iterations. These improvements aimed to create lattices that provided lower CTEs than the earlier iterations and to reduce unnecessary regions in the lattice outer parts. Figure 4.11 illustrates Iterations 2.1 - 2.4.

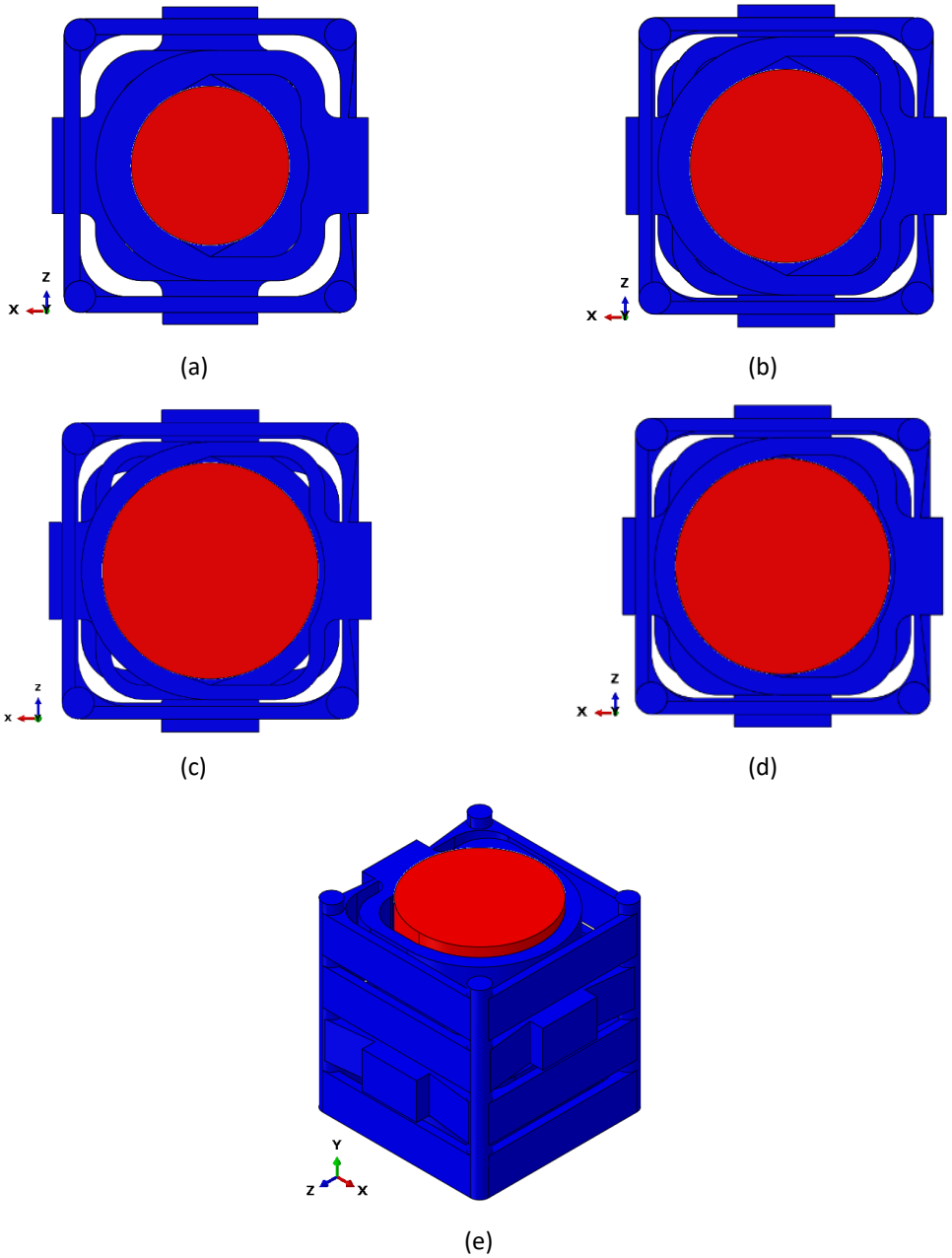


Figure 4.11 Illustration of Iteration 2 series (a) top view of Iteration 2.1, (b) top view of Iteration 2.2, (c) top view of Iteration 2.3, (d) top view of Iteration 2.4 and (e) isometric view of Iteration 2.4.

The five configurations considered for these improvements (as shown in Figure 4.12) were the ratio D/L, the ratio of the diameter of the connecting rod over L, the ratio of the thickness of the hollow cuboid frame over L, the ratio of the thickness of the thinnest section in deformation mechanism region over L and the ratio of the thickness of the cylindrical inner region over L. The values of the configurational parameters in each iteration are shown in Table 4.1. The ratios D/L were increased from 0.5 (Iteration 2) to 0.67 (Iterations 2.3 and 2.4), which reached the maximum size that could applied in this series, resulting in lower CTEs for Iterations 2.1, 2.2, 2.3 and 2.4. Thicknesses of the thinnest section in the deformation mechanism region over L were reduced from 0.025 to 0.02, increasing the flexibility of that region when the cylindrical inner part expanded in response to increased temperature. Thicknesses of the hollow cuboid frame over L and thicknesses of the cylindrical inner region over L were decreased from 0.075 - 0.1 (Iteration 2) to 0.04 - 0.065 (Iteration 2.3), minimising the overdesign in the regions and increasing void spaces for re-designing the larger size of the cylindrical inner parts. Additionally, the drawback of this series was it could not achieved near zero in-plane CTE, therefore, the next generations were proposed.

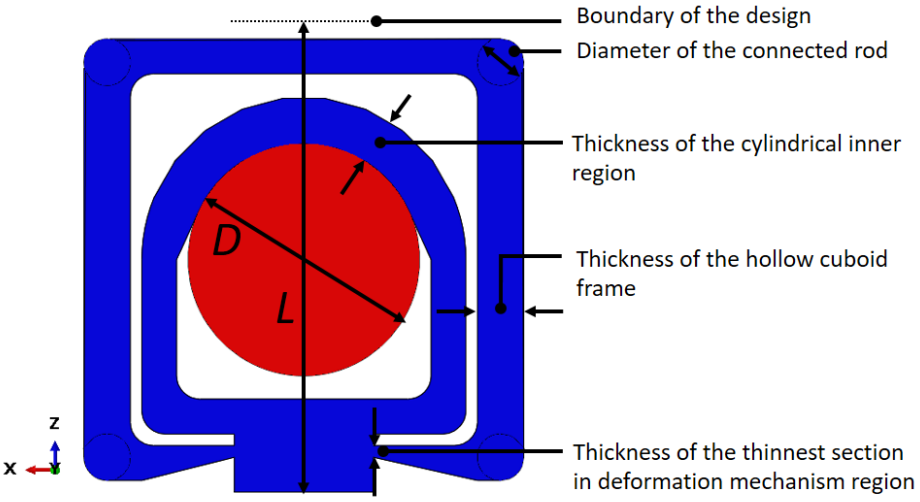


Figure 4.12 Iteration 2 with the five configurations considered.

Table 4.1 The configurational parameters of Iteration 2 series

Iteration	**2**	**2.1**	**2.2**	**2.3**	**2.4**
D/L	0.5	0.5	0.60	0.67	0.67
Diameter of the connected rod/L	0.1	0.1	0.1	0.1	0.1
Thickness of the hollow cuboid frame/L	0.075 - 0.1	0.05	0.04	0.04	0.04
Thickness of the thinnest section in deformation mechanism region/L	0.025	0.025	0.02	0.02	0.02
Thickness of the cylindrical inner region/L	0.075 - 0.1	0.075 - 0.1125	0.06 - 0.1	0.04 - 0.065	0.055 - 0.065

4.3.3. Iteration 3 series

These 2D (planar) controllable thermal expansion lattices were developed from Iteration 2 series. From the limitation of Iteration 2 series aforementioned, Iteration 3 series was developed to enlarge the limitation of the Iteration 2 series to achieve low-positive and low-negative thermal expansion. The main development of the Iteration 3 series compared to Iteration 2 series was removing the hollow cuboid layer regions, allowing more space for the cylindrical inner region.

1. Iteration 3

Iteration 3 (as seen in Figure 4.13) was proposed using a hollow cube composed of 12 strut rods to maintain the rigidity of the shape's structure and act as load-bearing structures. The lattice outer part was composed of the four CTE-minimising layers with different orientations around the Y-axis: 0°, 90°, 180°, and 270° connected by the hollow cube, as illustrated in Figure 4.13b.

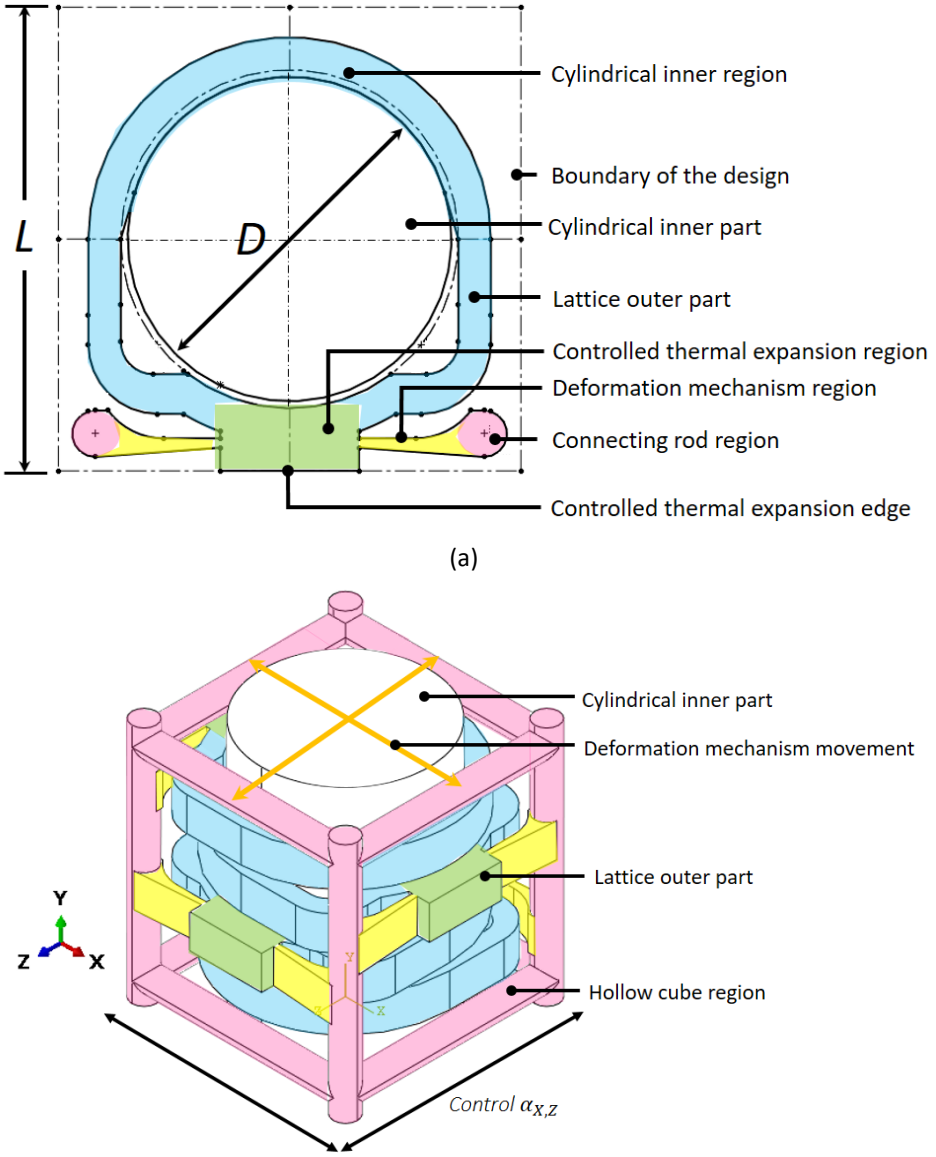


Figure 4.13 Iteration 3 (a) top view of a layer with annotations and (b) isometric view of a unit cell with annotations.

The deformation mechanism region was intended to bend, while the hollow cube composed of 12 strut rods was intended to be rigid when the cylindrical inner part expanded due to the increased temperature. Figure 4.14 demonstrates the contour plot of von Mises Stress of one of Iteration 3 series (Iteration 3.1), following temperature increase. In the lattice outer part, high bending stresses occurred in the deformation mechanism regions (highlighted in the circles in Figure 4.14) and provoked a large distortion in the structure. The resultant bending produced a complementary deformation that minimised the structure's planar CTE. Figure 4.15 shows the contour plots of the strain in the X- and Z-axes of Iteration 3.1, generated as part of the thermal expansion simulation using the same boundary conditions, which will be described in Subchapter 5.1. Stain in the YZ(+X) plane

and the XY(+Z) plane ranged between –6.0 × 10^{-3} and 9.0 × 10^{-3}, and between –5.5 × 10^{-3} and 8.5 × 10^{-3} in the XY(+Z) plane, as illustrated in Figure 4.15a and Figure 4.15b, respectively.

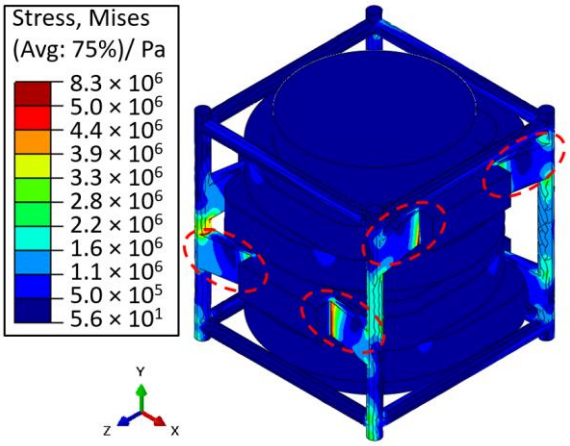
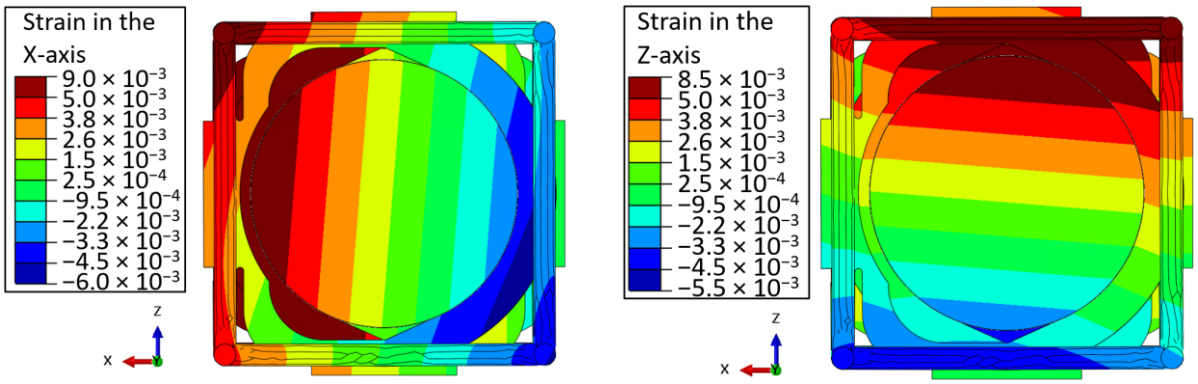


Figure 4.14 Contour plots of von Mises Stress after the temperature rise for Iteration 3.1 with a deformation factor of 1.



(a) (b)

Figure 4.15 Contour plots of strain after the temperature rise for Iteration 3.1 with a deformation factor of 1: (a) the unit cell strain in the X-axis and (b) the unit cell strain in the Z-axis.

2. Iterations 3.1 and 3.2

Iterations 3.1 and 3.2 were the improved designs from Iteration 3. The five configurations considered for these improvements (as shown in Figure 4.16) were the ratio D/L, the ratio of the diameter of the connecting rod over L, the ratio of the thickness of a layer over L, the ratio of the thickness of the thinnest section in the deformation mechanism region over L and the ratio of the thickness of the cylindrical inner region over L. The values of the configurational parameters in each iteration are shown in Table 4.2. The ratio D/L were increased from 0.7 (Iteration 3) to 0.73 (Iteration 3.1), which reached the maximum size applied in this series, resulting in negative CTE in Iteration 3.1. The diameter of the connecting rods over L was reduced from 0.1 (Iteration 3) to 0.06 (Iteration 3.1) and

0.07 (Iteration 3.2), minimising the overdesign in the regions and increasing void space by re-designing the larger size of the cylindrical inner parts. The thickness of a layer over L and thicknesses of the cylindrical inner region over L were decreased from 0.14 and 0.07 - 0.085 to 0.15 and 0.07 - 0.11, respectively, increasing the rigidity in the regions.

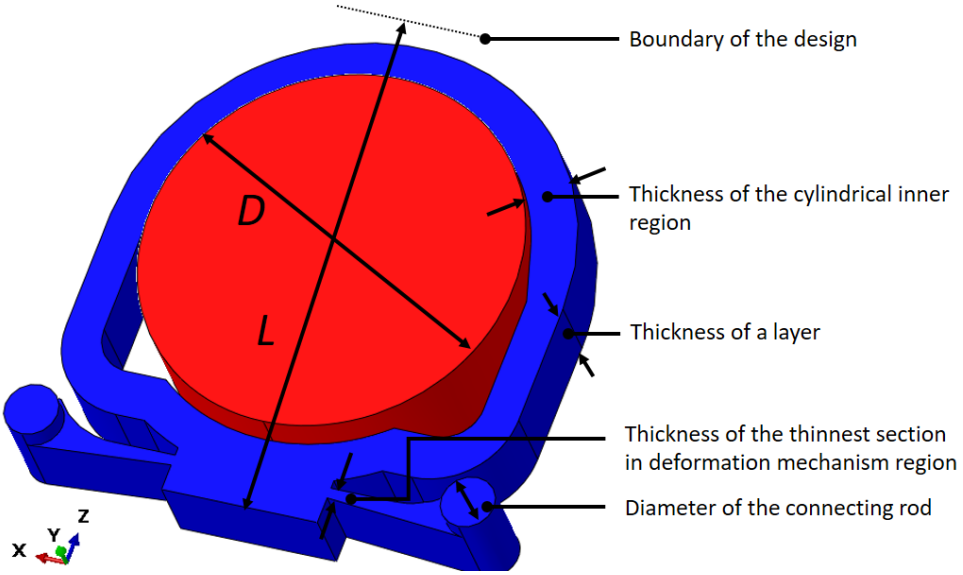


Figure 4.16 Iteration 3 with the five configurations considered.

Table 4.2 Configurational parameters of Iteration 3 series

Iteration	**3**	**3.1**	**3.2**
D/L	0.7	0.73	0.72
Diameter of the connected rod/L	0.1	0.06	0.07
Thickness of a layer/L	0.14	0.15	0.15
The thickness of the thinnest in deformation mechanism region/L	0.02	0.02	0.02
Thickness of cylindrical inner region/L	0.07 - 0.085	0.07 - 0.105	0.07 - 0.11

The drawback of this series was the high stress and moment placed on the four small rods (connecting to layers) when the lattice structure moved and bent during the temperature rise (highlighted in the circles in Figure 4.14), which led to the unexpected deformation of layers and damaged the four small rods. , therefore, the next generations were proposed.

4.3.4. Iteration 4 series

In the previous designs, the deformation mechanism movement was along the X- and Z- axes, and the four deformation mechanism edges were located in the middle of each face on the design boundary. The enlargement of the cylindrical inner part helped decrease the thermal expansion of the lattice structures, however, it led to a reduction in the design space of the lattice outer part. Figure 4.17a shows a unit cell with four design spaces. Each design space contained three regions: the controlled

thermal expansion region, the deformation mechanism region, and the allowance gap for the thermal expansion of the cylindrical inner part, as shown in Figure 4.17a. The design spaces were difficult to design as they were rectangular strips. Therefore, the deformation mechanism movement of the Iteration 4 series was designed to expand along diagonal directions, providing more space, as shown in Figure 4.17b. The design spaces of the Iteration 4 series were 0.2 times larger than the previous iteration, while the size of the cylindrical inner part and the boundary of the design remained the same.

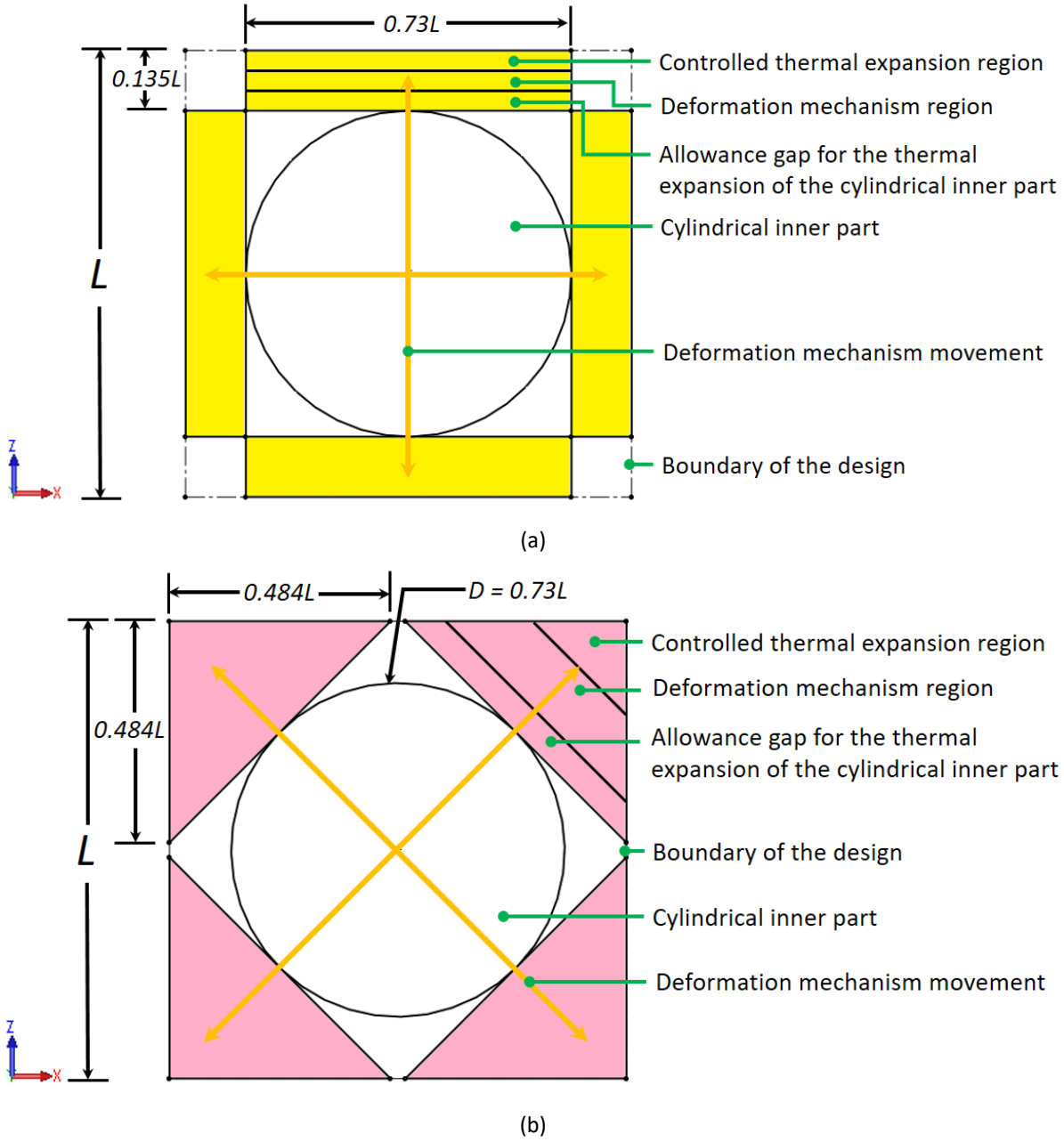


Figure 4.17 Designing spaces: (a) previous Iterations and (b) Iteration 4 series.

The design of this series introduced the separation of two main functions: the deformation mechanism and the load-bearing. The two functions were based on different geometrical designs: the deformation mechanism should be small enough to bend, while the load-bearing should be large enough to hold internal and external loads. Examples of the two functions will be discussed along the descriptions of Iterations 4 and 4.1 and their contour plots of von Mises Stress.

1. Iteration 4

The design of the lattice outer part in Iteration 4 is illustrated in Figure 4.18. The design comprised four CTE-minimising layers, each connected to a load-bearing pillar at one of design corners to control the expansion in specific corners. The four CTE-minimising layers had different orientations around the Y-axis: 0 °, 90 °, 180 °, and 270 °, connected to a hollow octagonal prism with eight connecting struts. The lattice outer part was composed of the lattice outer region, the controlled thermal expansion region, the deformation mechanism region, and the connected rod-layer region, while the cylindrical inner part was located in the centre of the lattice outer part (Figure 4.18a).

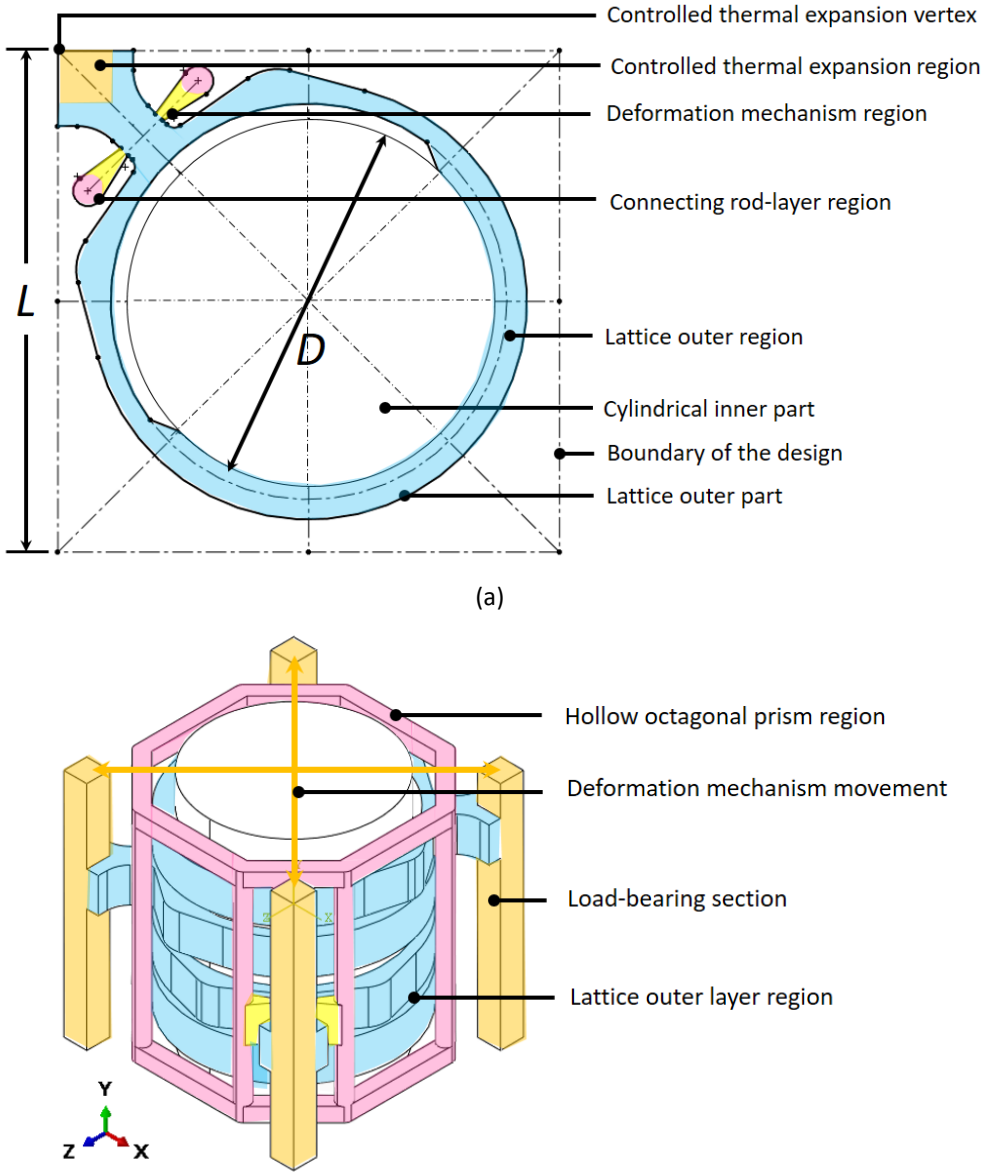
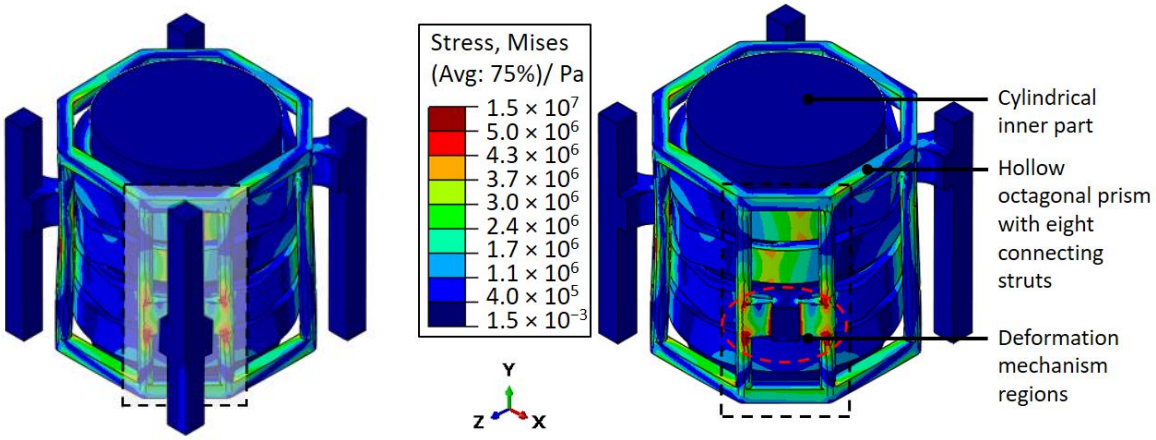


Figure 4.18 Iteration 4: (a) top view of a layer with annotations and (b) isometric view of a unit cell with annotations.

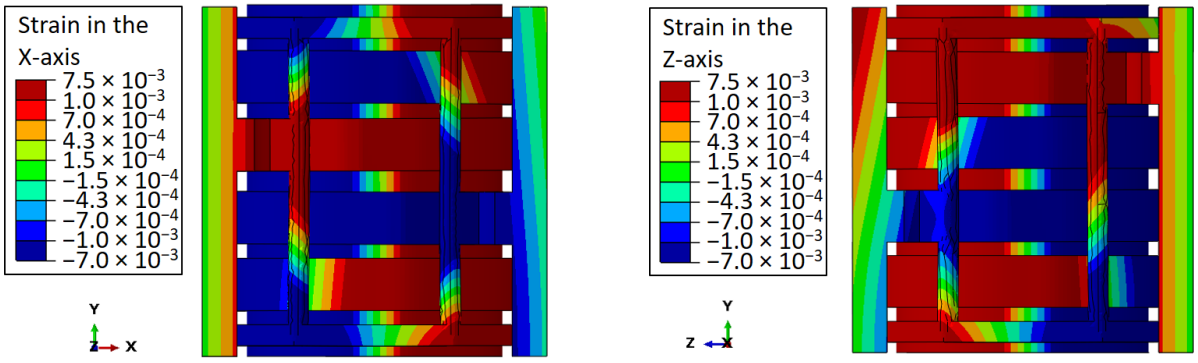
The deformation mechanism region was intended to bend, while the hollow octagonal prism with eight connecting struts was intended to be rigid when the cylindrical inner part expanded as result of the increased temperature. Figure 4.19 shows a contour plot of von Mises Stress of Iteration 4, following temperature increase. In the lattice outer part, high bending stresses occurred in the deformation mechanism regions (highlighted in the circle in Figure 4.19b) and provoked a large distortion in the structure, while low stresses occurred in the four load-bearing pillars leading to a low distortion in the structure in accordance with the two design functions as mentioned previously. The resultant bending produced a complementary deformation that minimised the structure's planar CTE. Figure 4.20 shows the contour plots of the strain in the X- and Z-axes of Iteration 4, generated as part

of the thermal expansion simulation using the same boundary conditions described in Subchapter 4.2. Stain in the YZ(+X) plane ranged between -4.3×10^{-4} and 1.5×10^{-4}, and between -1.5×10^{-4} and 7.5×10^{-3} in the XY(+Z) plane, as illustrated in Figure 4.20a and Figure 4.20b, respectively. In addition, the lattice was designed to expand along the diagonal directions, as shown in Figure 4.18b, providing additional space for the load-bearing pillars at the cell's corners, which enabled them to be thicker and stiffer than they would if they were placed on the cell's faces.



(a) (b)

Figure 4.19 Contour plots of von Mises Stress after the temperature rise for Iteration 4 with a deformation factor of 2: (a) the unit cell with a plane for cross-section and (b) the unit cell with the cross-sectional area.



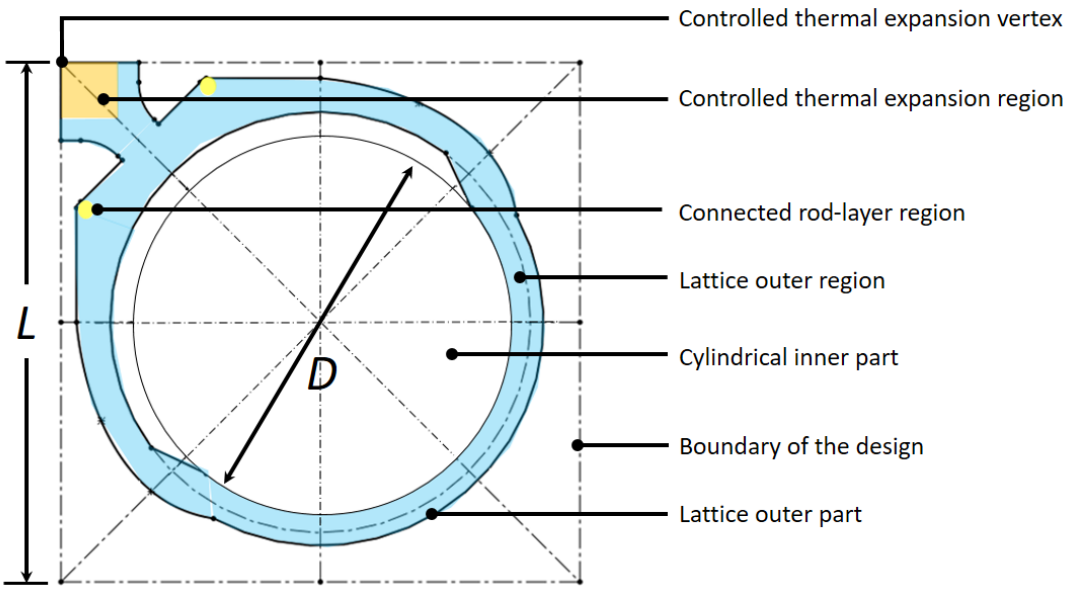
(a) (b)

Figure 4.20 Contour plots of strain after the temperature rise for Iteration 4 with a deformation factor of 1: (a) the unit cell strain in the X-axis and (b) the unit cell strain in the Z-axis.

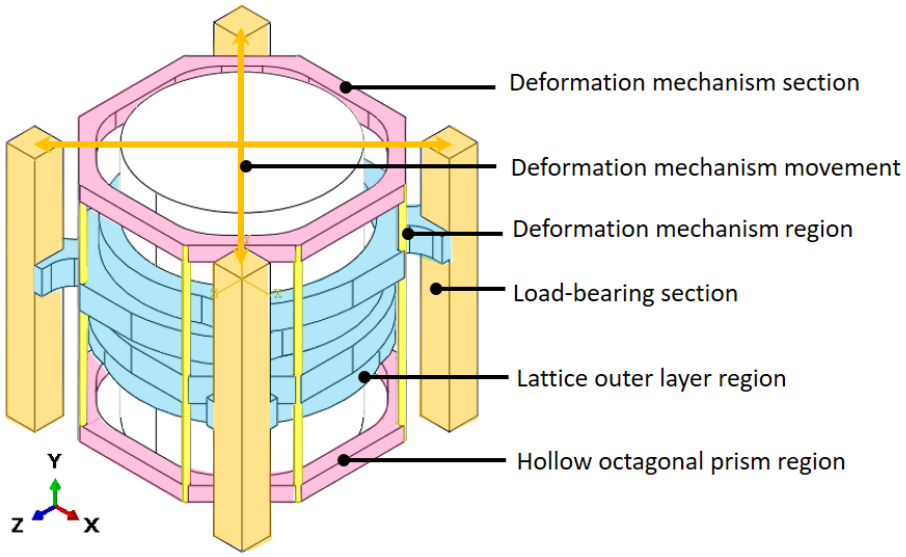
2. Iteration 4.1

This is the final design for this PhD. The main improvement in Iteration 4.1 was achieved through the inclusion of eight connecting struts in the deformation mechanism region (as shown in Figure 4.21b) instead of their previous locations (as shown in Figure 4.18a). This modification resulted in lower geometrical complexity and in fewer geometrical parameters to control. In this design iteration, the

unit cell of the lattice outer part can be divided into two sections according to their functions: the deformation mechanism and the load-bearing mechanism (see Figure 4.21b). The deformation mechanism section was designed as a hollow octagonal prism with eight connecting struts. The eight connecting struts were intended to bend when the cylindrical inner part expanded in response to increased temperature, as shown in Figure 4.22. This bending provided a complementary deformation that minimised the structure's planar CTE. Figure 4.23 shows the contour plots of the strain in the X- and Z-axes of Iteration 4.1 generated through the thermal expansion simulation with the same boundary conditions described in Subchapter 4.2. The YZ(+X) plane experienced strain in the range of -7.0×10^{-3} to -7.0×10^{-4} while the XY(+Z) plane strain results were between 7.0×10^{-4} and 7.5×10^{-3}, as illustrated in Figure 4.23a and Figure 4.23b, respectively. In addition, Figure 4.24 shows how Iteration 4.1 was tessellated in a $4 \times 1 \times 4$ lattice, and suggests possible locations for the application of loads on the lattice.

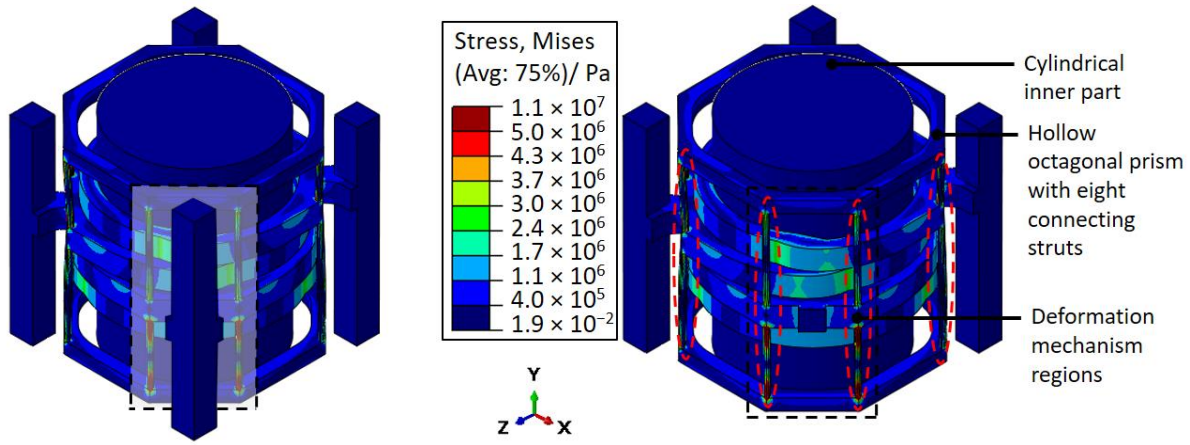


(a)



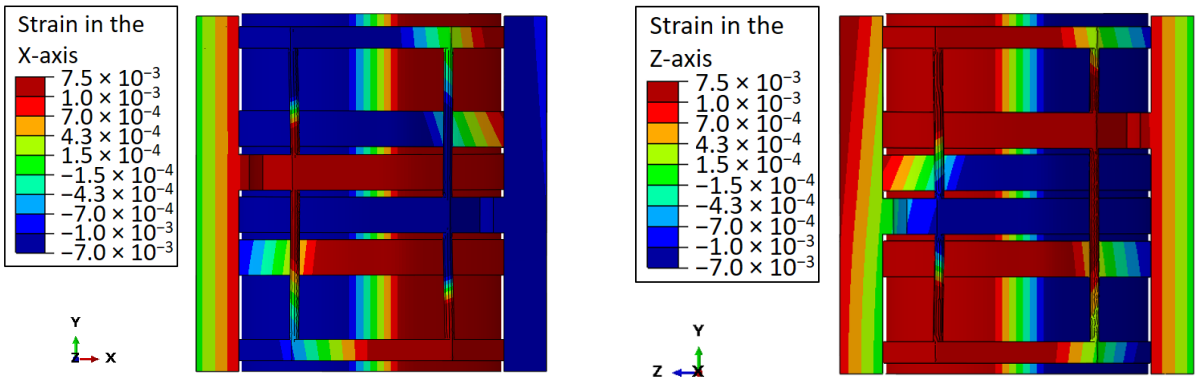
(b)

Figure 4.21 Iteration 4.1: (a) top view of a layer with annotations and (b) isometric view of a unit cell with annotations.



(a) (b)

Figure 4.22 Contour plots of von Mises Stress after temperature rise for Iteration 4.1 with a deformation factor of 2 (a) the unit cell with a plane for cross-section and (b) the unit cell with the cross-sectional area.



(a) (b)

Figure 4.23 Contour plots of strain after temperature rise for Iteration 4.1 with a deformation factor of 1: (a) the unit cell strain in the X-axis and (b) the unit cell strain in the Z-axis.

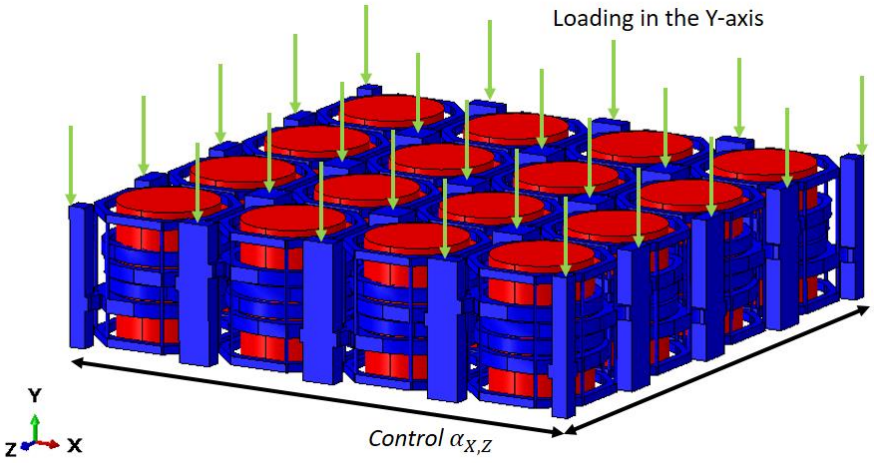


Figure 4.24 A 4 × 1 × 4 lattice of Iteration 4.1.

The tessellation of the unit cell of Iteration 4.1 was investigated for the construction of a lattice structure. This posed a challenge given that the unit cell was not rotationally symmetrical in the XZ plane, resulting in different CTEs in each direction. However, the design of a structure with isotropic planar CTE was prioritised, to facilitate the design of a metrology frame with low thermal expansion in the XZ plane. Using the unit cell design of Iteration 4.1, a lattice structure could be created by assembling unit cells following any orientation 0 °, 90 °, 180 °, or 270 ° around the Y-axis. In Figure 4.25, the layers in the unit cell were numbered according to the position of the load-bearing pillar (top view of Figure 4.25a). Layers 1, 2, 3, and 4 (front view of Figure 4.25a) were the lowest layer, the second-lowest layer, etc., respectively. The symbol 'P' was used to represent the orientation of the unit cell, as shown in Figure 4.25b. Five potential patterns were selected and implemented by changing orientations around the Y-axis and combining them into 2 × 1 × 2 lattices, as shown in Figure 4.25b. The first pattern was examined to verify whether it could demonstrate CTEs of a tessellated lattice and the difference between mean CTEs in the X- and Z-axes of each composed lattice. Lattice structures from 1 × 1 × 1 up to 4 × 1 × 4 (Figure 4.26) were chosen for this evaluation.

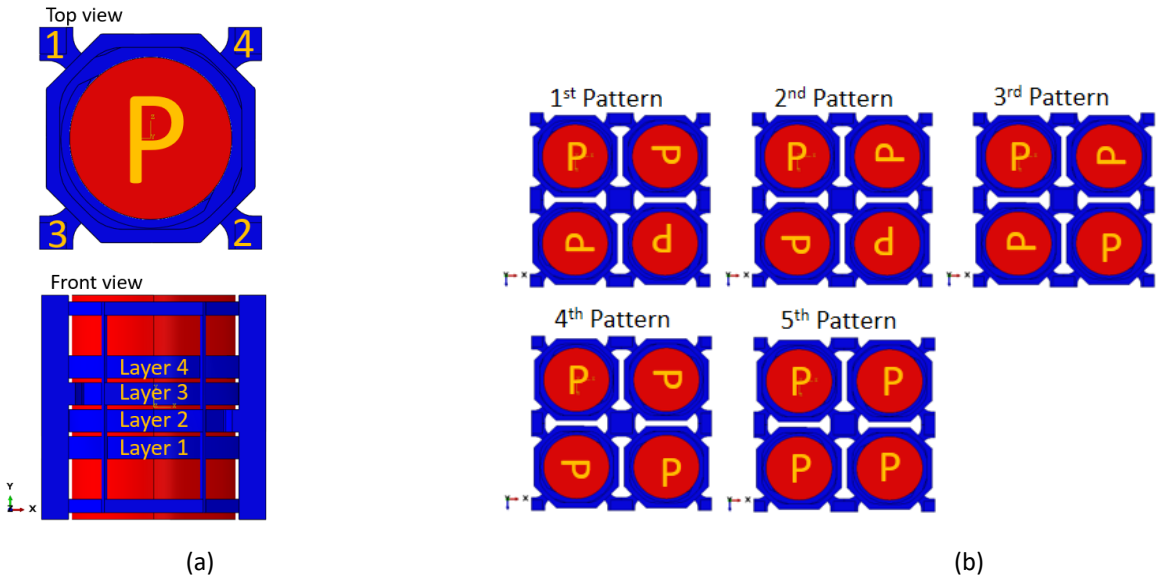


Figure 4.25 Annotation and patterns of the lattices of Iteration 4.1: (a) top view and front view of the unit cell and (b) patterns of 2 × 1 × 2 lattices.

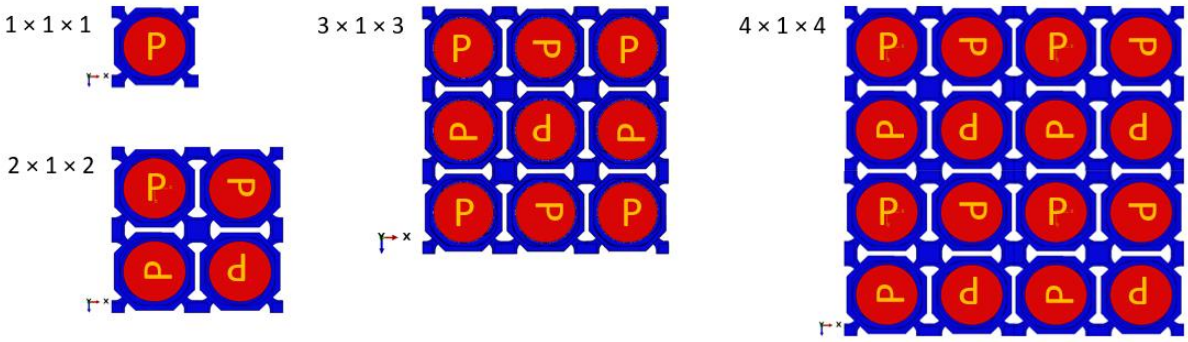


Figure 4.26 Illustration of 1 × 1 × 1, 2 × 1 × 2, 3 × 1 × 3 and 4 × 1 × 4 lattices of Iteration 4.1.

Additionally, Iterations 2.4, 3.1 and 4.1 were selected for fabricating. Their engineering drawings were provided in Appendix, so other researchers can duplicate it if needed, and clearly understand all details.

4.4. Results of the lattice structure for low coefficient of thermal expansion

4.4.1. Low planar CTE lattice results

The aim of the design presented in this research was to create a model that could yield a near-zero CTE. In the early stages, the lattice outer parts were modelled in Nylon 12 (CTE of 109×10^{-6} K^{-1}), while the cylindrical inner part material of Iteration 1, Iteration 2, Iteration 2.1 and Iteration 2.2 had not been chosen yet. The thermal expansion simulation was applied to test the performance of the CTEs of the lattice structures (as described in Subchapter 3.2, Subchapter 4.2 and Chapter 6). For the cylindrical inner part, the mechanical properties of Nylon 12 were assumed, in addition to a range of CTEs. The CTEs of the cylindrical inner part varied from 109×10^{-6} K^{-1} to 545×10^{-6} K^{-1} (five times the CTE of Nylon 12). This CTE range was assigned to ensure coverage of sufficient CTE values for zero thermal expansion results in all lattice structures. Similar CTE determination techniques can be found in previous research [82, 93]. The comparison of each iteration performance was conducted based on the simulation results presented, specifically the relationship between ΔL^* (the change in length of the designed lattice over the change in length of the solid volume of the lattice outer part material $\Delta L_{Lattice}/\Delta L_{solid\ mat1}$) and the ratio between the CTEs of the cylindrical inner part material and the lattice outer part material α_2/α_1. The relative change in length (ΔL^*) equalled 1 when the displacement of the lattice equalled the displacement of its solid volume material, while it equalled 0 when there was no change in length, and a negative value was rendered when the length of the lattice contracted. The changes in the lengths of Iteration 1, Iteration 2, Iteration 2.1 and Iteration 2.2 were found by subtracting the displacement of the initial stage from the maximum displacement of the final stage in each simulation.

Figure 4.27 shows the simulation results of Iterations 1, 1.1, 1.2, 2, 2.1 and 2.2. All iterations successfully achieved zero thermal expansion with different values for α_2/α_1 (3.8 for Iteration 1, 3.7 for Iteration 1.1, 4.0 for Iteration 1.2, 2.8 for Iteration 2, 2.4 for Iteration 2,1 and 2.2 for Iteration 2.2). For example, Iteration 1 required the cylindrical inner part material to yield a CTE of 3.8 times 109 × 10^{-6} K^{-1} equalling 414.2 × 10^{-6} K^{-1}. However, in the commercial market, such a CTE value would be challenging to find. Therefore, the design of iterations aimed at achieving the lowest possible value of the α_2/α_1 ratio, while still achieving zero thermal expansion.

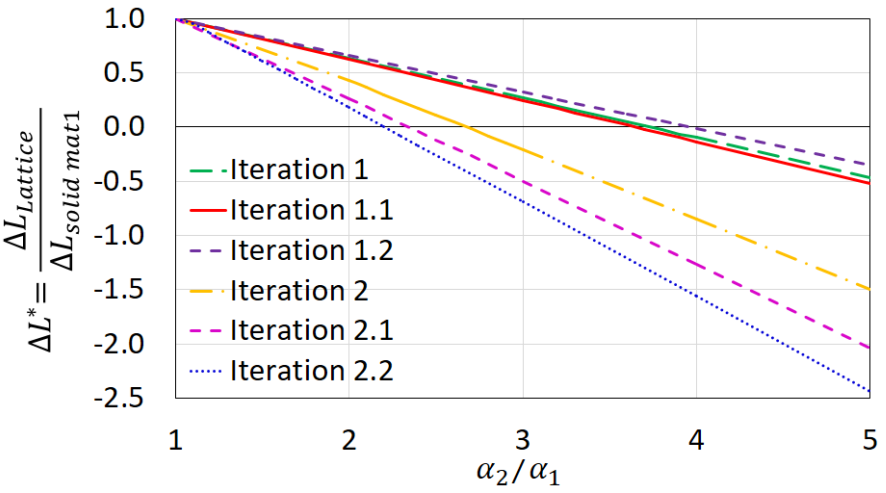


Figure 4.27 Simulation results of Iterations 1, 1.1, 1.2, 2.1 and 2.2 using trend lines, where ΔL^* is the relative change in the change in length, $\Delta L_{Lattice}$ is the change in length of the designed lattice, $\Delta L_{solid\ mat1}$ is the change in length of the solid volume of the lattice outer part material, α_1 is the CTE of the lattice outer part material, and α_2 is the CTE of the cylindrical inner part material.

It can be noted that Iteration 2.2 is the best iteration that provided the lowest ratio of α_2/α_1 and that could achieve zero thermal expansion. Thus, the first material selected for the cylindrical inner part was low-density polyethylene (LDPE) with a CTE of 220 × 10^{-6} K^{-1}. However, as far as its material properties are concerned, LDPE is soft, flexible and difficult to machine compared to other types of polyethylene. Therefore, it was substituted with ultra-high-molecular-weight polyethylene (UHMWPE) which has a slightly lower CTE of 200 × 10^{-6} K^{-1}. Subsequently, the iterations following Iteration 2.1 (Iterations 2.2 - 2.4, Iteration 3 series, and Iteration 4 series) showed significant improvement when simulated using the properties of the chosen materials (Nylon 12 for the lattice outer part and UHMWPE for the cylindrical inner part). Figure 4.28 shows the simulation results for Iterations 2.2 - 2.4 and the Iteration 3 series. With UHMWPE for the cylindrical inner part material, Iteration 2.4 yielded a larger CTE for the lattice (17.1 × 10^{-6} K^{-1}), compared to the one achieved with LDPE (4.7 × 10^{-6} K^{-1}). In general, there were numerous attempts to design a lattice with zero CTE, as shown in Figure 4.28, with Iteration 3.1 even obtaining a negative CTE (−5.3 × 10^{-6} K^{-1}). All results

shown here were found by subtracting the displacement of the initial stage from the maximum displacement of the final stage in each simulation, to calculate the coefficient of thermal expansion.

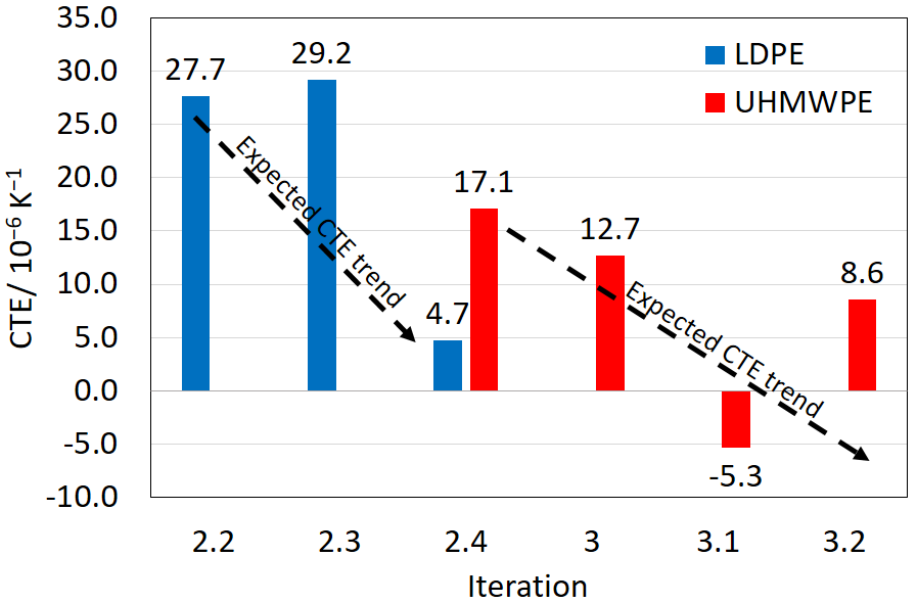


Figure 4.28 Effective CTE results for Iterations 2.2 - 2.4 and the Iteration 3 series.

Starting Iteration 2.4, the in-plane CTE was introduced to decide whether to improve or develop iterations. The in-plane CTE ($\alpha_{X,Z}$) was found by averaging structure CTEs in the X- and Z-axes over four orientations around the Y-axis: 0 ° (origin), 90 °, 180 °, and 270 °. The in-plane CTE is more accurate than the CTE obtained from maximum displacement, as the in-plane CTE represents the average of the linear thermal expansion in a specific plane. Table 4.3 shows the in-plane CTE results of Iterations 2.4, 3.1, 4 and 4.1. The final iteration, Iteration 4.1, yielded an extremely low CTE of 1×10^{-9} K^{-1}.

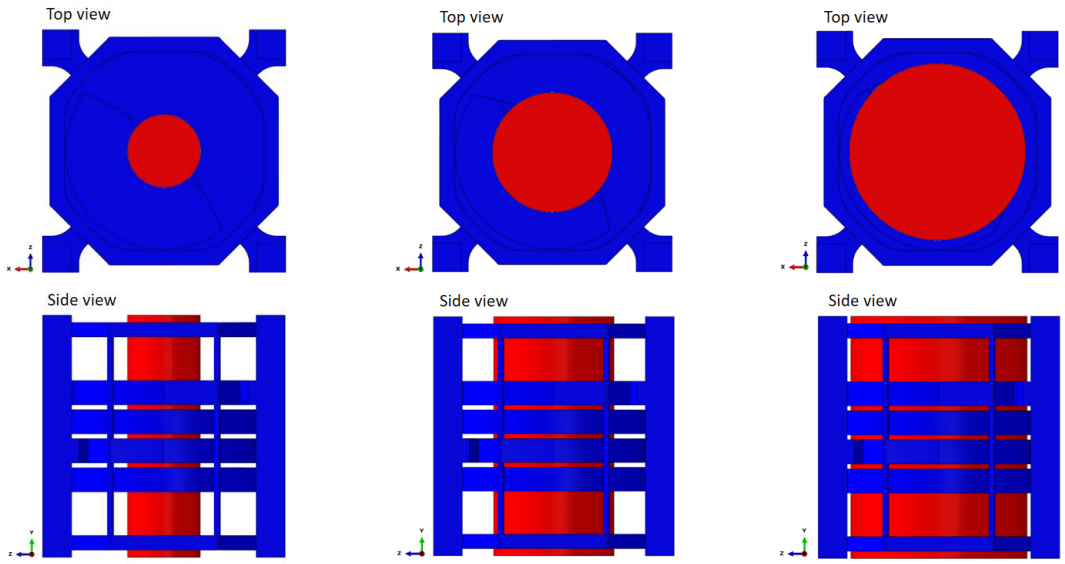
Table 4.3 In-plane CTEs of Iterations 2.4, 3.1, 4 and 4.1.

Iteration	**In-Plane CTE/ 10^{-6} K^{-1}**
2.4	8.2
3.1	−23.6
4	−0.8
4.1	0.001

4.4.2. Low planar CTE lattice results obtained by varying design parameters

The conceptual design presented in Subchapter 5.2 had several design parameters that could be varied to control the resulting structure's CTE. These parameters include the original length of the lattice L, the original diameter of the cylindrical inner part D, and the ratio between the CTEs of the cylindrical inner part material and the lattice outer part material α_2/α_1. In this section, Iteration 4.1 is investigated. The ratios D/L and α_2/α_1 of Iteration 4.1 were varied from 0.30 to 0.73 (the maximum

ratio for which the lattice was designed) and from 1.10 to 2.20. Examples of the resulting lattice cells are shown in Figure 4.29.



(a) (b) (c)

Figure 4.29 Illustration of Iteration 4.1's top view and side view of (a) the $(D/L) = 0.30$ model, (b) the $(D/L) = 0.50$ model, and (c) the $(D/L) = 0.73$ model.

Figure 4.30 demonstrates that the conceptual lattice unit cell yielded in-plane CTEs ($\alpha_{X,Z}$) ranging approximately between -62×10^{-6} K^{-1} and 96×10^{-6} K^{-1} by varying design parameters. $\alpha_{X,Z}$ data were fitted with a first-order polynomial surface function of the form

$$\alpha_{X,Z} = a + b\left(\frac{\alpha_2}{\alpha_1}\right) + c\left(\frac{D}{L}\right) \quad 4.1$$

which provides a guide allowing designers to customise the CTE of the proposed lattice structure. The fit provides an accurate description of the data (with R^2 = 0.994) over the examined range of D/L and α_2/α_1.

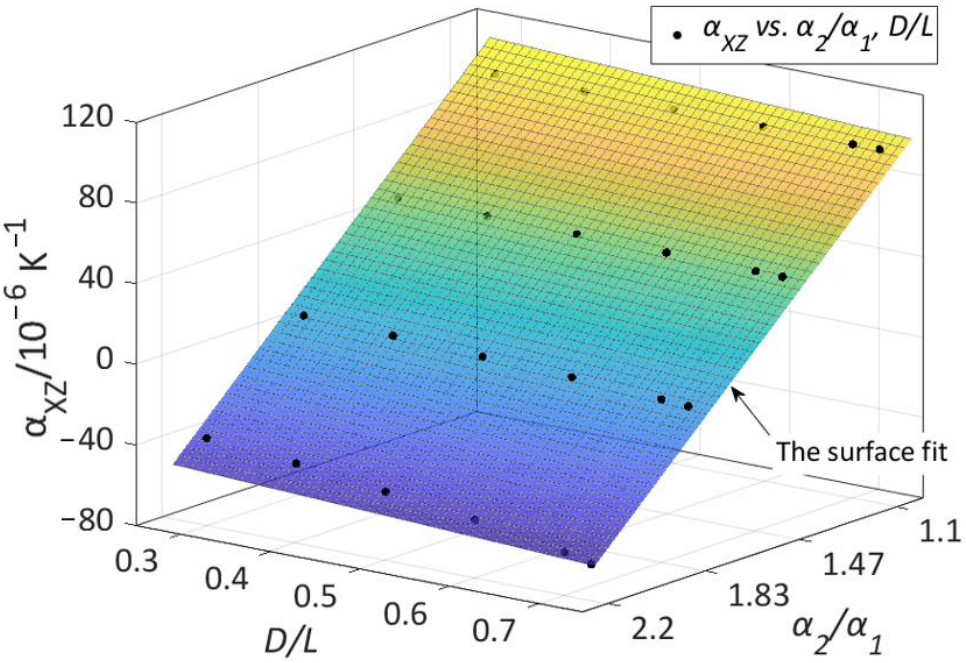


Figure 4.30 Low planar CTE lattice results of Iteration 4.1 obtained by varying the ratios D/L and α_2/α_1 and its surface fit, where L is the original length of the lattice, D is the original diameter of the cylindrical inner part, and α_2/α_1 is the ratio of CTEs of the cylindrical inner part material and the lattice outer part material.

The resulting fit parameters, with 95% confidence bounds, were found to be a = (253 ± 10) × 10^{-6} K^{-1}, b = (−132 ± 5) × 10^{-6} K^{-1}, and c = (−20 ± 10) × 10^{-6} K^{-1}, which could be used to determine the D/L and α_2/α_1 parameters to achieve a pre-defined CTE. The CTEs of Nylon 12 and UHMWPE are 109 × 10^{-6} K^{-1} and 200 × 10^{-6} K^{-1} [125], respectively. The ratio of α_2/α_1 for our chosen materials was, therefore, approximately 1.83, meaning that a unit cell made of such materials can provide CTEs between 7.8 × 10^{-6} K^{-1} and 1 × 10^{-9} K^{-1}. A near-zero CTE of a unit cell of Iteration 4.1 can be achieved when D/L = 0.73 and α_2/α_1 = 1.83.

In practice, the manufacturer's material properties might differ from the given datasheets. For Iteration 4.1, the elastic modulus and CTE were selected to demonstrate these uncertainties, which affect the resulting structure's CTE. The relative changes in the elastic moduli of each of Nylon 12 ${E_1}^*$ and UHMWPE ${E_2}^*$ were demonstrated as elastic modulus uncertainties. The relative change in the CTE of Nylon 12 ${\alpha_1}^*$ and the relative change in the CTE of UHMWPE 12 ${\alpha_2}^*$ were presented as uncertainties of material CTEs. These relative changes were presented in this chapter to express ratios between the original and final values of the studied material properties. For example, the relative change in the elastic modulus of Nylon 12 ${E_1}^*$ was represented by a ratio between the changed value and the original value of the elastic modulus of Nylon 12, which could be written as $\Delta E_1/E_1$. In this study, the relative changes in the elastic modulus of Nylon 12 and UHMWPE varied from −0.4 to 0.4.

The relative changes in the CTEs of Nylon 12 and UHMWPE varied between −0.4 and 0.4. This variation range was selected to ensure that the actual values would not exceed this range.

Figure 4.31 shows that the unit cell of Iteration 4.1 yielded in-plane CTEs ($\alpha_{X,Z}$) between approximately –191 × 10^{-6} K^{-1} and 191 × 10^{-6} K^{-1} by varying the CTEs of the chosen materials. $\alpha_{X,Z}$ data were fitted to a first-order polynomial surface function of the form, as expressed in Equation 4.1. The fits provide an accurate description of the data (with R^2 = 0.994) over the examined range. The resulting fit parameters for CTE variation, with 95% confidence bounds, were found to be a = (0 ± 1) × 10^{-6} K^{-1}, b = (−239 ± 1) × 10^{-6} K^{-1}, and c = (−239 ± 1) × 10^{-6} K^{-1}.

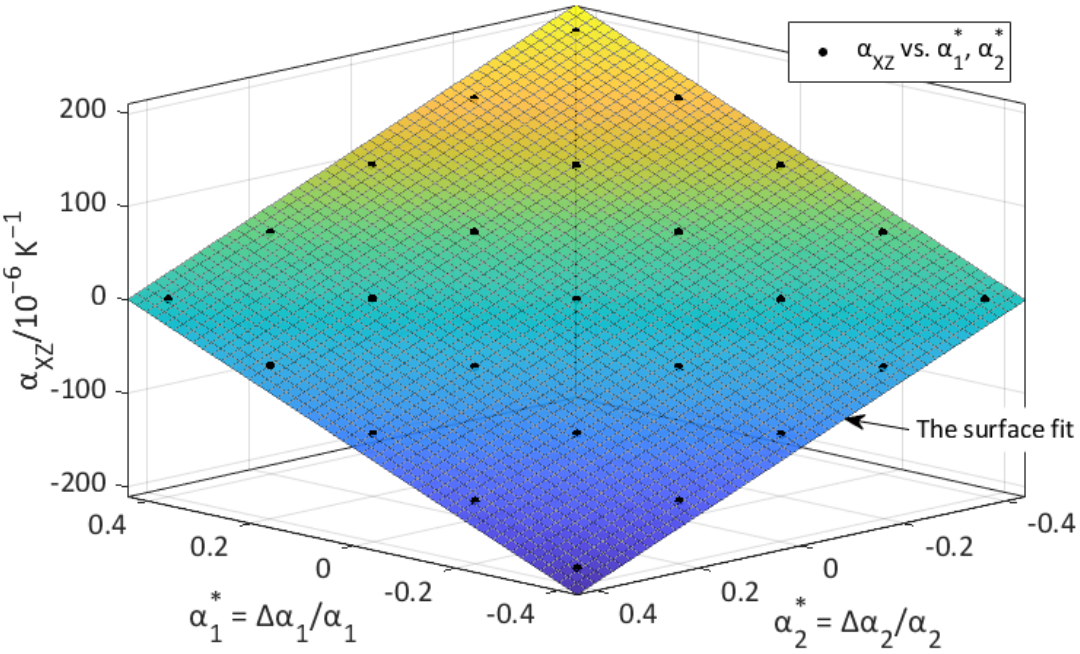


Figure 4.31 Low planar CTE lattice results of Iteration 4.1 by varying α_1 and α_2, and its surface fit, where $\alpha_1{}^*$ is the relative change in the CTE of Nylon 12, $\Delta\alpha_1$ is the change in the CTE of Nylon 12, α_1 is the original value of the CTE of Nylon 12, $\alpha_2{}^*$ is the relative change in the CTE of UHMWPE, $\Delta\alpha_2$ is the change in the CTE of UHMWPE, and α_2 is the original value of the CTE of UHMWPE.

Figure 4.32 shows that the concept lattice unit cell yielded in-plane CTEs ($\alpha_{X,Z}$) between approximately –1.6 × 10^{-6} K^{-1} and 1.3 × 10^{-6} K^{-1} by varying the elastic moduli of the selected materials. $\alpha_{X,Z}$ data of the plots were fitted to a first-order polynomial surface function described previously, as shown in Equation 4.1. The fits provide an accurate description of the data (with R^2 = 1) over the varied range. The resulting fit parameters for the variation of the elastic moduli, with 95% confidence bounds, were found to be a = (−0.1 ± 0.1) × 10^{-6} K^{-1}, b = (1.9 ± 0.1) × 10^{-6} K^{-1}, and c = (−1.7 ± 0.1) × 10^{-6} K^{-1}.

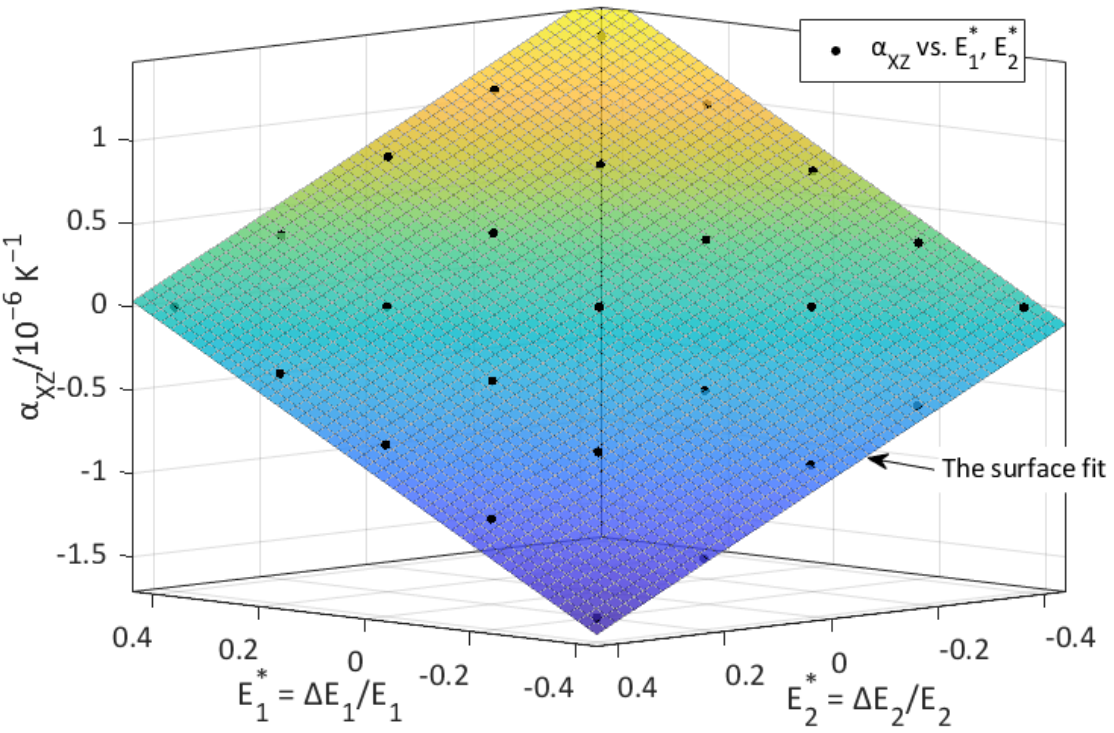


Figure 4.32 Low planar CTE lattice results of Iteration 4.1 by varying E_1 and E_2, and its surface fit, where ${E_1}^*$ is the relative change in the elastic modulus of Nylon 12, ΔE_1 is the change in the elastic modulus of Nylon 12, E_1 is the original value of the elastic modulus of Nylon 12 (1.8×10^9 Pa [126]), ${E_2}^*$ is the relative change in the elastic modulus of UHMWPE, ΔE_2 is the change in the elastic modulus of UHMWPE, and E_2 is the original value of the elastic modulus of UHMWPE (7×10^8 Pa [127]).

According to the plots in Figure 4.31 and Figure 4.32, the resulting structure's CTE was considerably influenced by the in-plane CTE (over a range of -191×10^{-6} K^{-1} to 191×10^{-6} K^{-1}) yet negligibly affected by the elastic modulus (over a range of -1.6×10^{-6} K^{-1} to 1.3×10^{-6} K^{-1}). These results show that the CTEs of materials required careful consideration due to the uncertainties involved in the material selection process, which could lead to the selection of a large and/or inaccurate CTE.

4.4.3. Pattern selection for low-CTE lattice design

When a ($20 \times 20 \times 20$) mm single-unit cell was examined using the FE analysis described in Chapter 6, there were differences between CTEs in the X- and Z-axes. This anisotropic thermal expansion would be challenging for the end application of the precision machine frame, where a predictable thermal expansion response was paramount. One solution to decrease the differences between CTEs in the X- and Z-axes was to arrange the unit cells in a manner that could compensate for the anisotropy. The in-plane CTE of Iteration 4.1 (in the XZ plane) was investigated for five unique orientation patterns (see Figure 4.25). In the 1st pattern, the lattice yielded the lowest in-plane CTE (5.4×10^{-8} K^{-1}), while the 4th pattern rendered the highest in-plane CTE (29.0×10^{-8} K^{-1}), as shown in Table 4.4.

Table 4.4 In-plane CTEs of the designs of the 2 × 1 × 2 lattice.

Pattern	In-Plane CTE/ 10^{-8} K^{-1}
1	5.4
2	12.8
3	8.9
4	29.0
5	9.5

Table 4.4 shows the in-plane CTE results of five unique orientation patterns. The lattice of the 1st pattern was composed of 0 °, 90 °, 180 °, and 270 ° counterclockwise orientated unit cells in the top left, top right, bottom right, and bottom left cells, respectively. The 1st pattern yielded the lowest in-plane CTE, as it was the only pattern where layers were connected in a single plane (the XZ plane) (see Figure 4.33c). In other words, the displacement of unit cells would only occur in the XZ plane. The lattice deformation due to the thermal expansion of the inner cylindrical part was, therefore, constrained to a single plane. Patterns 2 to 5 yielded higher in-plane CTEs due to the arrangements of the connecting layers which were out of the XZ plane, resulting in displacements originating from the XZ plane (see Figure 4.33d). When the 1st pattern lattice was tessellated over a greater number of cells, it was observed that the even numbers of the unit cells yielded low CTE anisotropy (3×10^{-8} K^{-1} for the 2 × 1 × 2 lattice and 1×10^{-8} K^{-1} for the 4 × 1 × 4 lattice), as shown in Table 4.5, given that the structures consisted of 2 × 1 × 2 lattices constraining deformation to a single plane (e.g., the 4 × 1 × 4 lattice was composed of four sets of 2 × 1 × 2 lattices). On the other hand, the odd numbers of the unit cells (the 1 × 1 × 1 lattice and the 3 × 1 × 3 lattice) yielded a high CTE anisotropy due to the arrangements of the connecting layers, which were not at the same level as the layer (Layer 2). As such, there were always unit cells that were not included in the set of 2 × 1 × 2 lattices, resulting in displacements originating from the XZ plane. Such information helped in the design of a less anisotropic thermal expansion for the precision machine frame. However, this research focused on design concepts, instead of the design of large lattices with several cells, which typically requires considerably greater computational resources than could be employed here.

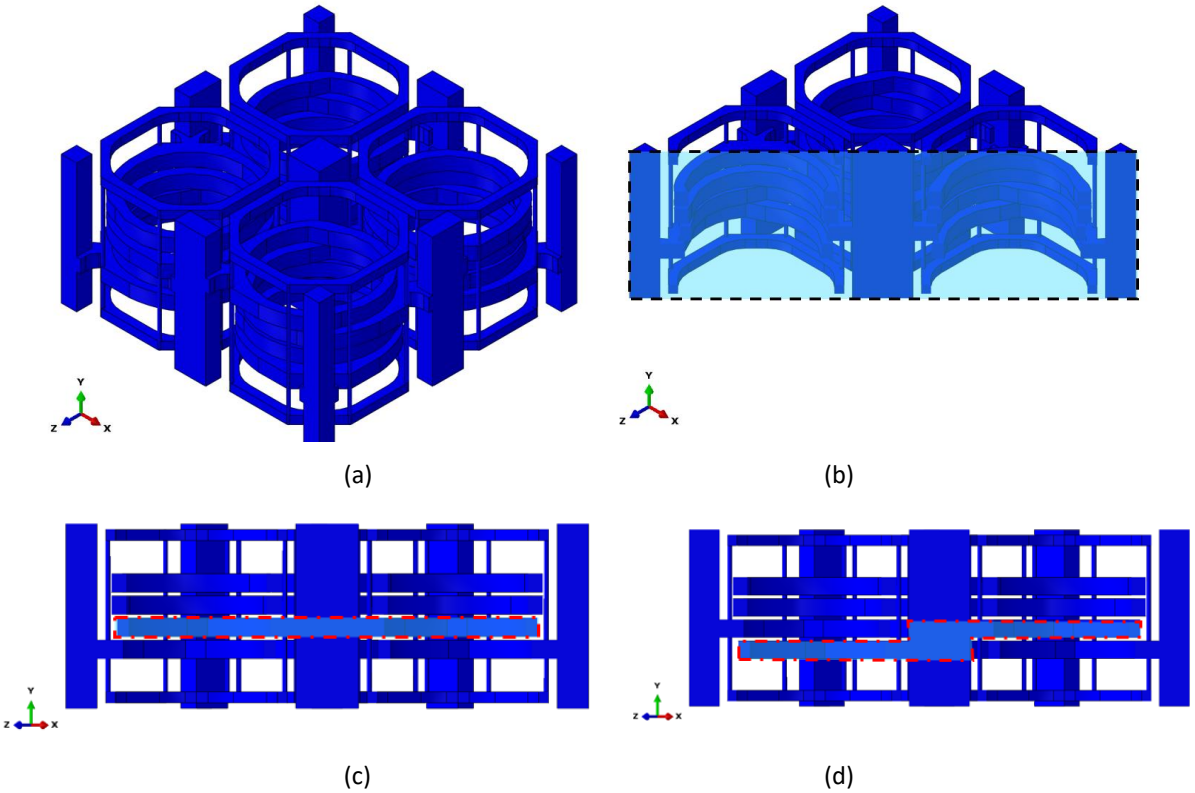


Figure 4.33 The effect of layer alignment on the deformation of the 2 × 1 × 2 lattice outer part of Iteration 4.1: (a) example of the 1st pattern, (b) example of the cross-section of the 1st pattern, (c) example of the cross-section of the 1st pattern at Layer 2, and (d) any of the connecting layers of the other patterns.

Table 4.5 In-plane CTEs of the designs.

Lattice	In-Plane CTE/ 10^{-8} K^{-1}	In-Plane CTE Anisotropy/ 10^{-8} K^{-1}
1 × 1 × 1	0.1	1379
2 × 1 × 2	5.4	3
3 × 1 × 3	8.7	149
4 × 1 × 4	0.03	1

4.5. Discussion of lattice structures for low coefficient of thermal expansion

The main purpose of the development of the lattice structures was to create lattice structures that yield zero CTE. The ratios D/L and α_2/α_1 were the first two parameters that were improved and developed in the designs to control the CTEs. The selection of D and L was carried out by modifying the geometry of the structure using CAD software. The parameters α_1 and α_2 were varied through the selection of materials for the lattice outer part and the cylindrical inner part materials. From the first (Iteration 1) to the final iteration (Iteration 4.1), the ratio D/L was increased from 0.4 to 0.73. This increase in the D/L ratio was ensured by replacing the cylindrical inner part with larger sizes while maintaining the length of the lattice outer part. A larger size of the cylindrical inner part could yield a larger thermal expansion than the smaller one, according to the thermal expansion equation. The purpose of this increase in the D/L ratio was to decrease the lattice structure's CTE.

Despite increasing the D/L ratio, certain iterations, such as Iteration 2.3 and Iteration 3.2, did not yield the expected results, as shown in Figure 4.28. The sizes of the cylindrical inner parts of Iteration 2.3 and Iteration 3.2 were too large for the designs, resulting in higher CTEs than the previous versions, instead of yielding lower CTEs as expected. Such unexpected results led us to establish new conceptual designs to reflect a reconfiguration of the design geometries. The core principle of the achieved development from Iteration 1 series to Iteration 2 series was the replacement of two layers with four layers to eliminate high stresses in the connecting rods and increase their stability within the unit cell. The development from Iteration 2 series to Iteration 3 series mainly consisted of the removal of the four CTE-minimising layers wall sections, providing more space for the cylindrical inner part. The performed development from Iteration 3 series to Iteration 4 series resulted in the relocation of the deformation mechanism movements and allowed for more space along the movements.

The CTE results of Iteration 4.1 showed that the CTE of the proposed lattice design could be tailored by changing the ratios D/L and α_2/α_1, as shown in Figure 4.30. The fitted surface provided a guide allowing designers to customise the CTE and simplified the modification of the material selection and geometry. Note that α_2 should be greater than α_1 for the deformation mechanism to function properly.

Based on the relationship between the cylindrical inner part and the lattice outer part under parametric constraints, when the size of the cylindrical inner part is increased, the internal geometry of the outer part is likely to increase to maintain physical contact. Such a situation occurred, which required the variation of material quantities in each part, as shown in Figure 4.34. In turn, this would affect the manufacturing cost of the lattice structure, since AM processes were relatively costly, especially LPBF [128]. However, the overall cost could be reduced by designing a lattice structure with a large D/L ratio. Nevertheless, to reach the target of zero CTE, restrictions were placed on the selected materials in terms of their CTE values.

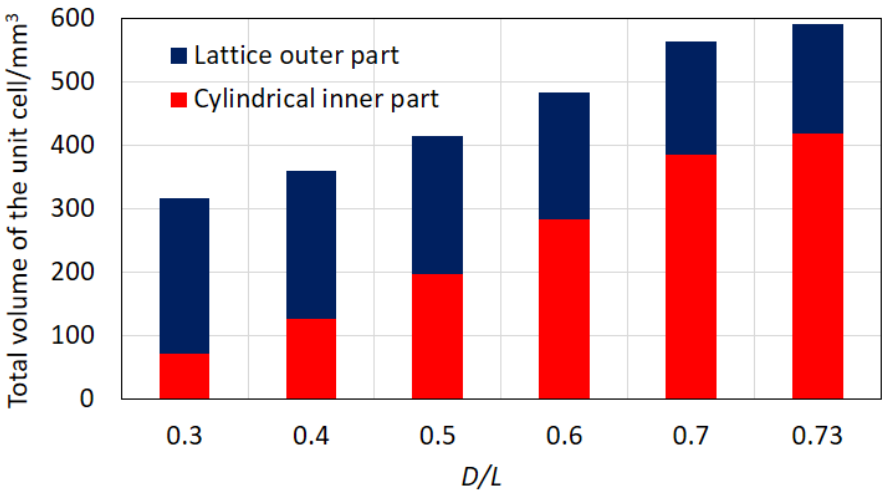


Figure 4.34 The total volume of Iteration 4.1's (10 × 10 × 10) mm unit cell by varying the D/L ratio between 0.3 and 0.73.

The uncertainties of two material properties, namely the CTE and the elastic modulus, were examined in terms of their influence on the in-plane CTEs of the conceptual design of the lattice unit cell of Iteration 4.1. The parameters ${E_1}^*$,${E_2}^*$, ${\alpha_1}^*$ and ${\alpha_2}^*$ were varied in the same range of −0.4 to 0.4. The varied CTEs of the unit cell materials yielded a much more comprehensive range of in-plane CTEs (−191 × 10^{-6} K^{-1} to 191 × 10^{-6} K^{-1}, as shown in Figure 4.31) than those yielded by the varied elastic modulus of unit cell materials (−1.6 × 10^{-6} K^{-1} to 1.3 × 10^{-6} K^{-1}, as shown in Figure 4.32). Therefore, in comparison, in-plane CTEs were dominated by material CTEs, while the elastic moduli of materials could be neglected in the design.

Using a similar assembly technique to that examined in this study, Jefferson et al. designed a structure Jefferson, Parthasarathy [93] that yielded a near-zero CTE. In comparison, Iteration 4.1 presented in this research could yield a broader range of CTEs including near-zero, achieved with $D/L = 0.73$ and $\alpha_2/\alpha_1 = 1.83$. Although other polymer-based structures could provide wider ranges of CTEs than the lattice presented in this research (i.e., −434 × 10^{-6} K^{-1} to 396 × 10^{-6} K^{-1} from Akihiro et al. [79] and –300 × 10^{-6} K^{-1} to 1000 × 10^{-6} K^{-1} from Takezawa and Kobashi [80] using admixture material of VeroWhitePlus and TangoBlackPlus), the internal geometries of such structures were more complex, required additional topology optimisation to model the structures, and required the use of advanced multi-material AM processes for fabrication. With the previously stated parameters, the structure of Iteration 4.1 could yield a CTE of 1 × 10^{-9} K^{-1}, which is a much lower CTE than that achieved by several commercial instruments and functional surfaces in optical breadboards (CTE of 23 × 10^{-6} K^{-1} for aluminium 7075 and 10 × 10^{-6} K^{-1} for stainless steel 431 CTE [87]).

The tessellations of the 1st pattern cell, composed of even numbers in both the X- and Z-axes of Iteration 4.1, are recommended for low-CTE applications. However, further investigation is required to identify the rationale behind such suitability. An added advantage of charactering CTEs using the fitted surface, shown in Figure 4.30, is that adjustments can be made for variations in material properties or geometries with just a few calibration experiments.

4.6. Conclusion

The iterations introduced in this research aimed at the creation of a planar near-zero thermal expansion lattice structure. The designs demonstrated that the thermal expansion could be controlled, via the deformation mechanism of the internal geometry, using a combination of two positive homogenous materials. The design introduced the separation of load-bearing sections and deformation mechanism sections and introduced the optimised functions in the internal geometry whose performance was increased. It was shown that the CTE could theoretically be reduced to 1×10^{-9} K^{-1} (For Iteration 4.1), which was the closest value to the near-zero CTE aimed for in this design.

In summary, the designs illustrated the steps followed to create lattices that could enable a wide range of CTEs, through changing the ratios of the diameter of the cylindrical inner part over the length of the lattice, and the ratio between the CTEs of the cylindrical inner part material and the lattice outer part material. Pattern selection methods were additionally introduced to reduce differences between CTEs in the X- and Z-axes and compensate for anisotropy in the lattice.

5. Finite element simulation of lattice structures

This chapter presents the effects of various finite element (FE) modelling parameters (element type, mesh density, etc.) on the thermal expansion of a newly proposed expansion-compensating lattice structure. First, an introduction to FE modelling of lattice structures is presented. Second, method for the finite element simulation of the lattice structures is described. Third, the parameters that affect simulated thermal expansion, including procedure type, boundary conditions, partitions for contact, partitions for reducing mesh density, and element type, are detailed. These are followed by a discussion and concluding remarks. Additionally, FE analysis validation/setup checks were performed for all designs (Iteration series 1, 2, 3 and 4). However, the lattice model known as 'the final iteration' (Iteration 4.1) is chosen to demonstrate the effects of the considered parameters for the purpose of this chapter.

5.1. Introduction to finite element simulation of lattice structures

Conceptual lattice designs were modelled in SolidWorks 2018 to obtain representative CAD models, and their performance was simulated using the FE analysis implemented in Abaqus 2018 and 2020. The initial lattice unit cell dimensions (i.e., in its unheated state) were (20 × 20 × 20) mm. The size was chosen in order to represent the minimum size with minimal loss in mechanical capabilities such as ultimate tensile strength and the elastic modulus, according to Tasch et al. [103], as described in Subchapter 2.5. The temperature of the elements in all models was raised from 19 to 23 °C, representing the temperature variation in a typical temperature-controlled metrology laboratory. All nodes on three of the lattice's cubic edges were constrained in space (as seen in Figure 5.1) to enable the calculation of thermally induced expansion. The XSYMM (Symmetry about a plane X = constant (U1 = UR2 = UR3 = 0)), YSYMM (Symmetry about a plane Y = constant (U2 = UR1 = UR3 = 0)), and ZSYMM (Symmetry about a plane Z = constant (U3 = UR1 = UR2 = 0)) boundary conditions were applied to the nodes on the surfaces of the YZ plane in the –X direction (labelled 'YZ (-X)' in Figure 5.1), the XZ plane in the –Y direction ('XZ (-Y)'), and the XY plane in the –Z direction ('XY (-Z)'), where U1 is the translation in the X-direction, U2 is the translation in the Y-direction, U3 is the translation in the Z-direction, UR1 is the rotation about the X-direction, UR2 is the rotation about the Y-direction, and UR3 is the rotation about the Z-direction. The thermal expansion of the lattice was calculated by examining the displacement of the nodes on the surfaces opposite to those that were constrained. Figure 5.1 shows a unit cell model meshed with over 440,000 elements.

More details on lattice thermal expansion, including a thorough explanation of Figure 6.1, can be found in the author's published work [124] in Low Thermal Expansion Machine Frame Designs Using Lattice Structures. Other thermal expansion parameters will be discussed in Subchapter 6.2.

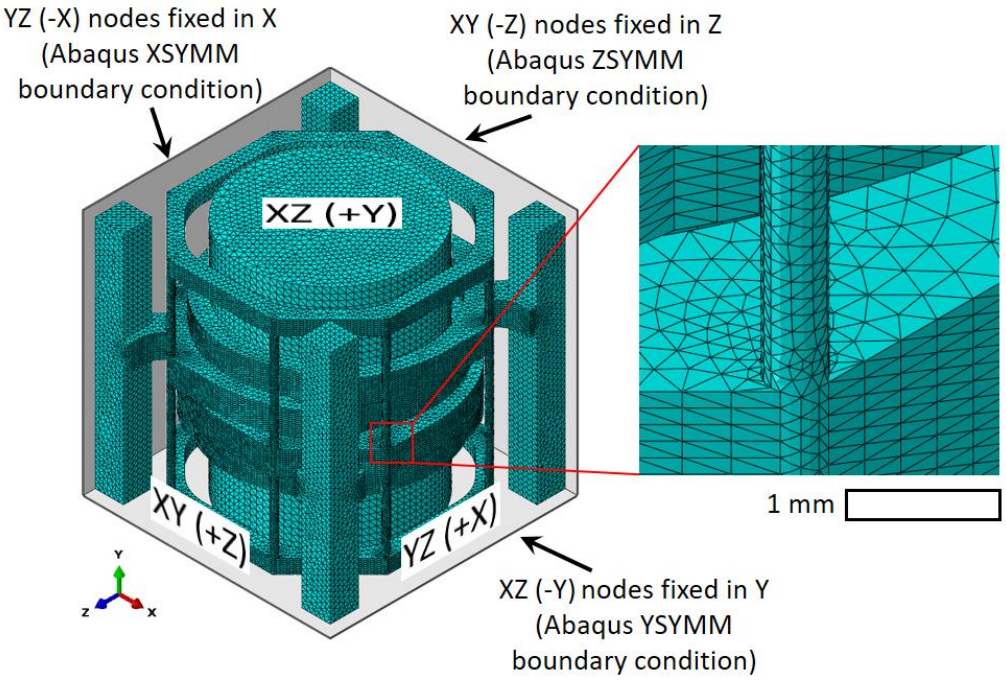


Figure 5.1 Representative example of the converged mesh of the (20 × 20 × 20) mm low-CTE concept lattice unit cell and its boundary conditions applied on a lattice unit cell design [124].

5.2. Method for the finite element simulation of the lattice structures

In this research, the performances of all lattice structures were examined using FE analysis. All models were tested in the same environmental conditions, such as boundary conditions. The simulations examined the structure's CTE by increasing temperature in the entire lattice. In the simulation, high-performance processors and a high memory capacity were required to analyse and restore the data. All simulations were analysed in Abaqus version 2018 and version 2021 (FE analysis software) through Augusta (High Performance Computer; HPC) of the University of Nottingham. Details of how the FE simulation was conducted step by step are described as follows:

Step 1: Problem definition – The lattice models integrated into the machine frame will be placed in a temperature-controlled laboratory. The temperature in the laboratory slowly changes between 19 °C to 23 °C. In the simulations, the lattice structures were re-evaluated for all changing temperature values, with the displacement changes and resulting stresses measured.

Step 2: Mathematical model definition – The concept of the physical problem was interpreted into Abaqus. All parameters were classified into four categories: parts, material, assembly and step. Details of the parameters used in this research are described as follows:

1. Parts

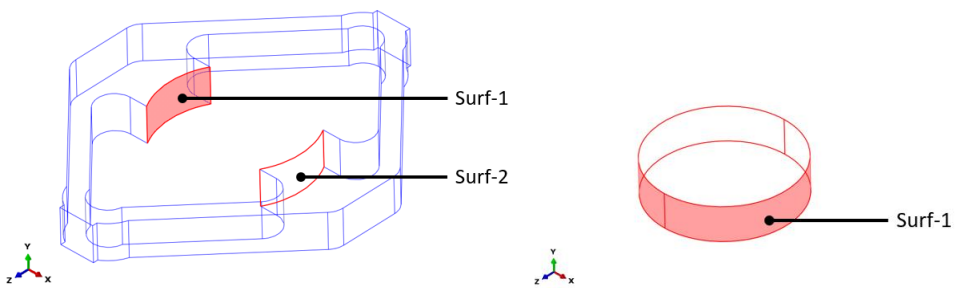
The lattice structures were composed of the lattice outer part and the cylindrical inner part. Parts were individually imported via the ".igs" extension file. Materials of the lattice outer parts and the cylindrical inner parts were assigned in this step. Sections in the parts were predefined (as shown in Figure 4.2 and Figure 4.3) for matching the contacts and meshing.

For the lattice outer part, three operations were performed as follows:

- "Create surface" –The two cylindrical inner surfaces of the 1D tailorable thermal expansion lattices (Iterations 1 and 1.1) were individually defined as Surf-1 and Surf-2 (as shown in Figure 5.2a). For 2D tailorable thermal expansion lattices (Iteration 2 series, Iteration 3 series and Iteration 4 series), the four cylindrical inner surfaces were individually defined (one surface for each layer) as Surf-1, Surf-2, Surf-3 and Surf-4, as demonstrated in Figure 5.3a.
- "Create sets from geometry" – The deformation mechanism geometry on the lattice outer part was defined as Set-1 (as shown in Figure 5.3c).
- "Assign section" – Nylon 12 was assigned as a material for the entire lattice outer part.

For the cylindrical inner parts:

- "Create surface" – The surface of the curved face of the cylindrical inner part was defined as Surf-1 (as shown in Figure 5.2a).
- "Assign section" – Ultra-high-molecular-weight polyethylene (UHMWPE) was assigned for the whole of the cylindrical inner parts.



(a) (b)

Figure 5.2 Example of a 3D model of the 1D tailorable thermal expansion lattice (Iteration 1.1) with the predefined surfaces (highlighted in red): (a) the lattice outer part and (b) the cylindrical inner part.

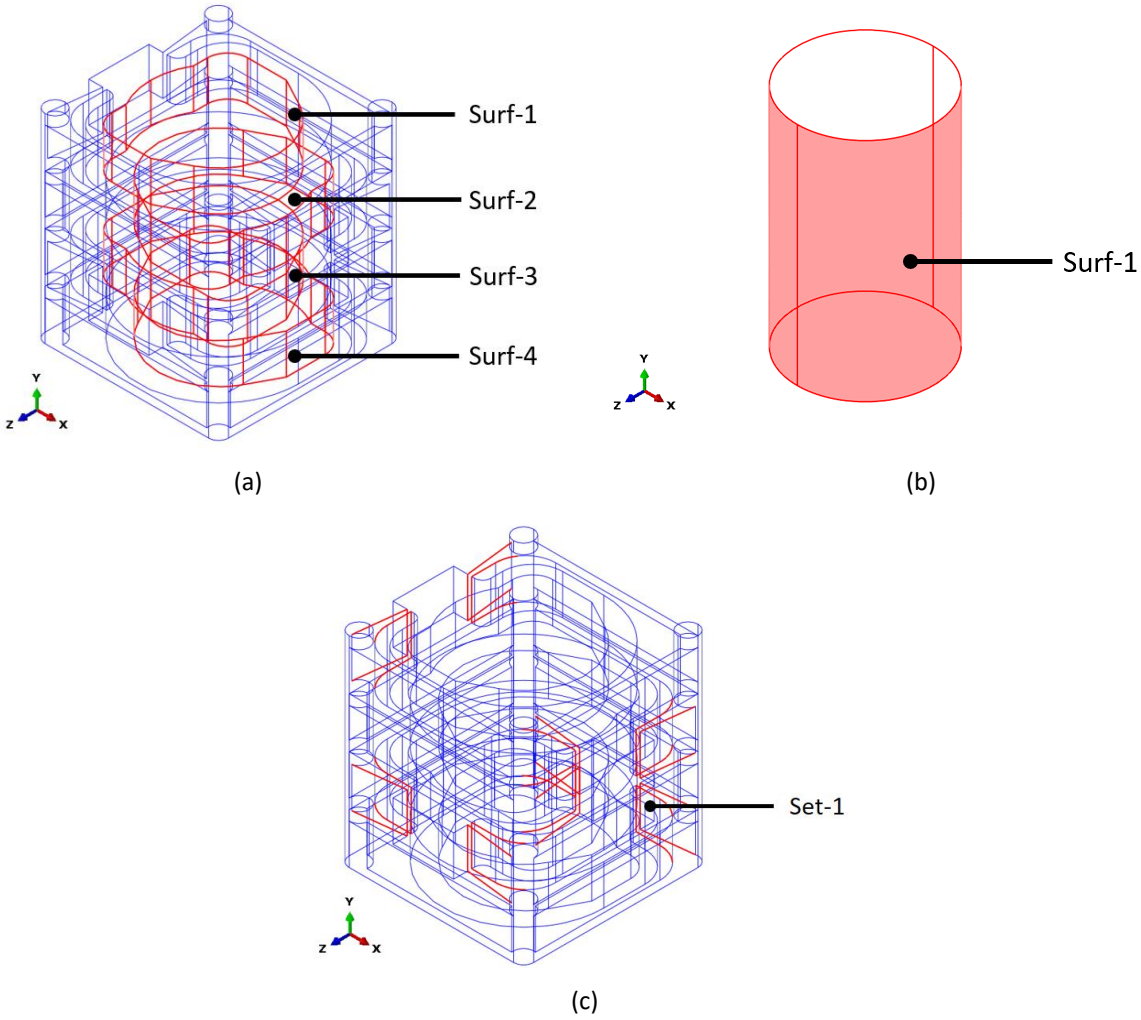


Figure 5.3 An example of a 2D tailorable thermal expansion lattice (Iteration 2.4) with the predefined sections (highlighted in red): (a) the lattice outer part with the predefined surfaces, (b) the cylindrical inner part with the predefined surfaces and (c) the lattice outer part with the predefined set (Set-1).

2. Materials

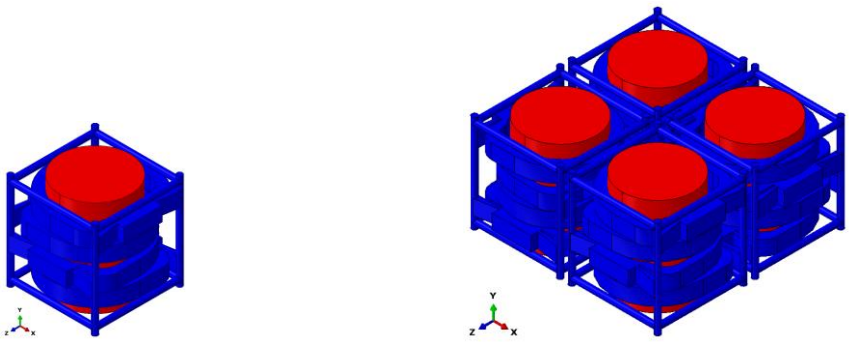
Two homogenous materials were added to the software's library database: Nylon 12 and UHMWPE. Table 5.1 shows the actual values of the properties of Nylon 12 [126, 129] and UHMWPE [127]. Once sections were assigned to parts, the properties of the chosen materials were entered as parameters in the simulations.

Table 5.1 Properties of Nylon 12 and UHMWPE.

Material / Property	Nylon 12 [126, 129]	UHMWPE [127]
Thermal conductivity, isotropic/ W/(m·K)	0.3	0.41
Density, uniform/ kg/cm^3	1020	930
Elastic modulus, isotropic/ GPa	1.8	0.7
Poisson's Ratio, isotropic	0.393	0.11
Thermal expansion, isotropic/ × 10^{-6} K^{-1}	109	200
Specific Heat, constant volume/ J/kg·K	2270	1840

3. Assembly (instances)

The lattice outer part and cylindrical inner part/s were assembled into one in this step. For the 1 × 1 × 1 lattice (one unit cell), the cylindrical inner part was placed into the centre of the lattice outer part (as shown in Figure 5.4 Example of the position of parts in a lattice structure: (a) a 1 × 1 × 1 lattice of Iteration 3.1 and (b) a 2 × 1 × 2 lattice of Iteration 3.1.Figure 5.4a). For a larger lattice structure, the cylindrical inner parts were placed into the centre of each unit cell in the lattice outer part (as shown in Figure 5.4b).



(a) (b)

Figure 5.4 Example of the position of parts in a lattice structure: (a) a 1 × 1 × 1 lattice of Iteration 3.1 and (b) a 2 × 1 × 2 lattice of Iteration 3.1.

4. Steps

In the simulation, the starting point is always the initial condition (called 'initial step') and is then simulated to attain the condition that we define (called 'analysis step'). Following ABAQUS/CAE User's Manual [130] and similar studies from other studies [65, 68, 87, 93], four parameters (interaction, boundary conditions, predefined fields and field output request) were defined in the simulation as follows:

- Interactions (using Surface-to-surface contact) – ***Initial step:*** A unit cell in a 1D tailorable thermal expansion lattice was characterised by two-pair contacts (1st pair and 2nd pair), while

one in a 2D tailorable thermal expansion lattice had four-pair contacts (1st pair, 2nd pair, 3rd pair and 4th pair). The cylindrical inner surfaces of the lattice outer part were defined as a master surface, and the surface of the cylindrical inner part was defined as a slave surface. These set-up parameters were applied separately for layers of the lattice outer part with one surface of the cylindrical inner part (as illustrated for the 2nd pair in Figure 5.5):

- The 1st pair – The top surface of the cylindrical inner surfaces in the lattice outer part (outer.Surf-1) was defined as a master surface, and the surface of the cylindrical inner part (inner.Surf-1) was defined as a slave surface.
- The 2nd pair – The second top surface of the cylindrical inner surfaces in the lattice outer part (outer.Surf-2) was defined as a master surface, and the surface of the cylindrical inner part (inner.Surf-1) was defined as a slave surface, as shown in Figure 5.5.
- The 3rd pair – The second bottom surface of the cylindrical inner surfaces in the lattice outer part (outer.Surf-3) was defined as a master surface, and the surface of the cylindrical inner part (inner.Surf-1) was defined as a slave surface.
- The 4th pair – The bottom surface of the cylindrical inner surfaces in the lattice outer part (outer.Surf-4) was defined as a master surface, and the surface of the cylindrical inner part (inner.Surf-1) was defined as a slave surface.

The described patterns were applied several times for larger lattice structures. For example, a 2 × 1 × 2 lattice of 2D tailorable thermal expansion would have four unit cells with 16 pairs of surface-to-surface contact. As for friction in the contacts, it was defined as 'hard' contact with the isotropic coefficient of friction of 0.1 for all contacts. ***Analysis step:*** none predefined.

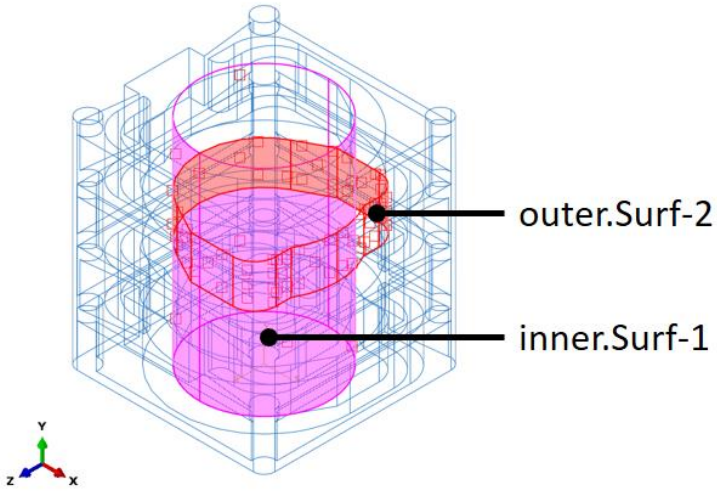


Figure 5.5 Illustration of defining a surface-to-surface contact for the lattice structure. The 2nd pair interaction (outer.Surf-2) was defined as a master surface and inner.Surf-1 was defined as a slave surface.

- Boundary conditions – ***Initial step:*** for all lattice structures, including the unit cell, the boundary conditions were applied (as shown in Figure 4.6) as follows: XSYMM (Symmetry about a plane X = constant (U1 = UR2 = UR3 = 0)) was applied on the nodes on the surfaces belonging to the YZ plane in the –X direction (labelled 'YZ (-X)'), YSYMM (Symmetry about a plane Y = constant (U2 = UR1 = UR3 = 0)) was applied on the nodes on the surfaces belonging to the XZ plane in the –Y direction (labelled 'XZ (-Y)'), and ZSYMM (Symmetry about a plane Z = constant (U3 = UR1 = UR2 = 0)) was applied on the nodes on the surfaces belonging to the XY plane in the –Z direction (labelled 'XY (-Z)'), as summarised in Figure 5.6. ***Analysis step:*** none predefined.

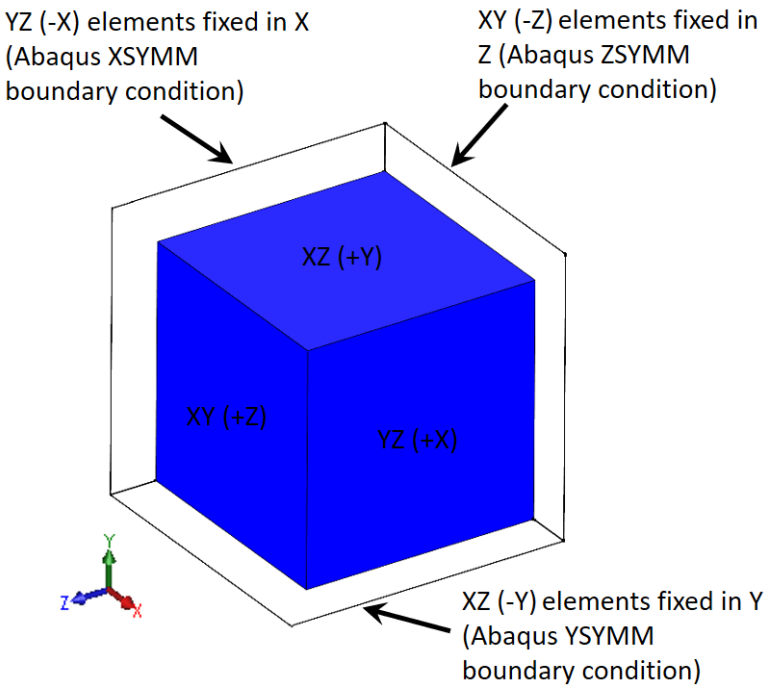


Figure 5.6 Summary of all the boundary conditions applied in the lattice structure.

- Predefined Fields – ***Initial step:*** the temperature for the entire part was set to be 296.15 K. ***Analysis step:*** the temperature for the whole part was set to be 300.15 K.
- Field output request – ***Initial step:*** none predefined. ***Analysis step:*** Stress (S) and displacement (U) were selected for the simulation outputs.

Step 3: Finite element parameter definition – Two types of element shapes are commonly utilised for mesh generation: tetrahedral and hexahedral. Tadepalli et al. [131] stated that tetrahedral meshing could be easily automated, while hexahedral meshing commonly required user intervention and was labour intensive. Therefore, ten-node tetrahedral elements (C3D10) were chosen for mesh, given the high degree of complexity of the lattice outer part. Two geometries: the lattice outer part and the

cylindrical inner part, were meshed separately. The mesh density of the cylindrical inner part was assigned equally throughout the entire structure, while the meshing of the lattice outer part was performed using two different mesh densities. The lattice outer part was divided into two sections: global geometry and deformation mechanism geometry (Set-1), which was defined in Step 2 to assign the mesh densities of the elements. The mesh density of the elements in Set-1 was chosen to guarantee a higher mesh density than the global geometry. After meshing, the nodes indicated the displacement changes of the lattice structure, which were defined in the "Assembly" step as follows:

- "Create sets from node" – Nodes on the surfaces of the YZ plane in the +X direction (YZ (+X) was defined as 'xdata' and nodes on the surfaces of the XY plane in the +Z direction (XY (+Z) were defined as 'zdata', as indicated in Figure 5.6. These two data sets were analysed to determine changes in the CTE of the examined lattice structure in the coming steps.

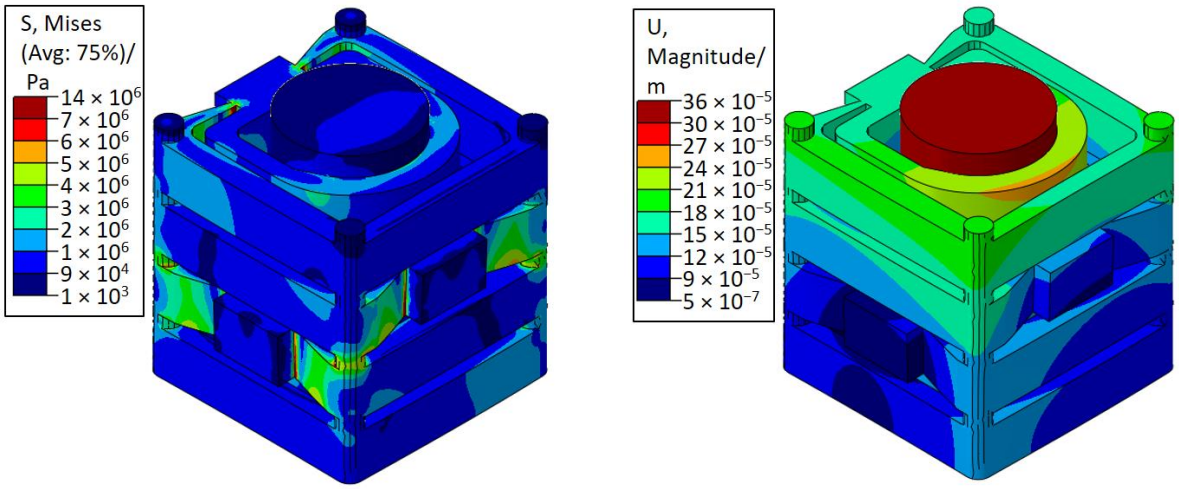
Step 4: Computation – A prepared single input file can be submitted to a computer processor via GUI. Each iteration required a different minimum memory (RAM) allocation to minimise inputs/outputs (ROM), as shown in Table 5.2. The data shown in Table 5.2 are values of the required memories for each 1 × 1 × 1 lattice (a unit cell). For larger structures, more memory was required. In this research, many files were required for analysis, hence, HPC was used to accelerate computational time.

Table 5.2 Summary of minimum memory requirements to analyse iterations.

Iteration	Required RAM/ MB	Required ROM/ MB
1	364	2,813
1.1	127	797
1.2	2,400	23,150
2	1,295	10,953
2.1	1,944	15,197
2.2	3,829	39,957
2.3	4,239	44,502
2.4	4,151	42,550
3	4,395	43,436
3.1	3,189	28,112
3.2	3,265	29,118
4	1,902	14,967
4.1	2,443	17,779

Step 5: Verification – After the input files had been completely processed, the processors of the HPC produced output files (e.g., animated output files (ODB files), as shown in Figure 5.7 parameter definition files in a text (DAT files), and diagnostic or informative messages about the progress of the solution (MSG files). There are many ways to verify the reliability of the results. In this research, several factors were taken into account before analysing the data in the files. The conditions verified to ensure reliability included:

- In DAT files, the message “THE ANALYSIS HAS BEEN COMPLETED” was written with the step time completed equal to 1.00
- In DAT files, the node results must have different values
- In ODB files, the lattice structures must expand or contract from YZ (-X), XZ (-Y) and XY (-Z) toward YZ (+X), XZ (+Y) and XY (+Z), respectively
- In ODB files, the lattice structure must consist of the lattice outer part and the cylindrical inner parts. The cylindrical inner parts were located in the centre of each unit cell at all times
- In ODB files, the lattice outer part and the cylindrical inner parts would not overlap with each other at any time, except when the deformation factor was equal to 1
- In ODB files, the highest stress was expected to appear in the deformation mechanism geometry of the contour plot of von Mises stress



(a) (b)

Figure 5.7 Examples of results from the FEA simulation of the lattice: (a) a contour plot of von Mises stress and (b) a contour plot of the magnitude of displacement change.

Step 6: Validation – Following the mesh refinement methodology presented in Chapter 3, we successfully reduced unnecessary elements and computational time. The mesh densities assigned in each iteration will be discussed in Chapter 6.

5.3. Parameters affecting finite element results

5.3.1. Method: procedure type

The coefficients of thermal expansion (CTEs) of lattice structures have been determined through general static analysis simulations. This analysis procedure enables the determination of the object or assembled object behaviour, such as stress and strain under given conditions (from an initial condition

to the attained condition), and uses the Newton–Raphson method to obtain results which are a consequence of the applied constraints and loads [132]. In our case, the temperature change is treated as a load, ignoring time-dependent material effects such as creep, swelling, and viscoelasticity.

5.3.2. Method: boundary conditions

Before the selection of final boundary conditions (BCs) (as described in Subchapter 6.1), five different boundary condition sets were examined and compared. Boundary conditions were considered for application to the nodes on the surfaces; YZ (+X), YZ (-X), XY (+Z), XY (-Z), XZ (+Y) and XZ (-Y), as seen in Figure 5.1. Each surface was individually assigned constraints according to its movement. Six degrees of freedom refer to the freedom of movement of a rigid body in three-dimensional space: U1, U2, U3, UR1, UR2 and UR3, as described in Subchapter 6.1.

Table 5.3 shows the boundary conditions applied on specific surfaces and the nodes measured to account for displacement change. BC1, BC2 and BC5 are the boundary conditions constrained at zero at the nodes on YZ (-X), XY (-Z) and XZ (-Y), to measure the displacement change of the nodes on YZ (+X) and XY (+Z). BC3 and BC4 are the boundary conditions that only constrained the nodes on XZ (-Y) and were employed to measure the displacement change of the nodes on YZ (+X), YZ (-X), XY (+Z) and XY (-Z).

Table 5.3 Five sets of boundary conditions applied to the lattice structure.

Boundary conditions	**BC1**	**BC2**	**BC3**	**BC4**	**BC5**
YZ (+X)	-	Fixed in UR2 and UR3	Fixed in UR2 and UR3	-	-
YZ (-X)	Fixed in U1, UR2 and UR3	Fixed in U1, UR2 and UR3	Fixed in UR1, UR2 and UR3	Fixed in UR1, UR2 and UR3	Fixed in U1
XY (+Z)	-	Fixed in UR1 and UR2	Fixed in UR1 and UR2	-	-
XY (-Z)	Fixed in U3, UR1 and UR2	Fixed in U3, UR1 and UR2	Fixed in UR1 and UR2	Fixed in UR1 and UR2	Fixed in U3
XZ (+Y)	-	Fixed in UR1 and UR3	Fixed in UR1 and UR3	-	-
XZ (-Y)	Fixed in U2, UR1, and UR3	Fixed in U2, UR1, and UR3	Fixed in U2, UR1, and UR3	Fixed in U2, UR1, and UR3	Fixed in U2
Measured nodes	YZ(+X) for U1 and XY(+Z) for U3	YZ(+X) for U1 and XY(+Z) for U3	YZ(+X) for U1, YZ(−X) for U1, XY(+Z) for U3 and XY(−Z) for U3	YZ(+X) for U1, YZ(−X) for U1, XY(+Z) for U3 and XY(−Z) for U3	YZ(+X) for U1 and XY(+Z) for U3

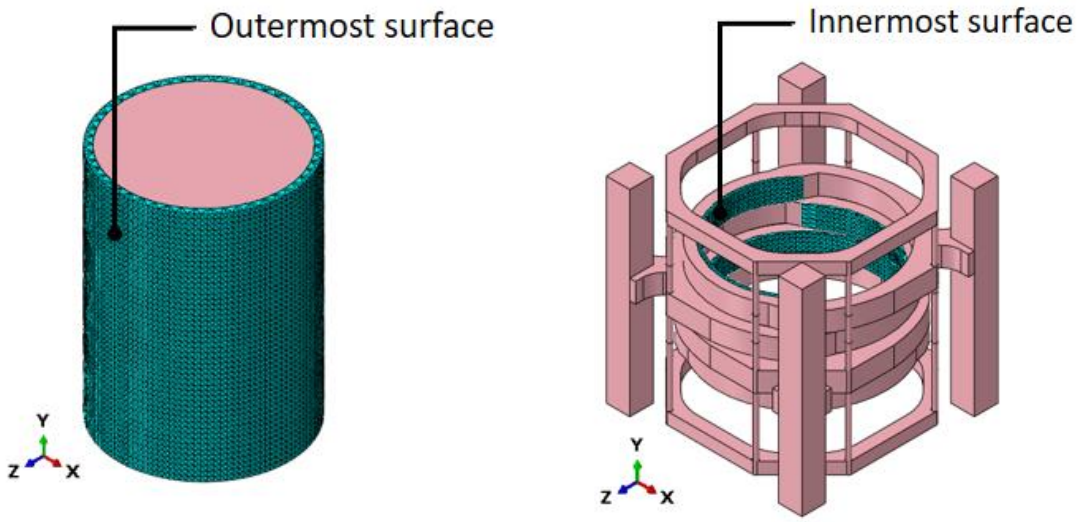
Table 5.4 shows the in-plane CTEs of the five sets of boundary conditions and their differences compared to BC1. It is clear that similar results were noted in the lattice structures under BC1, BC2 and BC5 when the nodes on YZ (−X), XY (−Z) and XZ (−Y) were fixed in U1, U3 and U2. Conversely, the lattice structures under BC3 and BC4 rendered different results due to the free movement of YZ (−X) and XY (−Z) in both BCs causing rigid body motion in the XZ plane. Therefore, BC3 and BC4 were not appropriate to determine CTE. Accordingly, BC1 was selected to conduct the thermal expansion simulation, the same as earlier studies [67, 68, 104].

Table 5.4 In-plane CTE of the boundary conditions and their percentage difference compared to BC1.

Boundary Conditions	**In-Plane CTE/ $\times 10^{-9}$ K^{-1}**	**% Difference Compared To BC1**
BC1	1.40	0.0%
BC2	1.40	0.0%
BC3	0.31	-77.9%
BC4	0.68	-51.2%
BC5	1.40	0.0%

5.3.3. Finite element mesh: creating partitions for contact

Lattice structures in this study are composed of the lattice outer part and the cylindrical inner part. The two parts were put in contact: the innermost surface of the lattice outer part and the outermost surface of the cylindrical inner part, as seen in Figure 5.8. In FE analysis, the contact of the two parts was simulated by creating master and slave surfaces. To assign master-slave contacts, two principal rules must be followed to achieve the best possible contact simulation. First, the slave surface should be the one with the finer mesh. Second, the surface with the softer underlying material should be selected as the slave surface, assuming similar mesh densities [130]. To control the master and slave nodes on the surfaces in contact, small sections were created with equal mesh densities in both the innermost surfaces of the lattice outer part and the outermost surface of the cylindrical inner part, as seen in Figure 5.8. By creating equal mesh densities, the first rule of the master-slave contacts was ignored. Following the second rule, the contact surfaces on the lattice outer parts were set to be master surfaces, whereas the contact surfaces on the cylindrical inner parts were selected as slave surfaces due to the cylindrical inner part material (UHMWPE with an elastic modulus = 0.7 GPa) being softer than the lattice outer part material (Nylon 12 with an elastic modulus = 1.8 GPa). Figure 5.9 shows a contour plot of contact pressure between the innermost surface of the lattice outer part and the outermost surface of the cylindrical inner part.



(a) (b)

Figure 5.8 Illustrations of (20 × 20 × 20) mm Iteration 4.1 with partitions for contact (a) the cylindrical inner part and (b) the lattice outer part.

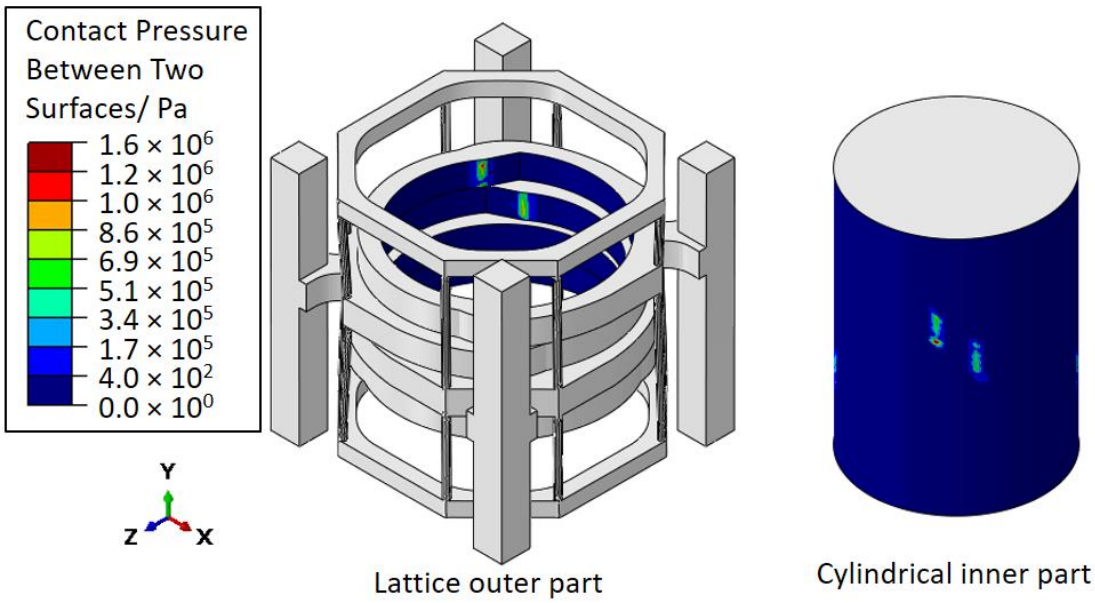
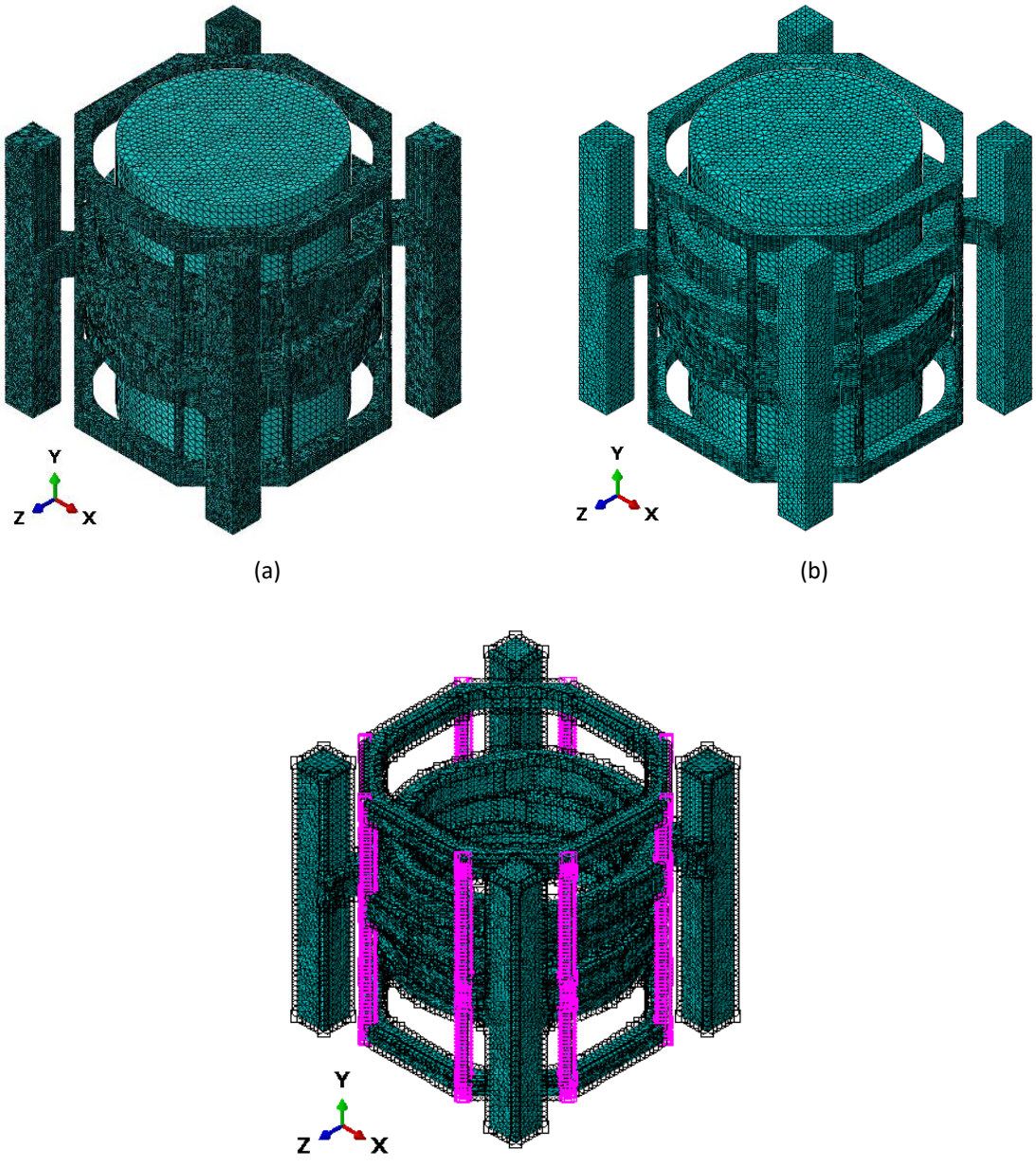


Figure 5.9 Contour plot of contact pressure between two surfaces of Iteration 4.1 when the temperature was raised.

5.3.4. Finite element mesh: creating partitions for mesh density reduction

Without partitions to reduce mesh densities, Iteration 4.1 needed approximately 2,468,572 tetrahedral elements (123,091 elements for the cylindrical inner part and 2,345,481 elements for the lattice outer part), as seen in Figure 5.10a, to obtain a sufficient mesh density to determine the lattice structure's CTE. Computing this meshed geometry entailed a lengthy computational time and many processors, which will be presented in Subchapter 6.3. Fortunately, the resources could be optimised

by reducing mesh densities in the regions where high stresses did not occur [115]. Figure 5.11 shows a contour plot of von Mises stress of Iteration 4.1 that indicated the regions where high stresses occurred (marked in the dashed boxes, as seen in Figure 5.11). Accordingly, eight partitions were created in the high stress regions with a high mesh density, while the other regions were meshed with a coarser mesh density. The steps of this partition creation were described in Subchapter 4.2. The mesh density in Iteration 4.1 was reduced to approximately 417,129 tetrahedral elements (123,091 elements for the cylindrical inner part and 294,038 elements for the lattice outer part), as shown in Figure 5.10b, to obtain a sufficient mesh density to determine the lattice structure's CTE.



(a) (b)

(c)

Figure 5.10 Illustrations of converged meshes of (20 × 20 × 20) mm Iteration 4.1: (a) without partitions and (b) with partitions in high stress regions and (c) with partitions and highlighted in high stress regions.

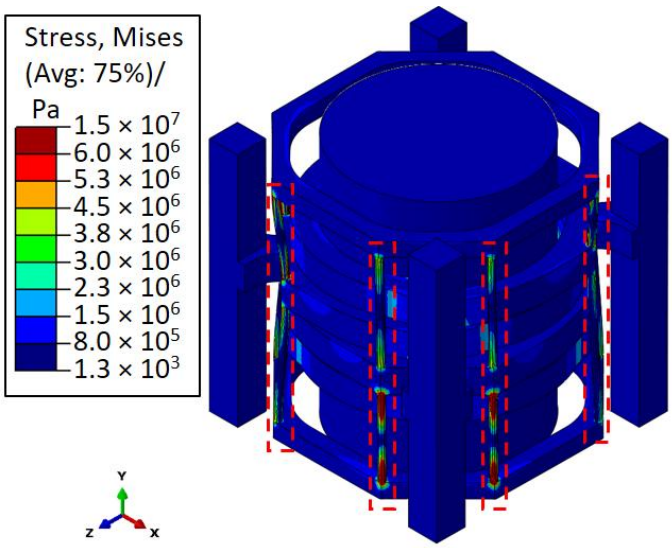


Figure 5.11 Contour plot of von Mises stress of Iteration 4.1 with the dashed boxes indicating high stress regions when the temperature was raised.

5.3.5. Finite element mesh: mesh type

Two types of element shapes are commonly utilised for mesh generation: tetrahedral and hexahedral, as illustrated in Figure 5.12. Tadepalli et al. [131] suggest that tetrahedral meshing can be easily automated, while hexahedral meshing commonly requires user intervention and is labour intensive. In addition, compared to hexagonal elements, tetrahedral elements generally provide a more accurate description of the complex lattice geometry, such as geometric curvature. However, the number of tetrahedral elements required is four to ten times higher than hexahedral elements for the same level of accuracy of results [133].

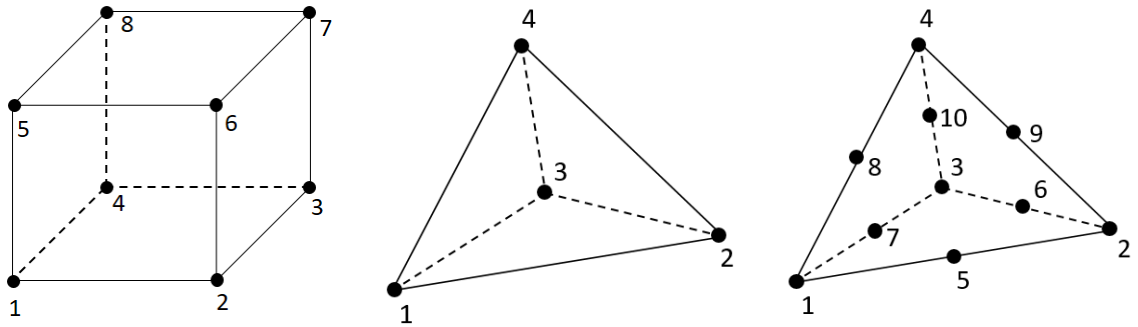


Figure 5.12 Illustrations of mesh element types: (a) the first-order hexahedral element C3D8, b) the first-order tetrahedral element C3D4 and (c) the second-order tetrahedral elements C3D10.

In this research, several attempts were conducted to apply hexahedral elements, such as eight-node linear brick elements (C3D8) (as seen in Figure 5.12a) and twenty-node quadratic brick elements

(C3D20). These were relatively straightforward to apply on the cylindrical inner part due to its simple geometry and highly challenging and time-consuming for the lattice outer part given its complex internal geometry. Therefore, the meshing type will not be particularly discussed in this study.

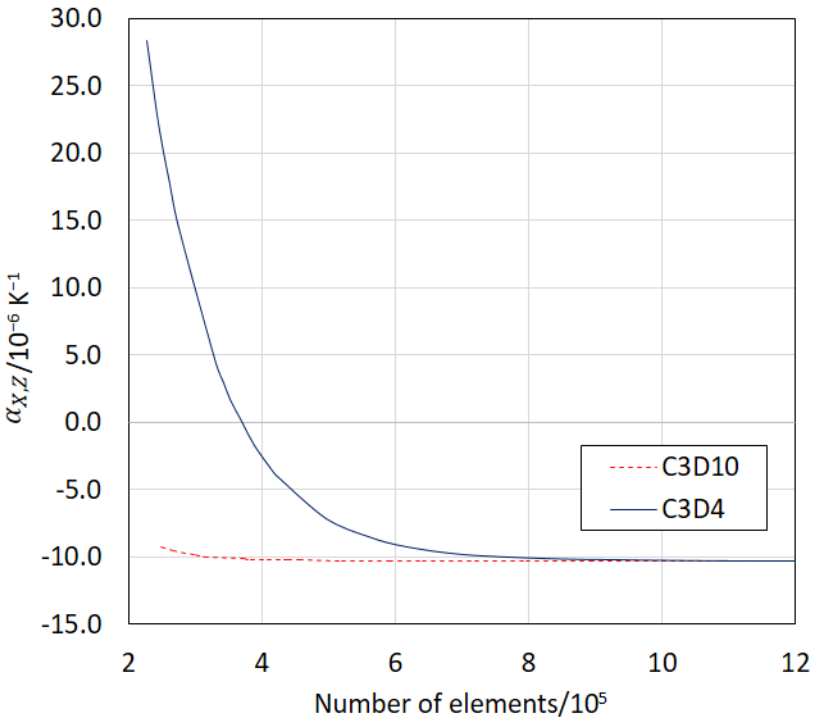
Two types of tetrahedral elements were applied: four-node linear tetrahedron elements (C3D4) and ten-node quadratic tetrahedron elements (C3D10), as shown in Figure 5.12b and Figure 5.12c, respectively. C3D4 elements are described as elements that only contain corner nodes (first-order), while CD10 are described as elements that contain both corner nodes and mid-side nodes (second-order). The polynomial functions presented in Equations 5.1 and 5.2, describe the behaviour of the displacements of the first-order and second-order tetrahedron elements, respectively.

$$P(x) = ax + b \tag{5.1}$$

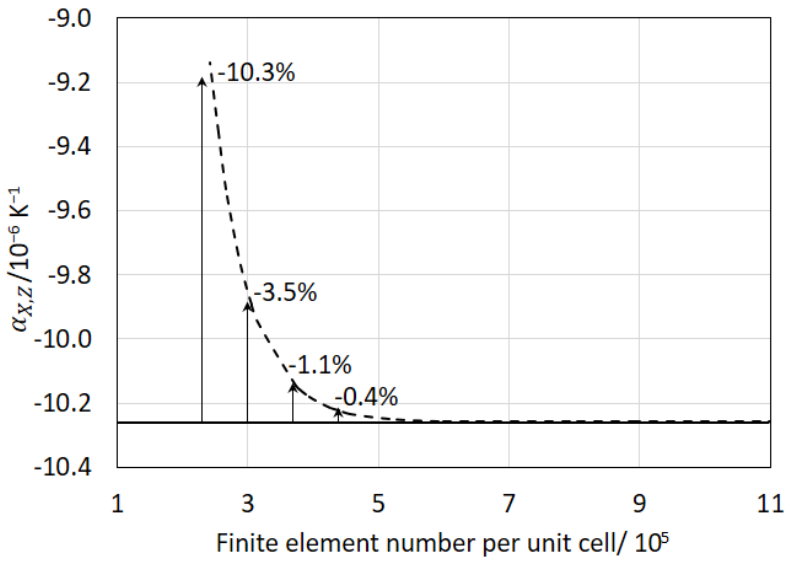
$$P(x) = ax^2 + bx + c \tag{5.2}$$

where, x is the position of the node and a, b and c are constant.

To investigate C3D4 and CD10 elements, the number of tetrahedral elements per unit cell was increased from 200,000 to 1,200,000 within a range of the in-plane CTE results (-15.0×10^{-6} K^{-1} to 30.0×10^{-6} K^{-1}), as shown in Figure 5.13a. For C3D10, a mesh density of 440,000 elements per unit cell was sufficient to determine the CTE of the lattice with a deviation of less than −0.4 % from the 1,200,000 element result, indicating that the result is well converged, as seen in Figure 5.13b. As for C3D4, CTE determination required about 930,000 elements, with a deviation of −0.54 % from the 1,200,000 element result, as shown in Figure 5.13a.



(a)



(b)

Figure 5.13 Finite element mesh density convergence for the low-CTE lattice cell: (a) comparison between C3D4 and C3D10, and (b) C3D10 and their deviations [124].

In accordance with the presented results, C3D10 elements were chosen for meshing due to the high degrees of complexity of the lattice outer part. Two geometries were meshed separately: the lattice outer part and the cylindrical inner part. A mesh density was assigned uniformly to the cylindrical inner part, while the outer part was assigned two different mesh densities.

5.4. Discussion of finite element simulation of lattice structures

Defining surface-to-surface contact between the outer part and the cylindrical inner part of a lattice structure is the core deformation mechanism to control lattice structure's CTE. By default, Abaqus/Standard contact pairings employ a pure master-slave contact algorithm, where nodes on the slave surface are unable to penetrate the segments on the master surface [130], as demonstrated in Figure 5.14. The algorithm places no restrictions on the master surface; it can penetrate the slave surface between slave nodes [134]. Since equal mesh densities were assigned to the innermost surfaces of the lattice outer part and the outermost surface of the cylindrical inner part, the second rule was applied by setting the lattice outer parts as master surfaces and the cylindrical inner part as the slave surface. In reality, this assignment helps prevent the following situation: when two materials crash, the softer one experiences damage first, UHMWPE (the slave).

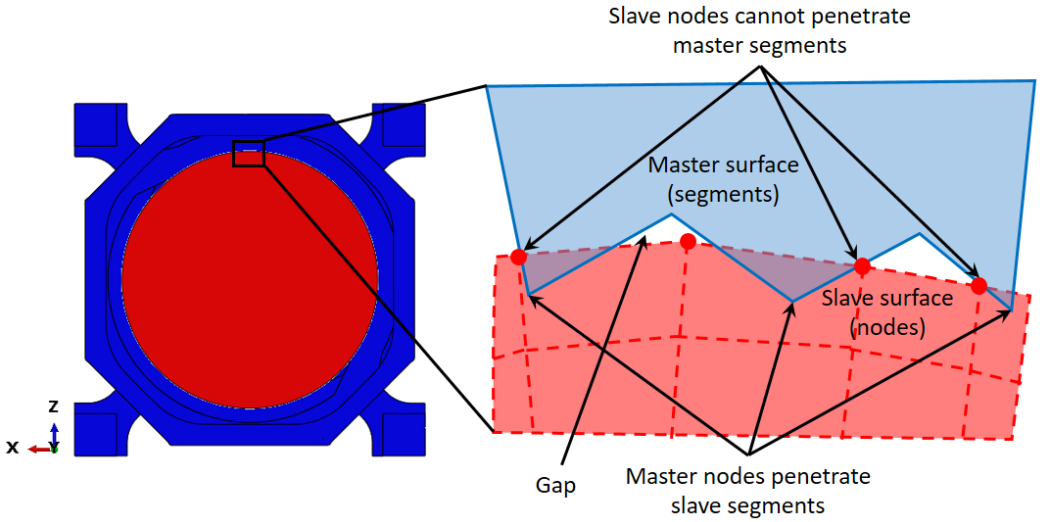


Figure 5.14 Illustration of contact properties between a master surface and a slave surface.

Creating partitions for mesh density reduction can significantly decrease the mesh density of the lattice structure. In Iteration 4.1, mesh density was reduced from 2,468,572 tetrahedral elements to 417,129 tetrahedral elements. This reduction in mesh density was predominantly observed in the lattice outer part, as seen in Figure 5.10. Compared to the lattice structure without partitions, the lattice structure with partitions showed a reduction in mesh density of about six times. Table 5.5 shows that the required RAM and ROM to simulate the lattice structure without partitions were, respectively, about four times and seven times larger than the lattice structures with partitions. Moreover, the lattice structure without partitions took approximately nine times the required CPU period to simulate the one without partitions.

Table 5.5 The required RAM, ROM and total CPU time for Iteration 4.1 with and without partitions.

Criteria	Required RAM/ MB	Required ROM/ MB	Total CPU time/ hr
Without the partitions	9,668	121,887	151.1
With the partitions	2,378	17,588	16.0

Various FE simulations were performed to study the effects of element type on the CTE of the lattice. Figure 5.13 shows that even at the lowest number of elements (about 200,000 elements), C3D10 achieved a mesh density convergence with a deviation of only −10.3 %, compared to C3D4 results, which showed a much larger deviation. In addition, even with a mesh density two times coarser, C3D10 achieved comparative results to those attained by C3D4. According to Equations 5.1 and 5.2, second-order elements (C3D10) can have curved edges, whereas the edges of first-order elements (C3D4) must remain straight. Therefore, second-order elements were preferred over first-order elements due to their superior accuracy and efficiency.

5.5. Conclusion

In the thermal expansion simulation, BC1 boundary conditions were considered to be sufficiently appropriate to examine the lattice structure's CTE, as they constrained all the nodes laying on three cubic edges of the lattice. In other words, the nodes on the surfaces of the YZ plane, XZ plane and XY plane have each become individually symmetrical about the following axes respectively: the -X direction, the -Y direction and the -Z direction, as seen in Figure 5.1. The CTE of the lattice structure was calculated by examining the displacement change of the nodes on the surfaces opposite to those constrained.

Creating partitions with equal mesh densities to examine surface-to-surface contact could be employed to control the number of master and slave nodes to simulate thermal expansion and calculate mesh convergence. Creating partitions for mesh density reduction could help minimise computational cost and time.

The type of the employed mesh is another critical parameter to consider. C3D10 were chosen as mesh elements in conformity with the high degrees of complexity of the lattice outer part. C3D10 were able to achieve satisfactory results with a mesh density nearly two times coarser than that utilised with C3D4 elements.

6. Lattice structure thermal expansion experiments

This chapter describes the thermal expansion experiments that have been developed and conducted, regarding the flowchart of the thermal expansion experimentation processes for lattice structures (as defined in Subchapter 3.4). Lattice structures typically need to be bigger than solid material specimens. The unavailability of commercial thermal expansion testing machines that could measure the designed lattices with the size of (50 × 50 × 50) mm was found, resulting in inventing an in-house thermal expansion measuring machine using an interferometer. In this chapter, the final development of the thermal expansion experimentation will be presented. First, method for thermal expansion experimentation for lattice structures is described. Second, the selected experimental hardware, including the heating system, laser interferometer system and thermal expansion experimental frame, are introduced. Third, the experimental correction and uncertainty are discussed. Then, the experimental validation and thermal expansion results are presented. Finally, the thermal expansion results are discussed, and a conclusion is drawn.

6.1. Method for thermal expansion experimentation for lattice structures

This experiment took place at the Manufacturing Metrology Laboratory in the Advanced Manufacturing Building, University of Nottingham. In this subchapter, the steps of the creation of a thermal expansion measuring machine and its usage for experimentation, referring to Chapter 3, are described:

Step 1: Identify the need for the equipment or machine – A thermal expansion measuring machine was needed to measure the thermal expansion of the lattice structures. The expected thermal expansion of reference materials and specimens in temperature changes of 4 °C is between 2×10^{-6} m and 35×10^{-6} m. The required resolution of the displacement measuring system (DMS) was 1×10^{-8} m, while the resolution of the heating source was one degree Celcius when operating between room temperature and 40 °C.

Step 2: Select a possible system and its mechanisms – As described in Step 1, two main systems were needed: heating and displacement measuring systems. The heating system was used to heat the lattices from the bottom, while DMS measured the displacement change from the top of the lattices. The heating system was divided into two parts: a heat source and a temperature measurement system. A hot plate from Cole-Parmer was selected to be the heating source. The temperature measurement system consisted of two main parts: a set of thermocouples and a data logger. In this experiment, two units of TC-08 thermocouple data loggers were selected to measure a wide range of

temperatures with 16 units (channels) of RS PRO Type K thermocouples. Specifications of the hot plate, the data logger and the thermocouple are presented in Table 6.1, Table 6.2 and Table 6.3, respectively.

Table 6.1 Specifications of Cole-Parmer StableTemp Ceramic Top Hot Plate [135].

Attribute	**Value**
Top Plate Length and Top Plate Width / cm	18.4
Top Plate Width/ cm	18.4
Top Plate Material	Ceramic
Min Temperature/ °C	30
Max Temperature/ °C	540
Temperature resolution/ °C	1
Max Load Capacity/ kg	4
Hot Plate Height/ cm	9.7

Table 6.2 Specifications of Pico Technology USB TC-08 Temperature Data Logger [136].

Attribute	**Value**
Sensor Type	B, E, J, K, N, R, S and T
Number of Input Channels	8
Maximum Temperature Measurement/ °C	+1200 (J), +1300 (N), +1370 (K), +1760 (S), +1820 (B), +400 (T) and +910 (E)
Temperature Measurement Resolution/ °C	0.025
Model Number	USB TC-08

Table 6.3 Specifications of RS PRO Type K Thermocouple [137].

Attribute	**Value**
Materials	Nickel Chromium and Nickel Aluminium
Temperature range/ °C	−75 to +250
Thermocouple Type	Type K
Probe Diameter/ mm	1/0.2

Regarding DMS, two systems were considered: a CCD camera and a laser interferometer. In general, interferometers offer a much higher resolution 1×10^{-9} m than CCD cameras 1×10^{-6} m [5]. Accordingly, a laser interferometer system was selected. The Renishaw XL-80 laser interferometer with its environmental compensator (XC-80) was selected to measure the thermal expansion of the specimens. The laser provides a linear resolution of 1 nm. The environmental compensator was used to measure the changes in the environment: air temperature, air pressure, air humidity and material temperature. Specifications of the Renishaw XL-80 laser system are shown in Table 6.4.

Table 6.4 Specifications of the Renishaw XL-80 laser system [138, 139].

Attribute	**Value**
XL-80 laser kit; laser frequency accuracy	± 0.05 ppm over three years is achieved by thermal control of the laser tube's length within nanometres.
XL-80 laser kit; linear measurement accuracy	± 0.5 ppm over the whole environmental range, i.e., from 0 °C − 40 °C and 650 mbar − 1150 mbar. Readings can be taken at up to 50 kHz, with a maximum linear measurement speed of 4 m/s and a linear resolution of 1 nm, even at maximum speed.
XL-80 laser kit; linear measurement range/ m	0 – 80
XL-80 laser kit; XL-80 laser dimensions/ mm × mm × mm	214 × 120 × 70
XL-80 laser kit; XL-80 laser weight/ kg	1.85
XC-80 compensator kit; compensating and operating range	0 °C – 40 °C for air temperature, 650-1150 mbar air pressure, 0 − 95% RH for air humidity and 0 °C – 55 °C for material temperature
XC-80 compensator kit; accuracy	± 0.2 °C for air temperature, ± 1 mbar for air pressure, ± 6% RH for air humidity and ± 0.1 °C for material temperature
XC-80 compensator kit; XC-80 compensator weight/ kg	0.49

Step 3: Analysis of forces – As described in Subchapter 3.4 Step 3, the only occurring forces were the weight of the measuring equipment and the structure itself. The mass of the XL-80 laser interferometer was 1.85 kg, which resulted in a negligible force compared to the weight of the metal structure. Therefore, there was no need to account for the weight of the interferometer.

Step 4: Selection of materials – Aluminium was selected for all components in the whole frame as well as for the fixtures in the experimental set-up, to avoid thermal misalignment in the system. Using the same material (same coefficient of thermal expansion) helped the researcher easily calculate the thermal expansion of the system, as presented in Subchapter 2.2.1.

Step 5: Design of elements – The thermal expansion measuring machine and its mathematical model were developed gradually. In the final development stage, many principles were involved in achieving an acceptable thermal expansion state, such as a kinematic design for the interferometer, structural symmetry, etc. Details will be provided in Subchapter 6.2.

Step 6: Modification – All structural members of the frame were commercial aluminium extrusions with a cross section of (30 x 30) mm, as shown in Figure 6.1. Brackets, screws and nuts were appropriately selected according to the size of the structural members and procured from an industrial supplier. Their detailed drawings were created using SolidWorks version 2018 and modified in the next step to create customised parts, such as kinematic design components. After selecting and

modifying components, a final assembly of the designed system was created using SolidWorks version 2018, as shown in Figure 6.1.

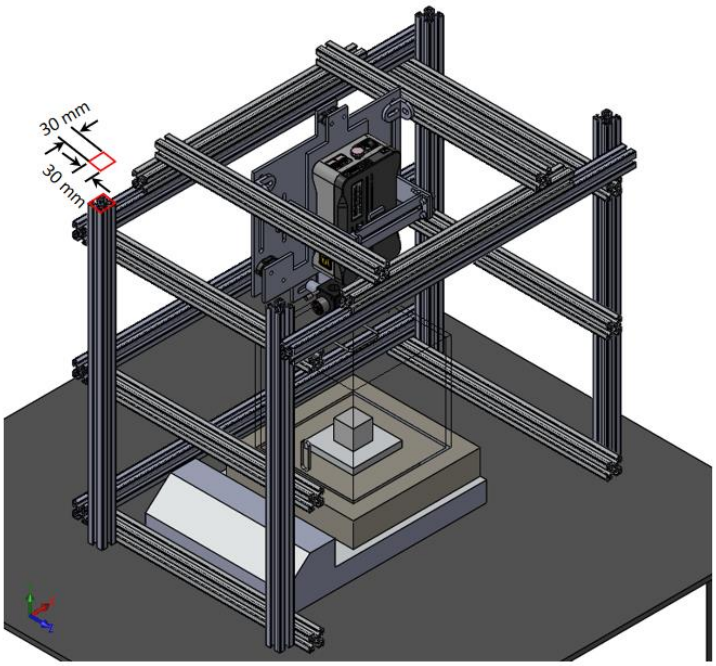
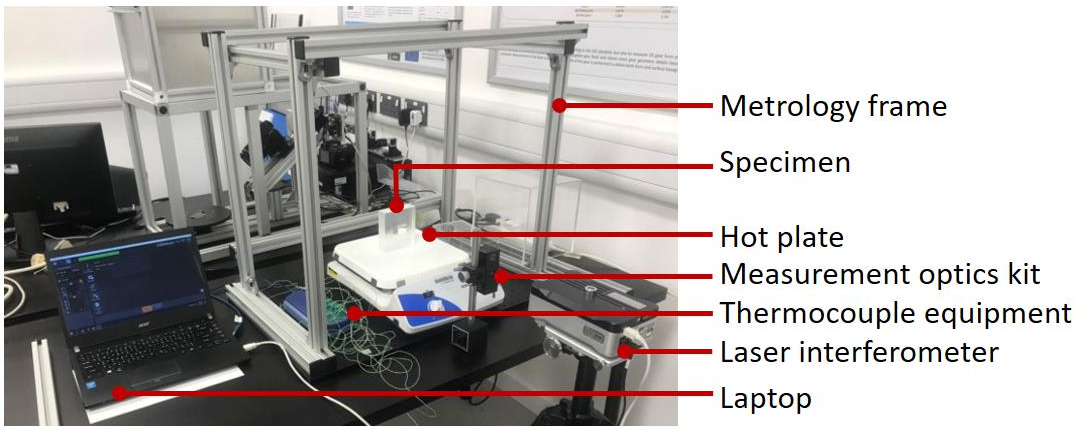
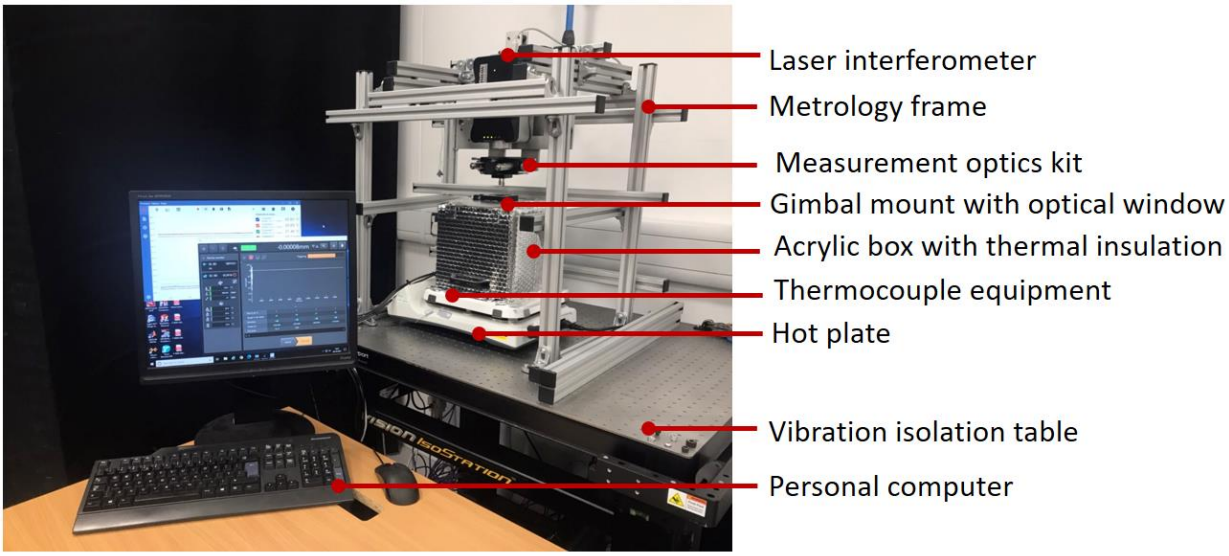


Figure 6.1 Final assembly of the thermal expansion experimental set-up using aluminium extrusions with a cross-section of (30 x 30) mm.

Step 7: Production – Some parts were ordered from industrial suppliers, such as members and their joints, while some others, which could not be found in the market, were manufactured at the L2 Engineering Applications Workshop, University of Nottingham. All components were hand assembled into one machine (as seen in Figure 6.2).



(a)



(b)

Figure 6.2 The thermal expansion experimental set-up: (a) the first development and (b) the final development.

Step 8: Experimental procedure design – Hardware parts were designed, manufactured and assembled in the previous steps. This step involved using two pieces of software to record all temperature and displacement data during the entire period of the experiment. Details of the two software packages are as follows:

- PicoLog 6 was the software used for the Pico Technology TC-08 data logger. It provides a visual, easy-to-use interface allowing a quick set-up, simple acquisitions, in addition to the possibility to record, view and analyse data. It can measure up to eight channels at a time, and it can also be combined with another TC-08 data logger to access more channels on the same personal computer (PC).
- CARTO Capture was the software used to operate alongside the Renishaw XL-80 laser interferometer for displacement measurement. Displacement data can be measured and

automatically corrected when the environmental compensator is installed. The environmental compensator (XC-80) is used to correct the displacement data in real-time in response to changes in the environment (the air refractive index): air temperature, air pressure, air humidity and material temperature.

In this research, the sampling rate for all software was 10 seconds, which was sufficient for all measurements. The temperature changes were measured in four increments (30 °C, 31 °C, 32 °C, 33 °C and 34 °C) to obtain accurate trends. The final experimental procedures to measure specimen CTEs are listed as follows:

Step 1: Switch on all devices: the PC, the hot plate and the Renishaw XL-80 laser interferometer. Run two software packages on the PC: PicoLog 6 and CARTO Capture.

Step 2: Open the front door of the acrylic box. Then, install the thermocouples onto a specimen and place the specimen on top of the aluminium plate and under the interferometer's laser beam, as shown in Figure 6.3.

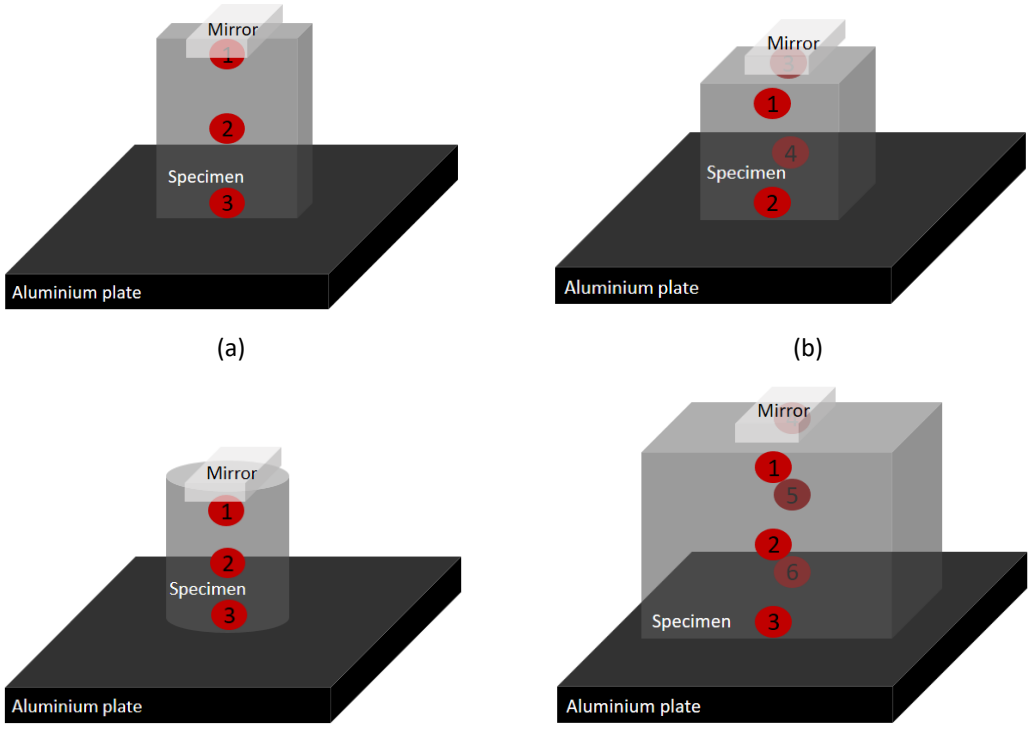


Figure 6.3 Illustration of the positions of the thermocouples and the mirror for (a) steel gauge blocks, (b) the nylon 12 lattice outer part, (c) the UHMWPE cylindrical inner part and (d) Iterations 2.4 and 3.1.

Step 3: Place an optical mirror on top of the specimen. Then, align the laser beam, mirror and optic lens as shown in Figure 6.4. Close the acrylic box's front door. Lights on the

interferometer indicated whether the components were aligned by four or five green lights, while red or yellow lights indicated a poor signal. In CARTO Capture, the sensor status bar also indicated the status of the interferometer: sensor connected and sending data (green), sensor not connected (grey), and sensor connected but a fault detected (red).

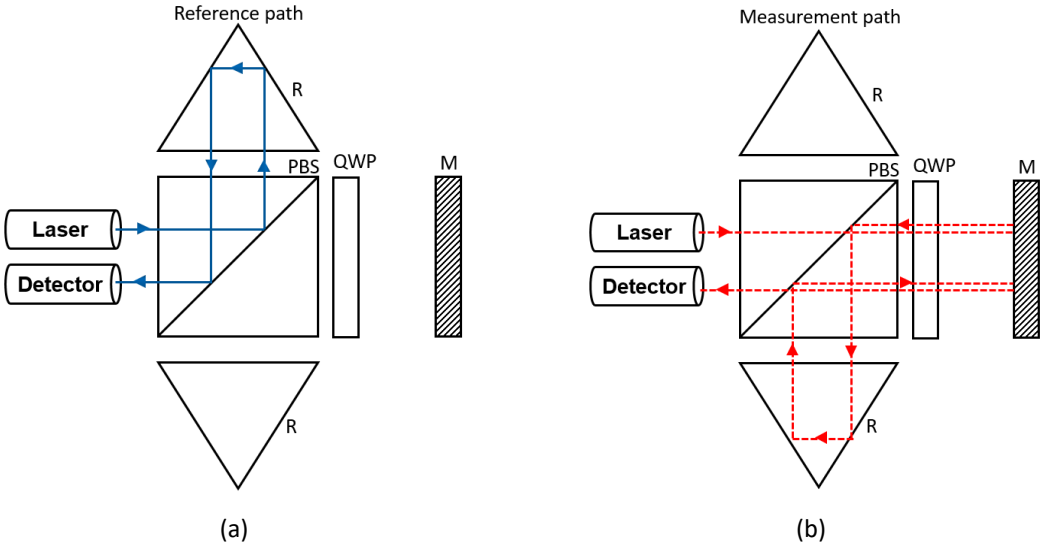


Figure 6.4 Plane mirror interferometer path set-up: (a) reference path and (b) measurement path, where R is the retroreflector, QWP is the quarter wave plate, PBS is the polarisation beam splitter, and M is the optical mirror.

Step 4: This involved the preheating process of the experiment. The hot plate was heated up to 30 °C for at least an hour or until the temperature of the specimens reached steady state.

Step 5: Measure and record all data (displacements and temperatures) via software packages. Manually change the hot plate temperature from 30 °C to 31 °C, 32 °C, 33 °C, then 34 °C, respectively. Figure 6.5 and Figure 6.6 show the interfaces of PicoLog 6 and CARTO Capture during the experiment, respectively. Each pattern duration coincided with the thermal steady state of the specimens, as shown in Table 6.5. Pattern 1 was followed for the 40 mm steel gauge blocks, 50 mm steel gauge blocks, 60 mm steel gauge blocks, the Nylon 12 lattice outer part and the UHMWPE cylindrical inner part. Pattern 2, with a longer duration, was used for 1 × 2 × 1 lattices of (50 × 50 × 50) mm unit cells of Iterations 2.4 and 3.1.

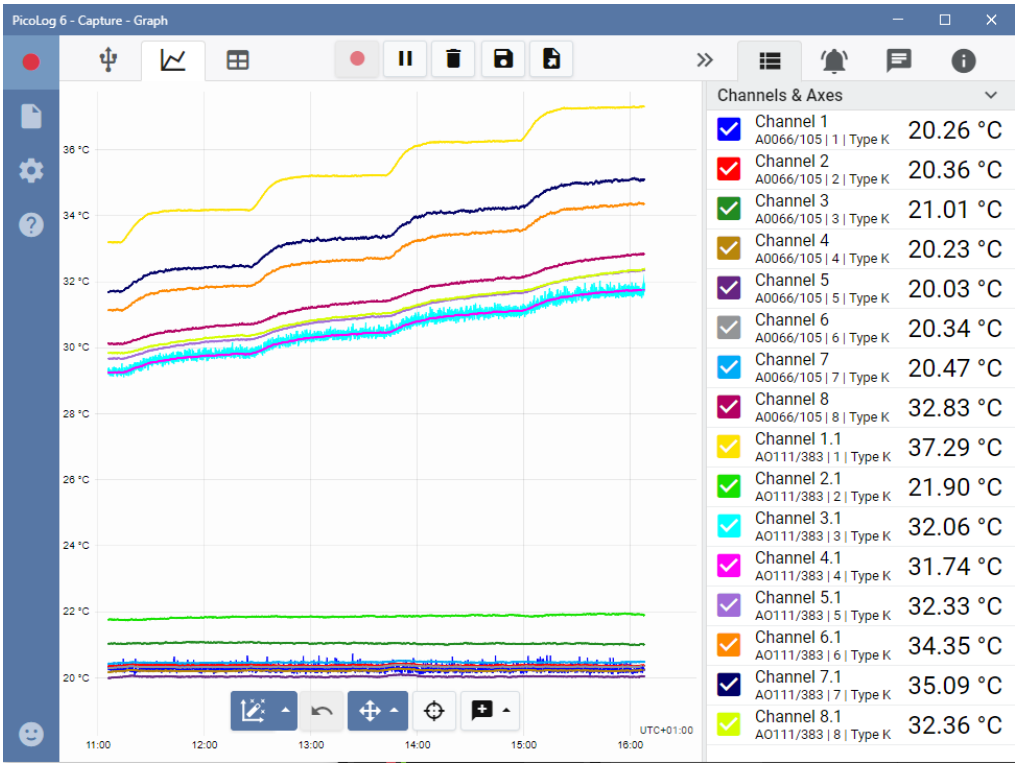


Figure 6.5 Interface of PicoLog 6 during the experiment.

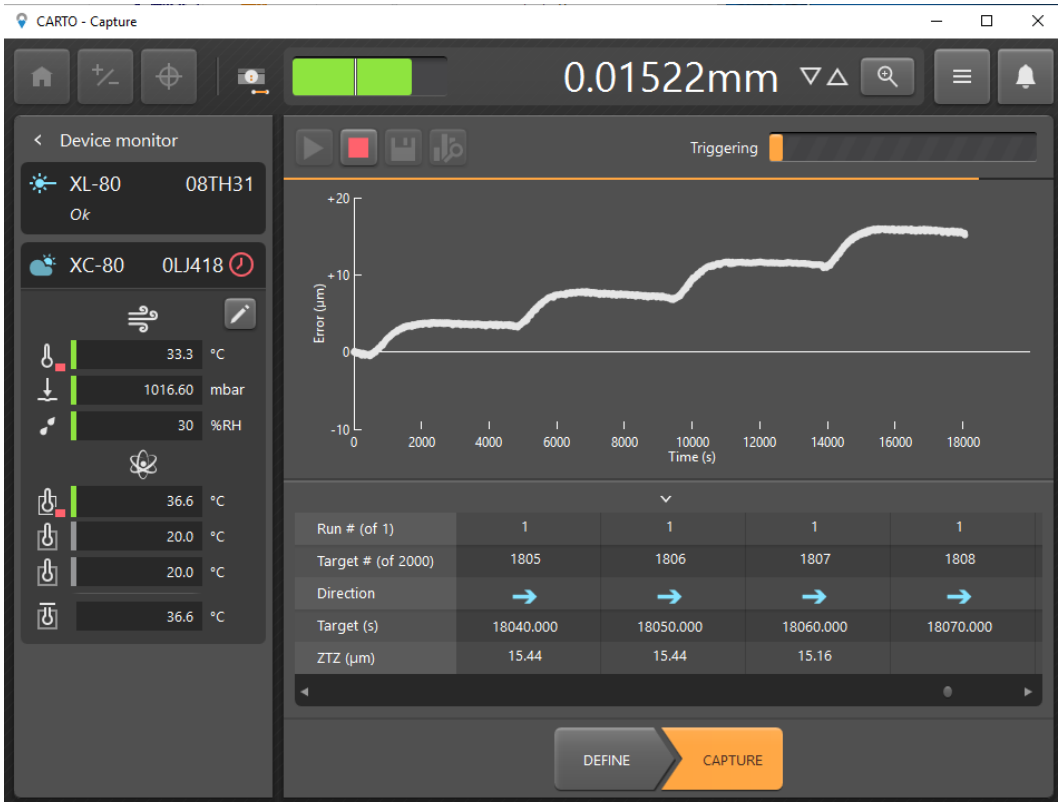


Figure 6.6 Interface of CARTO Capture during the experiment.

Table 6.5 Duration of the thermal expansion experimentation of the specimens.

Hot plate temperature/ °C	Pattern 1		Pattern 2	
	Time/ H:MM	Duration/ minutes	Time/ H:MM	Duration/ minutes
30	0:00 - 0:05	5	0:00 - 0:05	5
31	0:05 - 0:45	40	0:05 - 1:20	75
32	0:45 - 1:25	40	1:20 - 2:35	75
33	1:25 - 2:05	40	2:35 - 3:50	75
34	2:05 - 2:45	40	3:50 - 5:05	75

Step 6: Analyse all data with reference to the equations of thermal expansion of each of the metrology frame, the hot plate and the measured unknown. Then, calculate the structure's CTE. Details are described in Subchapter 6.3.

Step 7: Open the front door of the acrylic box. Take out the mirror and the specimen, then put the specimen back on top of the aluminium plate.

Step 8: Repeat Steps 3 through 7 (at least three times) to collect sufficient data to be plotted.

Step 9: Experimental validation – Steel gauge blocks with highly precise dimensions were used as reference materials. The gauge blocks were selected for three different sizes (lengths): 40 mm, 50 mm and 60 mm. Results from the experiment showed that an error of about ± 2 % error was produced compared to the reference data (CTE of 11.5×10^{-6} [4]), which was acceptable.

Step 10: Acceptation of the experimental procedure – The machine was accepted, and the uncertainty of the system was determined. The machine was then used to test lattice structures with unknown CTEs.

Step 11: Test specimens – The specimens (the Nylon 12 lattice outer part, the UHMWPE cylindrical inner part, the 1 × 2 × 1 lattice of (50 × 50 × 50) mm unit cells of Iterations 2.4 and 3.1) were carefully tested following the experimental procedures from Step 8 onwards. Results will be discussed in Subchapter 6.5.

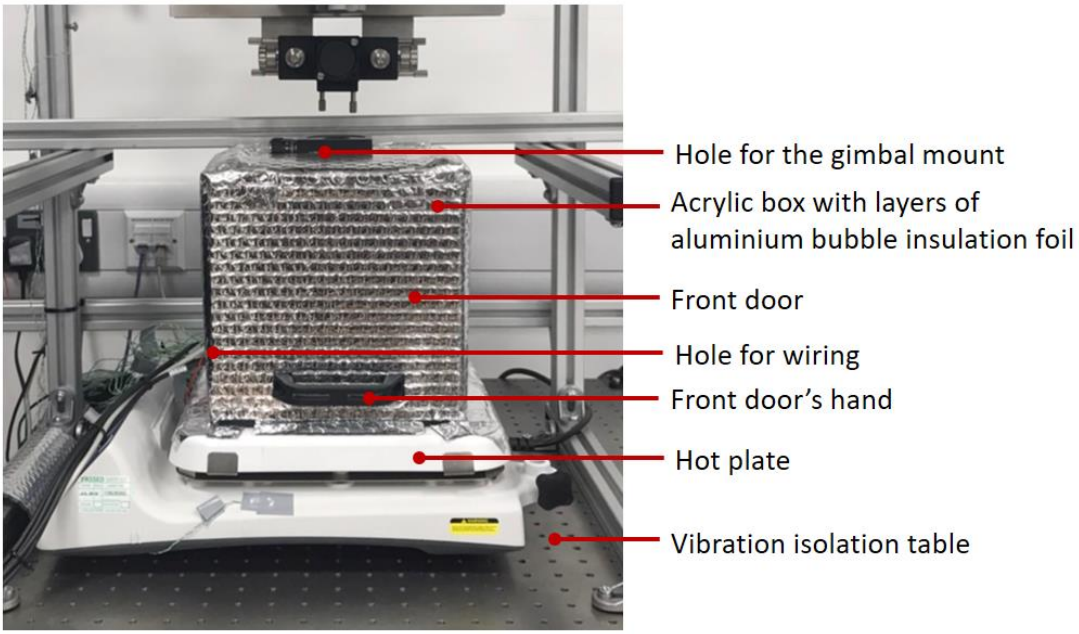
6.2. Experimental hardware design

The components of the thermal expansion experiment were divided into three main groups: the heating system, the displacement measurement system and the thermal expansion experimental frame. Other components, such as the vibration isolation table and the PC and its components (as shown in Figure 6.2), were excluded from these groups. The vibration isolation table was used to isolate vibration noise from the surrounding workspace. The PC and its components were used to

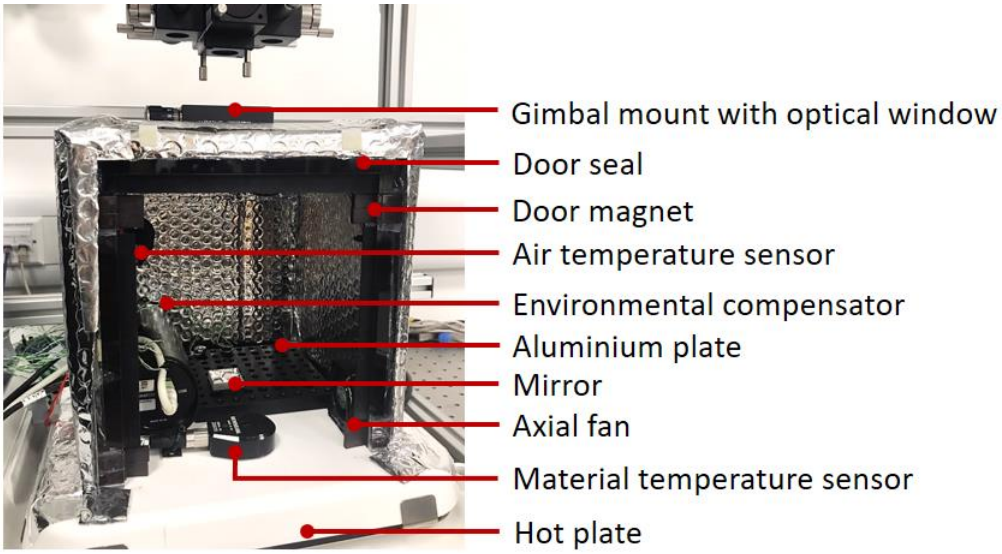
collect data from the interferometer system (displacement, air temperature, air pressure and air humidity) and from the data loggers (temperature).

6.2.1. Heating system

The Cole-Parmer StableTemp Ceramic Top Hot Plate was selected as a heating source in the experiment and placed on top of three hex head bolts installed on the vibration isolation table. The three bolts were used to adjust the height of the hot plate. An aluminium plate was placed on the top surface of the hot plate to stabilise the heat generated by the hot plate. A (200 × 200 × 200) mm acrylic box was placed and adhered to the top surface of the hot plate, as shown in Figure 6.7. The acrylic box was fitted with three layers of aluminium bubble insulation foil, two of which were placed outside and one was placed inside, to insulate the box from inside and outside air, and keep the temperature inside it constant. The environmental compensator (a device that is used to improve the measurement accuracy of the laser interferometer XL-80), including their air and material temperature sensors and a (40 × 40 × 10) mm axial fan, were placed inside the acrylic box. The environmental compensator and its sensors were used to compensate the wavelength of the laser beam for changes in air temperature, air pressure and relative humidity. The fan was used to stir the air inside the acrylic box to reduce temperature gradient due to the vertical air currents. Two holes and one door were manufactured on the acrylic box. One square hole was cut on top of the acrylic box to place the gimbal mount with an optical window and prevent air turbulence by separating the air inside and outside the acrylic box. A second hole was cut on the side of the acrylic box to drive cables outside the box. The front door of the acrylic box was used for placing specimens to be examined, specifically on top of the aluminium plate.



(a)



(b)

Figure 6.7 Experimental set-up of the heating system.

6.2.2. Laser interferometer system

The laser interferometer (Renishaw XL-80 laser), as illustrated in Figure 6.8, was placed above the heating system while the laser beam pointed down towards the mirror targeted at the specimen (single path technique), as shown in Figure 6.7. Kinematic design principles (as described in Subchapter 2.2.4) were applied to improve the accuracy and stability of the laser interferometer. The kinematic design of this system consisted of three sets of kinematic seats (KBS98, Thorlabs) arranged in a triangular pattern on the customised kinematic seats boards, as seen in Figure 6.9. Each kinematic seat set was composed of two plates: bottom and top. The bottom plate had a V-groove slot mounted

on the bottom kinematic seat board. The top plate had an insert ball that sat on the V-groove of the bottom plate and was mounted on the top kinematic seat plate. The three axes defined by the V-grooves intersected at a common point to maximise the system's stability. Each kinematic seat has a magnet, providing a holding force of about 44.14 N (generated by a mass of 4.5 kg) [140]. The measurement optics kit was also mounted on the bottom kinematic seat board. The laser interferometer was installed on the top kinematic seat board while the bottom kinematic seats board was attached to the metrology frame.

Additionally, a leaf spring was installed on the body of the interferometer using a fixture, to provide an extra holding force for the laser interferometer. The leaf spring acted as a flexure hinge [141], allowing the laser interferometer to move only along the Z-axis, as shown in Figure 6.8. All customised boards were made of aluminium, being the same material as the metrology frame and the body of the laser interferometer, which helped minimise thermal error sources [6].

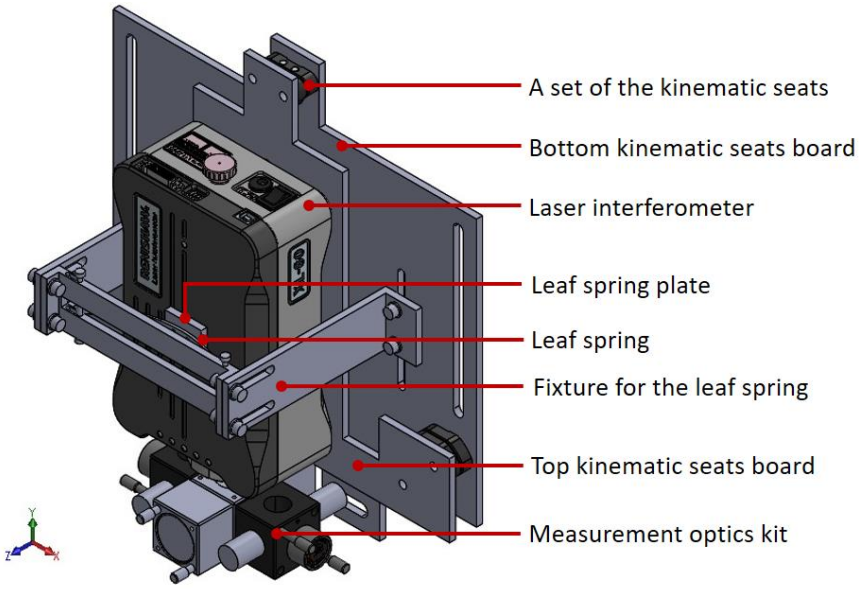


Figure 6.8 Schematic representation of the laser interferometer system.

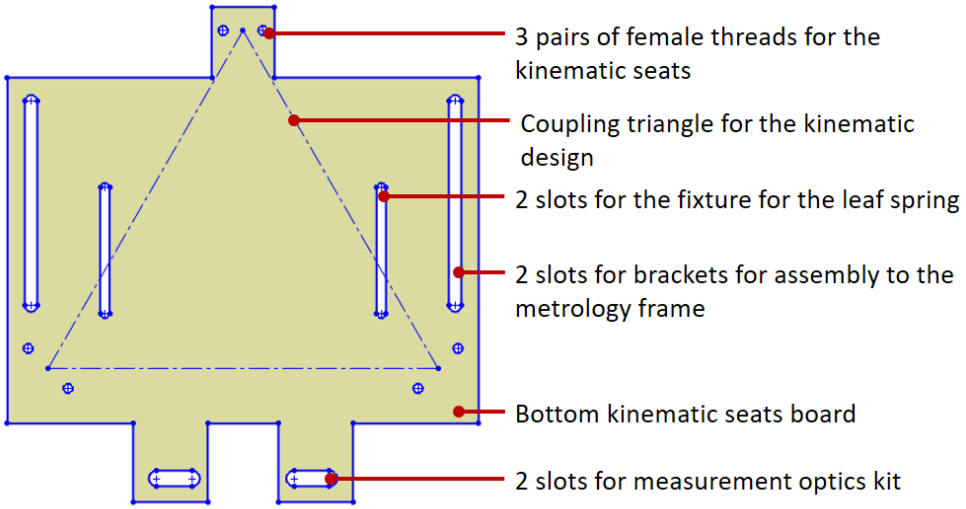
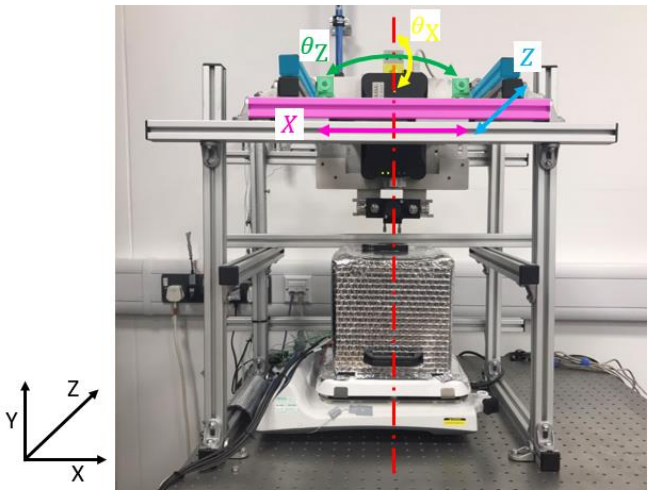


Figure 6.9 The bottom kinematic seat board.

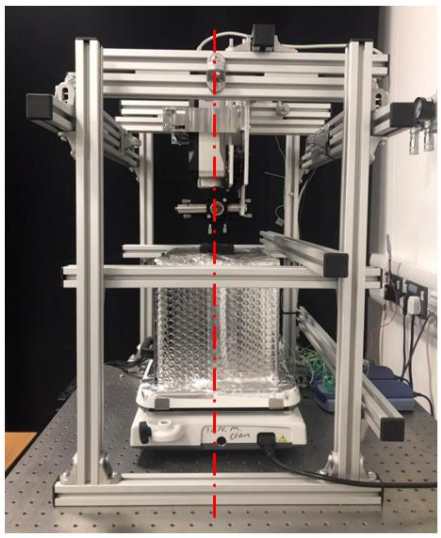
6.2.3. Thermal expansion experimental frame

The metrology frame was constructed as a closed section frame (as discussed in Subchapter 2.2.3) with the concepts of high rigidity and symmetry, as shown in Figure 6.10. The heat sources of the thermal expansion measuring machine were the laser interferometer and the hot plate, and the heat sources were positioned at the machine's centre following the thermal centre principle. The symmetrical concepts considered in this experiment included symmetry in geometry, heat transfer, thermal capacity, and coefficient of thermal expansion (CTE). These design concepts can reduce thermal deformation in the frame along the vertical axis [14]. However, temperature fluctuations, even in controlled laboratory environments, can cause alignment drift in high-precision measuring machines. Therefore, a mathematical model was applied to correct for unwanted thermal expansions during the experiment, which will be described in Subchapter 6.3.

In addition, washers were included in all member connections to prevent any loosening between screws and nuts [142]. Levelling was required for the vibration isolation table, the hot plate, the metrology frame, and the laser interferometer. Levelling helped align the laser beam of the displacement measurement equipment during the course of the experiment.



(a)



(b)

Figure 6.10 Illustration of the thermal expansion measuring machine: (a) front view and (b) side view, which can be adjusted by the laser interferometer system in multi-movement: X is the translation in the X-axis, θ_X is the rotation around the X-axis, Z is the translation in the Z-axis, θ_Z is the rotation around the Z-axis and the dashed dotted lines represent lines of symmetry in the Y-axis.

6.3. Experimental correction and uncertainty

The results yielded by the thermal expansion measuring machine were the displacement and temperature changes of the specimens, which were used to calculate their CTEs. In this research, all uncertainty calculations followed internationally accepted guidelines founded in GUM: Guide to the Expression of Uncertainty in Measurement [143].

In measurement uncertainty, measurement errors can be classified into two types: random and systematic, as shown in Figure 6.11. Type A refers to measurement uncertainty evaluations from a

statistical analysis perspective, where measured data, such as the standard deviation in a series of measurements, are examined [143]. Type B refers to measurement uncertainty evaluations resulting from other sources, such as the calibration uncertainty of a used physical reference specimen and the published uncertainty of a physical constant [143]. Type B can be divided into two groups: known and unknown. The known systematic error can be used to correct measurement results, for example, changes in the refractive index of air or thermal effects on the metrology frame. However, uncertainties still exist despite these corrections, and unknown systematic errors are included in the measurement uncertainty as a standard deviation.

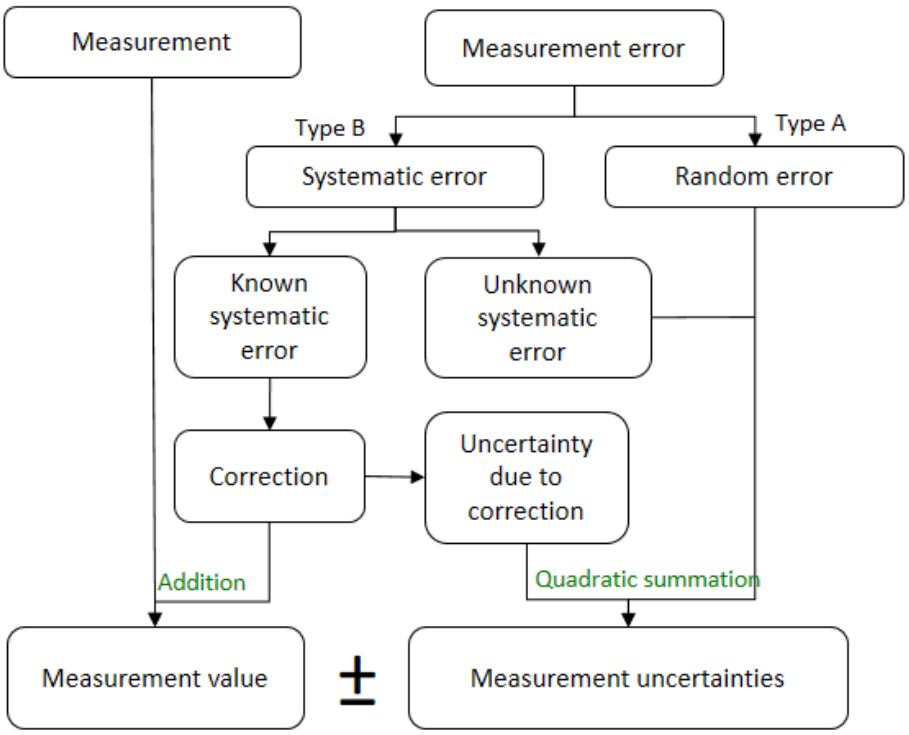


Figure 6.11 Schematic representation of the measurement and its errors.

To evaluate uncertainties in the thermal expansion measuring machine following the guide presented by Richard Leach [144], seven steps can be followed:

Step 1: Specify the measurement process.

Step 2: Identify the influencing quantities on the uncertainties.

Step 3: List any simplifying assumptions and their impact on the measurement.

Step 4: Form a mathematical model of the measurement in terms of the influencing quantities.

Step 5: Evaluate the sensitivity coefficients of the influencing quantities.

Step 6: Evaluate the standard uncertainties and degrees of freedom of the influencing quantities.

Step 7: Calculate the combined and expanded uncertainties and degrees of freedom for the overall process.

In the measurement procedure, a specimen with a plane mirror on top was placed on the aluminium plate inside the acrylic box. The hot plate heated the specimen. The interferometer measured the displacement change of the plane mirror along the Y-axis (as seen in Figure 6.12). Figure 6.12 shows schematic representation of the experimental set-up of the thermal expansion measuring machine with thermal loop and annotations of all components involved in the thermal loop. The influencing quantities were grouped and considered as presented in Table 6.6.

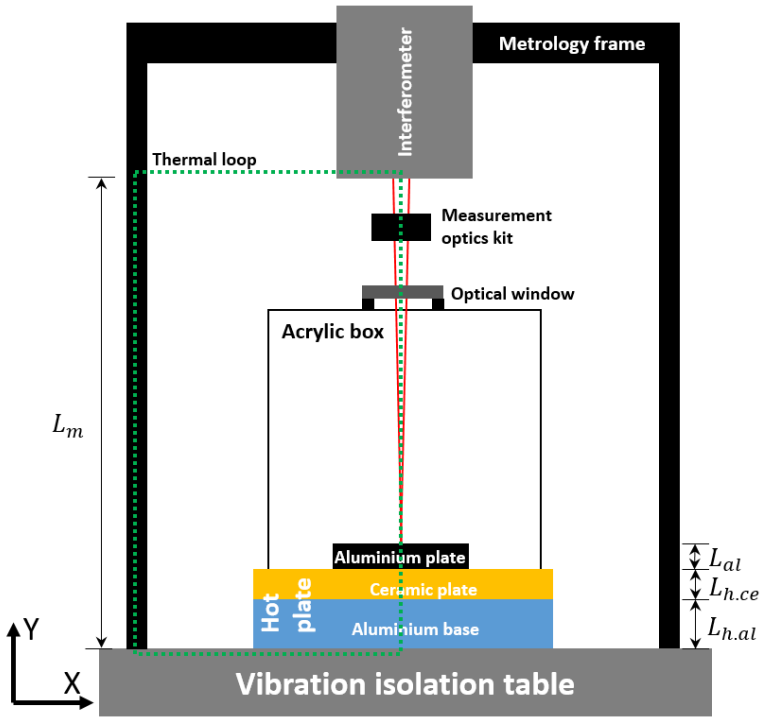


Figure 6.12 Schematic representation of the experimental set-up of the thermal expansion measuring machine.

Table 6.6 The influencing quantities considered in the experiment.

Source	Attribute
Laser source	• Short and long-term calibration • Frequency stability • Intensity stability • Intensity distribution • Wavefront characteristics • Polarisation
Interferometer characteristics	• Collimation/obliquity effects • Quality of the optical components • Stray beams • Diffraction effects • Dead path error • Air turbulence effects • Air refractive index • Interferometer noise
Metrology frame	• Thermal expansion • Coordinate orthogonality • Abbe error • Cosine error
Hotplate and aluminium plate	• Thermal expansion
Plane mirror	• Thermal expansion
Detection system	• Linearity of photodetectors • Electronic noise • Frequency response • Resolution
Computing/software	• Quality of mathematical fits and models • Timing errors

By identifying the specific characteristics of the measurement procedure and considering laboratory conditions, some of these influencing quantities could be considered negligible if the effect of an influencing quantity was less than 1×10^{-12} m which was diffractometer precision or it had been measured to be negligible. Besides, the final uncertainty in length measurements was specific for a strict range of conditions and techniques.

In an attempt to apply Step 3 to this experiment, there were no simplifying assumptions to be made with respect to the thermal expansion measuring machine. This experiment was conducted in an environment-controlled metrology laboratory, which meets the international standard: ISO/IEC 17025 General Requirements for the Competence of Testing and Calibration Laboratories [13] and was operated by an operator who was applying best laboratory practices.

The main influencing quantities taken into account are given in the schematic representation of the experimental set-up of the thermal expansion measuring machine, shown in Figure 6.12. The known systematic errors were the change in the refractive index of the air, thermal effects on the metrology frame, thermal effects on the hot plate (including the aluminium plate), thermal effects on the

experimental set-up, and dead path length. Random errors were the interferometer noise, the Cosine error and Abbe error. From these, the mathematical model of the measurement and its uncertainty can be formulated as presented in Subchapters 6.3.1 and 6.3.2:

6.3.1. Mathematical model of the measurement

The ideal measured value of displacement obtained by a Michelson interferometer is given by

$$L_\phi = \frac{\lambda}{2\pi}\Delta\phi \tag{6.1}$$

where λ is the wavelength of the laser source and $\Delta\phi$ is the difference in phase between the reference arm and measurement arm of the interferometer. The non-ideal measured value of displacement obtained by a Michelson interferometer is given by

$$L = L_\phi + L_n + L_f + L_h + L_u + L_d + L_i \tag{6.2}$$

where L_n is a correction due to a change in the refractive index of the air in which the laser operates, L_f is thermal effects on the metrology frame, L_h is thermal effects on the hot plate, L_u is thermal effects on the experimental set-up, L_d is the dead path length, and L_i is the measurement set-up, *i.e.,* Abbe and Cosine errors.

Correction due to changes in the refractive index of the air in which the laser operates

Air pressure, temperature and humidity, are the parameters that can change the refractive index of air, were determined throughout the duration of the experiment, using sensors of the XC-80 environmental compensator located in the acrylic box. The laser interferometer system could then automatically compensate linear readings for the effects entailed by changes in local atmospheric conditions [138]. The length correction that accounts for the refractive index of air is given by

$$L_n = -n \tag{6.3}$$

where n is the refractive index of air and can be found using either the Updated Edlén [145, 146] or the Ciddor equation [147]. The equations are established from the relationship of vacuum wavelength, air temperature, air pressure, humidity and carbon dioxide content.

Correction due to thermal effects on the metrology frame

During the experiment, the temperature of the metrology frame changed due to changes in the ambient temperature. To estimate the thermal expansion of the metrology frame in the vertical direction (the Y-axis shown in Figure 6.12), the average temperature change in the vertical structural member was measured and the length correction was calculated using

$$L_f = \alpha_m L_m \Delta T_m \tag{6.4}$$

where α_m is the CTE of the material of the metrology frame, L_m is the length of the metrology frame between the vibration isolation table and the laser interferometer beam head in the vertical direction, and ΔT_m is the average temperature change of the vertical structural member.

Correction due to thermal effects on the hot plate

The effects of the thermal expansion of the hot plate and the aluminium plate were accounted for in the displacement measurement system. The hot plate was divided into two parts: the aluminium base and the ceramic plate, as shown in Figure 6.12. The temperature change in the ceramic plate was assumed to be approximately equivalent to the average temperature change in both the hot plate and the aluminium plate. The temperatures of the aluminium base of the hot plate and the aluminium plate were measured and the thermal effects were corrected using the length correction given by

$$L_h = -\left(\alpha_{al} L_{al} \Delta T_{al} + \left(\alpha_{h.al} L_{h.al} \Delta T_h + \alpha_{h.ce} L_{h.ce} \Delta T_h\right)\right) \tag{6.5}$$

where α_{al} is the CTE of the aluminium plate material, L_{al} is the original length of the aluminium plate in the vertical direction, ΔT_{al} is the temperature change of the aluminium plate, $\alpha_{h.al}$ is the CTE of the aluminium base material, $L_{h.al}$ is the original length of the aluminium base in the vertical direction, ΔT_h is the temperature change of the hot plate, $\alpha_{h.ce}$ is the CTE of ceramic plate material and $L_{h.ce}$ is the original length of the ceramic plate in the vertical direction.

Correction due to thermal effects on the experimental set-up

The thermal expansions of each of the metrology frame, the hot plate, and the aluminium plate were corrected using the aforementioned equations. However, there are other materials, such as the components supported between the aluminium base and the ceramic plate, whose thermal expansion was not accounted for and cannot be included as part of the thermal effects on the metrology frame

and the hot plate. The thermal expansion of this experimental set-up was measured as a slope responding to the temperature change. The length correction is given by

$$L_u = -u\Delta T_{al} \tag{6.6}$$

where u is the CTE of a specific length of the experimental set-up, and ΔT_{al} is the temperature change of the aluminium plate.

Correction due to the dead path length

The dead path length is one of the error sources caused by installation. Dead path errors occur when a non-zero dead path and environmental conditions change during a measurement. The dead path length correction is given by [110]

$$L_d = d\frac{\Delta n}{n_2} \tag{6.7}$$

where d is the difference in distance in the air between the reference and measurement retroreflector and the beamsplitter, when the laser interferometer measurement is initiated, n_1 is the refractive index at the start of the measurement, n_2 is the refractive index at the end of the measurement, and $\Delta n = n_2 - n_1$.

According to Equation 7.7, the interferometer was moved as close to the zero position of the target as possible to reduce the dead path length. The dead path will drift the measured displacement by a specific length. However, this dead path contribution can be resolved by pre-setting the phase meter to zero.

Correction due to the measurement set-up

The Abbe error is defined from the measurement axis of the linear interferometer that is offset from the mounting surface. A plane mirror was used in this experimental set-up and placed on top of the specimens. There was no offset from the mounting surface, and therefore, the abbe error was equal to zero.

A Cosine error occurred in the experiment when the laser beam was not parallel to an axis measured by the interferometer. This misalignment error can cause by non-leveling of the interferometer and the plane mirror, due to the flatness of a specimen. Cosine errors cause interferometers to measure

shorter than the actual distance travelled. The length correction of the Cosine error for the plane mirror is given by [110]

$$L_i = \big(1 - cos(\alpha)cos(\beta)\big)L \tag{6.8}$$

where α represents the angle between the unit vector along the direction of the incident beam $\hat{\imath}$ and the unit vector $\widehat{N}$ (normal vector describing the orientation of the mirror along the angle α), and β represents the angle between $\widehat{N}$ and the direction of motion $\vec{D}$, as shown in Figure 6.13.

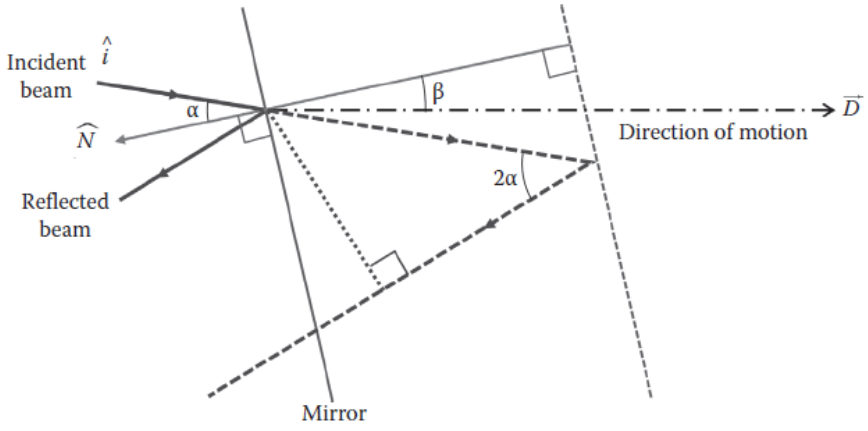


Figure 6.13 Misalignment parameters for a plane-mirror target from "Chapter 4 – Displacement Measuring Interferometry" of Handbook of Optical Dimensional Metrology [110].

From the experimental set-up in this thesis, α could be found with the assumption that the incident beam and the reflected beam of the interferometer (with a beam diameter of 7 mm) did not overlap about 20 % within the range of displacement between the laser interferometer head and the plane mirror. In this case, α was equal to 0.12° and β was assumed to be the same value as α. Therefore, L_i was equal to $4 \times 10^{-6}\ L$. This error had not been corrected in the non-ideal measured value of the displacement (Equation 6.2), therefore, it was included in the combined uncertainty of the displacement measurement system. However, it only had a minor effect on the measurement, due to the low expansions of the specimens' measured range (from zero to 31×10^{-6} m).

6.3.2. Standard uncertainties of the displacement measurement system

The combined standard uncertainty $u_c(L)$ is used to estimate the standard deviation of the distribution of possible length values L, measured using an interferometer. This value of uncertainty is found by summing in quadrature the standard uncertainties $u(x_i)$ of all influencing factors x_i, weighted by sensitivity coefficients. According to Section 5.1.2 of the GUM [143], the combined standard uncertainty can be written as

$$u_c^2(L) = \sum_{i=1}^{n} {c_i}^2\, u^2(x_i) + \sum_{i=1}^{N}\sum_{j=1}^{N}\left[\frac{1}{2}{c_{ij}}^2 + c_i c_{ijj}\right] u^2(x_i)u^2(x_j) \qquad 6.9$$

where the sensitivity coefficients

$$c_i = \frac{\partial L}{\partial x_i}, c_{ij} = \frac{\partial^2 L}{\partial x_i \partial x_J}, c_{ijj} = \frac{\partial^3 L}{\partial x_i \partial x_j^2} \qquad 6.10$$

are the partial derivatives of the mathematical model. Note that Equation 6.9 assumes that the input quantities are either independent or correlated. From Equation 6.9, the combined standard uncertainty is applied to the mathematical model, which is given by

$$u_c^2(L) = c_{L_\phi}^2 u_c^2(L_\phi) + c_{L_n}^2 u_c^2(L_n) + c_{L_m}^2 u_c^2(L_m) + c_{L_h}^2 u_c^2(L_h) + c_{L_u}^2 u_c^2(L_u) + c_{L_d}^2 u_c^2(L_d) + c_{L_i}^2 u_c^2(L_i) + higher\ order\ terms \qquad 6.11$$

where the sensitivity coefficients, c_i, for the first order terms are

$$c_{L_\phi} = \frac{\partial L}{\partial L_\phi}, c_{L_n} = \frac{\partial L}{\partial L_n}, c_{L_m} = \frac{\partial L}{\partial L_m}, c_{L_h} = \frac{\partial L}{\partial L_h}, c_{L_u} = \frac{\partial L}{\partial L_u}, c_{L_d} = \frac{\partial L}{\partial L_d}, c_{L_i} = \frac{\partial L}{\partial L_i} \qquad 6.12$$

To evaluate the uncertainty of input quantities, all input quantities need to be converted into standard uncertainties. In Type B uncertainty evaluation, data can commonly be represented as a rectangular distribution. Section 4.3.7 of the GUM [143] suggests that it may be possible to estimate the boundaries of an input quantity (with an upper limit of $+a$ and a lower limit of $-a$ for a range of equally probable values), if the data used to estimate the uncertainty distribution of an influencing parameter are limited. Following Section 4.3.7 of the GUM [143], the standard uncertainty of a given specification a and a meter read-out of resolution b can be found by integrating over the rectangular distribution to give $a/\sqrt{3}$ and $b/\sqrt{12}$, respectively.

Standard uncertainty due to the optical difference path

The calibration of the laser interferometer was calibrated by comparison to a reference HeNe laser (routinely calibrated against an iodine-stabilised HeNe laser supplied by the National Physics Laboratory) using an optical beat frequency technique. The calibration was carried out by Renishaw and the uncertainty of the measurement (K = 2) was ± 1 × 10^{-8} m over 1 hour. Moreover, the laser interferometer noise was measured in an environment-controlled metrology laboratory by the operator, and the laser interferometer noise measured over 10 seconds was 9 × 10^{-9} m. This

uncertainty resembles Type A uncertainty. Therefore, the laser interferometer noise is not included in this analysis.

Standard uncertainty due to the change in the refractive index of the air in which the laser operates

As described Subchapter 6.3.1, air pressure, temperature, and humidity are the parameters that can change the refractive index of air. Fortunately, the complicated equations (the updated Edlén equation [145, 146] and Ciddor equation [147]) were evaluated under standard conditions (P = 1013.25 hPa, T = 293.15 K, and H = 50 %RH) to yield the sensitivities T_a, p_a, and H of the refractive index of air with respect to changes in temperature, pressure, and humidity. The values of the sensitivities are presented in Table 6.7.

Table 6.7. Sensitivity of the measured length L with respect to environmental (atmospheric) conditions on a laser interferometer system [15].

Environmental Condition	**Change Or Uncertainty**	**Change Or Uncertainty In The Indicated Measured Length L Per Metre**
Air temperature T_a	1 °C	0.93×10^{-6} m
Air pressure p_a	1 hPa	-2.68×10^{-6} m
Humidity H	1 %RH	0.009×10^{-6} m

In this experimental set-up, an environmental compensator was used to real-time correct the change in the refractive index of the air during performing the experiment. Therefore, the uncertainties resulting from the change in the refractive index of air can only be found by the accuracy of the air temperature, the air pressure and the air humidity sensors (found in the Technical white paper: TE329 [138]). Table 6.8 summarises the contributions of the measurement of the refractive index of air to the uncertainty.

Table 6.8 Summation of uncertainties due to the measurement of the refractive index of air.

Source	Size	÷	Standard Uncertainty	Sensitivity Coefficient	Sensitivity Description	Contribution
Accuracy of the air temperature sensor	0.2 °C	√3	0.12 °C	$9.30 \times 10^{-7} L$/°C	$T_a L$	$1.07 \times 10^{-7}\ L$
Accuracy of the air pressure sensor	1 hPa	√3	0.58 Pa	$2.68 \times 10^{-7} L$/hPa	$p_a L$	$1.56 \times 10^{-7}\ L$
Accuracy of the air humidity sensor	6 %RH	√3	3.46 %RH	9.00×10^{-9} L/%RH	HL	$3.12 \times 10^{-8}\ L$
Accuracy of the Edlén equation	3×10^{-8} m	3.00	1×10^{-8} m	L/m	L	$1.00 \times 10^{-8}\ L$
						$1.92 \times 10^{-7}\ L$

Standard uncertainty due to thermal effects on the metrology frame

The correction due to thermal effects on the metrology frame was calculated by applying the thermal expansion equation in the measuring direction (the Y-axis, as shown in Figure 6.12). It is worth mentioning, however, that additional uncertainties originated from measuring devices and tools, such as the thermocouple set and a tape meter used for measuring the length of the metrology frame in the Y-axis. The estimated difference in the CTE of the metrology frame was taken into account and deemed to be reliable by 10 % compared to α_m (23.8×10^{-6} K^{-1} [121]). Table 6.9 summarises the contributions of the thermal effects on the metrology frame to the uncertainty.

Table 6.9 Summation of uncertainties due to the thermal effects on the metrology frame.

Source	Size	÷	Standard Uncertainty	Sensitivity Coefficient	Sensitivity Description	Contribution
Thermocouple set resolution	0.025 °C	√12	7.22×10^{-2} °C	3.53×10^{-11} m/°C	$L_m \times \alpha_m$	2.55×10^{-13} m
Frame temperature fluctuation	0.039 °C	1	3.90×10^{-2} °C	3.53×10^{-11} m/°C	$L_m \times \alpha_m$	1.38×10^{-12} m
Tape meter resolution	1.00×10^{-3} m	√12	2.89×10^{-4} m	9.28×10^{-6} °C/°C	$\Delta T_m \times \alpha_m$	2.68×10^{-10} m
Difference in CTE of the frame	2.38×10^{-6} /°C	√3	1.37×10^{-6} /°C	5.79×10^{-8} m·°C	$L_m \times \Delta T_m$	7.96×10^{-14} m
						2.68×10^{-10} m

Standard uncertainty due to thermal effects on the hot plate

The uncertainties caused by thermal effects on the hot plate were divided into three parts according to the components: aluminium plate, ADC12 aluminium base and ceramic plate. The aluminium base and the ceramic plate lengths were measured using a calliper, while the aluminium plate length was

provided by the manufacturer [148]. α_{al}, $\alpha_{h.al}$ and $\alpha_{h.ce}$ are assumed to be 23.8 × 10^{-6} K^{-1} [121], 21.1 × 10^{-6} K^{-1} [149], and 3.32 × 10^{-6} K^{-1} [150], respectively. The difference in the CTEs of the components are taken into account and deemed to be reliable by 10 % of their CTEs. Table 6.10 summarises the contributions of the thermal effects on the hot plate in the uncertainty.

Table 6.10 Summation of uncertainties due to the thermal effects on the hot plate.

Source	Size	÷	Standard Uncertainty	Sensitivity Coefficient	Sensitivity Description	Contribution
Thermocouple set measured aluminium plate resolution	0.025 °C	√12	7.22 × 10^{-5} °C	2.93 × 10^{-11} m/°C	$L_{al} \times \alpha_{al}$	2.11 × 10^{-13} m
Aluminium plate temperature fluctuation	0.064 °C	1	3.70 × 10^{-2} °C	2.93 × 10^{-11} m/°C	$L_{al} \times \alpha_{al}$	1.88 × 10^{-12} m
The difference in the CTE of aluminium plate	2.38 × 10^{-6} /°C	√3	1.37 × 10^{-6} /°C	7.88 × 10^{-8} m·°C	$L_{al} \times \Delta T_{al}$	1.08 × 10^{-13} m
Thermocouple set measured aluminium base resolution	0.025 °C	√12	7.22 × 10^{-3} °C	7.67 × 10^{-12} m/°C	$L_{h.al} \times \alpha_{h.al}$	5.54 × 10^{-14} m
Aluminium base temperature fluctuation	0.049 °C	1	2.83 × 10^{-2} °C	7.67 × 10^{-12} m/°C	$L_{h.al} \times \alpha_{h.al}$	3.76 × 10^{-13} m
Calliper measured aluminium base accuracy	2.00 × 10^{-5} m	√3	5.77 × 10^{-6} m	1.03 × 10^{-6} °C/°C	$\Delta T_h \times \alpha_{h.al}$	1.19 × 10^{-11} m
Difference in the CTE of aluminium base	2.11 × 10^{-6} /°C	√3	1.22 × 10^{-6} /°C	1.78 × 10^{-8} m·°C	$L_{h.al} \times \Delta T_h$	2.17 × 10^{-14} m
Thermocouple set measured ceramic plate resolution	0.025 °C	√12	7.22 × 10^{-3} °C	4.50 × 10^{-14} m/°C	$L_{h.ce} \times \alpha_{h.ce}$	3.25 × 10^{-16} m
Ceramic plate temperature fluctuation	0.049 °C	1	2.83 × 10^{-2} °C	4.50 × 10^{-14} m/°C	$L_{h.ce} \times \alpha_{h.ce}$	2.21 × 10^{-15} m
Calliper measured ceramic plate accuracy	2.00 × 10^{-5} m	√3	5.77 × 10^{-6} m	1.63 × 10^{-7} °C/°C	$\Delta T_h \times \Delta_{h.ce}$	1.88 × 10^{-12} m
Difference in the CTE of ceramic base	3.32 × 10^{-7} /°C	√3	1.92 × 10^{-7} /°C	6.65 × 10^{-10} m·°C	$L_{h.ce} \times \Delta T_h$	1.27 × 10^{-16} m
						1.22 × 10^{-11} m

Standard uncertainty due to thermal effects on the experimental set-up

Thermal expansion from the experimental set-up was measured as a slope that corresponded to the temperature change, for the purpose of correcting the measured length. A change in the measured x_0 was noticed following ΔT_{al}, yielding a slope of 3.39 ± 0.57 × 10^{-7} m/ °C. Table 6.11 summarises the contributions of the thermal effects on the experimental set-up to the uncertainty.

Table 6.11 Summation of uncertainties due to the thermal effects on the experimental set-up .

Source	Size	÷	Standard Uncertainty	Sensitivity Coefficient	Sensitivity Description	Contribution
Thermocouple set resolution	0.025 °C	√12	7.22 × 10^{-3} °C	5.70 × 10^{-8} m/°C	$x_0/\Delta T_{al}$	4.11 × 10^{-10} m
Aluminium temperature fluctuation	0.059 °C	1	5.90 × 10^{-2} °C	5.70 × 10^{-8} m/°C	$x_0/\Delta T_{al}$	3.36 × 10^{-9} m
Slope	5.70 × 10^{-8} m/°C	1	5.7 × 10^{-8} m/°C	0.059 °C	ΔT_{al}	3.36 × 10^{-9} m
						4.77 × 10^{-9} m

Standard uncertainty due to the dead path length

The corresponding uncertainty contributions from the dead path were caused by the devices and tools used to measure the reflective index, the difference in the air between the reference and measurement retroreflectors, and the beamsplitter. Table 6.12 summarises the contributions caused by the dead path length to the uncertainty.

Table 6.12 Summation of uncertainties caused by the dead path length.

Source	Size	÷	Standard Uncertainty	Sensitivity Coefficient	Sensitivity Description	Contribution
Accuracy of air temperature sensor	0.2 °C	√3	0.12 °C	5.20 × 10^{-13} m/°C	$T_a d$	6.00 × 10^{-14} m
Accuracy of air pressure sensor	1 hPa	√3	0.58 hPa	1.51 × 10^{-13} m/hPa	$p_a d$	8.71 × 10^{-14} m
Accuracy of air humidity sensor	6 %RH	√3	3.46 %RH	5.03 × 10^{-15} m/%RH	Hd	1.74 × 10^{-14} m
Tape meter resolution	1.00 × 10^{-3} m	√12	2.89 × 10^{-4} m	2.50 × 10^{-6}	$\frac{\Delta n}{n_2}$	7.21 × 10^{-10} m
						7.21 × 10^{-10} m

Standard uncertainty due to the measurement set-up

There will always be an angular misalignment between the measurement axis and the direction of the motion caused by the Cosine error. The contribution is proportional to the measurement. However,

the Cosine error has not been corrected for in the mathematics model (Equation 6.2). Therefore, it will be accounted for in the combined uncertainty instead.

Expanded uncertainty

The expanded uncertainty is used to express uncertainties provided by the measured value within the uncertainty range of the unknown true value. To calculate the expanded uncertainty for length measurement, the input quantities of all sources of measurement uncertainties need to be estimated with respect to their degrees of freedom. According to Section G.3.3 in the GUM [143], the degrees of freedom v for Type A uncertainty evaluation are equal to the number of observations minus one (n − 1) for a single quantity estimated by the arithmetic mean of n independent observations. If n are used to determine both the slope and intercept of a straight line using the least squares method, the degrees of freedom of their respective standard uncertainties are the number of observations minus two (n − 2). As for Type B uncertainty evaluation, the degrees of freedom can be estimated by the uncertainty of the uncertainty $\Delta u/u$ or via obtaining scientific judgement based on the available information (e.g., the value of u is reliable to about 25 %, which makes $\Delta u/u$ equal to 0.25). The degrees of freedom of the estimation of uncertainty are given by (Section G.4.2 in the GUM [143])

$$v_i \approx \frac{1}{2}\left[\frac{\Delta u(x_i)}{u(x_i)}\right]^{-2} \qquad 6.13$$

Section G.4.3 in the GUM [143] states that the number of degrees of freedom of Type B evaluation of standard uncertainty, obtained from rectangular distributions, is assumed to be infinite, or implies that the probability of a measured value lying outside the bounds (within $\pm a$) of the distribution is extremely small.

As a result, the degrees of freedom of all influencing parameter uncertainties are combined to yield an overall uncertainty called the “effective degrees of freedom” v_{eff}, obtained from the Welch-Satterthwaite formula given by (Section G.4.1 in the GUM [143])

$$v_{eff} = \frac{u_c^4(x)}{\sum_{i=1}^{N} \frac{u_i^4(x)}{v_i}} \qquad 6.14$$

By applying Equation 6.13 and Equation 6.14, the degrees of freedom of all uncertainties in the thermal expansion measuring system with their combined standard uncertainties are presented in Table 6.13

Table 6.13 Summation of sources of uncertainty and their associated degrees of freedom.

Source Of Uncertainties	Uncertainty/ nm	Degree Of Freedom
Air refractive index	0.19 L	∞
Thermal effects on the metrology frame	0.3	39
Thermal effects on the hot plate (including the aluminium plate)	0.01	42
Thermal effects on the experimental set-up	4.8	10
Dead path error	0.7	∞
Abbe error	0	∞
Cosine error	4 L	∞

After estimating all standard uncertainties and their degrees of freedom, the expanded uncertainty is next to be estimated. The expanded uncertainty U is defined as the combined uncertainty $u_c(L)$ multiplied by a coverage factor k (Section 6.2.1 in the GUM [143]), which can be written as

$$U = ku_c(L) \tag{6.15}$$

where the value of k is chosen based on the level of confidence that would facilitate the interpretation of the uncertainty and the number of degrees of freedom. Generally, k is in the range of 2 to 3 (Section 6.3.1 in the GUM [143]).

From Table 6.13, the combined standard uncertainty and the effective degrees of freedom can be calculated using Equation 6.9 and Equation 6.14. The combined standard uncertainty is equal to $\sqrt{4.8^2 + (4L)^2}$ nm with effective degrees of freedom of 10. A level of confidence of 95 % is assumed, and the coverage factor of k is equal to 2.23.

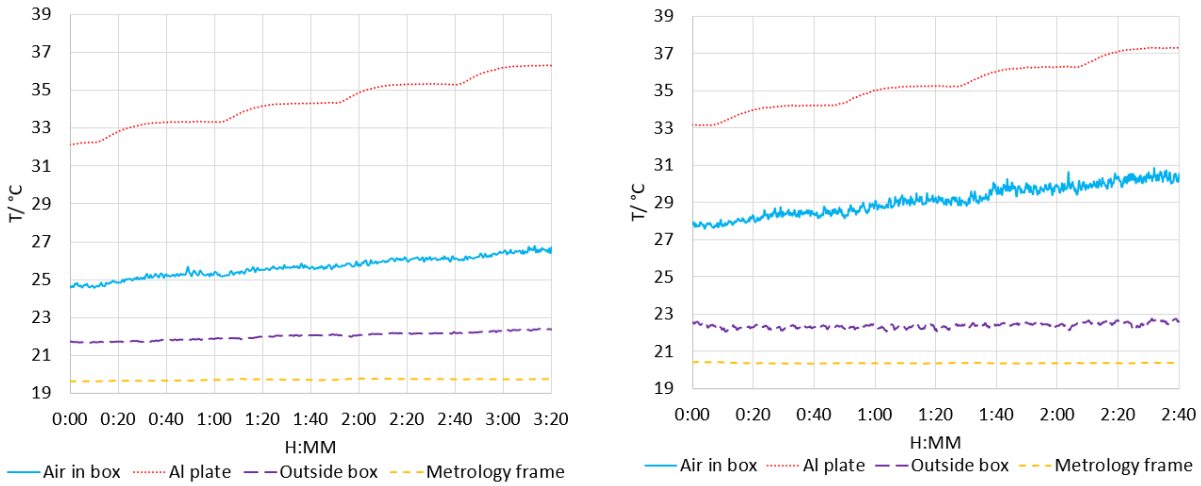
For example, if L were equal to (3.1 × 10^{-5}) mm (the maximum measured value in this experiment), then $u_c^2(L)$ would equal 4.84 nm, and if L were equal to (1 × 10^{-8}) mm, then $u_c^2(L)$ would equal 4.84 nm. It can be noticed that the length-dependent uncertainty contribution is negligible. The uncertainty in the thermal expansion measuring system is quoted as 4.84 nm at a coverage factor k = 2.23 with 10 degrees of freedom. This is fit for the purpose of measuring the CTE's of the lattices based on predictions of their thermal expansion. This demonstration does not include Type A uncertainty of the measurement presented in Subchapter 6.4.

6.4. Experimental validation and results

6.4.1. Experimental validation

Throughout the course of its development, the heating system was improved several times via the modification of its components using temperature data in specific locations. The purpose was to eliminate heat dissipation in the acrylic box.

Figure 6.14a shows the air temperature in the acrylic box, the aluminium plate, the outer surface of the acrylic box, and the metrology frame. To examine the temperature of all components, the surface temperature of the hot plate was increased by 1°C four times, each step lasting approximately 45 minutes. When the temperature changed, a change was rapidly noticed in the temperature of the air in the acrylic box and the aluminium plate, while the temperature of the metrology frame was not affected. This occurrence of this phenomenon was expected. However, the temperature of the outer surface of the acrylic box slightly varied, meaning that heat in the acrylic box dissipated to the environment. Accordingly, three layers of the aluminium bubble insulation foil were applied, which prevented the temperature of the outer surface of the acrylic box from changing during the experiment, as shown in Figure 6.14b.



(a) (b)

Figure 6.14 The air temperature in the acrylic box, the aluminium plate, the outer surface of the acrylic box, and the metrology frame (a) before installing the layers of the aluminium bubble insulation foil and (b) after installing the layers of the aluminium bubble insulation foil.

After applying the aluminium bubble insulation foil, the average temperature of a specimen (50 mm steel gauge box) was examined. It can be noticed that the average temperature of the specimen and the temperature of the air in the acrylic box were increased, as shown in Figure 6.15b. However, the

air temperature in the acrylic box fluctuated considerably compared to other data. An axial fan was installed in the heating system to circulate the airflow inside the acrylic box, resulting in a low fluctuation in the air temperature in the acrylic box (as seen in Figure 6.15c). Moreover, the average temperature of the specimen and the air temperature in the acrylic box approached the temperature of the aluminium plate, which meant that the performance of the heating system was improved.

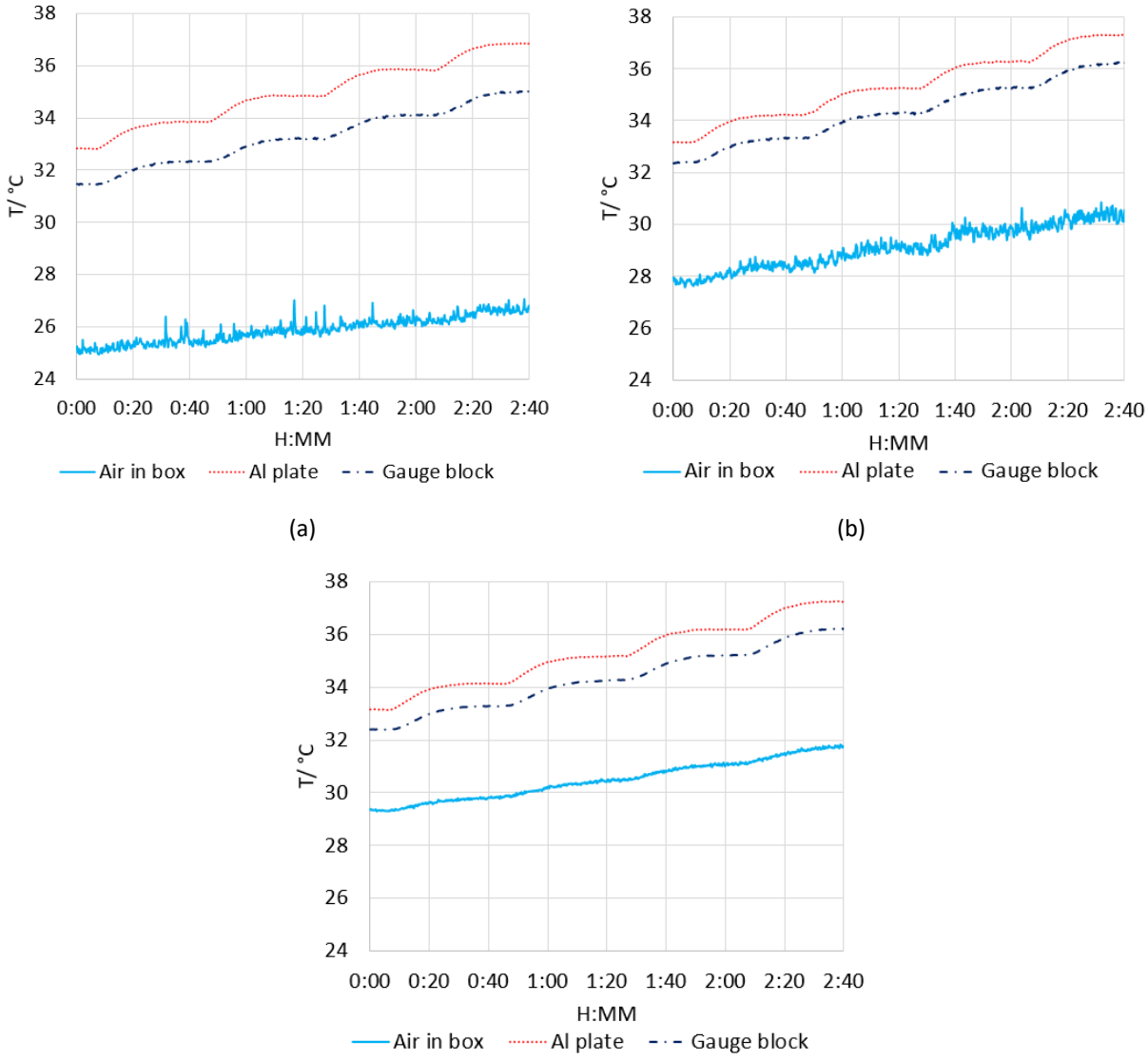


Figure 6.15 Temperature of the air in the acrylic box, the aluminium plate, and the average temperature of the 50 mm steel gauge box (a) before the installations, (b) after installing the layers of the aluminium bubble insulation foil, and (c) after installing the layers of the aluminium bubble insulation foil and the axial fan.

Following the improvement of the heating system and the laser interferometer system through correcting the mathematical model, three sizes (lengths of 40 mm, 50 mm and 60 mm) of steel gauge blocks were selected as reference materials with a CTE of 11.5×10^{-6} K^{-1}. This CTE value was taken from the Good Practice Guide No. 149 by NPL [4], however, it can vary by 10 % according to ISO 3650.

Figure 6.16 shows the CTE results of the three different sizes of the steel gauge blocks. Compared to the given datasheet, the percentage errors of the measured CTEs of the reference materials were approximately ± 2 %, which meets the requirement, as described in Chapter 3.

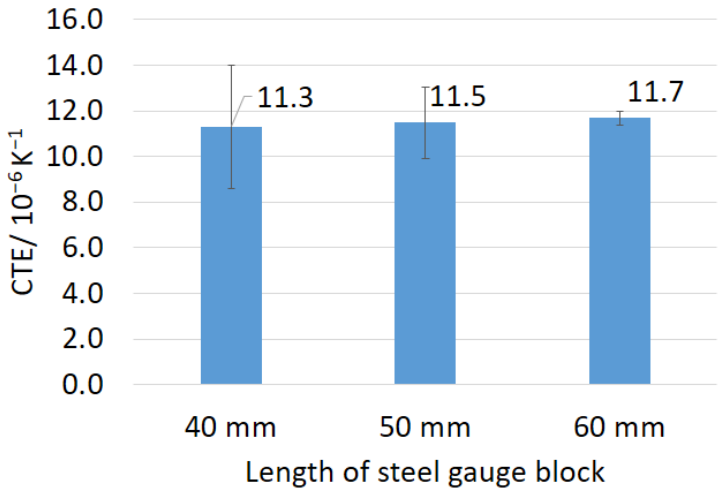
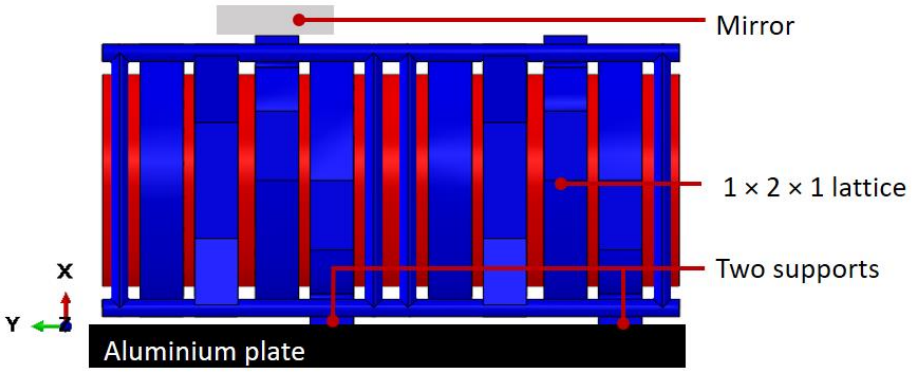


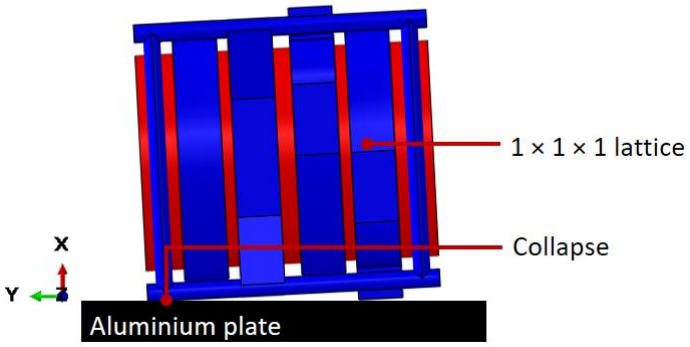
Figure 6.16 CTE results of the three different sizes of the steel gauge blocks.

6.4.2. Experimental results

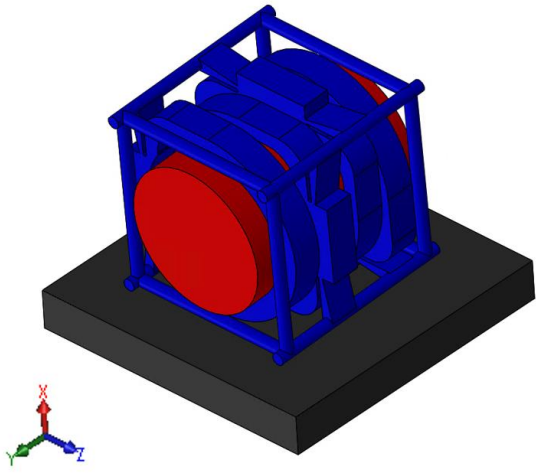
The Nylon 12 lattice outer part, the UHMWPE cylindrical inner part, Iteration 2.4 and Iteration 3.1 were selected for manufacture and testing as part of the thermal expansion experimentation. The CTEs of the Nylon 12 lattice outer part and the UHMWPE cylindrical inner part were tested for yielding the CTS values indicated in their respective datasheets. The 1 × 2 × 1 lattices of Iterations 2.4 and 3.1 were chosen to demonstrate whether the designed lattice could tailor the thermal expansion of their structures or not. A 1 × 2 × 1 lattice was selected instead a 1 × 1 × 1 lattice due to the inability of the former to be placed horizontally with two edges supported, as illustrated in Figure 6.17.



(a)



(b)



(c)

Figure 6.17 Illustration of the lattice structures placed in the experimental set-up: (a) a 1 × 2 × 1 lattice with a plane mirror (b) a 1 × 1 × 1 lattice and (c) a 3D view of the 1 × 1 × 1 lattice (three axes indicate the object coordinates).

The final iteration (4.1) was not selected as it could not be placed on the side, as illustrated for Iteration 3.1's position, as shown in Figure 6.17, due to the risk of separating design functions. The placement of a lattice of Iteration 4.1 along the X- and Z- axes (as illustrated in Figure 6.17) provided a more significant deformation, which was essential as the weight of the cylindrical inner part requires

support, especially around the deformation mechanism region of the structure. This could be resolved by measuring the lattice structure of Iteration 4.1 at the design position (as seen in Chapter 4) with a horizontal dilatometer. However, developing a horizontal dilatometer requires much more time than available for this PhD project.

For each specimen, the average measured displacement (L) and its standard deviation were calculated for the combined uncertainty, the expanded uncertainty, and the CTE computed from the expanded uncertainty, as shown in Table 6.14. Each individual specimen was assigned a set of values for the aforementioned quantities and calculations were made separately. Each combined uncertainty was quadratically summed from the standard deviation (Type A) and the Type B uncertainty value (as described in Subsection 7.2). The CTEs values, including the expanded uncertainties of all specimens, are presented in Table 6.15. The final results of the measurement can be stated as:

For a 50 mm steel gauge block, the CTE equalled (11.5 ± 2.42) × 10^{-6} K^{-1}, where the number following the symbol ± is the numerical value of the expanded uncertainty $U = ku_c$, with U determined from a combined standard uncertainty u_c = (1.05 × 10^{-6}) K^{-1} and a coverage factor k = 2.26 based on a t-distribution for v = 9 degrees of freedom, defining an interval estimated to have a level of confidence of 95 %. The corresponding relative expanded uncertainty is U/CTE = 0.210.

For the 1 × 2 × 1 lattice of Iteration 3.1, the CTE equalled (86.5 ± 5.70) × 10^{-6} K^{-1}, where the number following the symbol ± is the numerical value of the expanded uncertainty $U = ku_c$, with U determined from a combined standard uncertainty u_c = (2.59 × 10^{-6}) K^{-1} and a coverage factor k = 2.20 based on a t-distribution for v = 11 degrees of freedom, defining an interval estimated to have a level of confidence of 95 %. The corresponding relative expanded uncertainty is U/CTE = 0.066.

Table 6.14 Summation of the expanded uncertainty of all specimens.

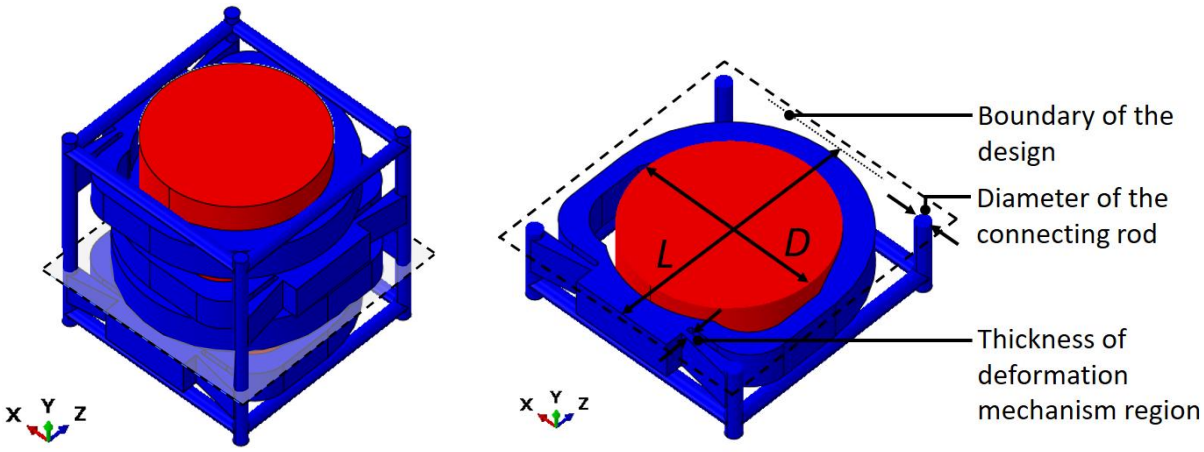
Material	Original Length/ mm	Average Measured Displacement (L)/ × 10^{-6} m		Average Measured Temperature Change On The Specimen (ΔT)/ °C	n	$u_c(L)$/ × 10^{-6} m	$v_{eff}(L)$	k	U_{95} / × 10^{-6} m	$u_c(L)$ CTE/ × 10^{-6} K^{-1}	Expanded Uncertainty CTE/ × 10^{-6} K^{-1}
		Mean	SD (Type A)								
Steel GB	40	4.81	0.16	3.825	5	0.16	4	2.78	0.44	1.05	2.90
Steel GB	50	5.97	0.21	3.928	10	0.21	9	2.26	0.48	1.07	2.42
Steel GB	60	5.62	0.26	3.717	5	0.26	4	2.78	0.72	1.17	3.24
Nylon 12	45.3	20.52	0.24	3.352	5	0.24	4	2.78	0.67	1.58	4.39
UHMWPE	50.1	30.43	1.59	2.876	5	1.59	4	2.78	4.41	11.0	30.6
Iteration 2.4	49.9	17.27	0.93	2.799	6	0.93	5	2.57	2.39	6.66	17.1
Iteration 3.1	49.9	15.94	0.38	2.943	12	0.38	11	2.20	0.84	2.59	5.70

Table 6.15 Summation of the coefficients of thermal expansion of all specimens.

Material	Original Length/ mm	CTE From Data Sheets Or Simulations/ × 10^{-6} K^{-1}	CTE From The Experiment/ × 10^{-6} K^{-1}	CTE Percentage Difference Between Data Sheets Or Simulations And The Experiment/ %
Steel gauge block	40	11.5	11.3± 2.90	−1.7
Steel gauge block	50	11.5	11.5± 2.42	0.0
Steel gauge block	60	11.5	11.7± 3.24	1.7
Nylon 12	45.3	109	111.1± 4.39	1.9
UHMWPE	50.1	200	178.5± 30.60	−10.8
Iteration 2.4	49.9	36.8	94.9± 17.10	157.9
Iteration 3.1	49.9	12.5	86.5± 5.70	592.0

6.5. Determination of the main influencing factors on CTE results of Iteration 3.1

Iteration 3.1 was selected to perform the thermal expansion experiment whether the designed lattice could tailor the thermal expansion of their structures while Iteration 4.1 was not selected as it could not be placed on the side, due to the risk of separating design functions, as described in Subchapter 7.3.2. Referring to the difference in the CTE results of the thermal expansion experimentation and the thermal expansion simulation (as discussed in Subchapter 6.4), six potential key parameters were investigated for their influences on the lattice structure's CTE using the thermal expansion simulation. The potential key parameters were grouped into two categories: physical geometries and material properties. Three physical geometries selected for the investigation were the ratio D/L, the deformation mechanism region thickness and the connecting rod diameter, as shown in Figure 6.18b. The other category investigated was material properties, including the ratio α_2/α_1, the ratio E_2/E_1 and the coefficient of friction between two materials (COF). All potential key parameters varied from −0.2 to 0.2, except for the D/L. The D/L varied from −0.2 to 0.1 as it reached the maximum ratio (about 0.096) that the lattice was designed for. The examined range was selected with the assumption that the actual values would not exceed this range. A (20 × 20 × 20) mm unit cell of Iteration 3.1 was selected to demonstrate the main influencing factors on CTE results. The lattice outer and cylindrical inner parts were modelled with Nylon 12 and UHMWPE, respectively.



(a) (b)

Figure 6.18 Illustration of Iteration 3.1 showing (a) a unit cell with the location of the cross-sectional area, and (b) the cross-section of the unit cell with annotations.

To reflect CTEs as close as possible to the actual result, the CTEs from the thermal expansion experimentation (as explained in Subchapter 6.4) were used in the thermal expansion simulation. During the thermal expansion experimentation, the CTEs of the specimens in Nylon 12 and UHMWPE were measured to be 111 × 10^{-6} K^{-1} and 178.7 × 10^{-6} K^{-1}, respectively. The ratio of α_2/α_1 was

approximately equal to 1.61. Material properties were kept unaltered during the thermal expansion simulation, with CTEs being the only redefined values, as mentioned in Subchapter 4.2.

Figure 6.19 shows differences in the in-plane CTE results of Iteration 3.1 when potential key parameters were varied (from −0.2 to 0.2), compared to the original design (in-plane CTE of 11.9 × 10^{-6} K^{-1}). The α_2/α_1 parameter rendered the highest range of the in-plane CTE, being −80 × 10^{-6} K^{-1} to 90 × 10^{-6} K^{-1}. The second highest range was reached when D/L was varied, such that the in-plane CTE ranged between −6 × 10^{-6} K^{-1} and 47 × 10^{-6} K^{-1}. When the relative change of D/L was greater than zero (the original design), the tailorable thermal expansion of its structure reached its limit, resulting in only a slight difference in CTE from the original design. The rest of the potential key parameters were considered less dominant, with the in-plane CTE ranging between −8 × 10^{-6} K^{-1} and 10 × 10^{-6} K^{-1}. To perform an in-depth analysis of the plots, a −0.1 relative change to all six potential key parameters was made to compare the effects of key parameters on the lattice structure's CTE, as shown in Table 6.16. It is clear that the ratios D/L and α_2/α_1 were the two major influencing factors that affected the lattice's CTE for a −0.1 relative change, with the following CTE values respectively: 27.33 × 10^{-6} K^{-1} and 37.83 × 10^{-6} K^{-1}, respectively, for a −0.1 relative change in the parameter.

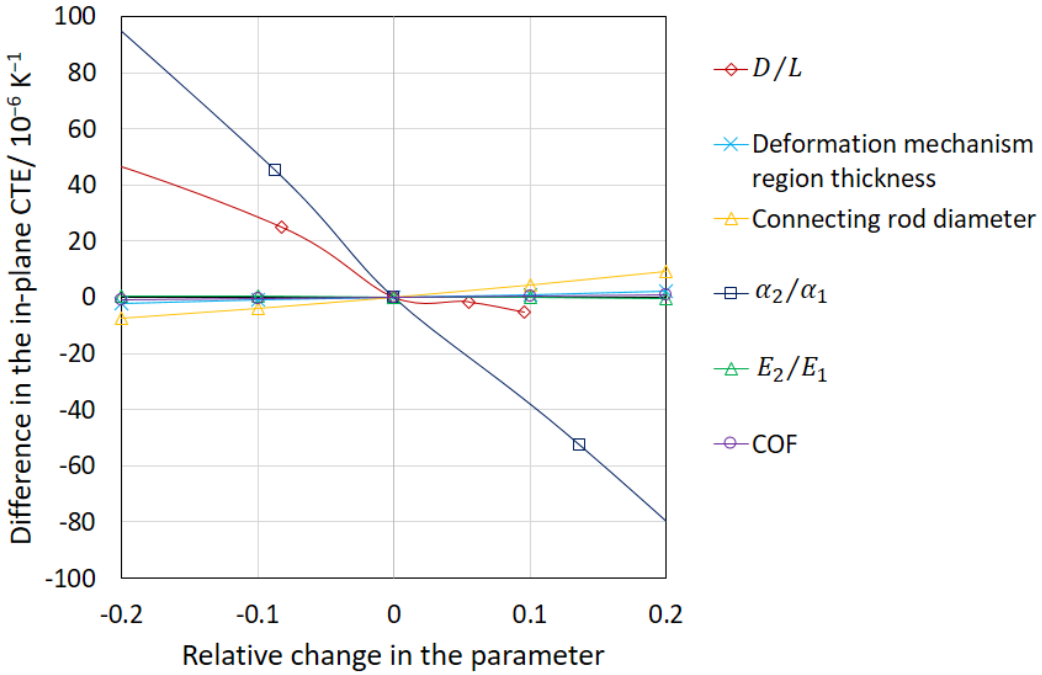


Figure 6.19 Differences in the in-plane CTE of Iteration 3.1 when potential key parameters were varied from −0.2 to 0.2.

Table 6.16 The potential key parameter changed and their effects on the in-plane CTE of Iteration 3.1.

Attribute	Original Value	Relative Change In The Parameter	Parameter Changed Effects On The In-Plane CTE/ × 10^{-6} K^{-1}
$\boldsymbol{\alpha_2/\alpha_1}$	1.61	−0.1	37.83
$\boldsymbol{D/L}$	0.73	−0.1	27.33
Deformation section thickness	$0.01L$	−0.1	−1.05
Connecting rod diameter	$0.06L$	−0.1	−3.74
$\boldsymbol{E_2/E_1}$	0.38	−0.1	−0.26
Coefficient of friction (COF)	0.1	−0.1	−0.08

Note that the original values are: α_2 = 178.7 × 10^{-6} K^{-1}, α_1= 111 × 10^{-6} K^{-1}, D = 14.6 mm, L = 20 mm, deformation section thickness = 0.2 mm, connecting rod diameter = 1.2 mm, E_2 = 0.7 GPa and E_1 = 1.8 GPa.

6.6. Discussion of lattice structure thermal expansion experiments

The described improvements and developments have been implemented in each of the hardware, the software and the experimental procedure. The hardware consisted of the heating system, the displacement measurement system and the thermal expansion experimental frame. During the experiment, software packages (PicoLog 6 and CARTO Capture) were used to record all data. The hot plate temperature increments were performed by manually turning the rotary switch on the hot plate panel at the setting time. During the improvement and development of the thermal expansion measuring machine, a number of challenges were encountered:

- To analyse the CTE of the specimen, the average measured temperature change of the specimen during the experiment was taken into consideration and had a significant impact on the calculation. Therefore, obtaining an accurate CTE value required the measurement of a high average temperature change by attaching thermocouples on the specimen. Three thermocouples were installed at the top, middle and bottom of the front side of the steel gauge block specimens. In other larger specimens, six thermocouples were attached at the top, middle and bottom of both the front and back sides of the specimens. All thermocouples were attached using adhesive tape, to avoid damage from tape removal at the end of the experiment.
- The use of adhesive materials to secure the component that the laser interferometer will directly measure was avoided, since adhesive materials can be an error source due to possible thermal effects. Dried adhesive glue can crack when the temperature changes due to the

different material CTEs, resulting in unexpected thermal expansion in the measurement. Such a temperature change can cause a displacement change in the adhesive glue adhered between the aluminium plate and the steel gauge block by 12.3×10^{-6} K^{-1}.

- Based on the author's experience during the development of the laser interferometer system, air turbulence was a notable challenge. The light indicator on the interferometer suddenly changed from five green lights to a red light, stopping the laser interferometer recording software. This phenomenon occurred due to a change in the temperature along the path of the beam by about 10 to 14 °C. The temperature of the interferometer was approximately room temperature (20 °C), while the air temperature in the acrylic box was in the range of 30 °C to 34 °C. To resolve this issue, a separation of the temperature along the path of the beams was required.

In the research, the interferometric dilatometer was developed using the interferometer and a plane mirror technique. Steel gauge blocks were measured in a temperature range of 30 °C to 34 °C. The total uncertainty of the measurement was estimated from the measurement of three different lengths of specimens, to be 2.4 to 3.3×10^{-6} K^{-1} on the steel gauge material with a linear CTE of 11.5×10^{-6} K^{-1}, as shown in Table 6.15. Despite yielding results with significant uncertainties compared to previous studies [2, 111-113], the proposed interferometric dilatometer utilised a less complicated approach (single path) in addition to the implementation of uncertainty corrections, as described in Subchapter 6.3. It was demonstrated that a single path interferometer, with the correction equations, can yield accurate measurement results.

To determine uncertainty sources that influence the displacement measurement, the ratio of each source with respect to the largest source was calculated by dividing the variance (square of the standard uncertainty) of the source by that of the largest source. Table 6.17 shows the ratios of different sources to the largest source (50 mm steel gauge block). This calculation indicates that the repeated measurement difference is only a significant source of uncertainty that is much higher among other sources. Therefore, further improvements should be implemented in repeated measurement differences.

Table 6.17 Summation of the ratios of uncertainty sources with respect to the largest source.

Source of uncertainties	Standard uncertainty/ nm	Standard uncertainty squared	Ratio to largest
Air refractive index	0.01	0.00	0.00
Thermal effects on the metrology frame	0.27	0.07	0.00
Thermal effects on the hot plate (including aluminium plate)	0.01	0.00	0.00
Thermal effects on the experimental set-up	4.77	22.79	0.00
Dead path error	0.72	0.52	0.00
Abbe error	0.00	0.00	0.00
Cosine error	0.2	0.00	0.00
Repeated measurement difference	2516.02	6330356.64	1

From Table 6.15, it can be seen that the CTEs of the experiment ± their expanded uncertainty for the 40 mm, 50 mm, 60 mm steel gauge blocks, 45.3 mm Nylon 12, and 50.1 mm UHMWPE, represented accurate CTE values close to the ones quoted in the components' datasheets. However, the CTE of the expanded uncertainty of UHMWPE was quite large compared to the others. As for Iterations 2.4 and 3.1, their experimental CTEs ± their expanded uncertainty did not match the CTEs from the simulation (157.9 % for Iteration 2.4 and 592.0 % for Iteration 3.1), as seen in CTE Percentage Difference Between Data Sheets Or Simulations And The Experiment, Table 6.15. There were two types of measurements in this experiment: temperature and displacement. The temperature data could have been affected by uncertainties of the temperature gradient in the specimens, the number of thermocouples measuring the specimens, and the positions of thermocouples on the specimens. Likewise, the displacement data might have been affected by the position of the specimens, the levelness of the top plane where the mirror was placed, and the uncertainties of the specimens. There are possible explanations for these uncertainties:

- The temperature difference in the specimens could have originated from the hot plate which generated a constant conduction heat to the specimens, leading to a rise in their temperature. Different materials, however, have their own heat conductivity properties. The thermal conductivity of steel is 52 W/(m·K) [37], which is larger than that of Nylon 12 and UHMWPE by 173 times (0.3 W/(m·K)) and 127 times (0.41 W/(m·K)), respectively. During the experiment, the temperature differences of all specimens were measured from the maximum temperature difference among the thermocouples. The steel gauge blocks had a temperature difference of about 1.6 °C, while the Nylon 12 lattice outer part and the UHMWPE cylindrical inner part had temperature differences of 4.4 °C and 5.1 °C, respectively. As for the 1 × 2 × 1 lattice of Iteration 2.4 and the 1 × 2 × 1 lattice of Iteration 3.1, the temperature difference

among the thermocouples located on the specimens was 2.8 °C and 2.9 °C, respectively. It can be noticed that the UHMWPE cylindrical inner part had a remarkable temperature difference, resulting in a more uncertain CTE.

- The number of thermocouples measuring the specimens was the same for both the UHMWPE cylindrical inner part (three thermocouples) and the steel gauge blocks, despite differences in the thermal conductivities of the materials, to measure temperatures (top, middle and bottom of a side, as illustrated in Figure 6.3). Therefore, the number of thermocouple pads placed on the specimen could have been insufficient to represent the overall temperature change. Thermocouples were only measured on the specimens, not inside the specimens, especially for larger cylindrical inner parts such as Iteration 2.4 and Iteration 3.1, resulting in inaccurate temperature results. Figure 6.20 shows lattice unit cells provided difference in CTEs from zero to 52.0 $\times$ 10^{-6} K^{-1} by varying the average temperature change of the entire experiment from true value to 1 °C. For example, a variation of 0.1 °C of the average temperature could affect to the lattice structure' CTEs by 3.5 × 10^{-6} K^{-1} for Iteration 2.4 and 3.3 × 10^{-6} K^{-1} for Iteration 3.1.

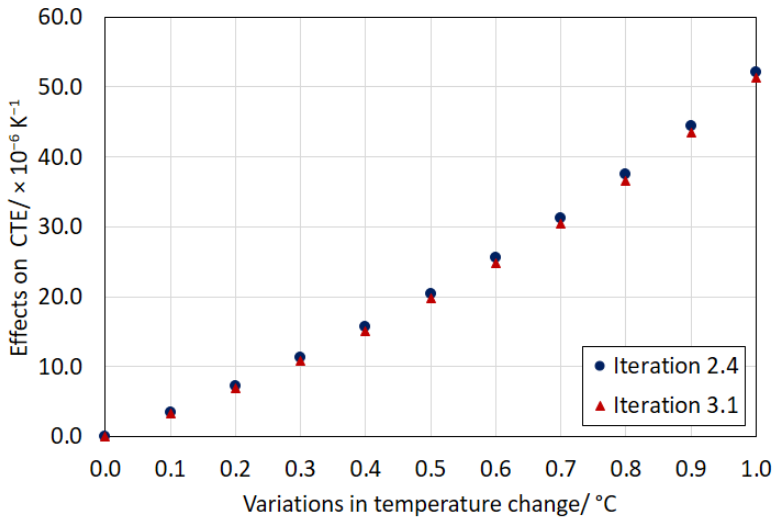


Figure 6.20 Low planar CTE lattice results of Iterations 2.4 and 3.1 by varying the average temperature change of the entire experiment.

- The positions of the thermocouples on the specimens might have been different in each test due to the experimental procedure: the thermocouples were installed on the specimens and removed at the end of each test, resulting in inaccurate temperature results.
- The position of the specimens might have changed. Each time the specimens were removed and replaced, the measurement point on the mirror placed at top of the specimens changed, resulting in differences in the measured CTEs.

- The flatness of the top plane where the plane mirror was placed is another potential source of uncertainty. Industrially manufactured parts, such as the Nylon 12 lattice outer part, the UHMWPE cylindrical inner part, the 1 × 2 × 1 lattice of Iteration 2.4 and the 1 × 2 × 1 lattice of Iteration 3.1, are generally produced without much attention to their flatness. Hypothetically, the mirror could have rotated from its original position during the experiment when the specimens were expanded by heat from the hot plate. Figure 6.21 shows lattice unit cells provided difference in CTEs from zero to 60.3 $\times$ 10^{-6} K^{-1} by varying the rotation of the plane-mirror of the entire experiment from true value to 0.30 degrees. On the other hand, there was an extremely low chance that the mirror on the steel gauge blocks could have slipped, since these materials were manufactured for precision measurement.

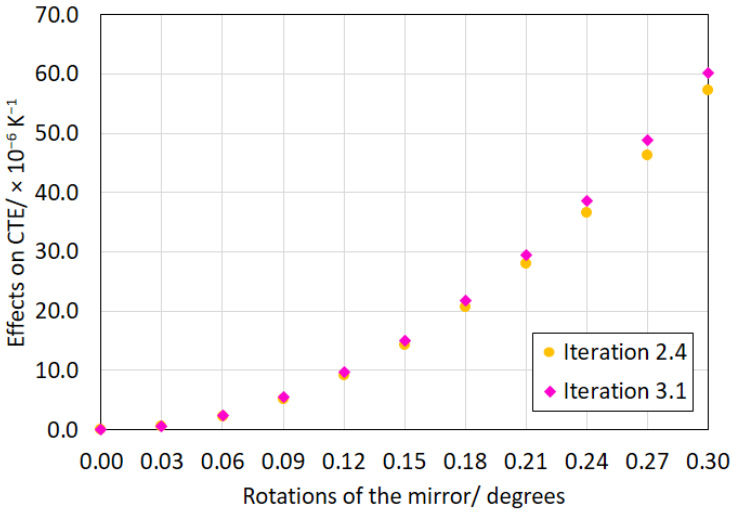


Figure 6.21 Low planar CTE lattice results of Iterations 2.4 and 3.1 by varying the rotations of the plane mirror of the entire experiment.

- The uncertainties of the specimens affect the overall system's CTE. These uncertainties include the specimens' dimensional configurations (such as the size of cylindrical inner part and size of internal geometries of lattice outer part for Iterations 2.4 and 3.1), friction, and the elastic modulus of individual parts. A study of the uncertainties of geometric configurations, as presented in Subchapter 6.5.

In light of the aforementioned issues, the system can be improved by:

- Taking more measurements to increase measurement accuracy and compute CTEs from expanded uncertainty, with smaller uncertainty values. Taking a sufficient number of measurements will reduce the coverage factor k, which is multiplied by a combined standard uncertainty u_c to compute the CTE from expanded uncertainty.

- Applying other temperature measurement systems such as thermal imaging cameras using infrared light to reflect the actual value of specimen temperature. The employment of such a system can also eliminate the procedure of installing and removing thermocouples on the specimens, which would make the experiment less tedious to carry out and significantly reduce human error.

Moreover, the effects of varying the six key parameters (the ratio D/L, the thickness of the region of the deformation mechanism, the connecting rod diameter, the ratio α_2/α_1, the ratio E_2/E_1 and the coefficient of friction between two materials (COF) during the thermal expansion simulation) on the CTE of a unit cell of Iteration 3.1 were investigated, as described in Subchapter 6.5. From the simulation results, the ratios D/L and α_2/α_1 were the two significant influencing factors that affected the lattice's CTE resulting in 27.33 × 10−6 K−1 and 37.83 × 10−6 K−1, respectively, for a −0.1 relative parameter change. It can be seen that uncertainties in the values of the key parameters, especially D/L and α_2/α_1, had significant impacts on the effective CTE of the lattice structure. As a result, selecting materials and manufacturing techniques must be prioritised for the fabrication of lattice structures with a low CTE. Alternative materials such as metallic and ceramic materials can preferably be choices because these materials can give a compromise of material properties with low uncertainties. Moreover, alternative manufacturing techniques can be considered for providing a high accuracy of manufacturing such as autonomous robot assembly and high-precision assembly.

6.7. Conclusion

Thermal expansion experiments have been developed and conducted using an interferometric dilatometer with a plane mirror technique that can measure the designed lattices with the size of (50 × 50 × 50) mm. Steel gauge blocks were measured in the range of 30 °C to 34 °C. The total uncertainty of the measurement was estimated from measurements of three different lengths of specimens to be 2.4 to 3.3 × 10^{-6} K^{-1} on the steel gauge material that had linear CTEs of 11.5 × 10^{-6} K^{-1}. The percentage errors of the measured CTEs of the steel gauge materials compared to the datasheet were approximately ± 2 %.

The thermal expansion experiments were used to measure the CTEs of the Nylon 12 lattice outer part, the UHMWPE cylindrical inner part, the 1 × 2 × 1 lattice of Iteration 2.4 and the 1 × 2 × 1 lattice of Iteration 3.1. It was found that thermal expansion experiments can be improved to achieve higher accuracy CTE results from measuring all specimens.

Finally, the effects of varying six key parameters (the ratio D/L, the deformation mechanism region thickness, the connecting rod diameter, the ratio α_2/α_1, the ratio E_2/E_1 and the coefficient of friction between two materials (COF) during the thermal expansion simulation) on the CTE of a unit cell of Iteration 3.1, were investigated. It can be concluded that the ratios D/L and α_2/α_1 are the two major influencing factors that affect the lattice structure's CTE. Therefore, the selection of materials and manufacturing techniques is of high importance in the fabrication of lattice structures with a low CTE.

7. Implementation of the lattice structures into a metrology frame

This chapter describes the implementation of the lattice structures into a metrology frame. First, the implementation of the final iteration (Iteration 4.1) is presented, highlighting the three main restrictions faced in implementation: elastic modulus determination, deformation mechanism determination, and implementation of Iteration 4.1 into an optical vertical dilatometer. Then, results of the implementation of Iteration 4.1 are discussed. Finally, a conclusion is drawn.

7.1. Implementation of Iteration 4.1 into a metrology frame

Iteration 4.1 is the final version of the lattice structure design that was adopted for implementation inside a machine frame to support precision measurement equipment. The frame was designed to in a typical temperature-controlled metrology laboratory, with temperatures fluctuating between 19 °C and 23 °C. Iteration 4.1 was designed to tailor 2D (planar) thermal expansion in the XZ plane and support loading in the Y-axis, as shown in Figure 7.1. Figure 7.1 shows an example of the tessellation of Iteration 4.1: a 4 × 1 × 4 lattice and possible locations for the application of loadings on the lattice structure.

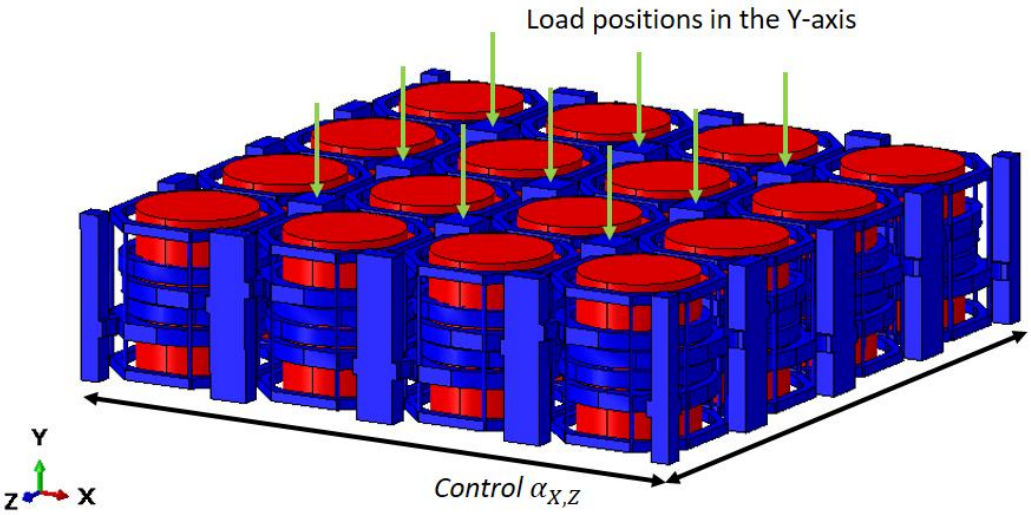


Figure 7.1 A 4 × 1 × 4 lattice of Iteration 4.1 with the possible locations for loading application on the structure.

There are three restrictions that need to be accounted for, for the implementation of Iteration 4.1, to guarantee a good performance of the lattice structure:

1. Aside from achieving an effective CTE, ensuring that the lattice structure is capable of supporting applied loads in the Y-axis is a key requirement. Applied loads must only be placed at the centre of the top surface of the lattice structure's load-bearing pillars, located inside the lattice structure (as shown in Figure 7.1). According to the elastic modulus determination

discussed in Subchapter 7.1.1, the stress corresponding to 0.1% strain of a (50 × 50 × 50) mm unit cell of Iteration 4.1 was 105.2 kPa. In other words, a unit cell of (50 × 50 × 50) mm can be deformed by a 0.1% strain along the Y-axis, when a loading of 26.81 kg is applied. 0.1% deformation has been chosen as a threshold to minimise the deformation caused by load application.

2. Due to differences between the CTEs of the cylindrical inner parts and the lattice outer part, the thermal expansion when the temperature is increased is always uneven along the Y-axis, as shown in Figure 7.2a. With a higher CTE, the cylindrical inner part expands more than the lattice outer part, resulting in an uneven surface texture at the top of the lattice structure. To avoid the occurrence of uneven surfaces, the cylindrical inner parts were modified by reducing their height, as shown in Figure 7.2b. This modification did not disrupt the deformation mechanism of the structure, as the trimmed parts were not located in the interacting regions between the contacts of the cylindrical inner part and the lattice outer part, as seen in Figure 7.2b.

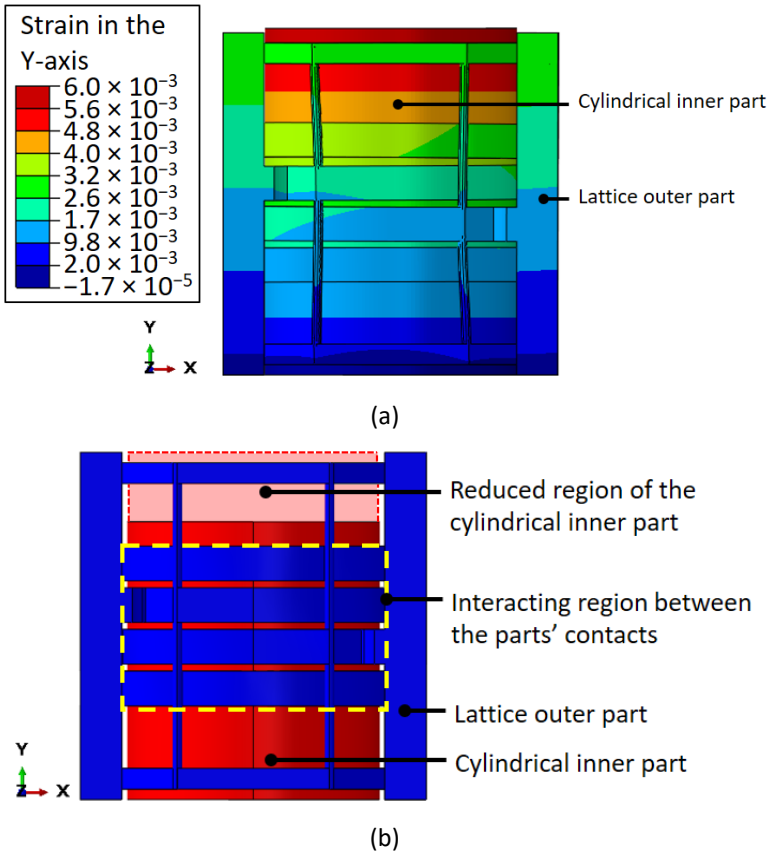


Figure 7.2 Illustration of a unit cell of Iteration 4.1: (a) contour plot of the strain along the Y-axis when the temperature was increased (with a deformation factor of 2) and (b) the reduced region to eliminate excess material in the parts along the Y-axis.

3. For the tessellation of Iteration 4.1's unit cells, sets of the 1st pattern of the 2 × 1 × 2 lattice in Iteration 4.1 were required. These could be grouped to form various sets of different sizes. For example, a 4 × 1 × 2 lattice (composed of two sets of 2 × 1 × 2 lattices), a 6 × 3 × 4 lattice (composed of 18 sets of 2 × 1 × 2 lattices), an 8 × 4 × 6 lattice (composed of 48 sets of 2 × 1 × 2 lattices), etc. The tessellation of the 1st pattern could help compensate for the anisotropy according to the thermal expansion results in Subchapter 4.4.

7.1.1. Elastic modulus determination

Elastic modulus determination refers to the computation of the ratio of stress to strain when a deformation is elastic in a finite element (FE) simulation. A methodology to determine the elastic modulus determination was presented by Maskery et al. [47], where a (50 × 50 × 50) mm unit cell was subjected to compressive displacements at the specific nodes of its top planes using the CAE software package Abaqus version 2021. The chosen size of the unit cell was the actual size fabricated and implemented into a precision machine frame. The lattice outer part was modelled with Nylon 12, while the cylindrical inner part was modelled with UHMWPE, as described in Chapter 4. All nodes were displaced by an equivalent 0.1 % of the height of the lattice structure, as illustrated in Figure 7.3. The 0.1% strain corresponded to the allowed deformation computed by the engineer designing the lattice structure. The 0.1% strain was selected within the proportional limit, such that the elongation at yield of Nylon 12 was about 6% of the strain [151]. The YSYMM boundary condition was applied to the elements on the bottom surfaces of the lattice structure, constraining them to translation in the XZ plane only and rotation around the Y-axis only.

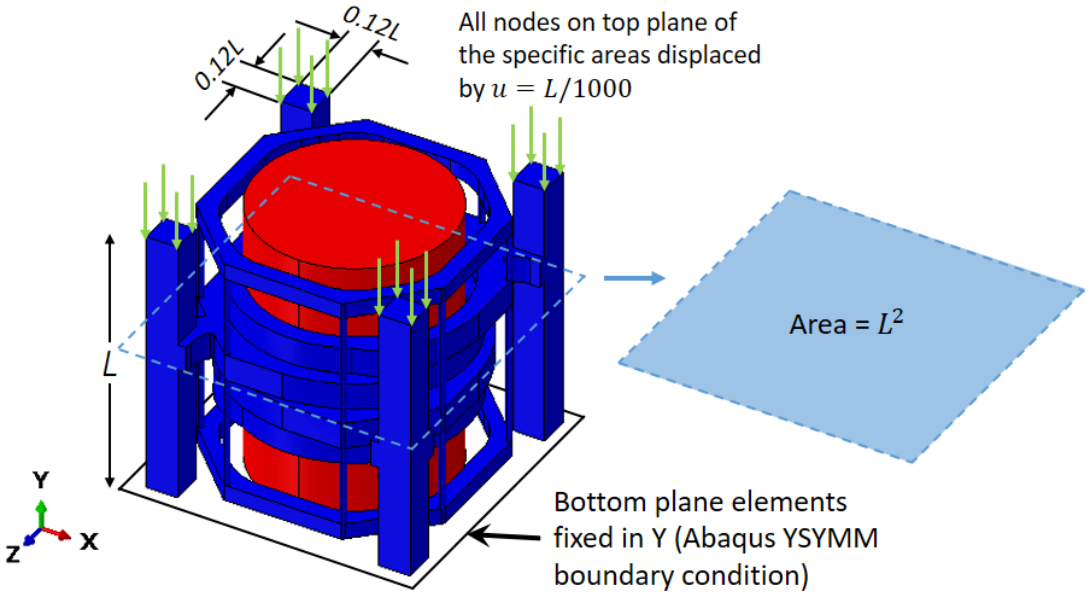


Figure 7.3 A representation of Iteration 4.1, used for FE structural analysis.

The elastic modulus of the lattice structure was computed using:

$$E = \frac{FL}{Au} \tag{7.1}$$

where E is the elastic modulus, F is the total reaction force of the top plane's nodes in the Y-axis, L is the height of the lattice structure, A is the cross-sectional area (L^2) of the structure, and u is the displacement of the top surface after applying the load.

Throughout the study presented by Maskery et al., the elastic modulus was assigned a value of 1.8 GPa [47]. The elastic modulus of the lattice $E_{latt.}$ could be found by substituting the total reaction force of the top plane's nodes in the Y-axis into Equation 7.1.

The total reaction force was calculated using Equation 7.1, with the top surfaces of the load-bearing pillars considered as the principal load-bearing areas. An area of (1.44×10^{-4}) m^2 was attributed to a unit cell of (50 × 50 × 50) mm, as illustrated in Figure 7.3. The total reaction force for a 0.1% strain along the Y-axis was calculated to be 259 N. This means that a (50 × 50 × 50) mm unit cell was deformed by 0.1 % of its height along the Y-axis when a load of 26.42 kg was applied. The results from both the elastic modulus simulation and the hand calculation were quite similar, with less than a 2 % deviation. The results confirmed that the four load-bearing pillars can support the applied loads as outlined in design requirements.

7.1.2. Determination of the deformation mechanism

This investigation aimed at indicating the effects of a rise in temperature on the compressed lattice structure's CTE and at determining the minimum applied load that could lead the deformation mechanism to fail. A (20 × 20 × 20) mm unit cell was chosen for the study, as this was the smallest size that can be produced without losing a minimal compromise of mechanical properties [103]. The lattice outer and cylindrical inner parts were modelled with Nylon 12 and UHMWPE.

In this study, two sequential steps were required. The first step was the application of loads on the lattice structure, which was equivalent to inducing a strain between 0% to 5% along the Y-axis (as described in Subchapter 7.1.1) to obtain the changes in the X− and Z−dimension axes. The second step was the application of temperature changes on the compressed lattice structure to obtain dimensional changes in the X− and Z−axes. The boundary conditions applied were the same ones chosen in the thermal expansion simulation, as described in Subchapter 5.1. Finally, the compressed lattice structure's CTE was found by:

$$\alpha_c = \frac{\Delta L_c}{L_c \Delta T} \tag{7.2}$$

where α_c is the linear coefficient of thermal expansion of the compressed lattice structure, ΔL_c is the change in length of the compressed lattice structure, L_c is the original length of the compressed lattice structure (before temperature change), and ΔT is the change in temperature between the initial and final temperatures.

Figure 7.4 shows the unit cell of Iteration 4.1, with in-plane CTEs ($\alpha_{X,Z}$) varying approximately between from approximately -4.4×10^{-6} K^{-1} and 1.4×10^{-9} K^{-1} due to changes in the applied loads causing a strain between 0 % and 5.0 % along the Y-axis. The magnitude of $\alpha_{X,Z}$ increased (in contraction) when the strain was increased within a range of 0 % and 1.5 %. At 1.5% strain, the magnitude of $\alpha_{X,Z}$ reached (in contraction) -4.4×10^{-6} K^{-1}. Then, the magnitude of $\alpha_{X,Z}$ began to decrease (in contraction) when the strain was greater than 1.5 %. From the data, it can be noted that the deformation mechanism was mostly active between 0 % and 1.5 % of the strain along the Y-axis.

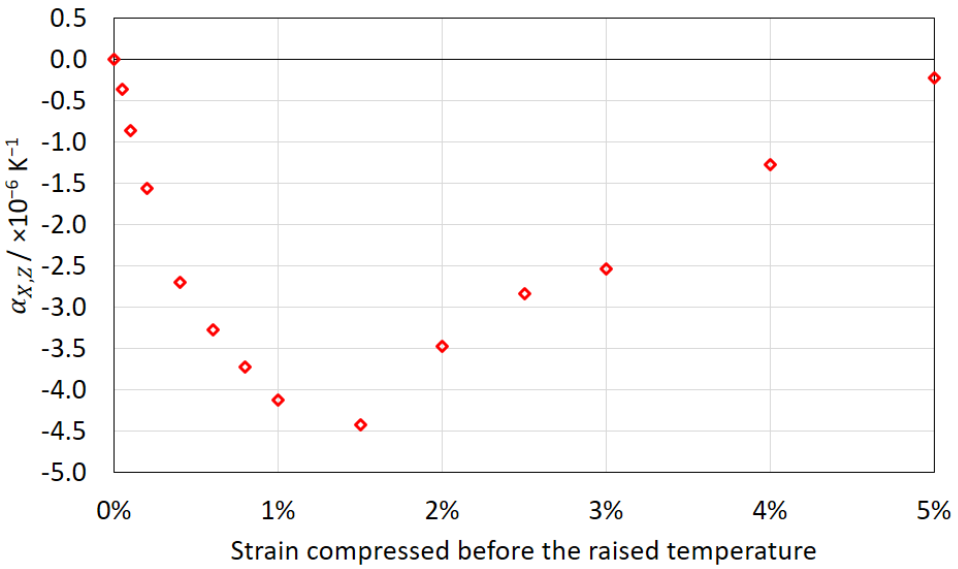
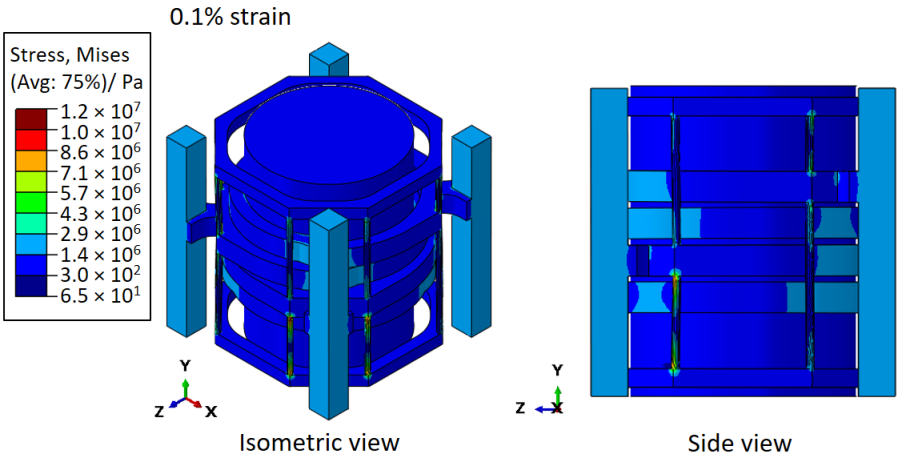


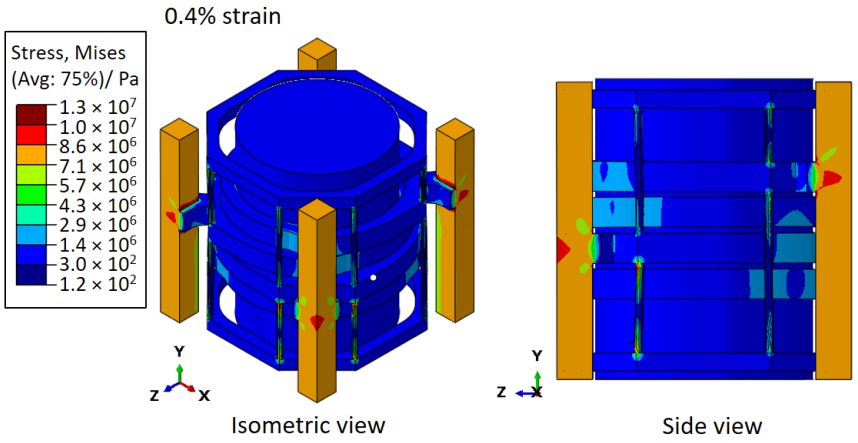
Figure 7.4 The in-plane CTE for a unit cell of Iteration 4.1 compressed by applied loads equivalent to a range of 0 % to 5.0 % strain along the Y-axis.

Figure 7.5 shows contour plots of the von Mises Stress after the temperature increase for the unit cell in Iteration 4.1 that was compressed by load application (strain along the Y-axis between 0.1 % and 5.0 %). The increments of the contour plots of von Mises Stress were set to be the same in all plots to accurately compare the differences in the occurred stress. The highest stress in the plots was in a range of 1.2×10^7 Pa to 1.7×10^8 Pa, between 0.1 % strain and 5.0 % strain.

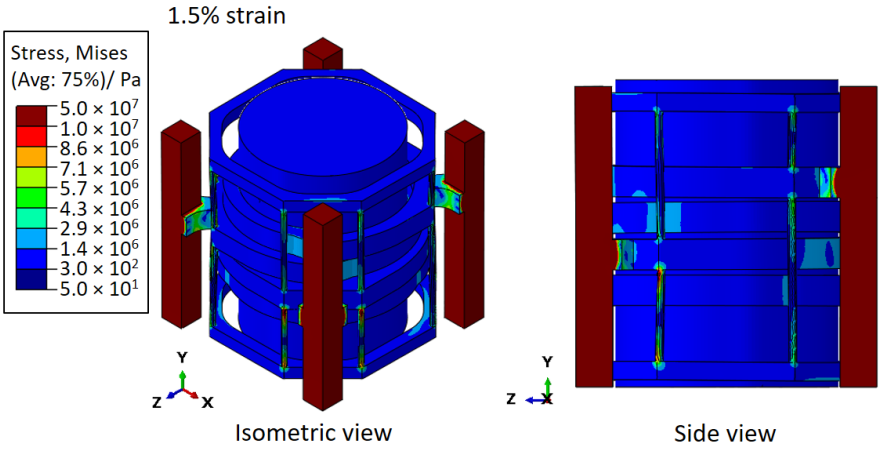
At 0.1 % strain (as shown in Figure 7.5a), it is clear that high stress (1.2×10^7 Pa) occurred only in the deformation mechanism regions. Similarly, at 0.4 % strain (as shown in Figure 7.5b), high stress (1.2×10^7 Pa) occurred in the deformation mechanism regions, however, stress in the load-bearing sections was remarkably larger than the stress at 0.1 % strain. At 1.5 % strain (as shown in Figure 7.5c), high stress occurred in the load-bearing sections, while stress in the deformation mechanism regions remained the same (1.2×10^7 Pa). Stress in the connected regions between a CTE-minimising layer and a load-bearing pillar was notable. Moreover, the configuration of the deformation mechanism section started to distort notably. At 2.0 % strain and 5.0 % strain (as shown in Figure 7.5d and Figure 7.5e, respectively), high stress occurred in the load-bearing sections (6.6×10^7 Pa for 2.0 % strain and 1.7×10^8 Pa for 5.0 % strain). Nonetheless, the stress in the deformation mechanism regions remained the same (1.2×10^7 Pa). It can also be noted that stress occurred in the deformation mechanism sections and their configurations were distorted.


0.1% strain
Stress, Mises
(Avg: 75%)/ Pa
1.2 × 10^7
1.0 × 10^7
8.6 × 10^6
7.1 × 10^6
5.7 × 10^6
4.3 × 10^6
2.9 × 10^6
1.4 × 10^6
3.0 × 10^2
6.5 × 10^1
Y
Z
X
Isometric view
Y
Z
Side view

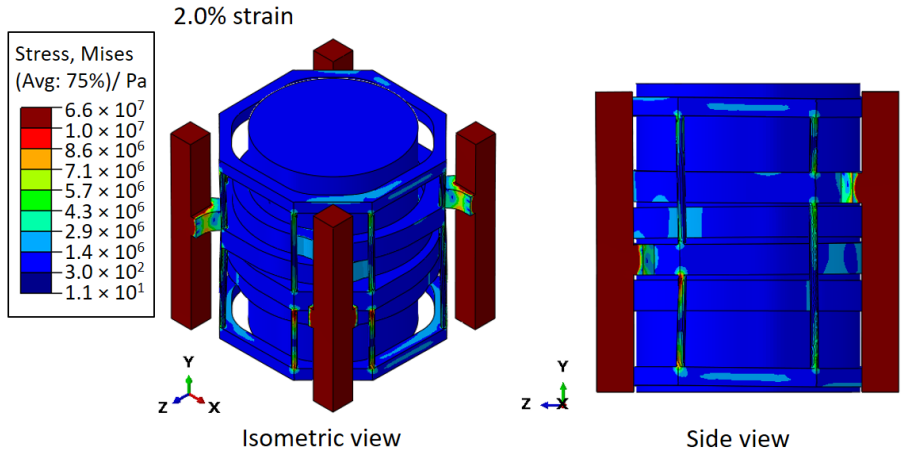
(a)


0.4% strain
Stress, Mises
(Avg: 75%)/ Pa
1.3 × 10^7
1.0 × 10^7
8.6 × 10^6
7.1 × 10^6
5.7 × 10^6
4.3 × 10^6
2.9 × 10^6
1.4 × 10^6
3.0 × 10^2
1.2 × 10^2
Y
Z
X
Isometric view
Y
Z
Side view

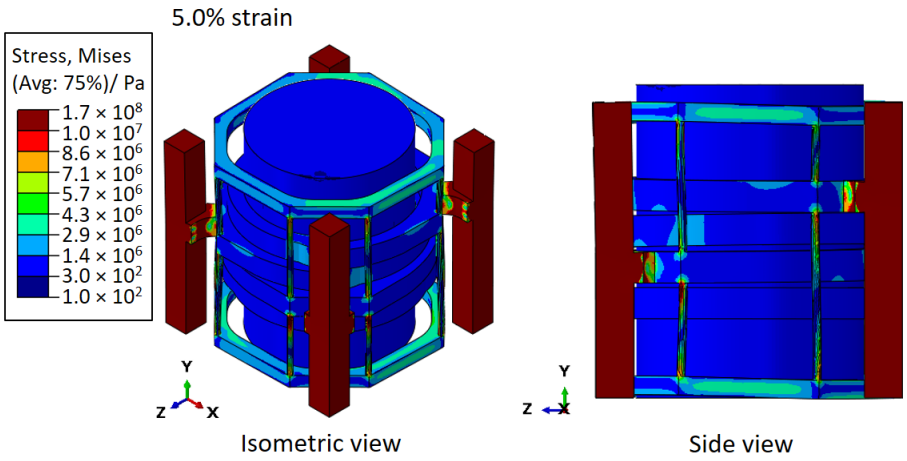
(b)


1.5% strain
Stress, Mises
(Avg: 75%)/ Pa
5.0 × 10^7
1.0 × 10^7
8.6 × 10^6
7.1 × 10^6
5.7 × 10^6
4.3 × 10^6
2.9 × 10^6
1.4 × 10^6
3.0 × 10^2
5.0 × 10^1
Y
Z
X
Isometric view
Y
Z
Side view

(c)



(d)

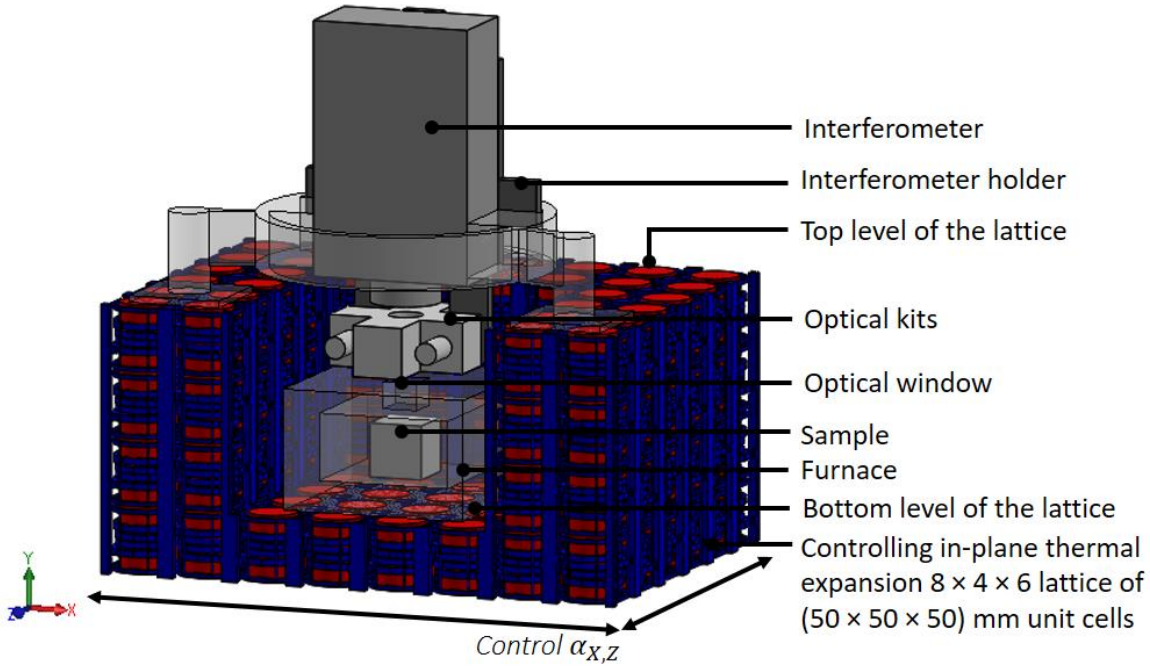


(e)

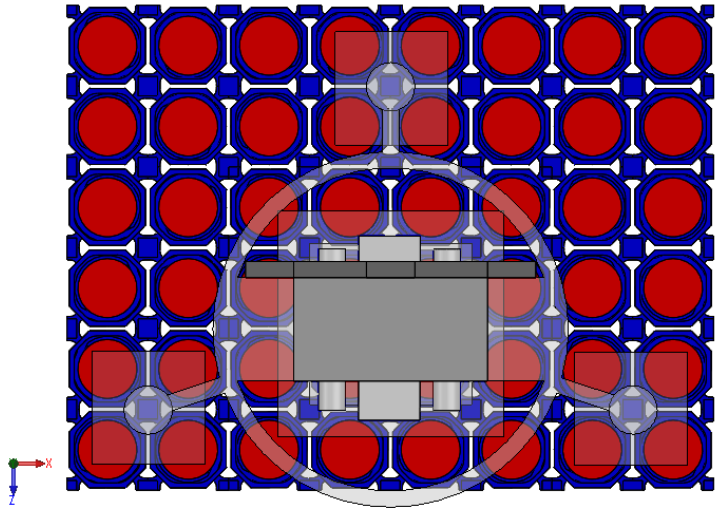
Figure 7.5 Contour plots of von Mises Stress after temperature increase (with a deformation factor of 1) for the unit cell of Iteration 4.1 compressed by applied loads equivalent to a value of strain along the Y-axis (a) 0.1 % strain, (b) 0.4 % strain, (c) 1.5 % strain, (d) 2.0 % strain and (e) 5.0 % strain.

7.1.3. Implementation of Iteration 4.1 for an optical vertical dilatometer

Figure 7.6 shows an example of the use of the (40 × 20 × 30) cm lattice to house an optical vertical dilatometer. The optical vertical dilatometer was composed of a DMS and a heating system. Thermal symmetry was implemented in the metrology frame design, resulting in an opposite and equal thermal expansion in the two symmetric sides of the frame [14]. The heat sources of the system (a laser interferometer and a furnace) were placed in the middle of the metrology frame.



(a)



(b)

Figure 7.6 Illustration of precision measurement equipment with the 8 × 4 × 6 lattice; an optical vertical dilatometer (taken and modified from Juasiripukdee et al.'s work [124]). (a) A 3D view and (b) a top view.

The estimated mass of the DMS, including an XL-80 laser interferometer, a measurement optics kit and a kinematic setup (interferometer holder), was approximately 4 kg. The DMS was mounted on the top level of the lattice (see Figure 7.6) with three sets of load-bearing pillars that could support a mass of up to 80.43 kg with 0.1 % strain. The heating system (a furnace) was placed on the bottom level of the lattice (see Figure 8.6) with nine sets of load-bearing pillars that could support a mass of up to 241.29 kg with 0.1 % strain. The estimated mass of the furnace was not greater than 15 kg. Therefore, a mass of 2 kg, applied on each (50 × 50 × 50) mm unit cell, was assumed, and the total reaction force was computed to be 19.6 N, equivalent to approximately 0.0076 % strain along the Y-axis. From the

deformation mechanism simulation, the CTE of a (50 × 50 × 50) mm unit cell in Iteration 4 with 0.0076 % strain along the Y-axis was found to be – 5.68 × 10^{-8} K^{-1}. Results for the (40 × 20 × 30) cm lattice, however, require considerably greater computational resources than could be employed here.

It can be noted that the lattice structure rendered an extremely low CTE in the XZ plane. However, since the lattice structure was not designed to control thermal expansion along the Y-axis, the metrology frame might thermally expand along this axis. For example, if the precision machine frame was made of Nylon 12 and the temperature increased by 1 °C, the thermal expansion of the structure would approximately be 2.18 × 10^{-5} m along the Y-axis. This thermal expansion was monitored by measuring the temperature of the structure, and minimised in the Y-axis by applying a thermal expansion correction, as described in the thermal expansion experimentation in Subchapter 6.4.

7.2. Discussion of Implementation of the lattice structures into a metrology frame

Iteration 4.1 was designed for implementation into a machine frame to support precision measurement equipment in a typical temperature-controlled metrology laboratory over the temperature fluctuation range of around 19 °C to 23 °C. With three restrictions, design a precision machine frame is simple, as discussed in the beginning of this chapter.

The determination of the elastic modulus and the deformation mechanism were performed, with tests showing that the selected unit cell of Iteration 4.1 could support the applied loads along the Y-axis. Figure 7.5 illustrates contour plots of von Mises Stress of the unit cell of Iteration 4.1, following the temperature increase and during its compression by applied loads generating 0.1 % to 5 % strain along the Y-axis. From Figure 7.5, it can be seen that there are two types of loads that generate stress in the structure, which are the applied loads and the temperature increase caused by mismatching CTEs in the parts. The unit cell of (50 × 50 × 50) mm was deformed by a 0.1 % strain along the Y-axis when the weight produced by a 26.81 kg mass was applied. With the total force applied being equivalent to a 0.1 % strain along the Y-axis, the unit cell yielded a CTE of −0.86 × 10^{-6} K^{-1}.

There are three methods to keep the in-plane CTE of a structure close to the original value it was designed for (1.4 × 10^{-9} K^{-1}). The first method consists of reducing and optimising the equipment weight to minimise strain along the Y-axis which normally affects the structure CTE. However, this method is challenging as the equipment supplied by the manufacturer is typically difficult to modify. The second method involves increasing the areas where loads are applied (load-bearing pillar's top surfaces, as shown in Figure 7.3) to reduce the strain along the Y-axis. In the design of Iteration 4.1, the top surfaces of the load-bearing pillar can be increased from 0.12 L up to 0.15 L (maximum value

that the lattice was designed for). A (50 × 50 × 50) mm unit cell with a load-bearing pillar's top surface of 0.15 L will likely be able to support a weight of about 1.6 times (produced by a 41.28 kg mass) more than the weight that can be supported by a unit cell with a load-bearing pillar's top surface of 0.12 L. This can be easy to calculate, as demonstrated in Subchapter 7.1.2. The third method consists of changing the material of the outer part of the lattice structure to other materials with higher strength, such as metals, to reduce strain along the Y-axis.

As described in Subchapter 7.1.3, the optical vertical dilatometer represents an example of the use of the (40 × 20 × 30) cm lattice as a precision metrology frame with several principles of precision machine frame design implemented. To increase measurement accuracy, the thermal expansion of the structure along the Y-axis is taken into account. This thermal expansion can be monitored and minimised by measuring the temperature of the structure and applying corrections with reference to its thermal expansion, as described in Subchapter 7.1.3.

As previously mentioned, choosing other materials, such as metals, can reduce thermal expansion along the Y-axis. In manufacturing aspects, LPBF machines allow for the fabrication of metallic lattice structures conveniently and effectively [152]. Examples of metallic structures include Ti–6Al–4V (with CTE = 11.5 × 10^{-6} K^{-1}) [66], which is about 0.1 times less than that of Nylon 12 and 0.2 times less than that of Al-Si10-Mg (with CTE = 20.5 × 10^{-6} K^{-1} [153]). If a precision machine frame is made of Ti–6Al–4V and the temperature was raised by 1 °C, the structure will thermally expand by approximately 0.46 × 10^{-6} m, which is relatively low compared to the expansion of a Nylon 12 structure in a similar scenario. Using Ti–6Al–4V as the structure's material, the elastic modulus of the lattice structure can increase to 113.5 GPa [154], which is 63 times higher than the elastic modulus of Nylon 12 (1.8 GPa), resulting in a higher capability to support applied loads. Choosing other materials also allows for the modification of lattice outer part geometries, such that the ratio α_2/α_1 would increase and the size of the cylindrical inner part would not need to be as large it is if the original material was kept. A smaller size of the cylindrical inner part of the lattice may possibly lead to a zero CTE.

7.3. Conclusion

Iteration 4.1 was designed for implementation into a machine frame to support precision measurement equipment. With three restrictions in place, as discussed in Subchapter 7.1.1, the design of a precision machine frame is a simple task. The determination of both the elastic modulus and the deformation mechanism was performed. Tests have shown that a selected unit cell of Iteration 4.1 can support applied loads along the Y-axis. The deformation mechanism fails when the strain along the Y-axis equals 1.5 %.

This chapter also described an example using the (40 × 20 × 30) cm lattice with the optical vertical dilatometer. The weight produced by a 2 kg mass was applied on each of the (50 × 50 × 50) mm unit cells, which was equivalent to approximately 0.0076 % of the strain along the Y-axis. Consequently, the CTE of a (50 × 50 × 50) mm unit cell of Iteration 4 with 0.0076 % strain along the Y-axis resulted to be $-5.68 \times 10^{-8}\ K^{-1}$.

8. General discussion, conclusions and future work

8.1. General discussion of the thesis

In this subchapter, I will summarise the findings of my PhD, with reference to the main aim set out at the beginning of this thesis: to design a low thermal expansion machine frame to support precision measurement equipment. Such a frame would ultimately be used in a temperature-controlled metrology laboratory. The research objectives, as reflected in the research questions stated in Chapter 1, are:

- To design, analyse and manufacture a range of novel structures with tunable thermal expansions
- To develop a thermal expansion measuring machine to experiment with a range of novel structures with tunable thermal expansions
- To implement the newly designed structures, with tunable thermal expansions, to produce a low thermal expansion machine frame

From the review conducted in Chapter 2, it is clear that, given the need for a low thermal expansion frame, designing a requirement compliant lattice structure is an evident solution. With reference to the literature, the existing studies on lattice structures with low coefficient of thermal expansion (CTE) are preliminary, and there is room for improvement as far as the development of lattice structures with low CTE is concerned. This aim was achieved by meeting the previously set objectives with the following research contributions:

- Contribution 1: Design of lattice structures for low coefficient of thermal expansion and the effects of various finite element modelling parameters on the thermal expansion of a newly proposed expansion-compensating lattice structure
- Contribution 2: In-house lattice structure thermal expansion experiments and their uncertainty analysis, and determining the main influencing factors on CTE results

8.1.1. Contribution 1

In Chapter 4, novel structures with tunable thermal expansion were proposed, and details of their design for low coefficients of thermal expansion were provided. The lattice outer and cylindrical inner parts were fabricated using an additive manufacturing (AM) process and a conventional manufacturing process, respectively, resulting in much higher differences in CTE between the two

materials compared to using a single AM process because there is no restriction by the limited material selection associated with AM. A combination of manufacturing processes provides a broader range of material selection and a lower price in a manufacturing process (conventional). The designed lattice structures yielded in-plane CTEs that were positive, negative and near zero. It was demonstrated that the CTE could be tailored by changing the ratio between the original diameter of the cylindrical inner part and the original length of the lattice, and the ratio between the CTEs of the cylindrical inner part material and the lattice outer part material. Additionally, pattern selection was introduced to reduce differences between CTEs in the X- and Z-axes of the lattices, which compensated for the anisotropy of the lattice. In the latter part of Chapter 4, the final design (Iteration 4.1) could yield a broader range of CTEs, including near-zero. Although other polymer-based structures could provide wider ranges of CTEs than the lattice presented in this research (i.e., -434×10^{-6} K^{-1} to 396×10^{-6} K^{-1} from Akihiro et al. [79] and -300×10^{-6} K^{-1} to 1000×10^{-6} K^{-1} from Takezawa and Kobashi [80]), the internal geometries of such structures were more complex, required additional topology optimisation to model the structures, and required the use of advanced multi-material AM processes for fabrication. The structure of Iteration 4.1 could yield a CTE of 1×10^{-9} K^{-1}, which is a much lower CTE than that achieved by several commercial instruments and functional surfaces in optical breadboards (CTE of 23×10^{-6} K^{-1} for aluminium 7075 and 10×10^{-6} K^{-1} for stainless steel 431 CTE [87]).

In Chapter 5, an investigation was conducted on the effects of various finite element modelling parameters on the thermal expansion of the newly proposed expansion-compensating lattice structures. The parameters that affect simulated thermal expansion, including procedure type, boundary conditions, partitions for contact, partitions for reducing mesh density, and element type, were investigated and compared with previous studies. Procedure type and boundary conditions (as described in Chapter 5) were specifically selected and assigned to conduct the thermal expansion simulation, the same as earlier studies [67, 68, 104]. More details on lattice thermal expansion, can be found in the author's published work [124] in Low Thermal Expansion Machine Frame Designs Using Lattice Structures. Additionally, finite element modelling provides a large number of design iterations possible, as well as options to extract lots of data that would be hard to measure. This work also represents an understanding of how thermal expansion simulations using finite element analysis can be optimised for novel structures.

8.1.2. Contribution 2

In Chapter 6, an in-house thermal expansion measuring machine and an interferometric dilatometer were constructed, based on the need for thermal expansion measurement system with large specimen size and small resolution, especially lattice structures. The thermal expansion measuring

machine was developed using a hot plate, a laser interferometer with a plane mirror technique, and a thermal expansion experimental frame. The machine could measure the designed lattices with the size of (50 × 50 × 50) mm. Kinematic design principles (as described in Subchapter 2.2) were applied to improve the accuracy and stability of the laser interferometer. The machine configurations were implemented following the design of precision machine frame methodologies, such as the thermal centre principle and the symmetrical concepts, as described in Subchapter 2.2. The mathematical model was applied to correct unwanted thermal expansions during the experiment. The research measured steel gauge blocks in a temperature range of 30 °C to 34 °C. The total uncertainty of the measurement was estimated from the measurement of three different lengths of specimens to be 2.4 to 3.3 × 10^{-6} K^{-1} on the steel gauge material with a linear CTE of 11.5 × 10^{-6} K^{-1}. All uncertainty calculations followed internationally accepted guidelines founded in GUM: Guide to the Expression of Uncertainty in Measurement [143]. Despite yielding results with significant uncertainties compared to previous studies [2, 111-113] (as described in Subchapter 2.6), the proposed interferometric dilatometer utilised a less complicated approach (single path). It was demonstrated that a single path interferometer, with the correction equations, can yield accurate measurement results which are capable of precise measurements. The proposed machine was successfully verified and evaluated to measure the coefficient of thermal expansion via comparing measured data with given data and employing the techniques discussed throughout this thesis. Additionally, the CTEs of the manufactured lattice structures (Iterations 2.4 and 3.1) were presented. Their experimental CTEs ± their expanded uncertainty did not match the CTEs from the simulation (157.9 % for Iteration 2.4 and 592.0 % for Iteration 3.1), as seen in CTE Percentage Difference Between Data Sheets Or Simulations And The Experiment, Table 6.15. The possible explanations for these uncertainties are presented in Subchapter 6.6. Then, the experimental CTE results presented in Chapter 6 were elaborated on and explained, by assessing the effects of varying certain key parameters on the CTE of a selected structure (Iteration 3.1). It can be concluded that the ratios D/L and α_2/α_1 are the two major influencing factors that affect the lattice structure's CTE. Therefore, selecting materials and manufacturing techniques is essential in fabricating lattice structures with a low CTE. In terms of the contribution made to science, the developed in-house thermal expansion measuring machine represents an example of a new method for measuring thermal expansion, especially that of lattice structures. This work also represents a fundamental step towards determining the main influencing factors on CTE results.

Additionally, Chapter 7 presented the lattice structures (final iteration) implementation into a metrology frame, including three restrictions for implementation (detailed in Chapter 7), elastic modulus and deformation mechanism determination, and the implementation of Iteration 4.1 into an

optical vertical dilatometer. This work also represents a fundamental step towards understanding the implementation of lattice structures into a metrology frame.

8.2. Conclusions

Several conclusions can be drawn from the work performed during this PhD. Primarily, I have demonstrated the implementation of a lattice structure into a metrology frame following well-defined steps. I began by proposing novel structures with tunable thermal expansion, composed of two different positive CTE materials and void spaces. The lattice outer parts were manufactured using an AM process, namely polymer laser powder bed fusion, and the cylindrical inner parts were selected from a range of conventional industrial materials.

The thermal expansion of the lattice structures was tested in both simulation and experiment. Results showed deviations due to the uncertainties of many factors described in Chapter 6. Accordingly, the lattice structures were assigned theoretically computed in-plane CTEs that are positive, negative and near zero. Such results can be used as guidelines to achieve tailorable thermal expansion in lattice structures fabricated using AM. I have also developed an interferometric dilatometer, which was used alongside a laser interferometer and a plane mirror technique to experiment on the thermal expansion of lattice structures.

Finally, I have demonstrated the implementation of a lattice structure with low thermal expansion into a low thermal expansion machine frame. Lattice structures designers can refer to these outcomes for assistance with designing parts for use in metrology and precision engineering applications.

8.3. Future work

8.3.1. Design of lattice structures for low coefficient of thermal expansion

In general, lattice structures benefit from advances in the precision, accuracy, and optimised manufacturable properties of AM techniques. The results presented in this thesis could still be applicable when such technological progress is achieved. Lattice structures with low CTE can be implemented not only in metrology frames but also in any structure requiring low thermal expansion.

To achieve alternative material properties, there is no need for a change of the entire unit cell as its features can be simply adjusted for variations in material properties, such as the CTE and the strength supported. The CTE results presented in this PhD can be used as guidelines to achieve a tailorable

property in lattice structures, and the strength-supported results can be easily calculated for their capacity.

The proposed unit cell in this work can tailor the thermal expansion in only two planar dimensions in the XZ plane, as described in Chapter 4. Therefore, there is an opportunity to develop novel lattice structures with similar concepts into 2D controlled thermal expansion lattice structures controlled in different planes, such as the XY plane and YZ plane, as well as 3D controlled thermal expansion lattice structures.

Additionally, these results open up prospects for the investigation of alternative materials, including new materials for AM, that can be utilised within structures for metrology and precision engineering applications. New hybrid materials could also be explored to design structures of enhanced load-bearing and tailorable thermal expansion capabilities compared to existing technologies.

8.3.2. Finite element simulation of lattice structures

One limitation of the finite element simulation proposed in this PhD is the memory shortage of the employed processors. This limitation can be overcome by increasing the memory of the processor or reducing the used memory within the processor. Finding larger memory processors is a challenge, which will possibly increase the processing cost. Nonetheless, such memory reduction can be achieved in alternative ways, such as decreasing mesh density in unnecessary regions and reducing the complexity of the mathematical equations by using a simpler mesh element type. However, these solutions could take much more time to investigate and optimise. Once memory usage is optimised, larger structures can be investigated.

8.3.3. Thermal expansion experiments for lattice structures

The in-house thermal expansion measuring machine was developed using a laser interferometer with a plane mirror technique and an interferometric dilatometer. The CTE experimental results measured by the machine showed that it could perform an accurate measurement, as discussed in Chapter 6. However, the machine can still be improved by:

- Increasing the number of components: increasing the number of heat sources can make the air temperature inside the box steadier, and increasing the number of axial fans can increase air circulation inside the box. The accuracy of these corrections can be enhanced by increasing the number of thermocouples mounted on the components and improving the accuracy of

the average temperature changes analysed in the mathematical model. However, all components must be carefully rearranged due to the limited space available within the box.

- Implementing a new temperature measurement system: the usage of thermal imaging cameras in the infrared (IR) range can improve the accuracy of average temperature changes, since IR cameras can measure the temperature of the entire environment, notably the specimens. This system can also potentially eliminate some steps in the experimental procedure, i.e., removing and reinstalling thermocouples on specimens.

The developed interferometric dilatometer can only be used for the measurement of lattice structures, including solid materials in the vertical direction. This is considered a drawback in the case where a lattice structure could be designed only for measurement in the horizontal direction, as discussed in Iteration 4.1 in Chapter 6. Therefore, there is room for improvement to enable the measurement of displacements in the horizontal direction.

8.3.4. Implementation of the lattice structures into a metrology frame

In this PhD, the designed lattice structure with low thermal expansion was implemented into a low thermal expansion machine frame. However, it was not possible to manufacture this implementation, due to the limited period of time allocated to carry out this research. This is, therefore, an opportunity for future researchers to fabricate the designed lattice structure and implement it in a physical application. Manufacturing and testing the structure can help verify the previous made assumptions and the computationally achieved results, in addition to aiding in the development of a better understanding of lattice structures.

Bibliography

1. Mohammed Wahed Hussain, M.Y.H.A., *Significance and Importance of Thermal Expansion.* IOSR Journal of Applied Physics 2017. **9**(5): p. 68-73.

2. Hughes, E.B., *Measurement of the linear thermal expansion coefficient of gauge blocks by interferometry.* SPIE, 1993. **2088**: p. 179-189.

3. Phillips, S.D., et al., *The 2016 Revision of ISO 1 - Standard Reference Temperature for the Specification of Geometrical and Dimensional Properties.* Journal of research of the National Institute of Standards and Technology, 2016. **121**: p. 498-504.

4. Bailey, S.L., Andrew, *Good Practice Guide No.149 Care and Use of Gauge Blocks*. 2017, National Physical Laboratory: Middlesex, UK.

5. Harding, K., *Optical Metrology Overview*, in *Handbook of Optical Dimensional Metrology*, K. Harding, Editor. 2013, CRC Press. p. 3-35.

6. Seugling, R.M., *System Modelling*, in *Basics of Precision Engineering*, R.K. Leach and S.T. Smith, Editors. 2018, CRC Press: Boca Raton. p. 369-415.

7. Lienhard IV, J.H. and J.H. Lienhard V, *A Heat Transfer Textbook*. 5th edition ed. 2019, New York, USA: Dover Publications.

8. Hill, K. *How Does an Oven Cook Food with Conduction, Convection, and Radiation?* 2022 [cited 2022 24 June]; Available from: https://zippyfacts.com/how-does-an-oven-cook-food-with-conduction-convection-and-radiation/.

9. News, B. *Reducing heat transfers – houses - Heat transfer - CCEA - GCSE Physics (Single Science) Revision - CCEA - BBC Bitesize*. 2023 [cited 2023; Available from: https://www.bbc.co.uk/bitesize/guides/zr7j382/revision/5.

10. Efficiency, A.E. *How to control heat transfer*. 2023 [cited 2023; Available from: https://andersonenergy.com.au/control-heat-transfer/.

11. Jia, G., et al., *Ambient temperature-induced thermal error modelling for a special CMM at the workshop level based on the integrated temperature regression method.* International journal of advanced manufacturing technology, 2022. **121**(9-10): p. 5767-5778.

12. Leach, R. and S.T. Smith, *Basics of Precision Engineering*. 2018, Florida, US: CRC Press.

13. UKAS, *LAB 36 Laboratory Accommodation and Environment in the Measurement of Length, Angle and Form*. 2019, United Kingdom Accreditation Service: UK.

14. Bosmans, N. and D. Reynaerts, *Force Loops*, in *Basics of Precision Engineering*, R.K. Leach and S.T. Smith, Editors. 2018, CRC Press: Florida, USA. p. 493-518.

15. Haitjema, H., *Measurement Uncertainty*, in *Basics of Precision Engineering*, R.K. Leach and S.T. Smith, Editors. 2018, CRC Press. p. 413-448.

16. Winter, R.E., et al., *Plate-impact loading of cellular structures formed by selective laser melting.* Modelling and Simulation in Materials Science and Engineering, 2014. **22**(2).

17. Maskery, I., et al., *Compressive failure modes and energy absorption in additively manufactured double gyroid lattices.* Additive Manufacturing, 2018: p. 24-29.

18. Maskery, I., et al., *An investigation into reinforced and functionally graded lattice structure.* Journal of Cellular Plastics, 2017. **53**(2).

19. Kirsch, K.L. and K.A. Thole, *Pressure loss and heat transfer performance for additively and conventionally manufactured pin fin arrays.* International Journal of Heat and Mass Transfer, 2017. **108**(PB): p. 2502-2513.

20. Syam, W.P., et al., *Design of mechanically-optimised lattice structures for vibration isolation*. 2017.

21. Elmadih, W., et al., *Mechanical vibration bandgaps in surface-based lattices.* Additive Manufacturing, 2019. **25**: p. 421-429.

22. Waiel, E., et al., *Multidimensional Phononic Bandgaps in Three-Dimensional Lattices for Additive Manufacturing.* Materials, 2019. **12**(11): p. 1878.

23. Economidou, S.N. and D. Karalekas, *Optical sensor-based measurements of thermal expansion coefficient in additive manufacturing.* Polymer Testing, 2016. **51**: p. 117-121.

24. Parsons, E.M., *Lightweight cellular metal composites with zero and tunable thermal expansion enabled by ultrasonic additive manufacturing: Modeling, manufacturing, and testing.* Composite Structures, 2019.

25. Lopez Taborda, L.L., H. Maury, and J. Pacheco, *Design for additive manufacturing: a comprehensive review of the tendencies and limitations of methodologies.* Rapid Prototyping Journal, 2021. **27**(5): p. 918-966.

26. 3Dprinting. *How 3D Printed Lattice Structures Improve Mechanical Properties*. 2019 [cited 2022 25 June]; Available from: https://3dprinting.com/tips-tricks/3d-printed-lattice-structures/.

27. Slocum, A.H., *Precision Machine Design*. 1992, USA: Penintence Hall.

28. Miller, J., *Metrology*, in *Basics of Precision Engineering*, R.K. Leach and S.T. Smith, Editors. 2018, CRC Press: Florida, USA. p. 25-49.

29. Leach, R.K. and S.T. Smith, *Introduction to Precision*, in *Basics of Precision Engineering*, R.K. Leach and S.T. Smith, Editors. 2018, CRC Press: Florida, USA. p. 1-23.

30. Kroll, E., *Design theory and conceptual design: contrasting functional decomposition and morphology with parameter analysis.* Research in engineering design, 2012. **24**(2): p. 165-183.

31. Leach, R.K., *Fundamental Principle of Engineering Nanometrology*. Second ed. Micro & Nano Technologies. 2014, USA: Elsevier.

32. Leach, R.K. and S.T. Smith, *Basics of Precision Engineering*, ed. R.K. Leach and S.T. Smith. 2018, Florida, USA: CRC Press.

33. Chetwynd, D.G., *Materials Selection in Precision Mechanics*, in *Basics of Precision Engineering*, R.K. Leach and S.T. Smith, Editors. 2018, CRC Press: Florida, USA. p. 519-563.

34. Liang, Y., et al., *Design and dynamic optimization of an ultraprecision diamond flycutting machine tool for large KDP crystal machining.* International journal of advanced manufacturing technology, 2013. **69**(1-4): p. 237-244.

35. Karim, S. and U. Weber, *Kinematic Design*, in *Basics of Precision Engineering*, R.K. Leach and S.T. Smith, Editors. 2018, CRC Press: Florida, USA. p. 207-263.

36. Mason, M.T., *Mechanics of Robotic Manipulation*. 2001, Cambridge, Massachusetts: Cambridge, Massachusetts: MIT Press.

37. Whitehouse, D.J., *Handbook of Surface and Nanometrology*. Second ed. 2010, Florida, USA: CRC Press.

38. Dornfeld, D.A. and D.-E. Lee, *Precision manufacturing*, ed. D.-E. Lee. 2008, London: Springer.

39. Williamson, J.B.P. and R.T. Hunt, *Relocation profilometry.* Journal of physics. E, Scientific instruments, 1968. **1**(7): p. 749-752.

40. Ashby, M.F., *Materials Selection in Mechanical Design*. fifth ed. 2016, Oxford, UK: Elsevier Science, Butterworth-Heinemann.

41. Chen, D. and X. Zheng, *Multi-material Additive Manufacturing of Metamaterials with Giant, Tailorable Negative Poisson's Ratios.* Scientific Reports, 2018. **8**(1).

42. Yang, L., et al., *Non-stochastic Ti–6Al–4V foam structures with negative Poisson's ratio.* Materials Science & Engineering A, 2012. **558**: p. 579-585.

43. Prawoto, Y., *Seeing auxetic materials from the mechanics point of view: A structural review on the negative Poisson's ratio.* Computational Materials Science, 2012. **58**(C): p. 140-153.

44. Bezazi, A. and F. Scarpa, *Mechanical behaviour of conventional and negative Poisson's ratio thermoplastic polyurethane foams under compressive cyclic loading.* International Journal of Fatigue, 2007. **29**(5): p. 922-930.

45. Ma, C., et al., *Macroscopic mechanical response of chiral-type cylindrical metastructures under axial compression loading.* Materials & Design, 2018. **158**: p. 198-212.

46. Zhang, X.G., et al., *A novel auxetic chiral lattice composite: Experimental and numerical study.* Composite structures, 2022. **282**: p. 115043.

47. Maskery, I., et al., *Effective design and simulation of surface-based lattice structures featuring volume fraction and cell type grading.* 2018.

48. Pan, C., Y. Han, and J. Lu, *Design and optimization of lattice structures: A review.* Applied sciences, 2020. **10**(18): p. 1-36.

49. Tao, W. and M.C. Leu, *Design of lattice structure for additive manufacturing*. 2016. p. 325-332.

50. Gibson, L.J. and M.F. Ashby, *Cellular Solids: Structure and Properties*. 2 ed. Cambridge Solid State Science Series. 1997, Cambridge: Cambridge University Press.

51. O'Neal, B. *Rice University Researchers Using OpenSLS 3D Printer to Create 3D Printed Lattices for Bone Tissue Engineering*. 2016 [cited 2019 9 July]; Available from: https://3dprint.com/121338/3d-print-lattices-bone-tissue/.

52. Saunders, S. *Additive Orthopaedics Receives 510(k) Clearance for Patient Specific 3D Printed Bone Segments*. 2018 [cited 2019 09 July]; Available from: https://3dprint.com/214299/additive-orthopaedics-3d-bone/.

53. Materialise. *Materialise Slicing Technology Enables Toyota's Lightweight Car Seat*. 2019; Available from: https://www.materialise.com/en/cases/materialise-slicing-technology-enables-toyota%E2%80%99s-lightweight-car-seat.

54. O'Neal, B. *Carbon Takes On Foam Innovation with 3D Printing.* 2017 [cited 2019 9 July]; Available from: https://3dprint.com/196746/carbon-foam-innovation/

55. Lane, L. *Tessa's Weekly Picks – 3D Printed Helmets - LEO Lane*. 2019 [cited 2019 10 June]; Available from: https://www.leolane.com/blog/tessas-weekly-picks-3d-printed-helmets/.

56. Dissolve. *Clip D30_33_213, from Dissolve*. 2019 [cited 2019 30 May]; Available from: https://dissolve.com/video/Bone-tissue-Animated-coloured-scanning-electron-micrograph-rights-managed-stock-video-footage/002-D30-33-213.

57. Lincsaquatics. *Oase BioSmart 18-36000 Replacement Filter Foams*. 2019 [cited 2019 10 June]; Available from: https://www.lincsaquatics.co.uk/products/oase-biosmart-18-36000-replacement-filter-foams.

58. PipingRock. *Honey Fragrance Oil 2 oz (59 ml) Dropper Bottle | Piping Rock Health Products*. 2019 [cited 2019 10 June]; Available from: https://www.pipingrock.com/fragrance/honey-honeycomb-fragrance-oil-12-fl-oz-15-ml-dropper-bottle-6882.

59. Matlack, K.H., et al., *Composite 3D-printed metastructures for lowfrequency and broadband vibration absorption.* Proceedings of the National Academy of Sciences of the United States of America, 2016. **113**(30): p. 8386-8390.

60. Wang, X., et al., *Natural frequency optimization of 3D printed variable-density honeycomb structure via a homogenization-based approach.* Additive Manufacturing, 2018. **20**: p. 189-198.

61. Hart, L.R., et al., *3D Printing of Biocompatible Supramolecular Polymers and their Composites.* ACS applied materials & interfaces, 2016. **8**(5): p. 3115.

62. Aboulkhair, N.T., et al., *Selective laser melting of aluminum alloys.* MRS Bulletin, 2017. **42**(4): p. 311-319.

63. Ashby, M.F., *The properties of foams and lattices.* Philosophical transactions. Series A, Mathematical, physical, and engineering sciences, 2006. **364**(1838): p. 15.

64. Maconachie, T., et al., *SLM lattice structures: Properties, performance, applications and challenges.* Materials & design, 2019. **183**: p. 108137.

65. Berger, J., et al., *The Design of Bonded Bimaterial Lattices that Combine Low Thermal Expansion with High Stiffness.* Journal Of The American Ceramic Society, 2011. **94**(S6): p. S42-S54.

66. Hang, X. and P. Damiano, *Structurally Efficient Three-dimensional Metamaterials with Controllable Thermal Expansion.* Scientific Reports, 2016. **6**(1).

67. Ai, L. and X.L. Gao, *Metamaterials with negative Poisson's ratio and non-positive thermal expansion.* Composite Structures, 2017. **162**: p. 70-84.

68. Ai, L. and X.L. Gao, *Three-dimensional metamaterials with a negative Poisson's ratio and a non-positive coefficient of thermal expansion.* International Journal of Mechanical Sciences, 2018. **135**: p. 101-113.

69. Xu, S., et al., *Design of lattice structures with controlled anisotropy.* Materials & Design, 2016. **93**: p. 443-447.

70. Ngim, D.B., J.S. Liu, and R.C. Soar, *Design optimization of consolidated granular-solid polymer prismatic beam using metamorphic development.* International Journal of Solids and Structures, 2009. **46**(3-4): p. 726-740.

71. Zhang, C., et al., *Multiscale topology optimization for solid-lattice-void hybrid structures through an ordered multi-phase interpolation.* Computer aided design, 2023. **154**.

72. Kim, T., et al., *Convective heat dissipation with lattice-frame materials.* Mechanics of Materials, 2004. **36**(8): p. 767-780.

73. Cheng, L., et al., *Coupling lattice structure topology optimization with design-dependent feature evolution for additive manufactured heat conduction design.* Computer Methods in Applied Mechanics and Engineering, 2018. **332**: p. 408-439.

74. Abueidda, D.W., et al., *Effective conductivities and elastic moduli of novel foams with triply periodic minimal surfaces.* Mechanics of Materials, 2016. **95**(C): p. 102-115.

75. Zhou, H., et al., *Lightweight structure of a phase-change thermal controller based on lattice cells manufactured by SLM.* Chinese Journal of Aeronautics, 2018.

76. Pelanconi, M., et al., *Thermal design, optimization and additive manufacturing of ceramic regular structures to maximize the radiative heat transfer.* Materials & Design, 2018: p. 107539.

77. Sigmund, O. and S. Torquato, *Composites with extremal thermal expansion coefficients.* Applied Physics Letters, 1996. **69**(21): p. 3203-3205.

78. Werner, M.R. and W.R. Fahrner, *Review on materials, microsensors, systems and devices for high-temperature and harsh-environment applications.* IEEE transactions on industrial electronics (1982), 2001. **48**(2): p. 249-257.

79. Akihiro, T., K. Makoto, and K. Mitsuru, *Porous composite with negative thermal expansion obtained by photopolymer additive manufacturing.* APL Materials, 2015. **3**(7): p. 076103-076103-6.

80. Takezawa, A. and M. Kobashi, *Design methodology for porous composites with tunable thermal expansion produced by multi-material topology optimization and additive manufacturing.* Composites Part B, 2017. **131**: p. 21-29.

81. Lakes, R., *Cellular solid structures with unbounded thermal expansion.* Journal of Materials Science Letters, 1996. **15**(6): p. 475-477.

82. Lakes, R., *Cellular solids with tunable positive or negative thermal expansion of unbounded magnitude.* Applied Physics Letters, 2007. **90**(22).

83. Lehman, J. and R. Lakes, *Stiff lattices with zero thermal expansion.* Journal of Intelligent Material Systems and Structures, 2012. **23**(11): p. 1263-1268.

84. Lehman, J. and R. Lakes, *Stiff lattices with zero thermal expansion and enhanced stiffness via rib cross section optimization.* International Journal of Mechanics and Materials in Design, 2013. **9**(3): p. 213-225.

85. Zhang, Y.C., et al., *A new design of dual-constituent triangular lattice metamaterial with unbounded thermal expansion.* Acta Mechanica Sinica/Lixue Xuebao, 2018.

86. Wu, L., B. Li, and J. Zhou, *Isotropic Negative Thermal Expansion Metamaterials.* ACS applied materials & interfaces, 2016. **8**(27): p. 17721.

87. Yu, H., et al., *Drastic tailorable thermal expansion chiral planar and cylindrical shell structures explored with finite element simulation.* Composite Structures, 2019. **210**: p. 327-338.

88. Hopkins, J., et al., *Polytope Sector-Based Synthesis and Analysis of Microstructural Architectures With Tunable Thermal Conductivity and Expansion.* Journal of Mechanical Design (Transactions of the ASME), 2016. **138**(5).

89. Jin, Z.H., *A microlattice material with negative or zero thermal expansion.* Composites Communications, 2017. **6**: p. 48-51.

90. Steeves, C.A., et al., *Concepts for structurally robust materials that combine low thermal expansion with high stiffness.* Journal of the Mechanics and Physics of Solids, 2007. **55**(9): p. 1803-1822.

91. Yamamoto, N., et al., *Thin Films with Ultra-low Thermal Expansion.* Advanced Materials, 2014. **26**(19): p. 3076-3080.

92. Berger, J. and R.M. McMeeking, *Mechanical characterization of a bonded tailorable coefficient of thermal expansion lattice with near optimal performance.* Journal Of Materials Research, 2018. **33**(20): p. 3383-3397.

93. Jefferson, G., T.A. Parthasarathy, and R.J. Kerans, *Tailorable thermal expansion hybrid structures.* International Journal of Solids and Structures, 2009. **46**(11-12): p. 2372-2387.

94. Yang, H. and L. Ma, *1D to 3D multi-stable architected materials with zero Poisson's ratio and controllable thermal expansion.* Materials & Design, 2020. **188**.

95. Wei, K., et al., *Additively manufactured bi-material metamaterial to program a wide range of thermal expansion.* Materials & design, 2021. **198**: p. 109343.

96. Phys.org. *Hot firing of world's first 3D-printed platinum thruster chamber*. 2019 [cited 2019 15 June]; Available from: https://phys.org/news/2015-06-hot-world-3d-printed-platinum-thruster.html.

97. International, A. *Standard Terminology for Additive Manufacturing Technologies*. ASTM F2792-12a 2012.

98. Lee, J.-Y., J. An, and C.K. Chua, *Fundamentals and applications of 3D printing for novel materials.* Applied Materials Today, 2017. **7**: p. 120-133.

99. Formlabs. *Form 3: Industrial-Quality Desktop SLA 3D Printer*. 2019 [cited 2019 20 June]; Available from: https://formlabs.com/3d-printers/form-3/.

100. Dizon, J.R.C., et al., *Mechanical characterization of 3D-printed polymers.* Additive Manufacturing, 2018. **20**: p. 44-67.

101. Stratasys. *J735 & J750 3D Printers for Realistic Prototypes | Stratasys*. 2019; Available from: https://www.stratasys.com/3d-printers/j735-j750.

102. MKSTechnologies. *POLYJET TECHNOLOGY – MKS Technologies Pvt Ltd.* 2019; Available from: http://www.mkstechgroup.com/polyjet-technology/.

103. Tasch, D., et al., *Thickness dependency of mechanical properties of laser-sintered polyamide lightweight structures.* Additive manufacturing, 2018. **23**: p. 25-33.

104. Abueidda, D.W., et al., *Micromechanical finite element predictions of a reduced coefficient of thermal expansion for 3D periodic architectured interpenetrating phase composites.* Composite Structures, 2015. **133**(C): p. 85-97.

105. Babaee, S., et al., *3D Soft Metamaterials with Negative Poisson's Ratio.* Advanced Materials, 2013. **25**(36): p. 5044-5049.

106. Cheng, L., J. Liu, and A.C. To, *Concurrent lattice infill with feature evolution optimization for additive manufactured heat conduction design.* Structural and Multidisciplinary Optimization, 2018. **58**(2): p. 511-535.

107. Shen, Y.L., *Thermal expansion of metal-ceramic composites: A three-dimensional analysis.* Materials Science and Engineering A, 1998. **252**(2): p. 269-275.

108. De Strycker, M., et al., *Measuring the thermal expansion coefficient of tubular steel specimens with digital image correlation techniques.* Optics and Lasers in Engineering, 2010. **48**(10): p. 978-986.

109. Ferrucci, M., H. Haitjema, and R.K. Leach, *Dimensional Metrology*, in *Basics of Precision Engineering*, R.K. Leach and S.T. Smith, Editors. 2018, CRC Press: Florida, USA. p. 151-2-3.

110. Badami, V.G. and P.J.d. Groot, *Displacement Measuring Interferometry*, in *Handbook of Optical Dimensional Metrology*, K. Harding, Editor. 2013, CRC Press: Florida, USA. p. 157-238.

111. Okaji, M. and H. Imai, *A practical measurement system for the accurate determination of linear thermal expansion coefficients.* Journal of physics. E, Scientific instruments, 1984. **17**(8): p. 669-673.

112. Wostenholm, G.H., et al., *Apparatus for the absolute measurement of the linear thermal expansion coefficient of solids over a wide temperature range.* Journal of physics. E, Scientific instruments, 1989. **22**(4): p. 222-229.

113. Okaji, M., N. Yamada, and H. Moriyama, *Ultra-precise thermal expansion measurements of ceramic and steel gauge blocks with an interferometric dilatometer.* Metrologia, 2000. **37**(2): p. 165-171.

114. Corsetti, J.A., et al., *Simultaneous interferometric measurement of linear coefficient of thermal expansion and temperature-dependent refractive index coefficient of optical materials.* Applied optics. Optical technology and biomedical optics, 2016. **55**(29): p. 8145-8152.

115. Bathe, K., *Finite element procedures*. 2 ed. 2014, Delhi: PHI Learning Private Limited.

116. Hesse, N., et al., *Analysis of tribo-charging during powder spreading in selective laser sintering: Assessment of polyamide 12 powder ageing effects on charging behavior.* Polymers, 2019. **11**(4): p. 609.

117. Tao, G., et al., *Exploring the entangled state and molecular weight of UHMWPE on the microstructure and mechanical properties of HDPE/UHMWPE blends.* Journal of applied polymer science, 2021. **138**(30): p. 50741-n/a.

118. GmbHEOS. *PA 2200 Balance 1.0*. 2018 [cited 2018 10 April]; Available from: https://www.sculpteo.com/static/0.30.0-49/documents/materials/polyamide_PA2200/PA2200_Product_information_03-10_en.pdf.

119. Khurmi, R.S. and J.K. Gupta, *A Textbook of Machine Design*. 34 ed. 2005, India: Chand (S.) & Co Ltd.

120. Ignatiev, A.A., et al., *Analysis of errors in measuring displacement by a laser interferometer used as a feedback sensor precision lathe module feed drive*. 2021, Bristol: IOP Publishing: Bristol. p. 52039.

121. kjn, A.P. *PRODUCT CATALOGUE*. 2018 [cited 2018 5 Jan].

122. Pirisinu, M. and V. Mazzarello, *3D profilometric characterization of the aged skin surface using a skin replica and alicona Mex software.* Scanning, 2016. **38**(3): p. 213-220.

123. Juasiripukdee, P., et al., *Low thermal expansion machine frame designs using lattice structures*, in *Special Interest Group: Thermal Issues*. 2020, euspen: Aachen, Germany.

124. Juasiripukdee, P., et al., *Low thermal expansion machine frame designs using lattice structures.* Applied Sciences, 2021. **11**(19): p. 9135.

125. MatWebLLC. *Polikim ULPOLEN® 500 UHMWPE Standard*. 2020 [cited 2020 10 August 2020]; Available from: http://www.matweb.com/search/DataSheet.aspx?MatGUID=e6f135cc9c044ae888668c396453307b&ckck=1.

126. Plastim. *Nylon 12*. 2015 [cited 2018 20 Dec]; Available from: https://plastim.co.uk/wp-content/uploads/2019/07/Nylon-12-Technical-Data-Sheet.pdf.

127. DirectPlastics. *UHMWPE Natural*. 2019 [cited 2019 21 Nov]; Available from: https://www.directplastics.co.uk/pdf/datasheets/UHMWPE%20Natural%20Data%20Sheet.pdf.

128. Qin, Q., et al., *Design and optimization of projection stereolithography additive manufacturing system with multi-pass scanning.* Rapid prototyping journal, 2021. **27**(3): p. 636-642.

129. GmbHEOS. *PA 2200 Product information*. 2001 [cited 2018 10 April]; Available from: https://www.sculpteo.com/static/0.30.0-49/documents/materials/polyamide_PA2200/PA2200_Product_information_03-10_en.pdf.

130. ABAQUS, I., *ABAQUS/CAE User's Manual*, in *ABAQUS Online Documentation: Version 6.6-1*. 2006, ABAQUS, Inc: Rhode Island, United States.

131. Tadepalli, S.C., A. Erdemir, and P.R. Cavanagh, *Comparison of hexahedral and tetrahedral elements in finite element analysis of the foot and footwear.* Journal of biomechanics, 2011. **44**(12): p. 2337-2343.

132. ABAQUS, I., *Static stress analysis*. 2022, ABAQUS, Inc: Rhode Island, United States.

133. Botella, A., B. Lévy, and G. Caumon, *Indirect unstructured hex-dominant mesh generation using tetrahedra recombination.* Computational geosciences, 2015. **20**(3): p. 437-451.

134. Zhou, J., et al., *Investigation and simulation based on mesoscopic model of SiCp/Al composites during precision machining: deformation mechanism and surface quality.* International journal of advanced manufacturing technology, 2021. **119**(3-4): p. 2173-2186.

135. Cole-Parmer. *Cole-Parmer StableTemp StableTemp Ceramic Top Hot Plate, 7" x 7", 230 V*. 2021 [cited 2021 21 Oct]; Available from: https://www.coleparmer.co.uk/i/cole-parmer-stabletemp-stabletemp-ceramic-top-hot-plate-7-x-7-230-v/0340516?pubid=OU.

136. TechnologyPICO. *TC-08 Cloud-connected 8-channel thermocouple data logger*. 2021 [cited 2021 2 Oct]; Available from: https://www.picotech.com/download/datasheets/usb-tc-08-thermocouple-data-logger-data-sheet.pdf.

137. RS. *RS PRO Type K Thermocouple 1m Length, 1/0.2mm Diameter → +250°C*. 2021 [cited 2021 21 Oct]; Available from: https://uk.rs-online.com/web/p/thermocouples/3630250.

138. Chapman, M.A.V., *Environmental Compensation of linear interferometer reading.* Renishaw Technical white paper, 2013(TE329).

139. RenishawPLC. *XL-80 laser measurement system*. 2021 [cited 2021 21 Oct]; Available from: https://uk.rs-online.com/web/p/thermocouples/3630250.

140. Thorlabs. *Kinematic Bases*. 2021 [cited 2021 28 Dec]; Available from: https://www.thorlabs.com/newgrouppage9.cfm?objectgroup_id=1546.

141. Neale, M.J., *Tribology Handbook*. 2nd ed. 1995, Oxford: Butterworth-Heinemann.

142. Jiang, X., et al., *Finite element analysis for the self-loosening behavior of the bolted joint with a superelastic shape memory alloy.* Materials, 2018. **11**(9): p. 1592.

143. JCGM100, *GUM 1995 with minor corrections*, in *Evaluation of measurement data—Guide to the expression of uncertainty in measurement*. 2008, International Bureau of Weights and Measures (BIPM): France.

144. Leach, R., *NanoSurf IV: Traceable measurement of surface texture at the nanometre level*. 2000, University of Warwick: Warwick.

145. Birch, K.P. and M.J. Downs, *Correction to the Updated Edlén Equation for the Refractive Index of Air.* Metrologia, 1994. **31**(4): p. 315-316.

146. Birch, K.P. and M.J. Downs, *An Updated Edlén Equation for the Refractive Index of Air.* Metrologia, 1993. **30**(3): p. 155-162.

147. Ciddor, P.E., *Refractive index of air: New equations for the visible and near infrared.* Applied optics (2004), 1996. **35**(9): p. 1566-1572.

148. Thorlabs. *MB2020/M - Aluminum Breadboard, 200 mm x 200 mm x 12.7 mm, M6 Taps* 2022 [cited 2022 2 Jan]; Available from: https://www.thorlabs.com/thorproduct.cfm?partnumber=MB2020/M.

149. Dynacast. *Aluminium Alloy A383 | ADC12 | 46000 | Aluminium Die Casting*. 2021 [cited 2021 10 Oct]; Available from: https://www.dynacast.com/en-gb/resources/material-information/die-cast-metals/aluminium/aluminum-alloy-383-adc12.

150. Stabler, C., et al., *Thermal properties of SiOC glasses and glass ceramics at elevated temperatures.* Materials, 2018. **11**(2): p. 279.

151. O'Connor, H.J., A.N. Dickson, and D.P. Dowling, *Evaluation of the mechanical performance of polymer parts fabricated using a production scale multi jet fusion printing process.* Additive manufacturing, 2018. **22**: p. 381-387.

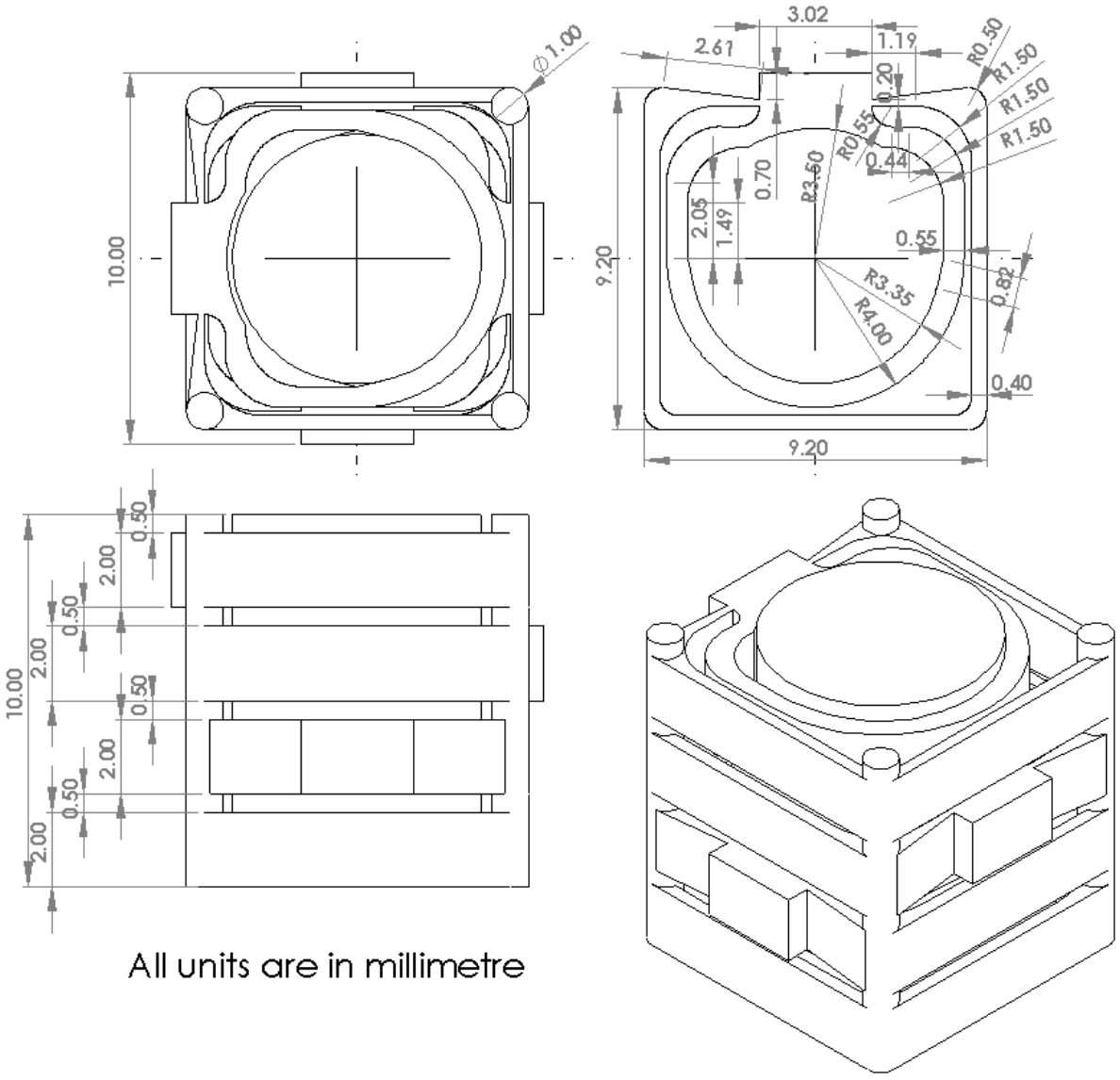
152. Zhou, H., et al., *Sheet and network based functionally graded lattice structures manufactured by selective laser melting: Design, mechanical properties, and simulation.* International journal of mechanical sciences, 2020. **175**: p. 105480.

153. Gumbleton, R., et al., *Evaluating the coefficient of thermal expansion of additive manufactured AlSi10Mg using microwave techniques.* Additive manufacturing, 2019. **30**: p. 100841.

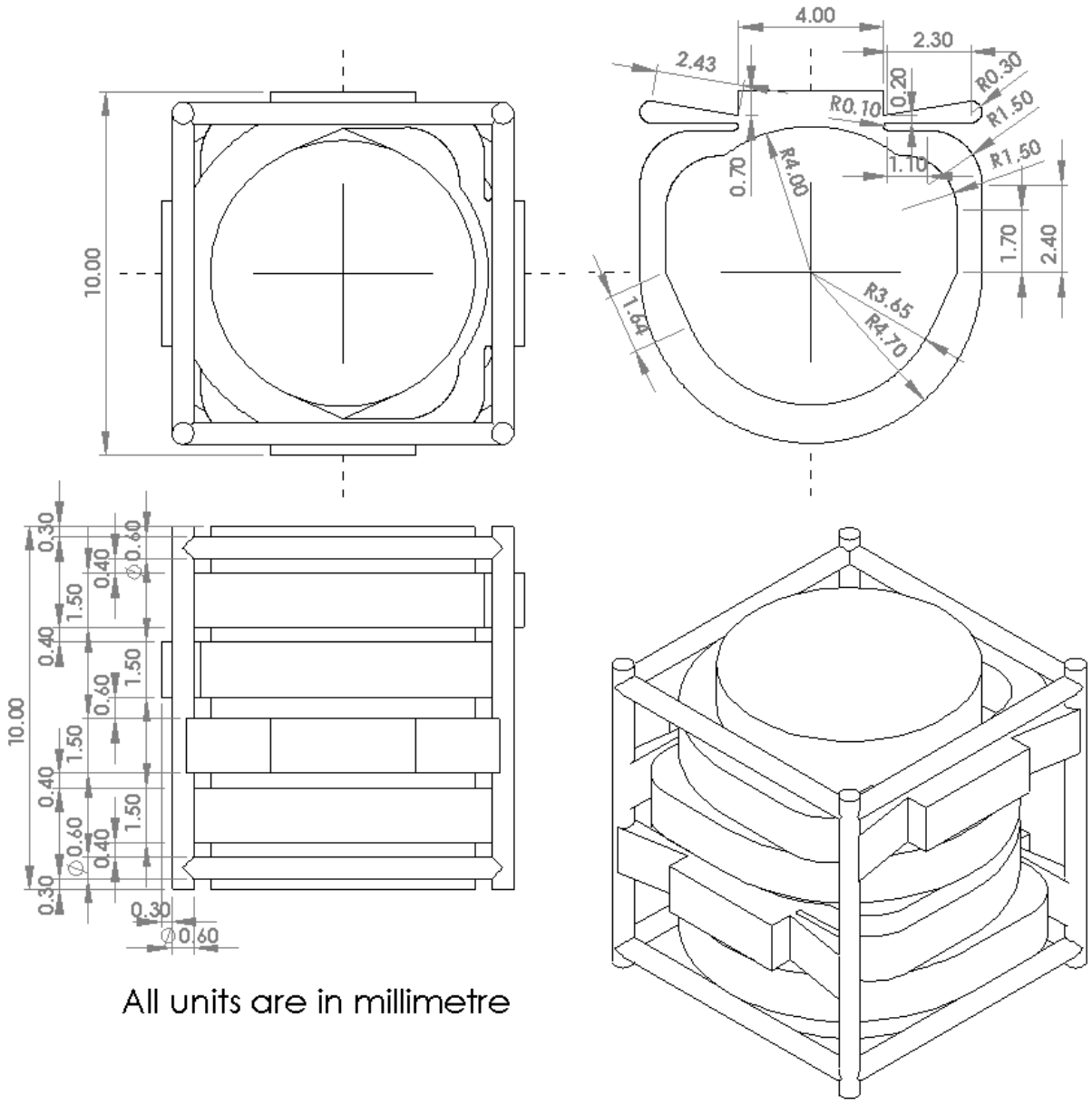
154. Liu, Z., et al., *Effect of yield criterion and variable elastic modulus on springback prediction of Ti-6Al-4V sheet V-shaped bending.* International journal of advanced manufacturing technology, 2021. **116**(5-6): p. 1925-1936.

Appendix

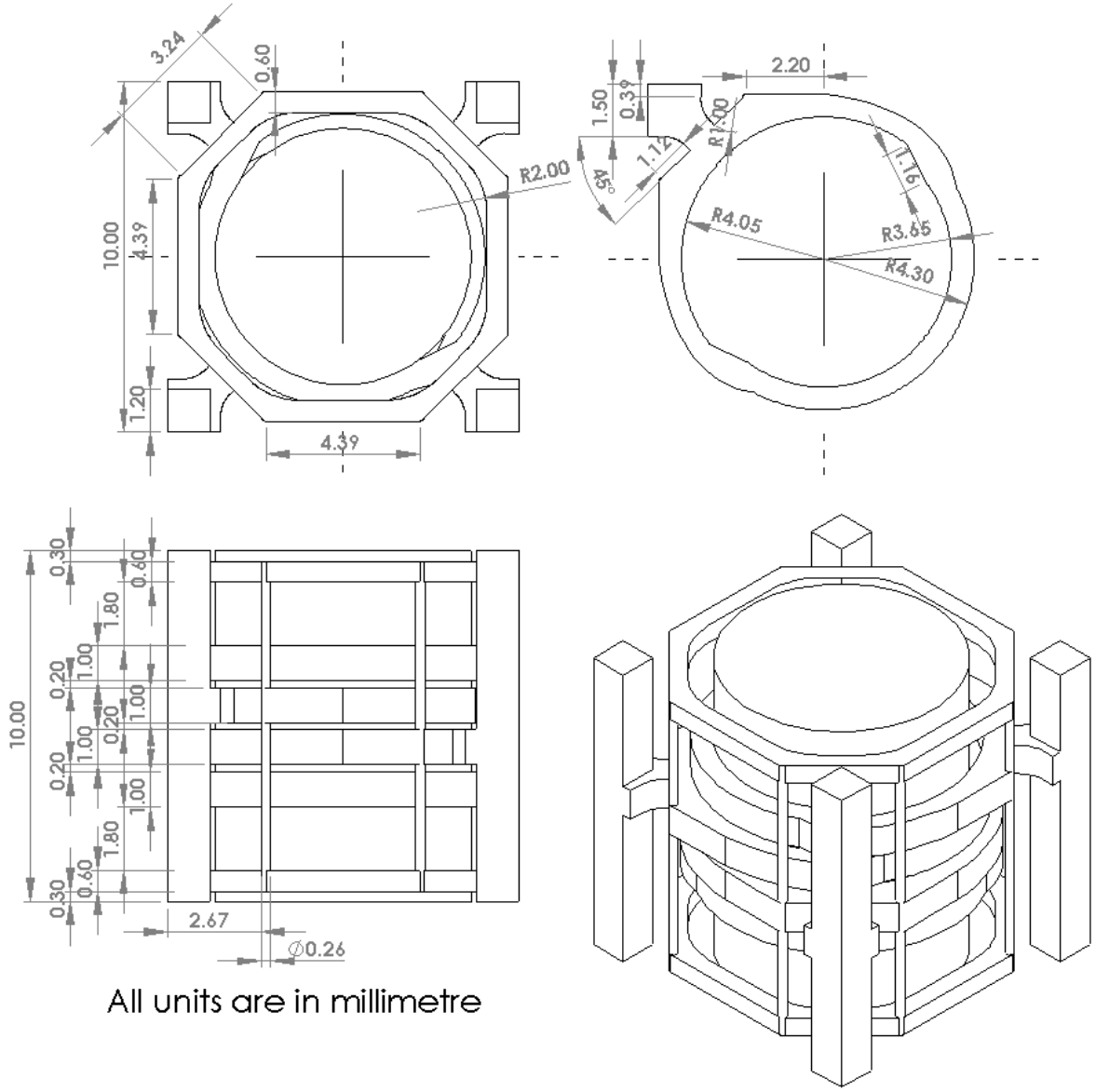
Engineering drawing of Iteration 2.4



Engineering drawing of Iteration 3.1



Engineering drawing of Iteration 4.1



All units are in millimetre